AFRPL-TR-79-79

(2) LEVEL II

AD A079117

SOLAR ROCKET SYSTEM CONCEPT ANALYSIS

Final Technical Report

SATELLITE SYSTEMS DIVISION
SPACE SYSTEMS GROUP
ROCKWELL INTERNATIONAL

Study Manager: F.G. Etherlige

For Period Covering 19 February 1979 - 30 September 1979

DECEMBER 1979

AIR FORCE ROCKET PROPULSION LABORATORY
DIRECTOR OF SCIENCE AND TECHNOLOGY
AIR FORCE SYSTEMS COMMAND
EDWARDS AFB, CALIFORNIA 93523

NOTICES

When U.S. Government drawings, specifications, or other data are used for any purpose other than a definitely related government procurement operation, the government thereby incurs no responsibility nor any obligation whatsoever and the fact that the government may have formulated, furnished, or in any way supplied the said drawings, specifications or other data, is not regarded by implication or otherwise, or in any manner licensing the holder or any other person or corporation, or conveying any rights or permission to manufacture, use or sell any patented invention that may in any way be related thereto.

This final report was submitted by the Satellite Systems Division of the Rockwell International Space Systems Group under Air Force Contract FC4611-79-C-0007, Solar Rocket Systems Concept Analysis. The Rocketdyne Division of Rockwell International provided a significant contribution to the study.

The Satellite Systems Division (SSD) of Rockwell International wishes to recognize the individuals responsible for technical work described herein.

Subject	Responsible Engineer
Study Guidelines	Fred Etheridge
Collector Analysis	Bud Brux
Thruster/Absorber Performance	Jim Shoji (Rocketdyne)
Orbital Mechanics	Janis Indrikis
Spacecraft Design	Dave Reed
Vehicle Synthesis and Performance	Jack Roddy

The SSD also wishes to acknowledge the guidance, direction and suggestions provided by Mr. Curtis Seiph, the AFRPL Study Manager.

This report has been reviewed by the Information Office and is releasable to the National Technical Information Service (NTIS). At NTIS it will be available to the general public, including foreign nations.

This technical report has been reviewed and is approved for publication; it is unclassified and suitable for general public release.

VINCENT N. BENHAM, 1Lt, USAF
Project Manager

FOR THE COMMANDER

EDWARD E. STEIN, Deputy Chief
Liquid Rocket Division

Unclassified

SECURITY CLASSIFICATION OF THIS PAGE *(When Data Entered)*

REPORT DOCUMENTATION PAGE	READ INSTRUCTIONS BEFORE COMPLETING FORM
1. REPORT NUMBER: AFRPL-TR-79-79	2. GOVT ACCESSION NO. / 3. RECIPIENT'S CATALOG NUMBER
4. TITLE *(and Subtitle)*: SOLAR ROCKET SYSTEM CONCEPT ANALYSIS	5. TYPE OF REPORT & PERIOD COVERED: Final rept. 19 Feb [redacted] 30 Sep 79
	6. PERFORMING ORG. REPORT NUMBER: SSD-79-175
7. AUTHOR(s): F. G. Etheridge	8. CONTRACT OR GRANT NUMBER(s): F04611-79-C-0007
9. PERFORMING ORGANIZATION NAME AND ADDRESS: Rockwell International Corporation, Satellite Systems Division/Space Systems Group, 12214 Lakewood Blvd, Downey CA 90241	10. PROGRAM ELEMENT, PROJECT, TASK AREA & WORK UNIT NUMBERS: 573005 EK
11. CONTROLLING OFFICE NAME AND ADDRESS: Air Force Rocket Propulsion Laboratory, Edwards AFB CA 93523	12. REPORT DATE: [redacted]979 / 13. NUMBER OF PAGES: 242
14. MONITORING AGENCY NAME & ADDRESS *(if different from Controlling Office)*	15. SECURITY CLASS. *(of this report)*: Unclassified / 15a. DECLASSIFICATION/DOWNGRADING SCHEDULE

16. DISTRIBUTION STATEMENT *(of this Report)*

APPROVED FOR PUBLIC RELEASE
DISTRIBUTION UNLIMITED

17. DISTRIBUTION STATEMENT *(of the abstract entered in Block 20, if different from Report)*

18. SUPPLEMENTARY NOTES

19. KEY WORDS *(Continue on reverse side if necessary and identify by block number)*

solar rocket
solar concentrator
solar absorber/thruster

20. ABSTRACT *(Continue on reverse side if necessary and identify by block number)*

The objective of the solar rocket concept analysis was to determine the potential value of solar-thermal rockets in large delta velocity space missions. A specific impulse of 872 seconds was achieved by passing hydrogen through a heat exchanger placed at the focal spot of a large parabolic dish solar concentrator mirror. With a windowed chamber type of thruster and a particle-laden hydrogen flow the specific impulse was 1041 seconds. Inflatable construction techniques were determined to be optimum for the large concentrating mirrors based on ease of

DD FORM 1 JAN 73 1473 EDITION OF 1 NOV 65 IS OBSOLETE

Unclassified

SECURITY CLASSIFICATION OF THIS PAGE *(When Data Entered)*

AD A080 887

deployment and low specific mass. It was concluded that the solar rocket offers the mission planner a viable option between the high payload-long trip time of the mercury ion bombardment system and the lower payload-short trip time of a LO_2-LH_2 stage.

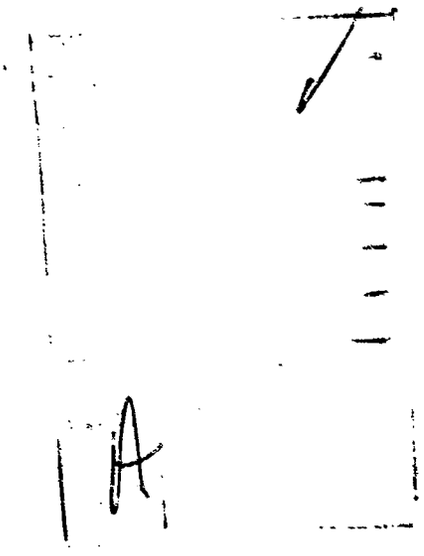

TABLE OF CONTENTS

ILLUSTRATIONS

TABLES

1.0 INTRODUCTION

The use of solar energy to heat propellant for application to earth orbital/planetary propulsion systems is of interest because of its unique performance capabilities. A representative solar heated hydrogen rocket propulsion system is capable of generating thrust measured in pounds and specific impulses ranging between 870 and 1040 seconds. The achievable specific impulse values are approximately double those delivered by a chemical rocket system and the thrust is at least an order of magnitude greater than that produced by a mercury bombardment ion propulsion thruster. The primary advantage the solar heater thruster has over a mercury ion bombardment system is that its significantly higher thrust permits a marked reduction in mission trip time. The low earth orbit (LEO) to geosynchronous equatorial orbit (GEO) maneuver provides a representative example of the transit times. The solar rocket can conduct the maneuver in approximately 14 days whereas the ion system requires on the order of 180 days. In comparison, a conventional chemical rocket system, the Centaur, for example, can perform the same missions in a few hours. There are, however, significant differences in payload capability between the propulsion concepts described above. The solar rocket offers the mission planner a viable alternative between the high payload-long trip time of an ion propulsion device and the relatively low payload-short trip time of the chemical system.

The concept of using solar energy to heat propellants for use in an earth orbital/planetary rocket propulsion system is not new. In 1962, for example, the Air Force Rocket Propulsion Laboratory (AFRPL) sponsored an analytical and experimental program to demonstrate the feasibility of the solar heated rocket engine. In a test program conducted at the AFRPL, a specific impulse of 680 seconds was achieved. The thruster utilized hydrogen as the propellant. Although the initial results were encouraging, the program was not pursued. The performance capabilities of the launch vehicles available in the early 60's were such that the full potential of the solar rocket could not be realized. The development of the Space Transportation System (STS), however,

offers the opportunity to utilize the full performance potential of the solar rocket. In addition, the use of hydrogen as an orbit transfer vehicle propellant is now a well understood technology and would require little, if any, additional development for use in a solar rocket system. The development of inflatable, high performance concentrators, a key element in the solar rocket system, has also shown significant progress since the completion of the earlier AFRPL program. An additional factor to be considered is that as the 1980-1990 time period approaches, a far greater number and variety of mission requirements may be identified than was possible in the early 60's. These factors all contributed to the decision to reexamine the potential of the solar thermal rocket. As a result, the AFRPL sponsored the Solar Rocket Systems Concept Analysis Study described herein.

The following sections of this report will discuss concentrator and thruster/absorber design and performance. The Rocketdyne Division of Rockwell International was responsible for the work conducted on the absorber/thruster system. The key factors in the area of orbital mechanisms and spacecraft design parameters, as they relate to integration into the Shuttle Orbiter, will be discussed. Parametric and point design performance analyses were conducted and are discussed in detail in the appropriate sections of the report. Recommendations and suggestions for future work are also presented.

2.0 SUMMARY

GUIDELINES

The objectives of the Solar Rocket System Concept Analysis study were to provide an assessment of the value of solar thermal propulsion relative to more conventional propulsion concepts and to develop an understanding of the factors which bear on its technical feasibility.

The Space Transportation System (STS) was selected as the launch vehicle for the solar thermal rocket powered spacecraft. STS performance capability from both KSC and VAFB was established. The major portion of the trade studies conducted were based on KSC launch performance. The STS 65,000 lb KSC payload capability has been reduced 3000 lbs to allow for the cradle required to install the vehicle and payload in the cargo bay. Similarly, the usable cargo bay length has been reduced to 56 ft. The reduction is due to a requirement that Shuttle crew members be able to enter the cargo bay through the airlock. In order to obtain an insight into both spacecraft densities and length of potential payloads, data were obtained on representative SAMSO spacecraft. The P80-1, GPS, DSCS III, DSP and FLTSATCOM spacecraft were included in the analysis. The FLTSATCOM was used in preparing configuration layouts and checking cargo bay capability. It should not be construed, however, that the FLTSATCOM was selected as the baseline payload for the solar rocket; it was used only on a representative example. Additional discussion of this material may be found in Section 7.0, Spacecraft Design.

COLLECTOR CONCEPT AND PERFORMANCE

The primary requirements of a solar collector for a solar rocket system are deployability, low specific mass, and high concentration ratio. The latter is necessary to achieve high temperature and specific impulse of the heated propellant. Of the various candidates considered, only an inflated, non-rigidized concentrator design meets these requirements. Experience gained from fabrication and testing of a 44.5 ft. diameter paraboloidal collector of this design in 1964 under Project ASTEC (Reference 1) supports the feasibility of such an approach. An off-axis version was selected to avoid impingement and heating from the engine exhaust plume. Analysis indicates that

fluid temperatures of over 7000°R are achievable with this design. This discussion is based on a concentrator surface error standard deviation of 1/8° and a peak concentration ratio of 14,328:1. Additional information is presented in Section 4.0 - Collector Concept and Performance.

THRUSTER/ABSORBER PERFORMANCE

The theoretical propellant performance potential was evaluated for six propellant candidates. These propellants included hydrogen (H_2), methane (CH_4), ammonia (NH_3), hydrazine (N_2H_4) hydrogen/hydrazine (H_2/N_2H_4) mixture, and hydrogen/carbon (H_2/C) mixture. Hydrogen resulted in the highest theoretical vacuum specific impulse (77-percent higher than the next highest propellant) and therefore was selected as the primary propellant.

As presented in Table 1, the delivered vacuum specific impulse of two absorber/thruster concepts were evaluated to assess their potential. The two concepts included: (1) the heat exchanger cavity absorber/thruster, and (2) the particulate absorber/thruster. For the heat exchanger cavity absorber/thruster, the propellant temperature was limited to a maximum of 5000°R due to wall material limitations. As shown in Table 1, this concept using hydrogen and a 100-to-1 area ratio nozzle achieved a delivered vacuum specific impulse of 872 lb_f sec/lb_m for a one thruster-two absorber configuration and 861 lb_f sec/lb_m for a two thruster-two absorber configuration. Using ammonia at 5000°R, the heat exchanger cavity absorber/thruster resulted in a delivered specific impulse of 440 lb_f sec/lb_m.

The delivered vacuum specific impulse for the particulate absorber/thruster with a 7000°R propellant (hydrogen/carbon) temperature and a 100-to-1 area ratio nozzle was 1041 lb_f sec/lb_m (table 1) for a one thruster-two absorber configuration. Higher gas temperatures are possible (i.e., higher specific impulses) with the particulate absorber/thruster than with the heat exchanger cavity absorber/thruster since the propellant is heated directly by solar radiation as well as through the use of a heat exchanger. A detailed discussion of the above material is presented in Section 5.0, Thruster/Absorber Performance.

SPACECRAFT PERFORMANCE

Based on the engine performance data presented above, a series of parametric spacecraft performance charts were prepared. The purpose of this analysis was

Table 1. Solar Rocket Delivered Specific Impulse Summary

	Heat Exchanger Cavity Absorber/Thruster			Particulate Absorber/Thruster
	Hydrogen(H_2)		Ammonia(NH_3)	Hydrogen/Carbon (H_2/C)
Collector:				
Number	2		2	2
Diameter, Ft	100		100	Equivalent to 100 ft dia using optimistic absorber analysis
Surface Angular Error, Degree	1/4		1/4	1/8
Absorber/Thruster				
Number of Thrusters for Two Absorbers	1	2	1	1
Propellant Gas Temperature, ^{o}R	5000	5000	5000	7000
Throat Diameter, In.	0.826	0.584	0.576	0.489
Area Ratio	100	100	100	100
Chamber Pressure, Psia	50	50	50	50
Flowrate, Lb/Sec	0.050	0.025	0.20	0.013
Thrust, Lb_f	44	21.5	88	14
Delivered Vacuum Specific Impulse Lb_f Sec/Lb_m	872	861	440	1041

to select the most promising concepts which would be examined in more detail later in the study. Parametric performance estimates were also prepared for LO_2-LH_2, N_2O_4-MMH and mercury ion bombardment systems. This material was used in performance comparisons with the solar rocket. Some representative performance data is presented in Table 2.

Table 2. Solar and Chemical Rocket Performance Comparisons

Parameter	Solar #1	LO_2-LH_2	N_2O_4-MMH	Ion	Solar #2
ΔV, ft/sec	19,200	14,000	14,000	19,200	15,750
Trip Time	14 days	5 hrs	5 hrs	180 days	40 days
Isp, sec	872	475	320	2940	872
Mass Fraction	0.85	0.90	0.92	0.68	0.85
Payload, lbs	20,500	20,400	11,000	44,000	29,000

NOTE: Solar rocket performance is based on the use of a 40 x 14.5 ft. hydrogen tank; all other data is based on a 62,000 lb Shuttle separation weight. Mass fraction is defined as the ratio of the weight of usable propellant to the sum of the weight of propellant loaded, tankage and all spacecraft hardware except the payload.

It should be observed that the solar #1 and LO_2-LH_2 performance is essentially the same. Increasing the trip time to 40 days, however, results in a significant increase in the performance of the solar rocket. Because the solar rocket is heavily trip time dependent, the more detailed performance analysis (Section 8.0) is presented as a function of trip time. Payload data for the "exact" case is presented in Figure 1. By "exact", it is meant that insulation, collector, spacecraft components, etc. are computed for each case rather than assume a mass fraction as was done in Table 1. For that reason, the information in Table 1 and Figure 1 may not be in exact agreement. Additional details on the parametric analysis may be found in Section 3.0, Performance Boundaries; the detailed performance analysis is presented in Section 8.0, Vehicle Synthesis and Recommendations.

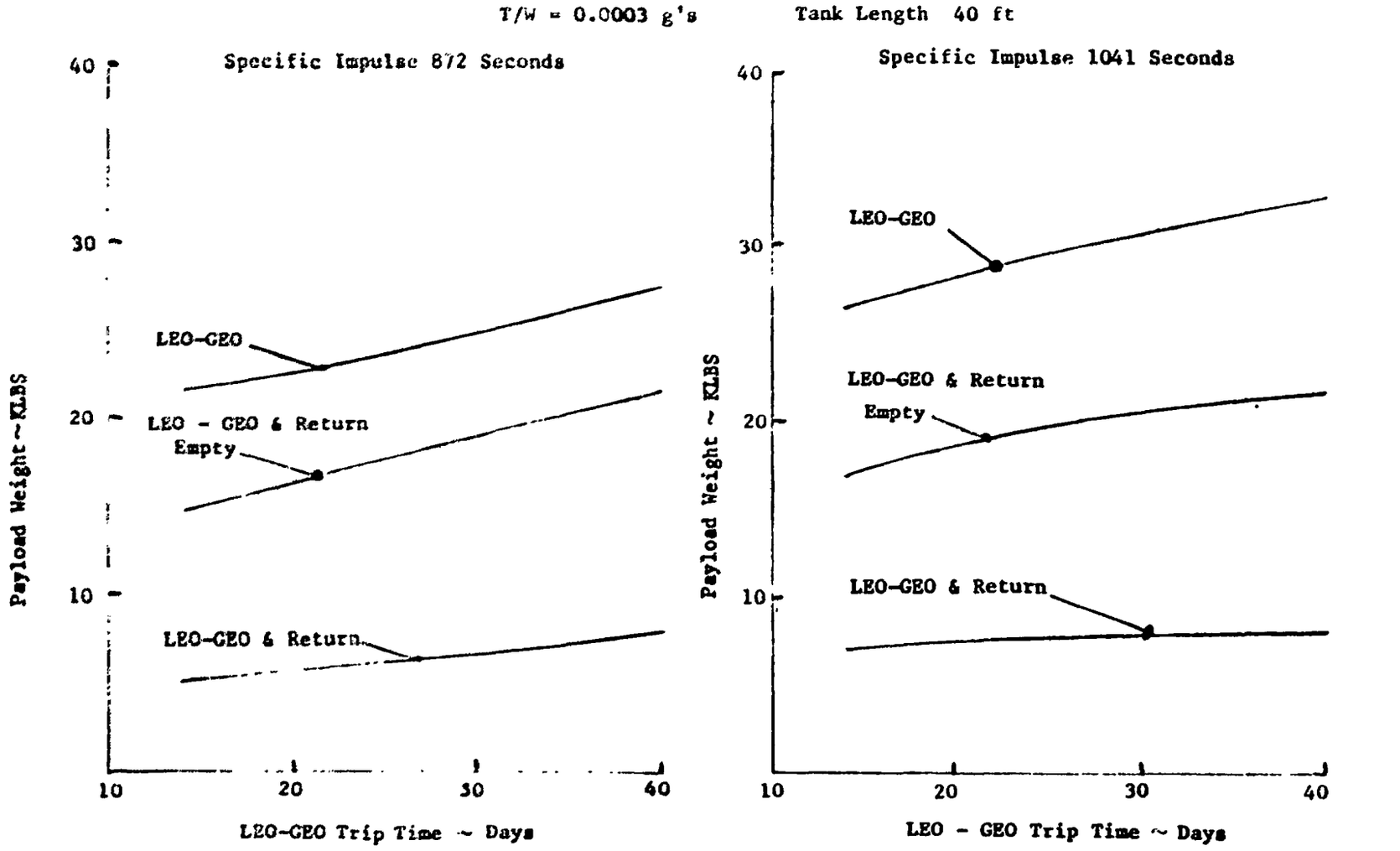

Figure 1. Single Orbiter Launch - Payload Capability

CONCLUSIONS

It was concluded that the solar rocket offers the mission planner a viable option between the high payload-long trip time of the mercury in bombardment system and the lower payload-short trip time of a LO_2-LH_2 stage. The study also shows that the 5000°R hydrogen thruster system and associated collector are within the state-of-the-art, and recommends the fabrication of test hardware.

3.0 STUDY GUIDELINES

The guidelines, assumptions, and performance boundaries used in the study are described in this section of the report. A brief, parametric analysis is also included to establish attainable performance boundaries. This was done to identify the most promising options to be analyzed in detail in Section 8.0, Vehicle Synthesis and Performance. In accordance with the contractual Statement-of-Work (SOW), the LEO-GEO maneuver is the baseline mission. Both one way and the spacecraft-only return to the Shuttle mission modes were used. Other mission studies are presented in Section 6.0, Orbital Mechanics. Parametric comparisons of the solar rocket with LO_2-LH_2, N_2O_4-MMH and mercury ion bombardment propulsion systems are also presented in this section of the report.

SHUTTLE CAPABILITY

The decision to use the Shuttle as a solar rocket spacecraft launch vehicle allowed some design criteria to be established. The Shuttle performance capability for both the KSC and VAFB launch sites is presented in Figures 2 and 3, respectively. For the analysis conducted herein, the Shuttle KSC payload weight was assumed to be 65,000 lbs. These values reflect a 28.5 degree launch inclination and payload separation altitude of 150 n.mi. The corresponding data for VAFB shows a payload capability of 39,000 lbs with a 90° inclination and a 150 n.mi. payload separation altitude. A cradle weight of 3,000 lbs was assumed for launches from both sites. Based on this assumption, an on-orbit launch weight of 62,000 lbs was used for KSC flights and 36,000 lbs for VAFB launches. It should be observed, however, that for the KSC launch case, that the Shuttle can carry 65,000 lbs to 220 n.mi. The difference in the delta V required to raise the orbit from 150 or 220 n.mi. to geosynchronous equatorial orbit is insignificant. The drag, and attendant ΔV losses on a large spacecraft, such as the solar rocket system, varies significantly between 150 and 220 n.mi. It will be shown in Section 6, Orbital Mechanics, that there is an order of magnitude reduction in vehicle drag between 150 and 220 n.mi. For that reason, the higher altitude has been used in the study.

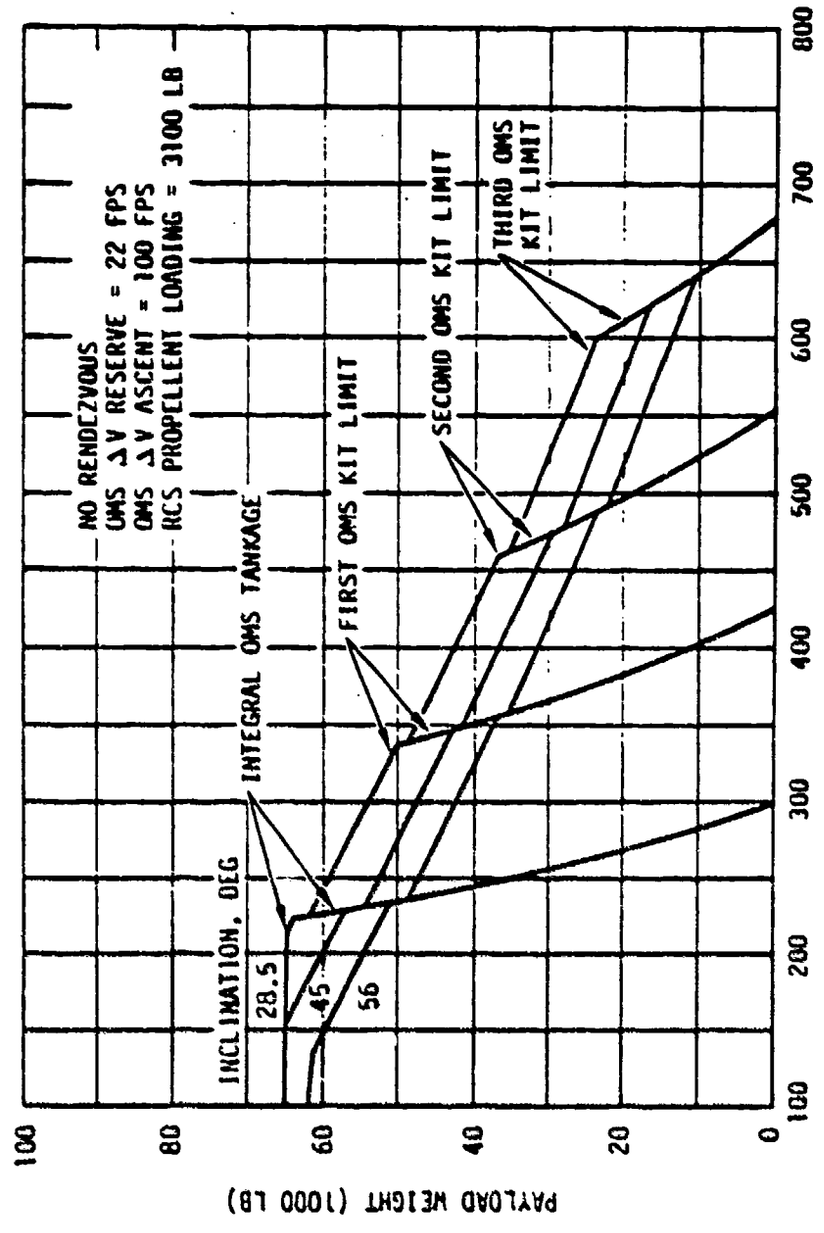

Figure 2. Payload to Circular Orbit - KSC Launch

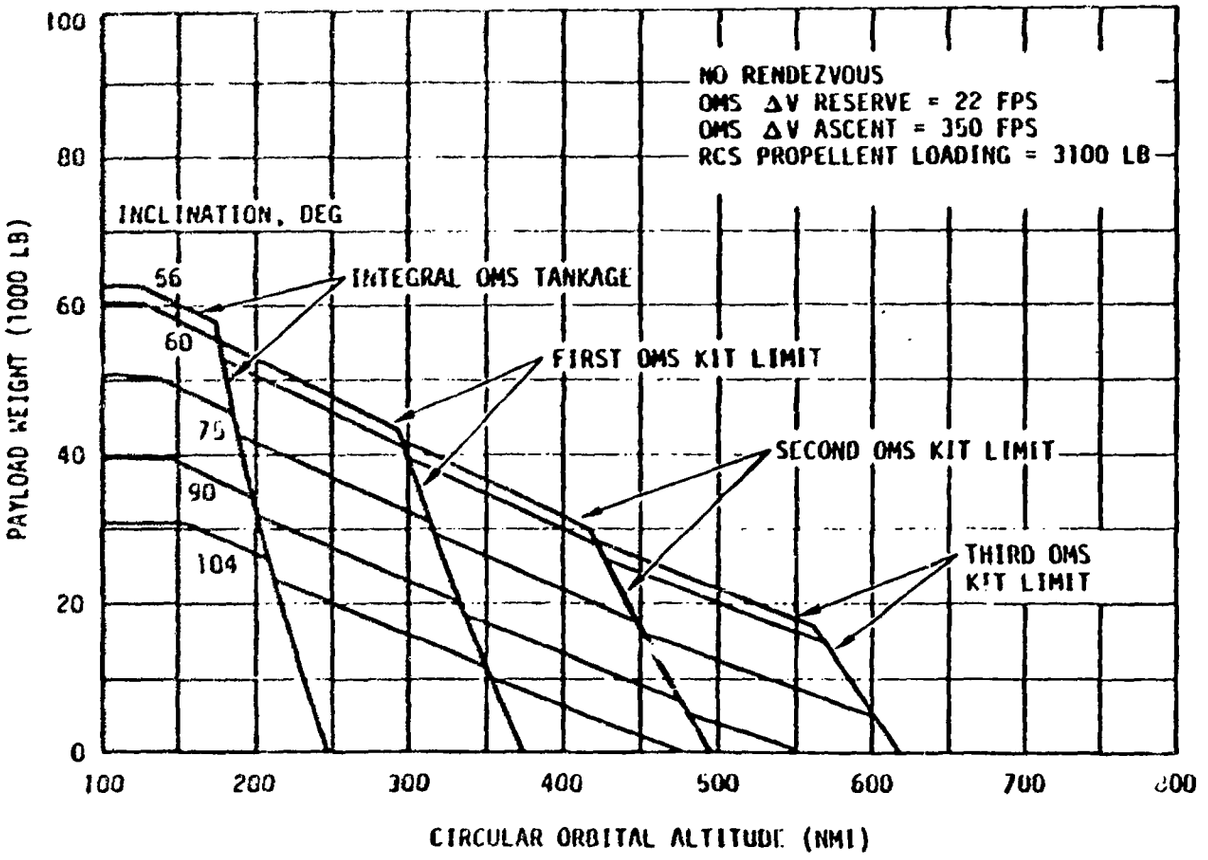

Figure 3. Payload to Circular Orbit - VAFB Launch

The required delta V for a mission to geosynchronous equatorial altitude is shown in Figure 4 as a function of thrust to weight ratio and trip time. (Additional discussion on this figure is presented in Section 6.0). Assuming a 62,000 lb Shuttle separation weight and a solar rocket thrust of 10 lbs, the resulting T/W is 1.6×10^{-4}. This value indicates the required delta V is 19,200 ft/sec. It may also be seen that increasing the thrust to 40 lbs does not change the value of the required delta V. Payload weight for a range of delta V's is presented in Figure 5 for specific impulse values ranging between 500 and 1100 seconds. A stage mass fraction of 0.80 was used to prepare this curve. More precise mass fractions were computed and are discussed in Section 8.0, Vehicle Synthesis and Performance. To show the effect of improved mass fraction, a case for Isp = 1100 seconds and $\nu_b = 0.90$ was computed.

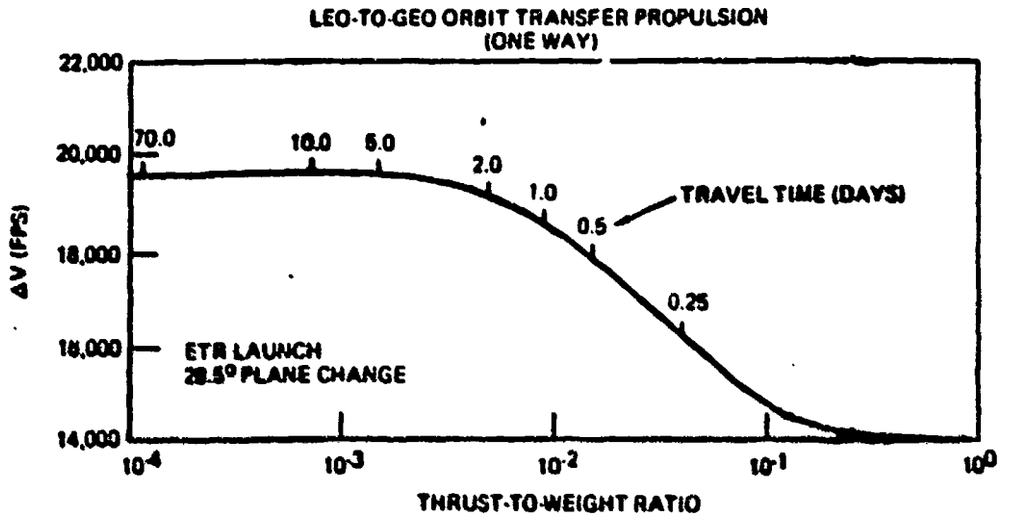

Figure 4. Delta-V Requirements Versus Thrust to Weight

Several key factors relative to solar rocket performance are indicated on the curve. It should be observed, for example, that increasing delta V from 14,000 to 19,200 ft/sec reduces the payload 9,000 lbs for an assumed Isp of 900 seconds. This is a significant reduction and suggests a strong effort should be made to reduce the delta V requirements by a means of flying different trajectories. The curve also indicated that a spacecraft with a 19,200 ft delta V requirement would require a 300 second increase in specific impulse to obtain the same performance as a vehicle operating with a 14,000 ft/sec

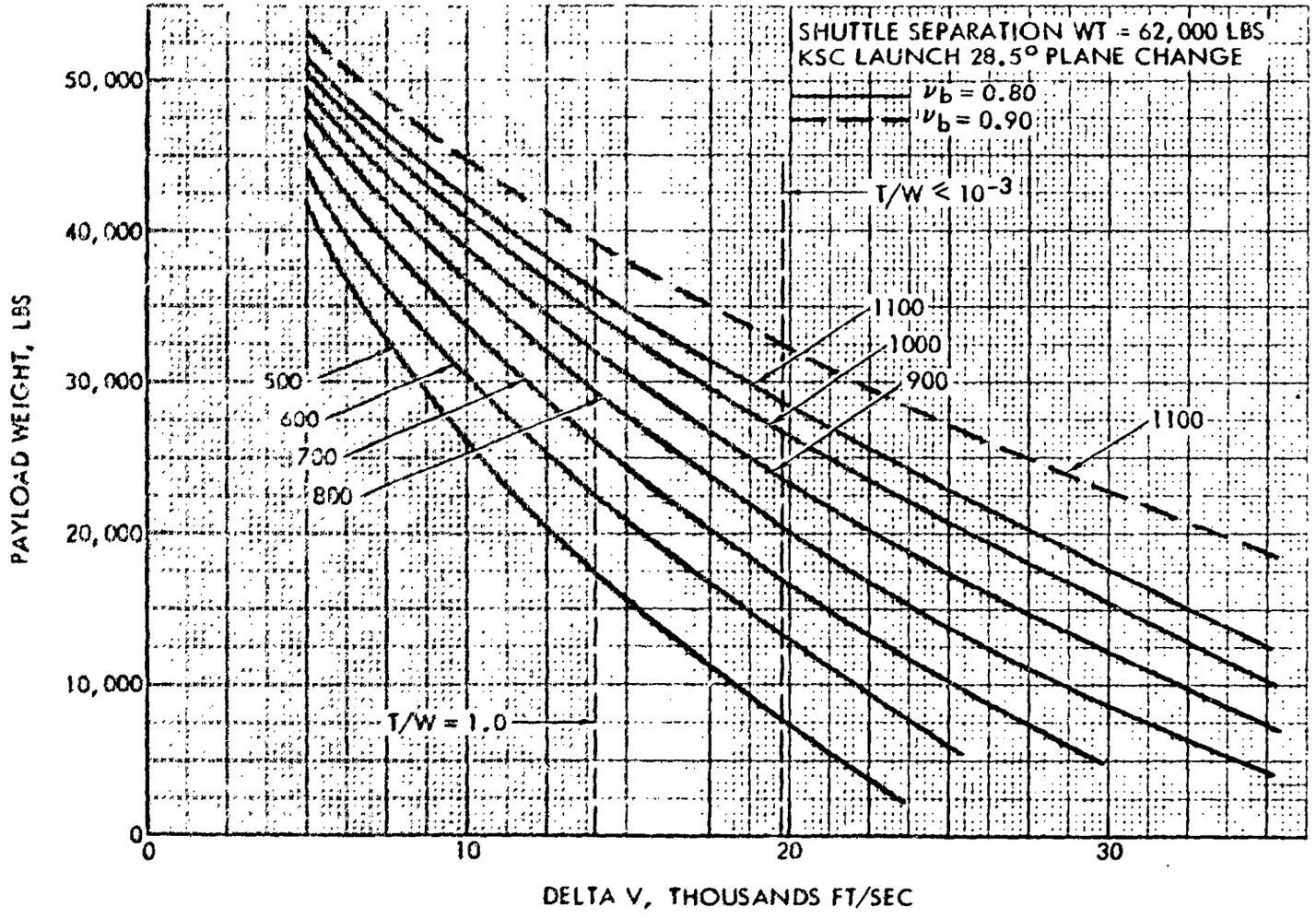

Figure 5. Payload Weight as a Function of Delta V and Specific Impulse

delta V requirement. The figure also indicates the payload gain resulting from increasing the mass fraction from 0.80 to 0.90 for the 62,000 lb vehicle under consideration. Increasing the mass fraction by this amount represents a significant achievement; it requires the reduction of the inert weight of the spacecraft with an 0.80 mass fraction by 40%.

The nominal dimensions of Shuttle cargo bay are 15 ft diameter and 60 ft long. The LH_2 propellant will require the use of multilayer insulation systems and an allowance for cradle thickness must be made. Tankage inside diameters of 13.5, 14.0, and 14.5 ft have been assumed. In Section 8.0 of this report, insulation thickness as a function of mission duration has been computed. The purpose of assuming a range of tank diameters is to show the effect of diameter on tank volume. This relationship is presented in Figure 6. It has also been assumed that the usable length of the cargo bay is 56 ft. The reduction from the nominal value of 60 ft is due to a crew access requirement. This factor is discussed in detail in Section 7.0, Spacecraft Design. The tankage geometry assumed $\sqrt{2}$ elliptical heads. Elliptical heads were shown because such a tank will, for the same required volume and diameter, always be shorter than a tank with hemispherical heads.

Because of the low density of liquid hydrogen (4.4 lbs/cu. ft.) concern was expressed that the tank volume required to hold the quantity of propellant consistent with a 62,000 lbs separation weight may exceed the volume of the cargo bay. Using the material presented in Figure 6 and assuming a 5% ullage fraction, an analysis was conducted to determine the length of the hydrogen tank required as a function of diameter for the 62,000 lbs separation case. This information is presented in Figure 7. The figure indicates that no space is available for the solar rocket vehicle or payload for the case assumed. Because of the desirable cost factors associated with a single Shuttle launch, a brief study was conducted to determine the maximum payload that could be carried into geosynchronous equatorial orbit with a single Shuttle launch. Reference was made to a program SSD conducted for SAMSO in 1971, Orbit-to-Orbit Shuttle Feasibility Study. SAMSO has specified certain payload conditions which restricted the length of the propulsion system to approximately 40 ft. Using this guideline, the information presented in Figure 8 was generated. The figure indicates the tank length for the 62,000 lb case for a specific impulse of 872 seconds. Superimposed on the same figure is the corresponding

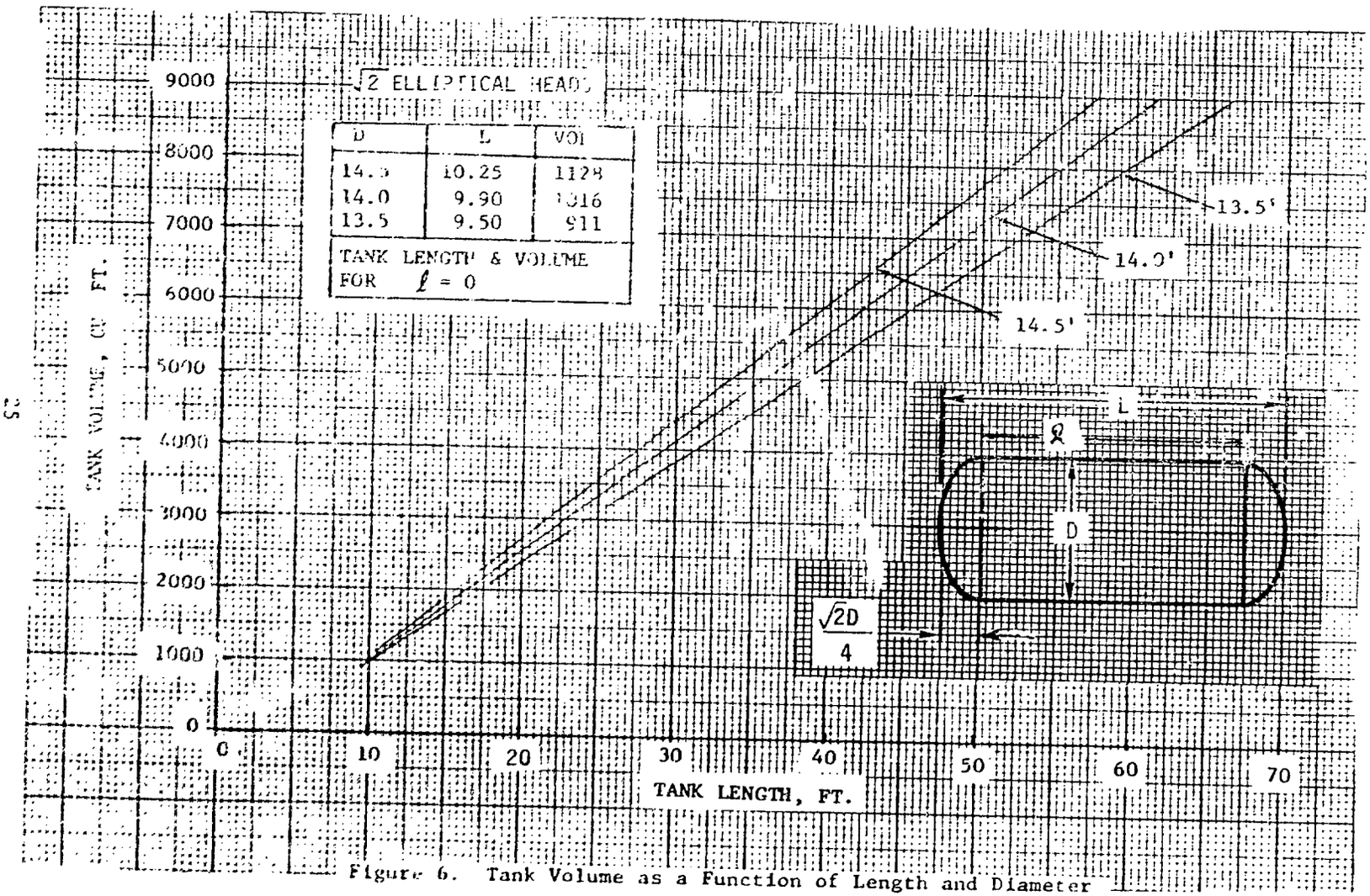

Figure 6. Tank Volume as a Function of Length and Diameter

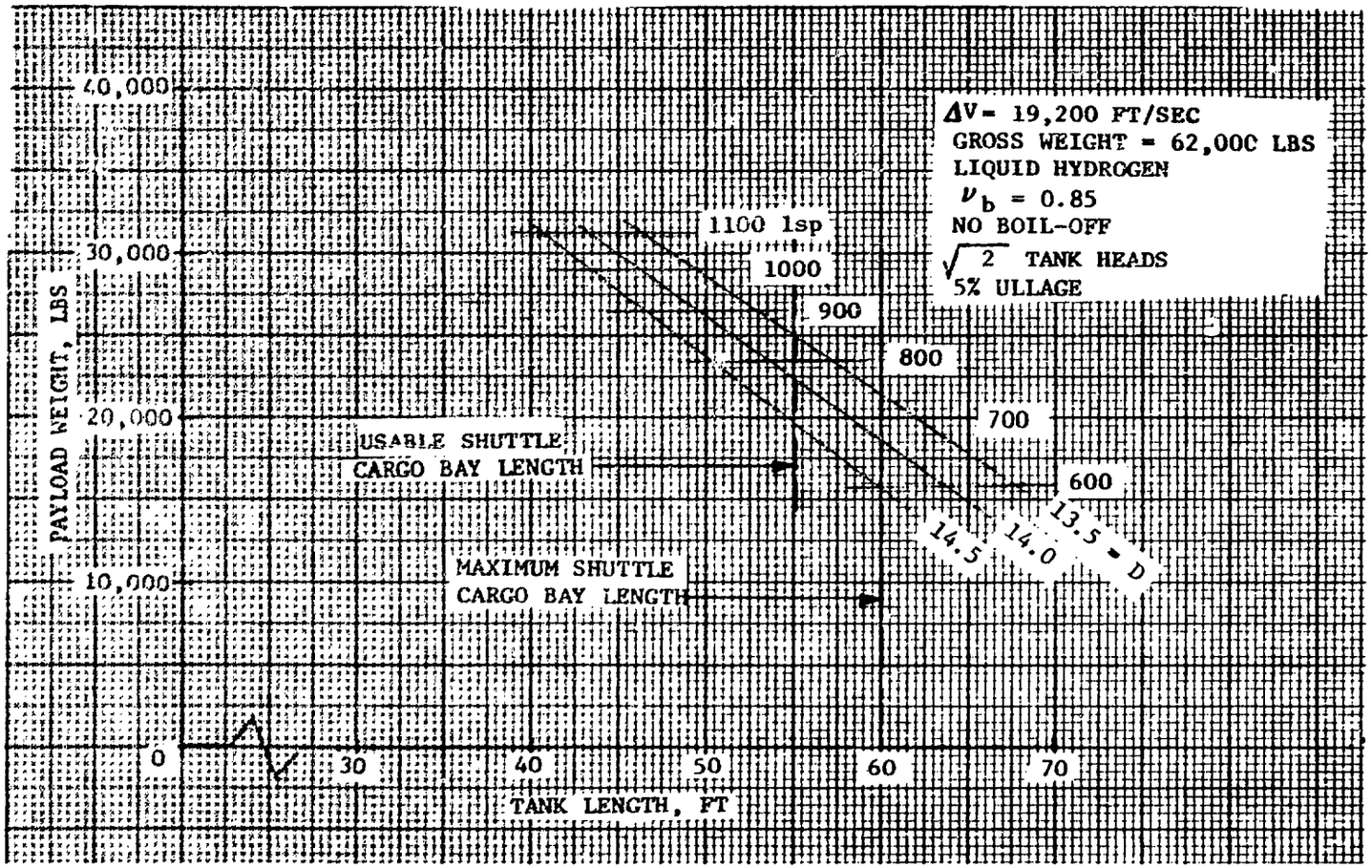

Figure 7. Payload as a Function of Tank Geometry and Specific Impulse

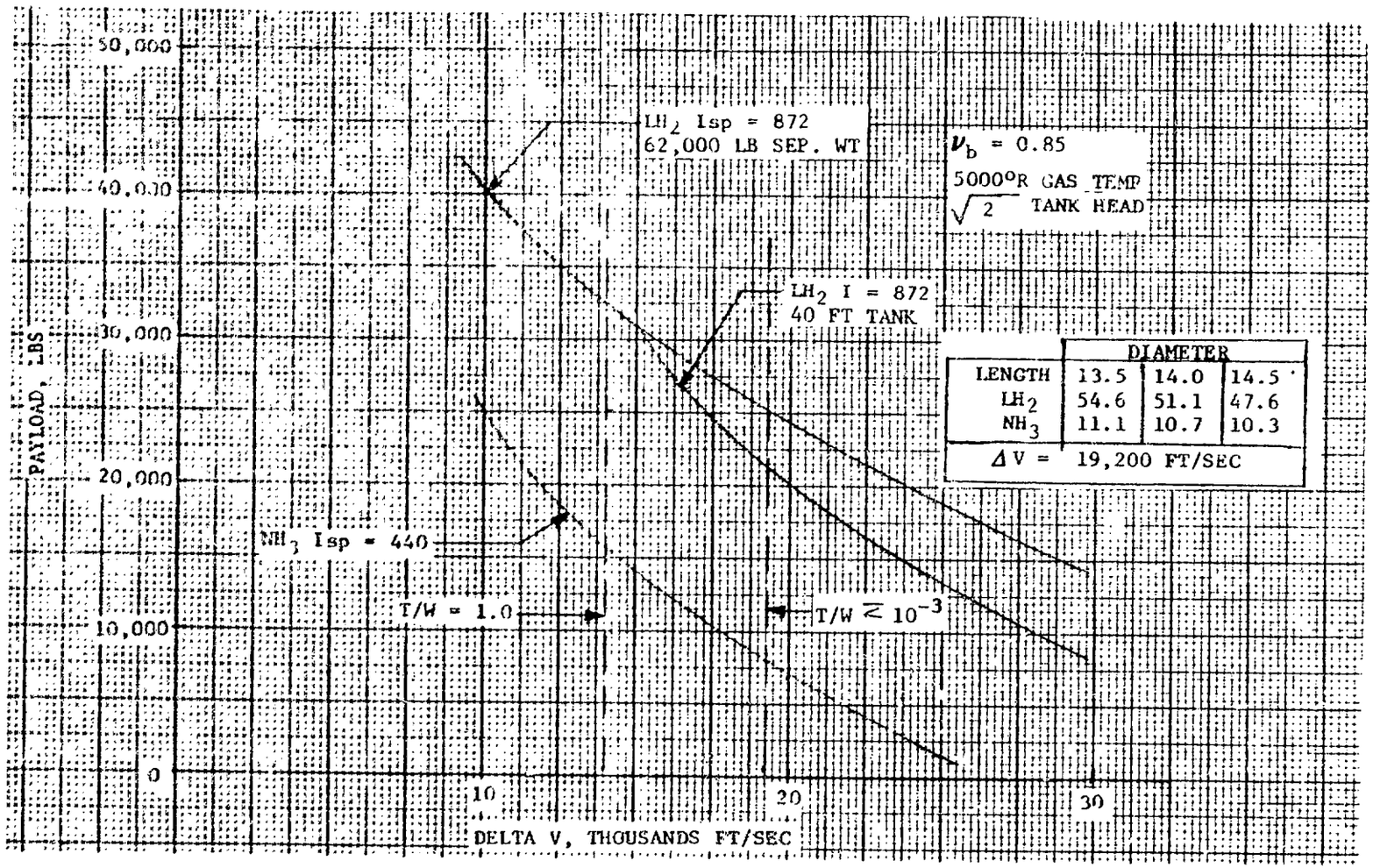

Figure 8. Payload Weight as a Function of V-LH_2 and NH_3

performance for a 40 ft. length tank.

The AFRPL indicated that additional propellants were to be studied. Details of the other propellants analyzed are discussed in Section 5.0, Thruster/Absorber Performance. Ammonia is one of the propellants discussed in that section and the corresponding performance is also shown in Figure 8. Note that the overall tank length of the ammonia tank is very short. The resulting payload performance however, is at best marginal and ammonia did not receive additional consideration as a propellant.

In order to make it possible to determine the effect of specific impulse and mass fraction on solar rocket performance, several carpet plots were prepared. The solar rocket information is presented in Figure 9 and is based on a hydrogen tank 40 ft. long and 14.5 ft. in diameter. As indicated on the figure, the information presented is for a one way trip, LEO to GEO.

CHEMICAL STAGE ANALYSIS

A brief study was conducted to provide a basis for a comparison between the solar rocket and a representative chemical system. The data utilized was the Centaur, SAMSO Orbit-to-Orbit Shuttle and the NASA Future Earth-to-Geosynchronous Orbit Transportation System Study, References 2, 3 and 4, respectively. A carpet plot, Figure 10 was prepared to show the effect of specific impulse and mass fraction on the payload capability of Shuttle launched cryogenic systems. The Centaur data was obtained from References 5 and 6 and telephone conversations with personnel of the Convair Centaur project office. Convair is currently under NASA contract to conduct a comprehensive study relating to the installation of the Centaur in the Shuttle cargo bay. Convair reported the Shuttle/Centaur combination can place a payload of 12,200 lbs into geosynchronous equatorial orbit. Note the Figure 10 has been prepared using a 62,000 lb Shuttle separation weight. For the ΔV and Isp values selected, approximately 37,000 lbs of propellant are required. The Centaur propellant capacity, however, is approximately 30,000 lbs. Entering the figure at ν_b = 0.85 and Isp = 444 seconds, the indicated payload is 16,500 lbs. This value exceeds the 12,220 lbs indicated for the Centaur because the data in the figure is based on a larger propellant capacity. The intent is to show the payload potentially attainable with Centaur technology in addition to the estimated capability of the current Centaur vehicle.

The effect of improved technology may be seen by the OOS and BAC examples. Due to mission peculiar requirements, the weight of both the OOS and BAC

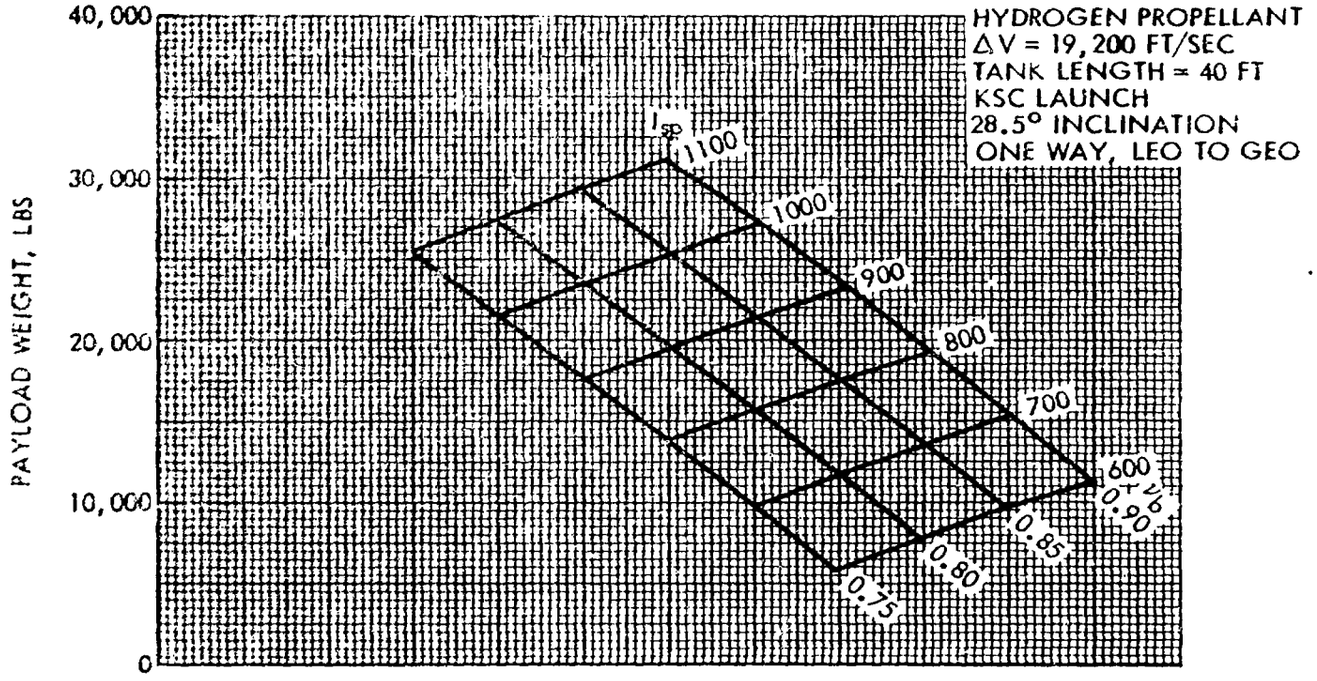

Figure 9. Payload Weight as a Function of Specific Impulse and Mass Fraction - 40 Ft. Tank Cue - 14.5 Ft. Tank Diameter

VEHICLE	ν_b	I_{sp}	PAYLOAD
CENTAUR D-IT	0.85	444	12,200
OOS STUDY*	0.88	470	19,500
BAC STUDY*	0.92	476	21,600

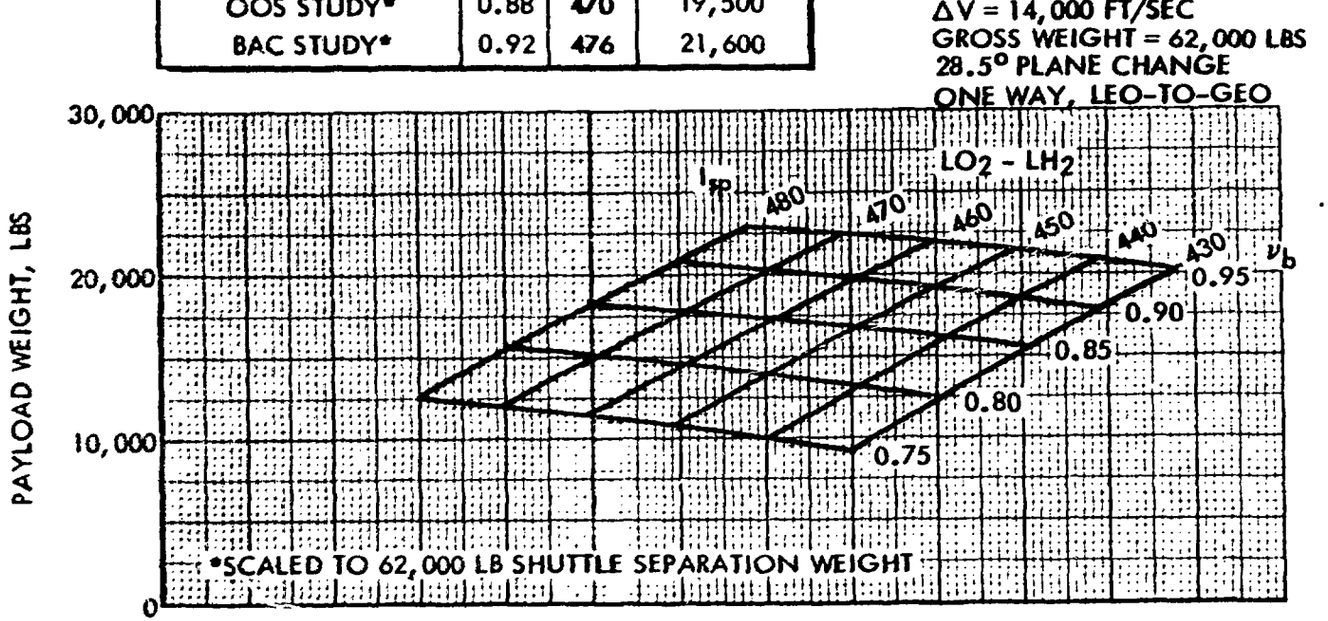

Figure 10. Payload as a Function of Specific Impulse and Mass Fraction for LO_2-LH_2 Stage

vehicles exceeds the capability of a single Shuttle launch. The mass fractions and Isp values used in these studies were applied to the 62,000 lb Shuttle separation weight case and payloads indicated in Figure 10 were computed.

As previously indicated, the carpet plots presented in this section of the report are for the "up only" case. "Up and down" cases are discussed in Section 8.0, Vehicle Synthesis and Performance. A brief check of the Centaur round trip capability was made. It was found that, despite the ability to place 12,200 lbs in GEO, the stage has no round trip capability.

A carpet plot for the N_2O_4-MMH propellant combination is presented in Figure 11. (Note the payload scale change relative to Figure 10). A comparison of the data in Figures 10 and 11 indicates the performance of the solar rocket is significantly superior to the N_2O_4-MMH system.

ELECTRIC PROPULSION SYSTEMS

The performance of a mercury bombardment ion propulsion system is presented in this section of the report. The studies conducted in anticipation of the MSFC Solar Electric Propulsion System (SEPS) activities provided the background for the ion propellant spacecraft baseline. The spacecraft was sized to accommodate a 60 kw solar array and assumed the use of ten 30 cm mercury thrusters. The total dry weight of the spacecraft was estimated to be 3900 lbs. The weight includes allowances for the solar array, power distribution/storage, astronics, structure/thermal control, propulsion (thrusters, power conditioning, etc.) plus a growth allowance. As an indication of the weight of the propellant and tankage, consider the "up only" case for a 62,000 lb Shuttle separation weight and Isp = 3000 seconds. Analysis indicates the weight of the mercury and positive expulsion tankage is 13,500 lbs., bringing the total weight of the spacecraft to 17,400 lbs with a corresponding payload of 44,600 lbs. When the analysis is expanded to include the up and down case, the weight of the spacecraft increases to 19,000 lbs with a corresponding payload of 43,000 lbs. Because of the very high density of mercury, the propellant for both the up and down phases of the trip can be carried in the same tank.

Parametric performance of a representative mercury bombardment system is presented in Figure 12. It should be observed that the mercury system can utilize the full 62,000 lb capability of the Shuttle whereas the separation weight of the 40 x 14.5 ft tank LH_2 case is on the order of 51,500 lbs.

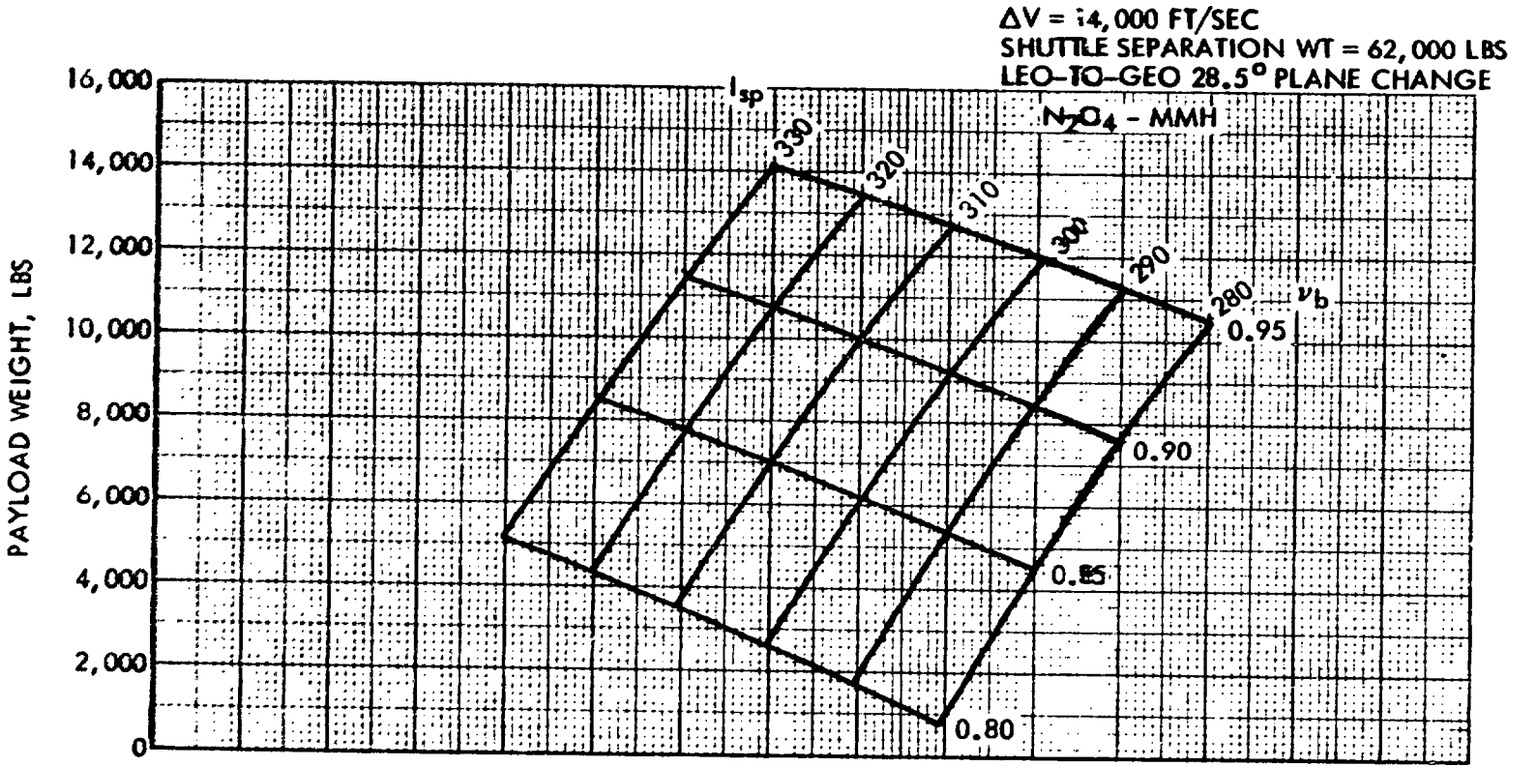

Figure 11. Payload Weight as a Function of Specific Impulse and Mass Fraction, N_2O_4 - MMH

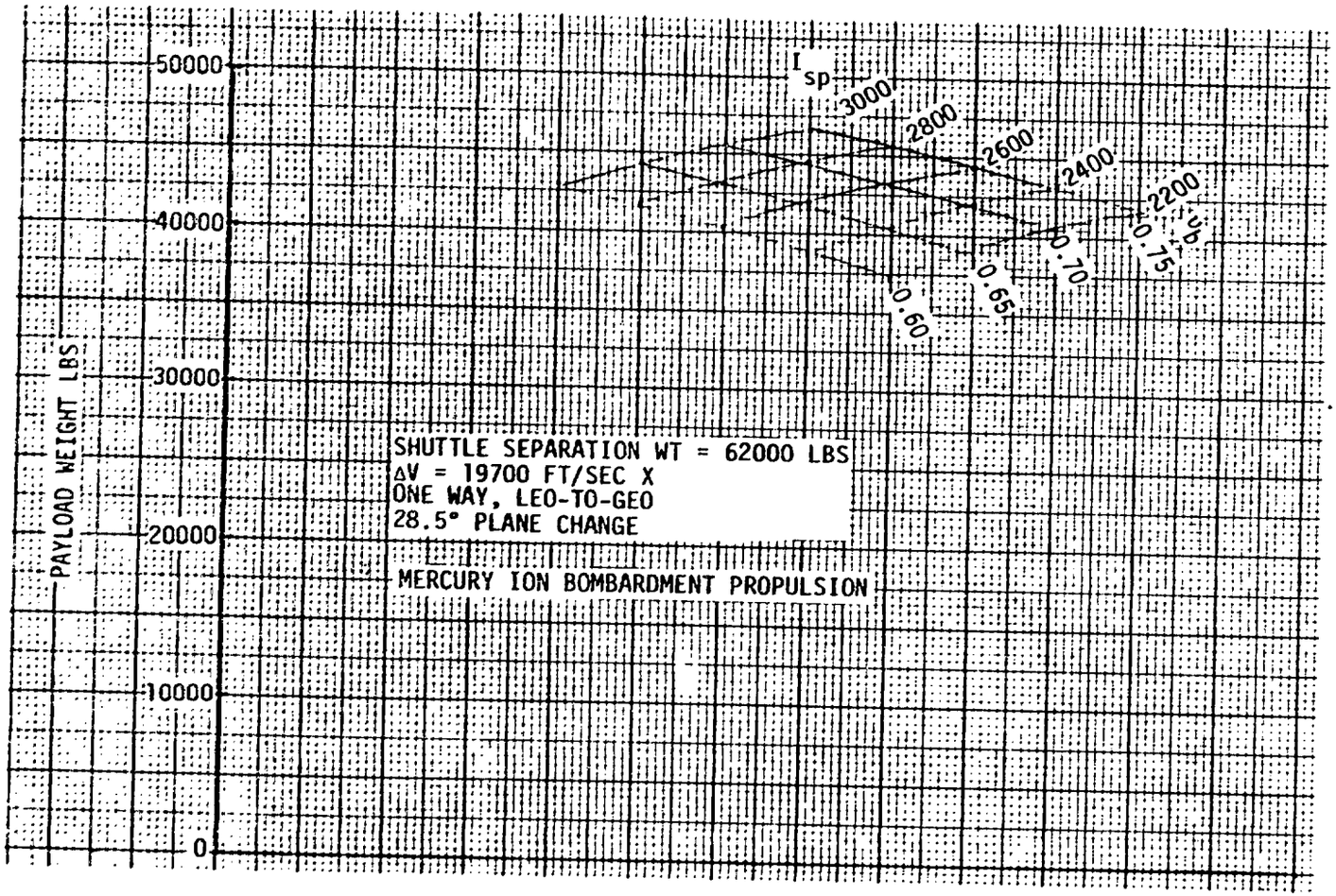

Figure 12. Payload Weight as a Function of Specific Impulse and Mass Fraction - Mercury Propellant

NASA LeRC has indicated the Isp range anticipated for the SEPS thrusters. Some of this information is presented in Table 3.

Table 3. J-Series Thruster Data

THRUSTER INPUT POWER, WATTS	SCREEN VOLTAGE VOLTS	BEAM CURRENT SMPS	Isp SEC	THRUST MILLI-NEWTONS
2700	1100	2.0	2940	125
1927	940	1.6	2667	97
1431	820	1.3	2412	73
1008	700	1.0	2123	53
710	600	0.75	1877	37

Because of the relatively high value of specific impulse associated with electric propulsion systems, the required propellant is a smaller fraction of the spacecraft weight than is the case with chemical systems. The mass fraction for the mercury system is on the order of 0.70 whereas 0.85 is representative of a comparable value for a chemical system.

The current MSFC SEPS activity requires the use of the IUS to boost the spacecraft and payload into a high earth orbit. There are two basic reasons for this maneuver. First, the spacecraft is boosted beyond the Van Allen radiation belts and second, mission trip time is drastically reduced. The primary SEPS mission requires earth escape hence there is no concern with a round trip, i.e., returning through the Van Allen belt. Boosting the vehicle beyond the Van Allen radiation belt and then deploying the array adds significantly to life and performance. Comparison of the trip times between the basic and IUS boosted SEPS shows that a SEPS mission requiring 180 days to conduct with a basic SEPS can, dependent on the IUS configuration selected, be accomplished between 60 and 90 days. Other factors, such as the cost of the IUS and operational factors such as SEPS reuse for LEO-GEO-LEO missions should also be considered. For the comparison presented in this report, however, the non-boosted case has been assumed.

PERFORMANCE COMPARISON

With the material presented in this section of the report, it is possible

to compare the performance of the propulsion systems analyzed. The estimated performance of the solar rocket engine is discussed in detail in Section 5.0, Thruster/Absorber Design and Performance. The Isp values of 872 and 1041 seconds reflect gas temperatures of 5000 and 7000°R, respectively. The materials and cooling problems of the 5000°R thruster are significantly less than the higher temperature concept. For the performance comparison with the chemical systems, the 5000°R performance has been used. Entering Figure 9 at an Isp of 872 seconds and a mass fraction of 0.85, it may be seen that the payload is on the order of 20,000 lbs. Using an Isp of 475 seconds and a mass fraction of 0.90, Figure 10 indicates the LO_2-LH_2 system payload is approximately 20,000 lbs. It is apparent that the high specific impulse of the solar rocket has been negated by the high ΔV requirement. As indicated earlier in the discussion of Figure11, a study should be undertaken to devise a method to reduce the solar rocket ΔV requirement. The results of the study are presented in Figure13. The perigee burn technique used to generate the information is discussed in detail in Section 6.0, Orbital Mechanics. The ΔV's required to conduct 20 and 40 day missions were used to prepare the carpet plots presented in Figures 14 and 15, respectively. For an Isp of 872 and a mass fraction of 0.85, the payload indicated in Figure15 is on the order of 29,000 lbs, a significant increase over the 20,000 lb value indicated for the 14 day trip solar rocket and LO_2-LH_2 system. Because trip times were not identified in the SOW, the detailed performance estimates presented in Section 8.0, Vehicle Synthesis and Performance, will be presented as a function of trip time.

As indicated in Figures 14 and 15, the performance presented was based in the utilization of a 40 x 14.5 ft propellent tank. Based on a useable cargo bay length of 56 ft., 16 ft remains to accommodate the spacecraft and payload. A brief analysis was conducted to determine the effect that shortening the propellant tank has in payload. A 35 x 14.5 ft tank was examined for the 40 day trip time case with Isp = 872 and ν_b = 0.85. The resulting payload was 25,000 lbs. For the 40 x 14.5 ft tank, the corresponding payload was approximately 29,000 lb (Figure 15). The trade-off shows that increasing the length available for the payload/spacecraft from 16 to 21 ft is accompanied by a payload loss of 4000 lb.

The preceding material presented a comparison of the LEO-to-GEO performance capabilities of solar thermal and chemical propulsion systems. The ΔV's selected for the solar thermal rocket were those associated with 14, 20, and 40 day trip times. Performance estimates for these cases are presented in

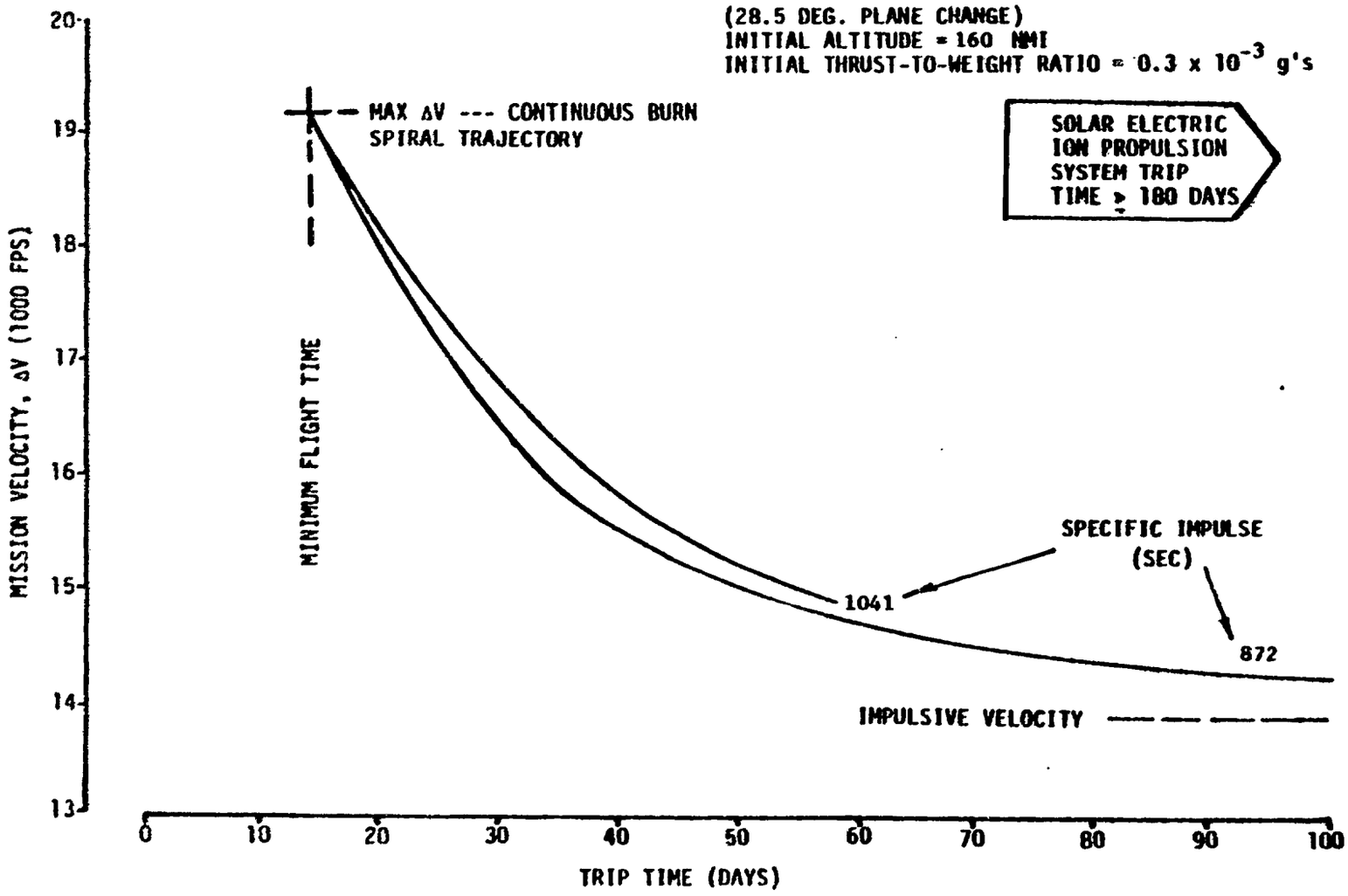

Figure 13. Specific Impulse Effect - Multiple Impulse Transfer

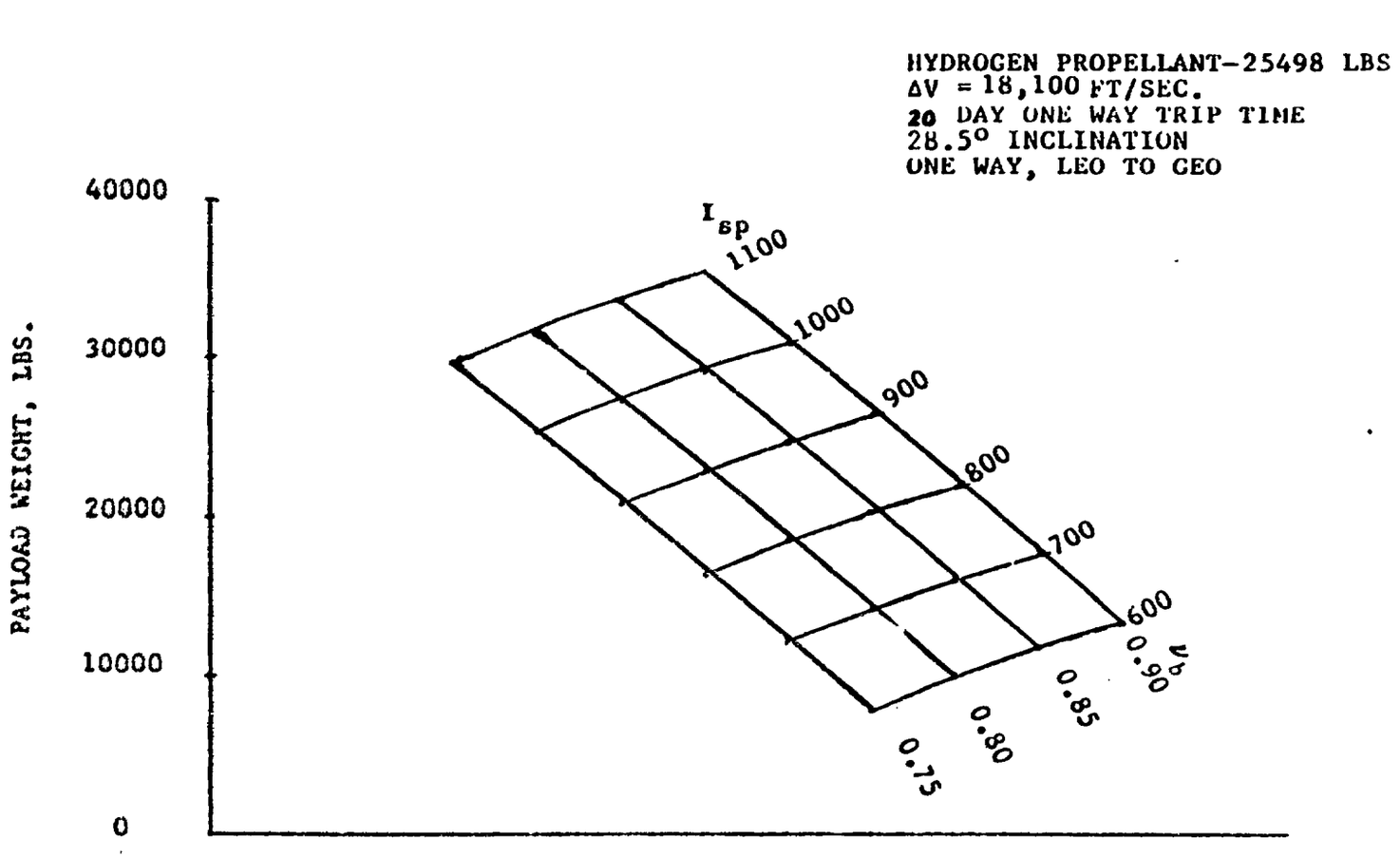

Figure 14. Payload Weight as a Function of Specific Impulse and Mass Fraction - 14.5 Ft. Diameter - 40 Ft. Tank

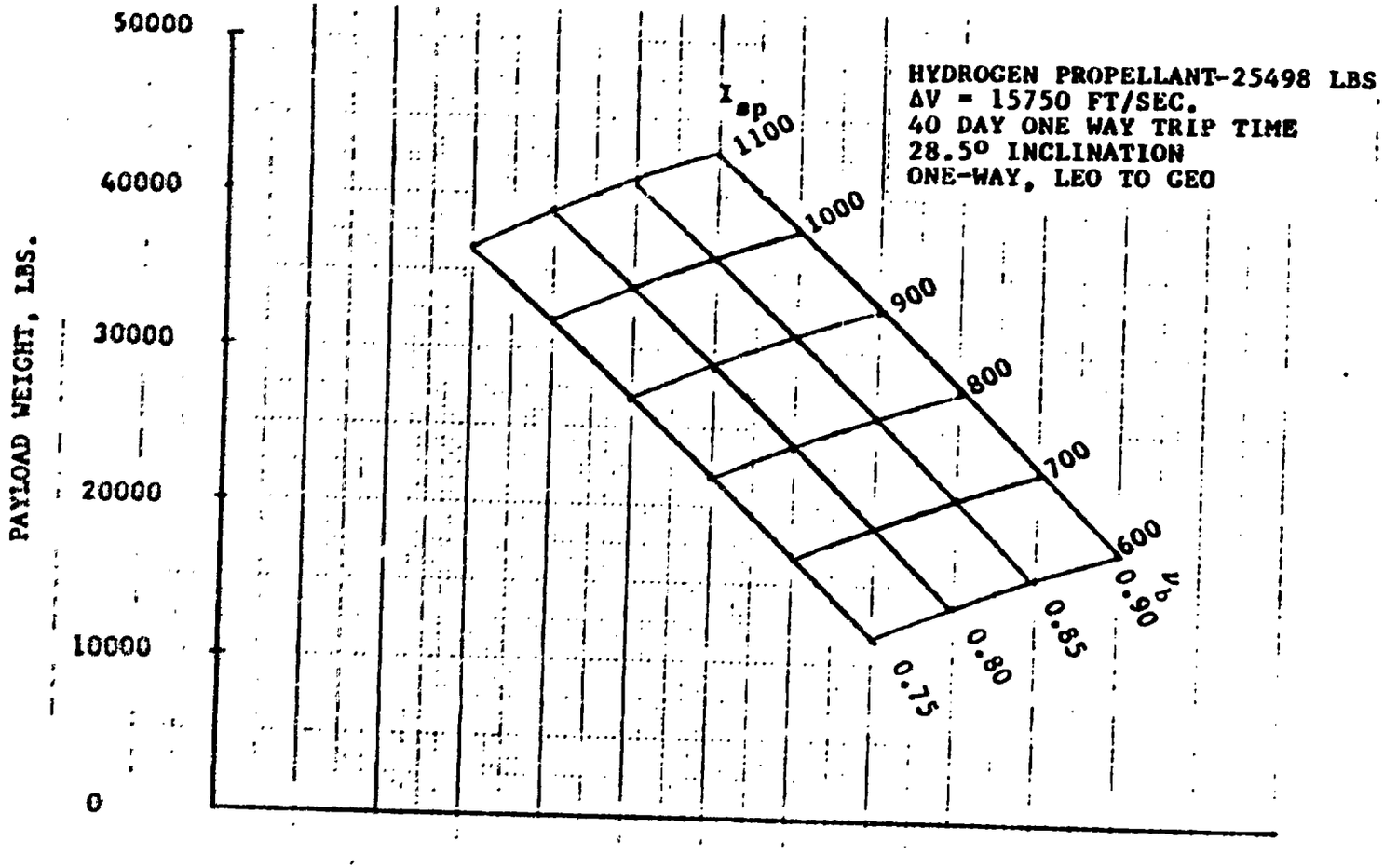

Figure 15. Payload Weight as a Function of Specific Impulse and Mass Fraction - 14.5 Ft. Diameter -40 Ft. Tank

Figures 9, 14, and 15, respectively. The LO_2-LH_2 rocket assumed an impulsive ΔV maneuver which corresponded to a ΔV of 14,000 ft/sec for the one-way LEO-to-GEO case. The Centaur is representative of a vehicle capable of providing an "impulsive" burn. Centaur thrust is provided by two 15,000 lb thrust P&W RL-10 LO_2-LH_2 engines. Based on a Shuttle separation weight of 62,000 lbs, it may be seen that the resulting T/W = 0.48. The use of a velocity increment 14,000 ft/sec is, therefore, a reasonable assumption.

Not all payloads of interest, however, may be able to accept a T/W as high as 0.48. The NASA LeRC has recognized this possibility and has initiated programs to investigate the subject. Aerojet and Rocketdyne are studying primary liquid rocket propulsion systems of the type required to propel large space structures from LEO-to-GEO. The thrust levels of interest range from 100 to 3000 lbs. LeRC has also indicated that the Shuttle separation weight shall be 60,000 lbs. It may be seen that, for these assumptions, the resulting $T/W \lesssim 5 \times 10^{-2}$. A T/W of this magnitude precludes the use of the impulsive ΔV technique. The ΔV's required for low thrust chemical systems have been computed and are presented in Figure 16. Note the significant increase in ΔV for the single perigee/apogee burn case compared to the eight perigee/single perigee burn mode. Performance estimates for the single and multiple perigee burn modes are presented in Figures 17 and 18, respectively. It may be seen, for Isp = 475 and ν_b = 0.90, that the multiple burn case payload is 2500 lbs (~12%) greater than the single burn mode although the trip time has increased from approximately 6 to 22 hours. For comparison purposes, the payload for a single burn/1000 lb thrust case was computed. The input parameters used were; ΔV = 16,500 ft/sec., Isp = 475, ν_b = 0.90. The resultant payload was approximately 16,000 lbs. The purpose of the preceding discussion is to illustrate that the performance capability of a chemical system is payload sensitive and that impulsive ΔV methods cannot necessarily be employed under all conditions and that these factors should be considered in solar/chemical comparisons.

Table 4 has been prepared to summarize the performance parameters discussed in this section of the report. The results of the detailed performance estimates are presented in Section 8.0, Vehicle Synthesis and Performance.

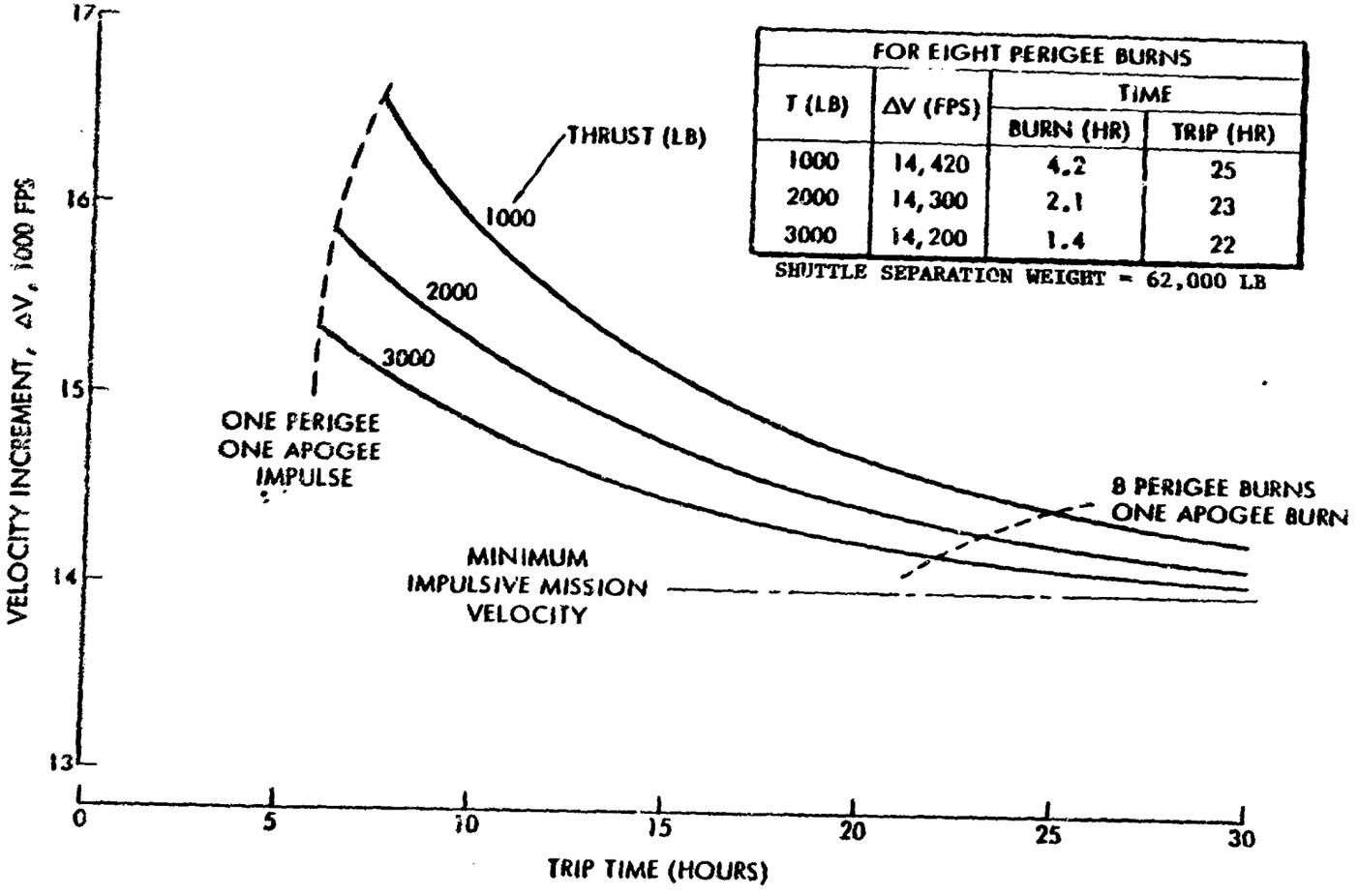

Figure 16. Mission Velocity as a Function of Trip Time

VEHICLE	ν_b	I_{sp}	PAYLOAD
CENTAUR D-IT	0.85	444	12,200
OOS STUDY*	0.88	470	17,097
BAC STUDY*	0.92	476	19,315

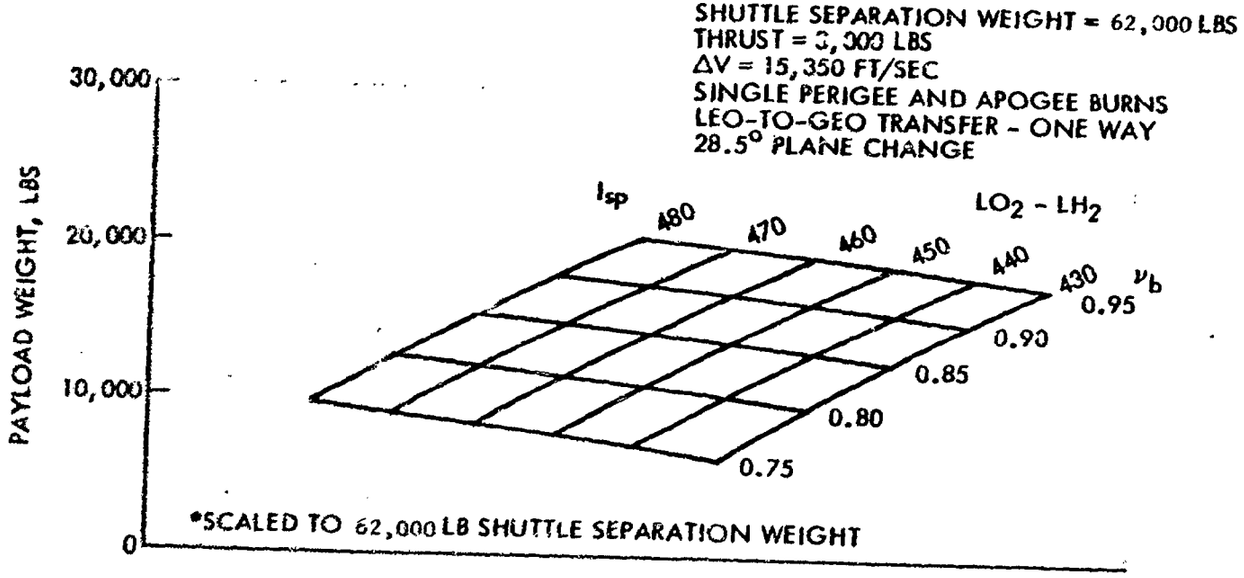

Figure 17. Payload as a Function of Specific Impulse and Mass Fraction - Single Perigee and Apogee Burns

VEHICLE	ν_b	I_{sp}	PAYLOAD
CENTAUR D-1T	0.85	444	12,200
OOS STUDY*	0.88	470	17,097
BAC STUDY*	0.92	476	19,315

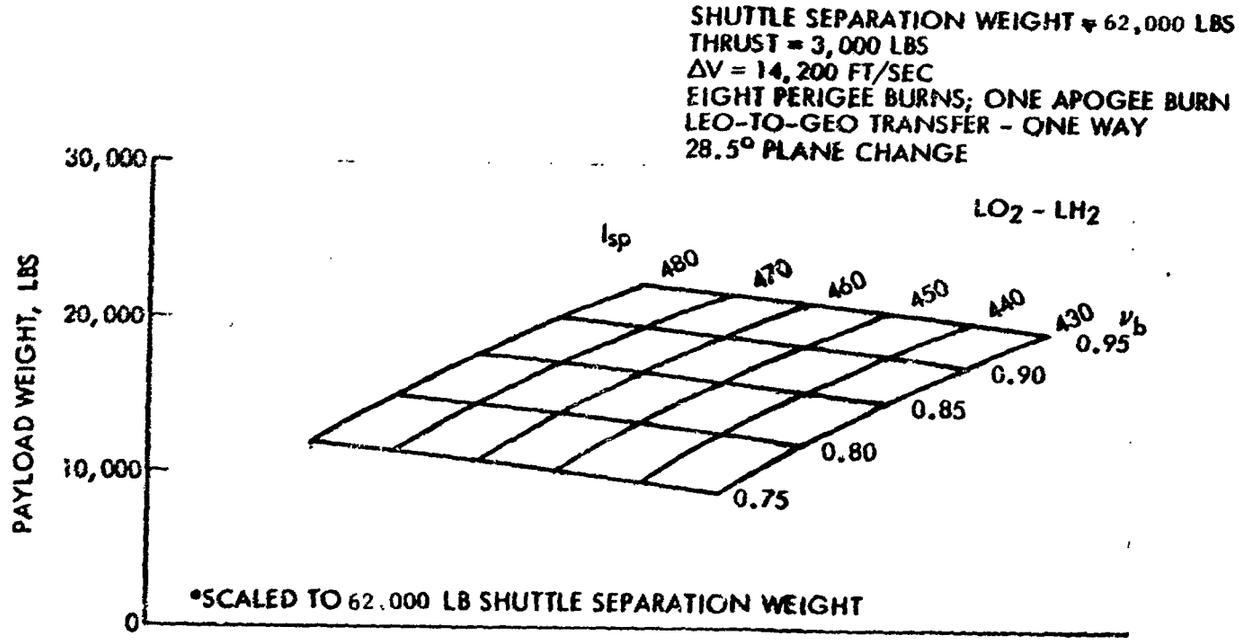

Figure 18. Payload as a Function of Specific Impulse and Mass Fraction - Multiple Perigee Burns

Table 4. Performance Boundary Summary, Single Shuttle Launch

SOLAR THERMAL ROCKET

		TIME ΔV	14 DAYS 19,200	20 DAYS 18,100	40 DAYS 15,750
I_{sp} = 872	PAYLOAD, UP ONLY		20,500	23,000	29,000
	PAYLOAD, UP, S/C DOWN		14,000	17,000	21,000
I_{sp} = 1041	PAYLOAD, UP ONLY		27,000	30,000	34,600*
	PAYLOAD UP, S/C DOWN		20,000	22,500	29,000
40' X 14.5' TANK ν_b = 0.85			*36.5' X 14.5' TANK		

CHEMICAL ROCKET

		TIME ΔV	5.4 HRS 14,000	7.0 HRS 15,750
I_{sp} = 475	PAYLOAD, UP ONLY		20,400	18,000
	PAYLOAD UP, S/C DOWN		12,400	8,800
17' TANK LENGTH ν_b = 0.90				

4.0 COLLECTOR CONCEPT AND PERFORMANCE

A basic requirement of the solar collector system is to maintain a high concentration of sunlight at the engine absorber surface. The concentration ratio achieved strongly affects the temperature and efficiency of the absorber and consequently the size and mass of the collector system required for a given engine thrust.

At high values of specific impulse, which require high absorber temperatures, reradiation losses are high and concentration ratio becomes a critical factor in keeping collector size and mass within reasonable limits.

The technical problems inherent in large, high performance solar concentrators include the following:

- Figure accuracy - Advanced fabrication techniques and possibly active figure control is required.
- Pointing accuracy - A solar pointing accuracy of ± 0.1 degree or less is desired.
- Radiation damage - In the Van Allen belt, the proton flux can cause bubbling of the plastic substrate beneath the reflective surface and degrade its specular reflectance.
- Meteorite damage - For continuous use, refurbishment must consider small amounts (~ 0.001 percent) of reflector surface erosion by meteorite bombardment. Inflated designs will require makeup gas.
- Exhaust plume impingement - Adequate clearance must be provided for the engine exhaust plume to avoid disturbing forces on the concentrator dish and excessive heating.

  Eclipse effects - Temperature gradients and transients imposed by eclipse periods can cause temporary defocusing, and overheating of the structure adjacent to the focal point.
- Deployment and construction - In large sizes associated with the higher payloads, fully deployable petal concentrators become unweieldy and may require on-orbit assembly.
- Optical transfer devices - Multiple reflection losses degrade overall performance.

The principal types of concentrators considered for the solar thermal rocket concept include the following:

- Solid
- Petal
- Inflated, rigidized
- Inflated, non-rigidized
- Tensioned-net/membrane
- Electrostatic tensioned membrane
- Whirling membrane
- Fresnel facets
- Spherical facets

Anyone of the above types can be used in conjunction with Cassegrain mirrors, light tubes, or other optical transfer devices such as those shown in Figure 19.

SELECTION OF COLLECTOR CONCEPT

The primary criteria used in selecting the baseline concentrator design are listed below in approximate order of importance:

1. Performance (concentration ratio and efficiency)
2. Specific mass
3. Deployability
4. Operational life
5. Focusing control
6. Compatibility with both solar pointing and mission thrust vector steering requirements
7. Compatibility with vehicle C.G. control.

These considerations were major driving factors in both the collector design and the overall vehicle configuration. To fly every conceivable mission and orbit inclination, the thrust vector must be capable of being pointed in any direction relative to the sun line, while at the same time maintaining orientation of the collector with the sun. This requires two axes of freedom for the thruster, with the collector(s) located away from the exhaust plume and its heating and contamination effects. The simplest solution is to locate the collector(s) outside of the plane of rotation

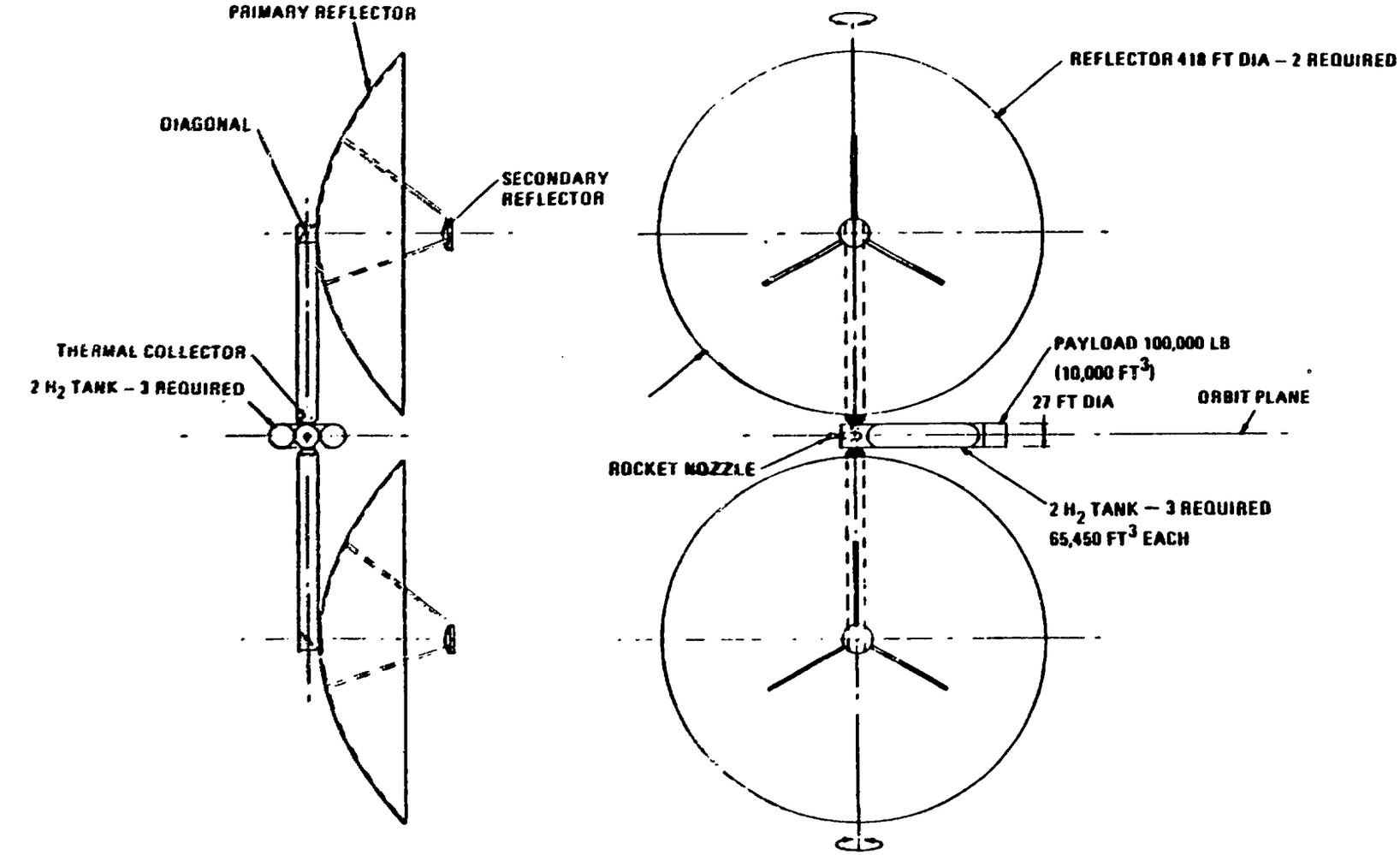

Figure 19. Vehicle Concept With Transfer Optics

of the thrust vector and roll the entire spacecraft about the sunline as needed to obtain the other axis of freedom for thrusting. The propellant tanks and payload rotate continuously with the thruster as a unit about a bearing axis, with the engine(s) gimballed slightly relative to the propellant tank and payload to provide vehicle steering control. This arrangement is illustrated in the candidate designs of Figures 19 and 20.

Based on the above considerations and the stated selection criteria, the choice of a baseline collector concept quickly narrows down to that of Figure 20, namely inflated, non-rigidized, off-axis paraboloidal collectors, focusing directly onto the engine absorbers, each which include a compound parabolic reflector skirt or Winston reflector horn to further concentrate the centermost rays. The efficiency losses, weight and deployability problems of the transfer optics shown in Figure 19, and other optical devices such as heliostat mirrors, are thereby avoided. Additional versions of the selected collector/vehicle concept are shown in Section 7.0, Spacecraft Design.

The solid and petal type collector designs were rejected because of their high specific masses (~ 0.25 lb/ft^2), especially in large sizes. This compares to a specific mass of ~ 0.03 lb/ft^2 for the inflatable, non-rigidized designs. The inflatable, rigidized design was rejected because of relatively high mass and low optical quality caused by graininess of the rigidizing foam or backing, and the thermal and mechanical distortions inherent in such a design. The mechanically tensioned-net/membrane and electrostatically tensioned membrane designs both require a complex deployment scheme. The whirling membrane concept uses centrifugal force to maintain a paraboloidal shape but requires a central axis of symmetry and is incompatible with an off-axis configuration. The Fresnel concept uses a large number of planar facets mounted on a flat structure, each facet focused on the engine absorber. The deployment and alignment problems of this approach are formidable, in addition to the significant weight penalties that are incurred. A much more viable approach is the use of large inflated spherical facets which are joined so as to closely approximate a true off-axis paraboloidal surface. A key advantage of this approach over a one-piece inflated paraboloid is the ease of achieving constant membrane stress (and creep) over the entire collector surface, as discussed in Section 7, Spacecraft Design. This is one of the versions of the baseline collector concept which should be evaluated in follow-on study effort.

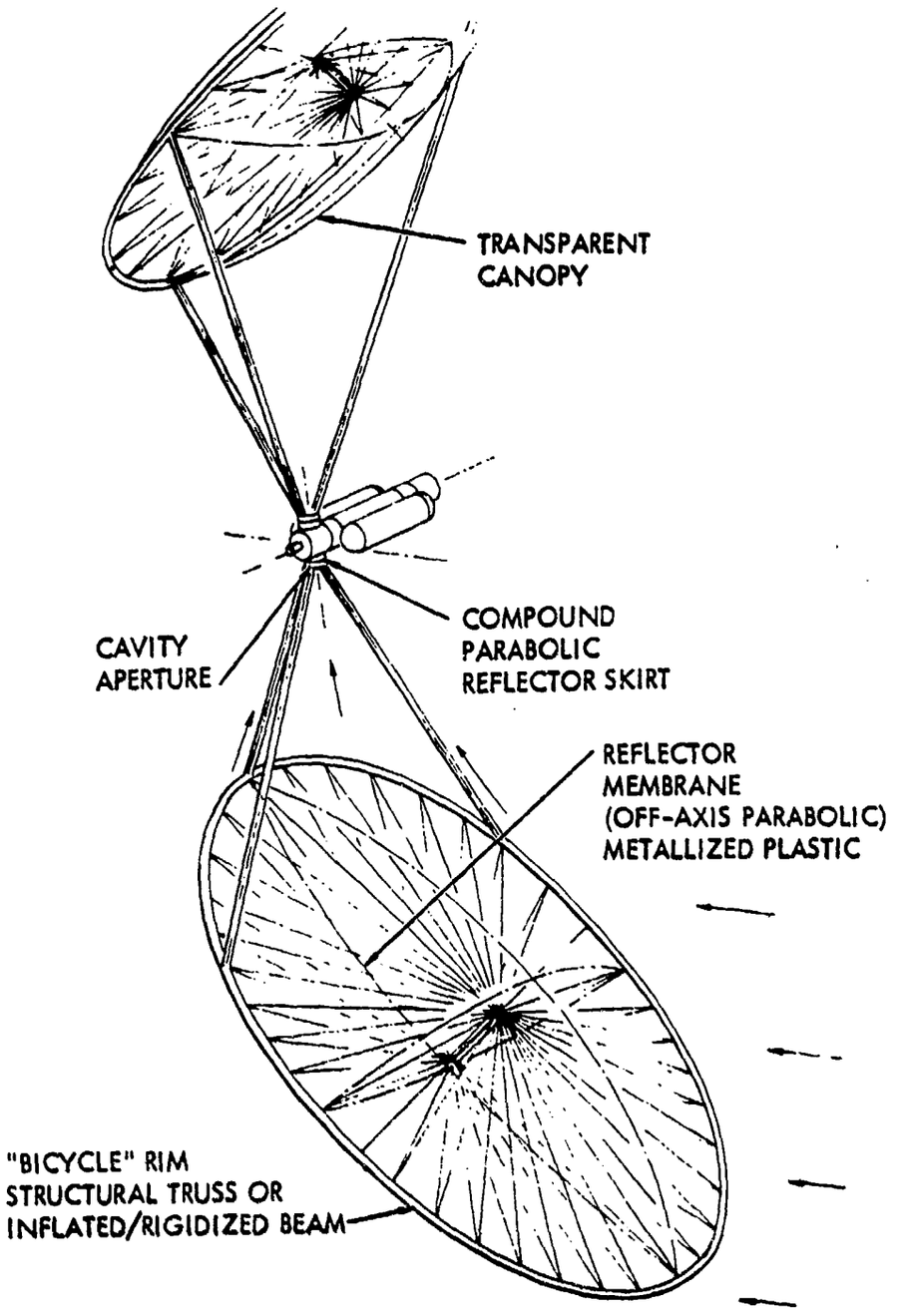

Figure 20. Non-Rigidized, Inflatable, Off-Axis Concentrator Configuration

The chosen generalized concept (inflated, non-rigidized, off-axis, paraboloid) scores highly in each of the prescribed selection criteria except possibly C.G. control and operational life. Present information indicates that one-way light transmission through the transparent canopy may degrade from 95% to 90% or less in 10 years of operation in space. Present material candidates are FEP teflon and specially treated mylar, but other promising new films are being developed for commercial solar energy applications. Although standard mylar degrades from radiation exposure (including UV) in ground applications, data shows that in the absence of oxygen such damage is greatly reduced. This is especially true for the reflector membrane which can be metallized on both sides to exclude UV. Other radiation damage occurs chiefly in the Van Allen belt from low energy protons which can be trapped within the membrane film and create minute hydrogen bubbles which destroy the optical smoothness of the metallized surface. This effect is believed to be slight for the expected operational life cycle exposure but further lab testing is required to verify that. Figure 21 shows specular reflectance values for Kapton and FEP Teflon metallized film, from Reference 7.

For ideal C.G. control, the C.G. of the collector should be located on the rotation axis of the thruster. As shown in the baseline design of Figure 22, this condition is not satisfied, and for large collector sizes, engine gimbal deflections of up to 30 degrees may be required in the plane of rotation to achieve steering control. This requirement is reduced considerably by alternate versions of the baseline design shown in Section 7.0, Spacecraft Design.

COLLECTOR SIZE, MASS AND VOLUME CHARACTERISTICS

Two collectors are required per spacecraft for C.G. control. Figure 23 presents estimates of collector size as a function of total spacecraft thrust for three propellants (H_2, NH_3 and N_2H_2) at assumed values of Isp and other parameters.

Qualitative validation of an inflated torus concept was provided by a 10 ft. O.D. inflated model fabricated for another Rockwell IR&D project by L'Garde, Inc. of Newport Beach, Calif. This torus model was made by taping together flat sheet, 1 mil mylar and used a central flat mylar membrane. Structural stability and ridigity were remarkable even at less than 1 psi inflation pressure in the torus. Weight of the assembly was 1.3 lb

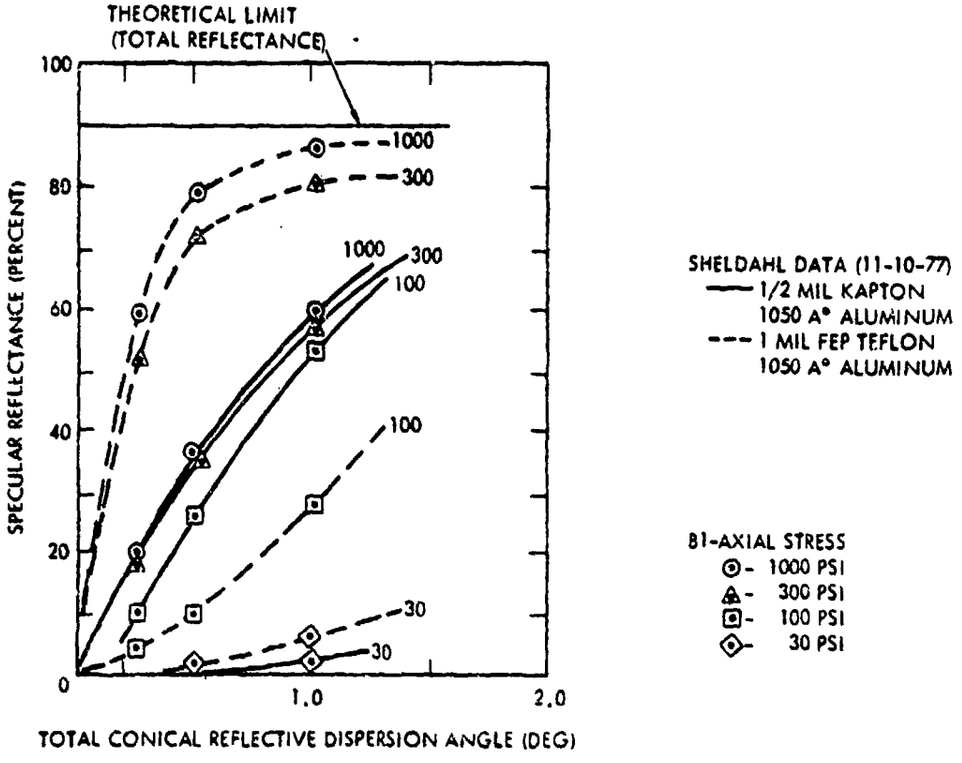

Figure 21. Specular Reflectance of Aluminized Plastic Film

($\sim$ 0.02 lb/ft^2) and packaged dimensions were quoted as 6.5 x 6.5 x 2 inches. Makeup gas requirements, however, for maintaining this relatively high pressure would be prohibitive. It is estimated that 3000 lbs of hydrogen gas would be required for a 100 ft. dia. torus for a 20-day trip, due to leakage from micrometeoroid punctures accumulated in 10 years of service. This penalty can be avoided by use of an erectile shell concept proposed by L'Garde, Inc. in which the inflatable torus is fabricated from aluminum foil. During inflation and deployment, the foil is stressed beyond its yield point which locks it into an "egg-shell" structural surface which remains rigid after leakage of the inflation gas. A lighter version of this concept was proposed by Goodyear Inc. in their Project Able studies (Reference 8). As shown in Figure 24, they proposed an inflated wire-grid truss rim composed of soft aluminum wires woven in a coarse open grid and laminated with 1/2 mil mylar. Figure 25 shows the weights estimated by Goodyear for such a design. Based on this data and a 0.5 mil mylar reflector membrane and canopy with a film stress of 100 psi, the estimated mass of a 100 ft. dia. collector (projected dia. to sun) is 220 lbs, or 0.028 lb/ft^2 of projected area. The packaged volume is 5.5 ft^3 based on a conservative packing efficiency of 25%. Figure 26 presents mass and volume characteristics for a range of collector diameters. The largest single collector which can be carried on a single Shuttle load of 62,000 lbs has a projected diameter of $\sim$ 1600 ft.

Gas Leakage Calculations

The inflation pressure required to achieve 100 psi film stress in a 100 ft. collector (projected dia) with a 0.5 mil reflector membrane is given by

$$P = \frac{4\,St}{D} = \frac{4(100)(0.0005)}{400 \times 12}$$

$$= 4.17 \times 10^{-5} \text{ psia}$$

where

- P = pressure, psi
- S = stress, psi
- t = film thickness, inches
- D = diameter of curvature, inches

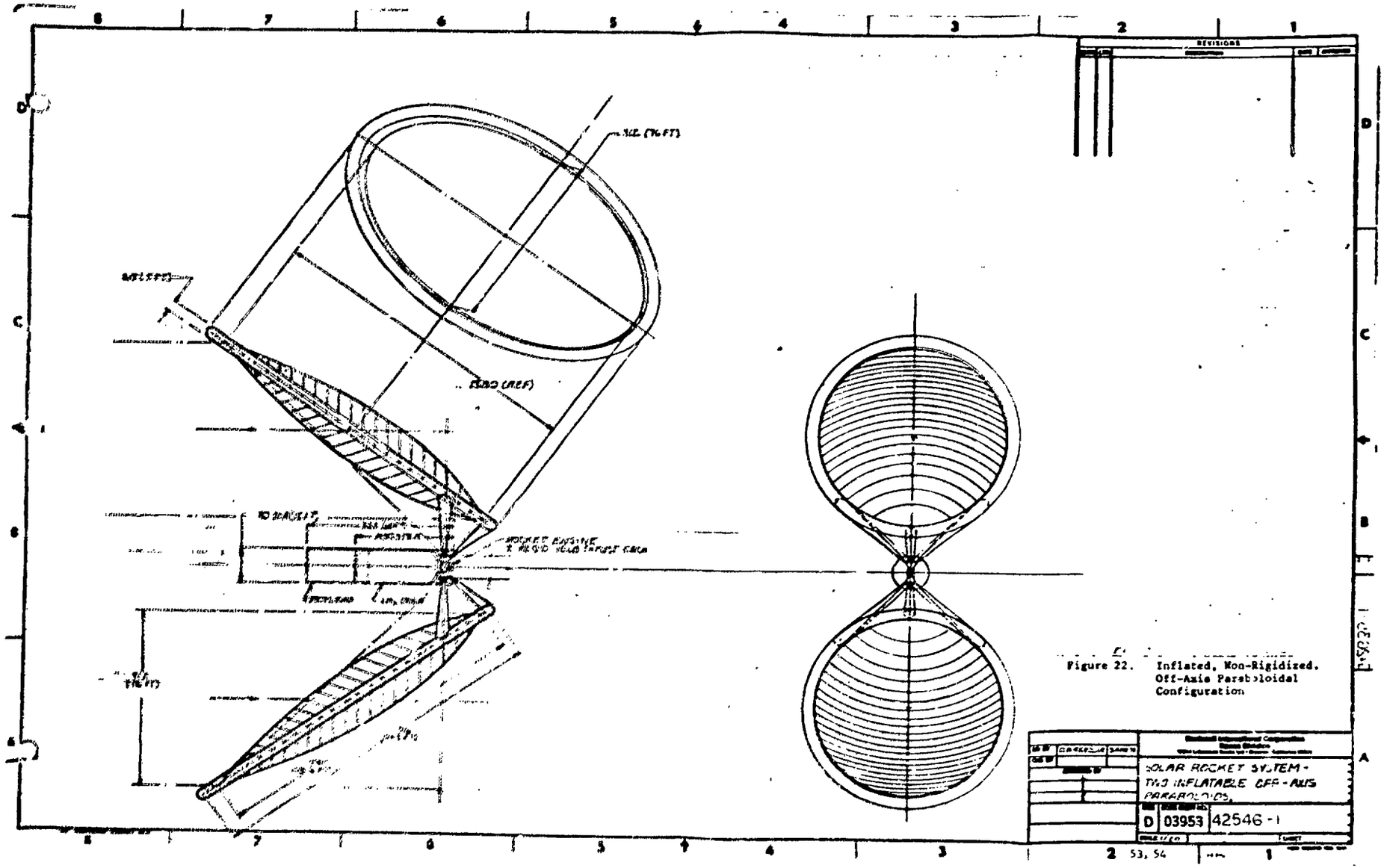

Figure 22. Inflated, Non-Rigidized, Off-Axis Paraboloidal Configuration

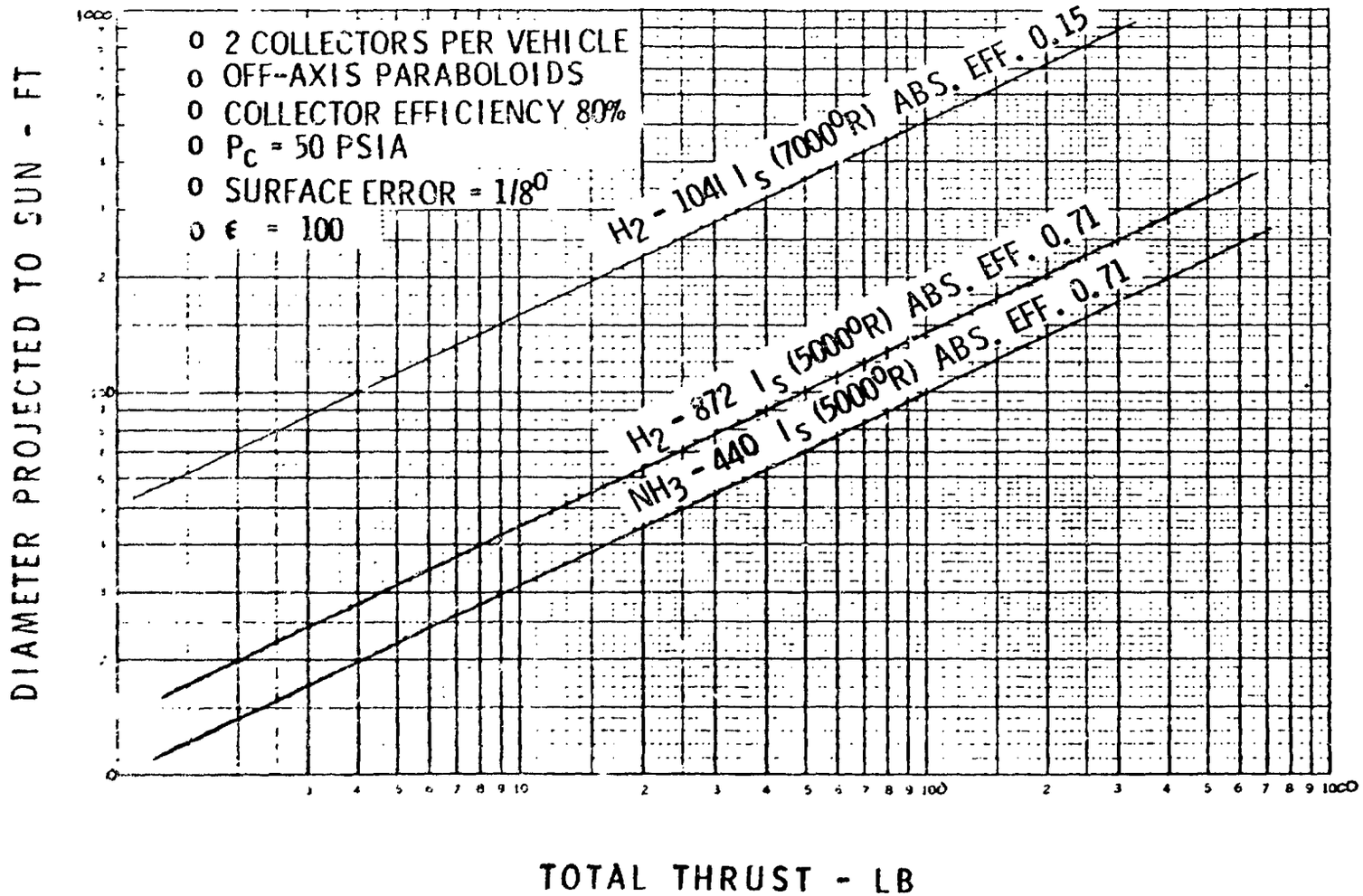

Figure 23. Required Concentrator Diameter

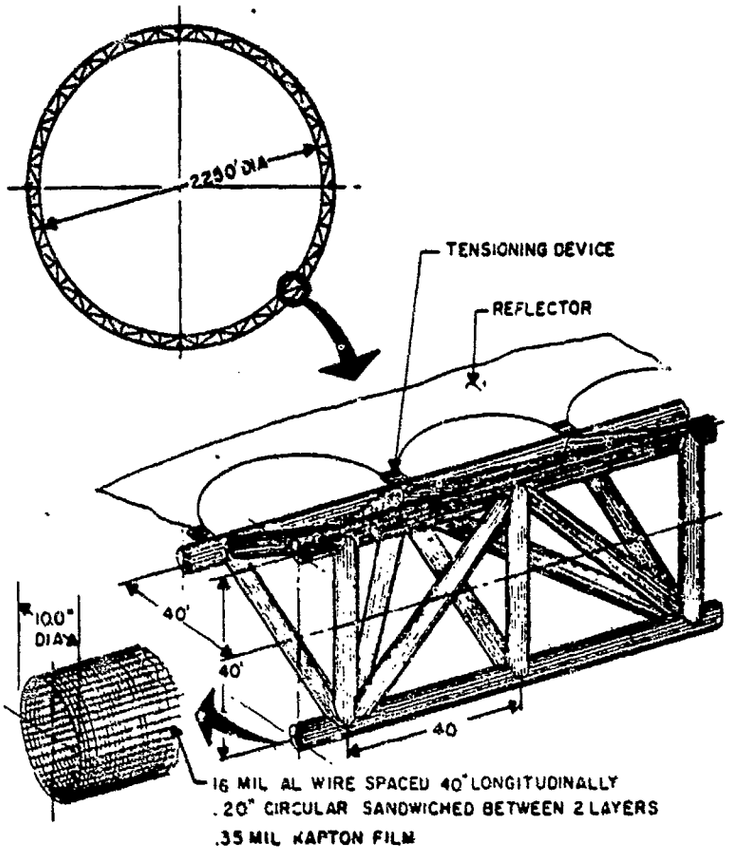

Figure 24. Goodyear Wire Grid Truss Rim Concept

(Reproduced from Ref. 8)

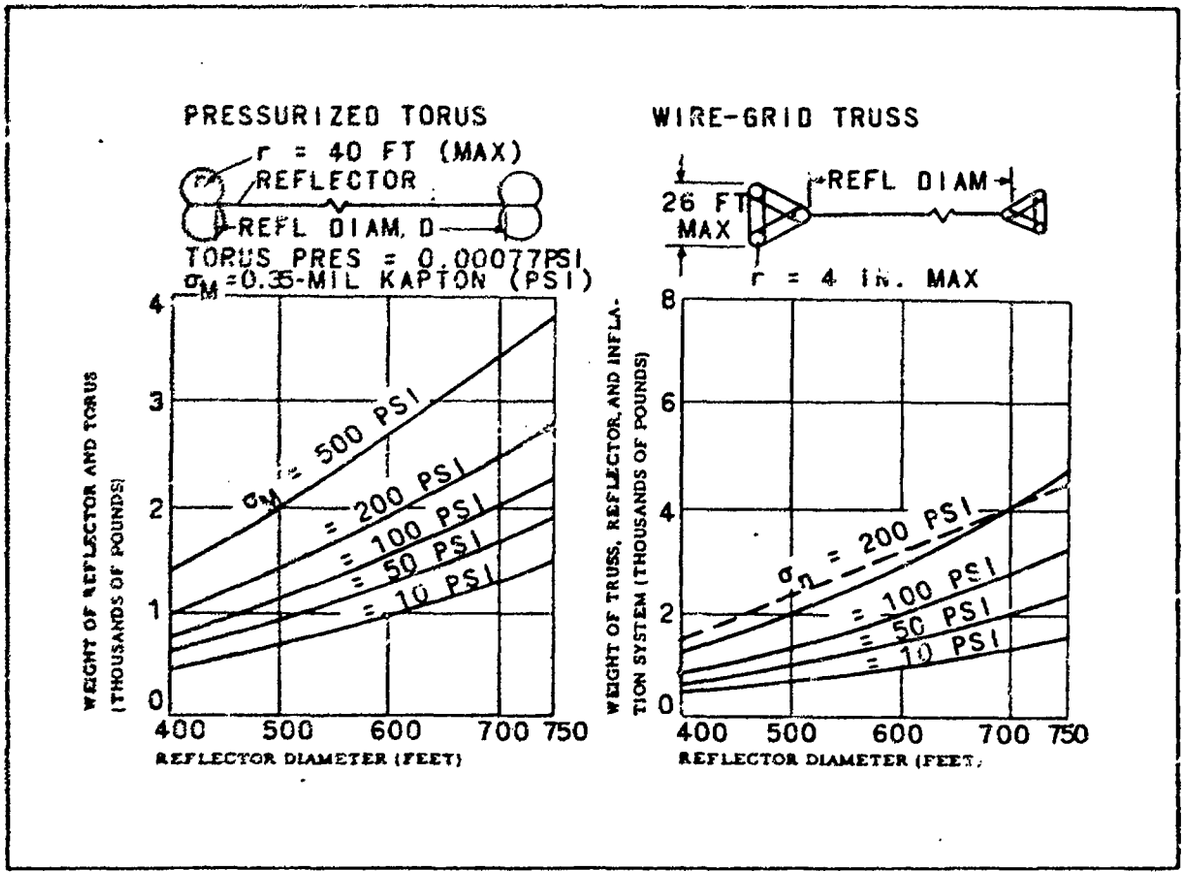

Figure 25. Pressurized Torus and Wire-Grid Tube Truss Weights for 400- to 750-Ft-Diameter Reflector

(Reproduced from Ref. 8)

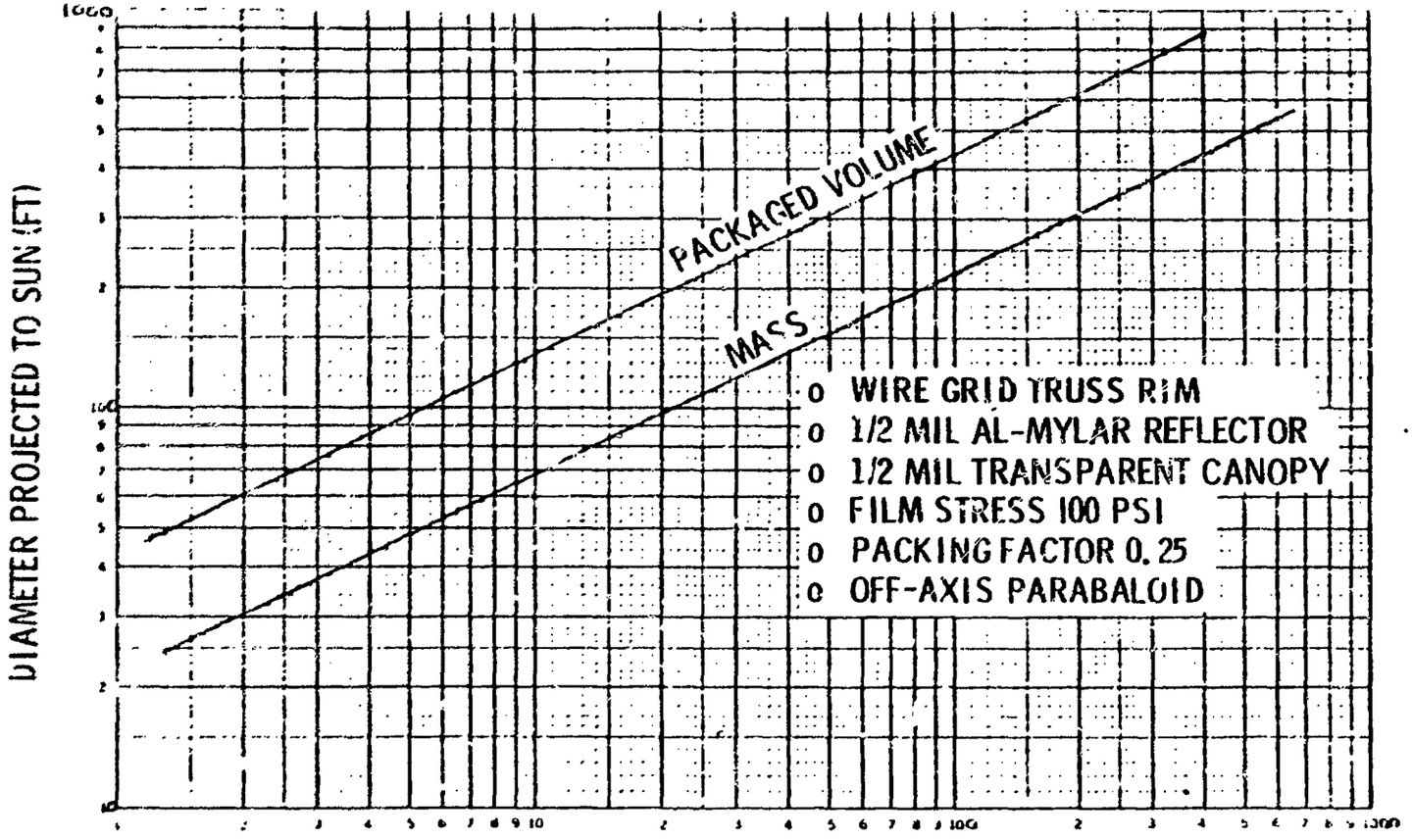

Figure 26. Inflated Solar Concentrator Mass and Volume

The total leakage area resulting from micrometerite puncture after 10 years is estimated to be 0.001% of the total membrane area (Ref. 7) or .31 ft^2. Assuming that the inflation gas is hydrogen at 70^oF, the leakage mass rate is approximately:

$$\dot{M} = \frac{\varrho VA}{4} = \frac{1.49X10^{-8}\ (4000)(.31)}{4}$$

$$= 4.63 \times 10^{-6} \quad lb/sec$$

or 7.98 lb in 20 days, per collector

where

ϱ = density, lb/ft^3
V = sonic velocity, ft/sec
A = area, ft^2

This amount of makeup gas is entirely negligible and can be tapped off of the engine LH_2 feed line. The divisor of 4 used in the above equation accounts for flow in the molecular regime vs. viscous regime.

The above calculation applies to leakage from an inflated reflector membrane and canopy of the type shown in Figure 22. It is independent of the type of collector rim used (inflated torus, erectile shell, wire-grid truss, etc.).

Solar Flux Distributions

Figures 27 and 28 show the results of analysis of the solar flux distribution at the focal plane of an on-axis parabolic concentrator, for use in SRSCA engine analysis. The concentrator characteristics used are:

Rim angle $\pm 45^{\circ}$

Total reflectivity 0.9

Pointing error 0.0 degrees

This data was obtained by numerical integration of the reflected energy falling on the focal plane and includes the effects of:

1. Sun disc subtended angle ($\pm$ 16')
2. Angular errors of concentrator surface
3. Ellipsoidal images at focal plane produced by oblique rays from other regions of concentrator
4. Increased length of rays reflected from outer regions of concentrator

The peak concentration ratio at the center of the focal plane of a perfect paraboloid (σ = 0.0 degrees) is given by:

$$C_{peak} = \frac{2Z}{\tan^2 16'} \int_0^1 \frac{\cos\theta \, R \, dr}{\ell^2}$$

where $\theta = \arcsin \frac{R}{\ell}$

$$\ell = 1.2071 + \frac{R^2}{4.8284}$$

R = collector radius, dimensionless

Z = reflectivity of collector

The flux distribution obtained for σ = 0.0 degrees was modified by applying a normal Gaussian probability density function corrected for three dimensional space coordinates, to obtain the flux distributions for σ = 1/8, 1/4 and 1/2 degrees.

These distributions are 3-dimensional bodies of revolution having equal volumes. Consequently, their cross-sectional areas, as shown in Figure 27 increase with decreasing surface errors.

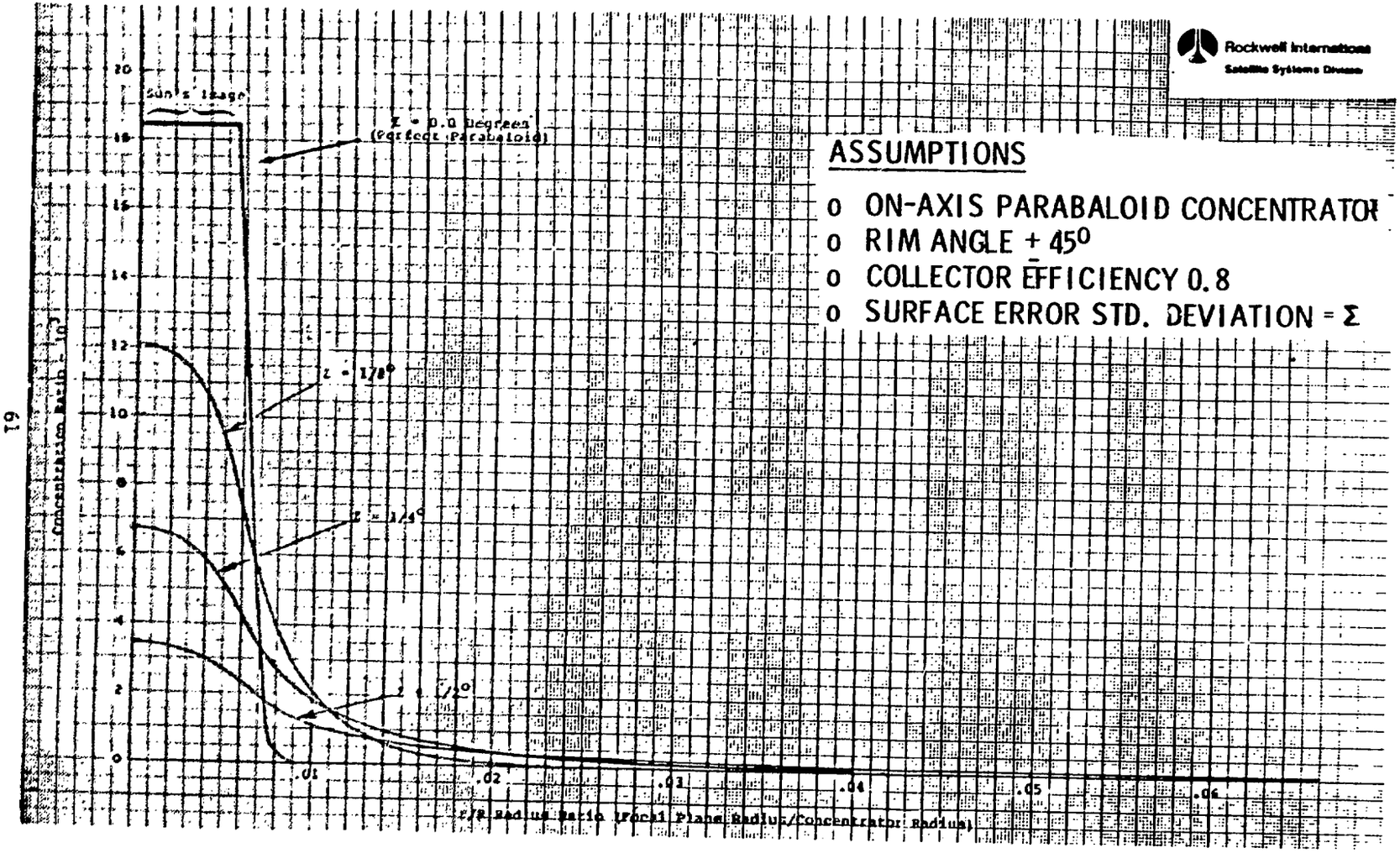

Figure 27. Solar Flux Distribution at Focal Plane

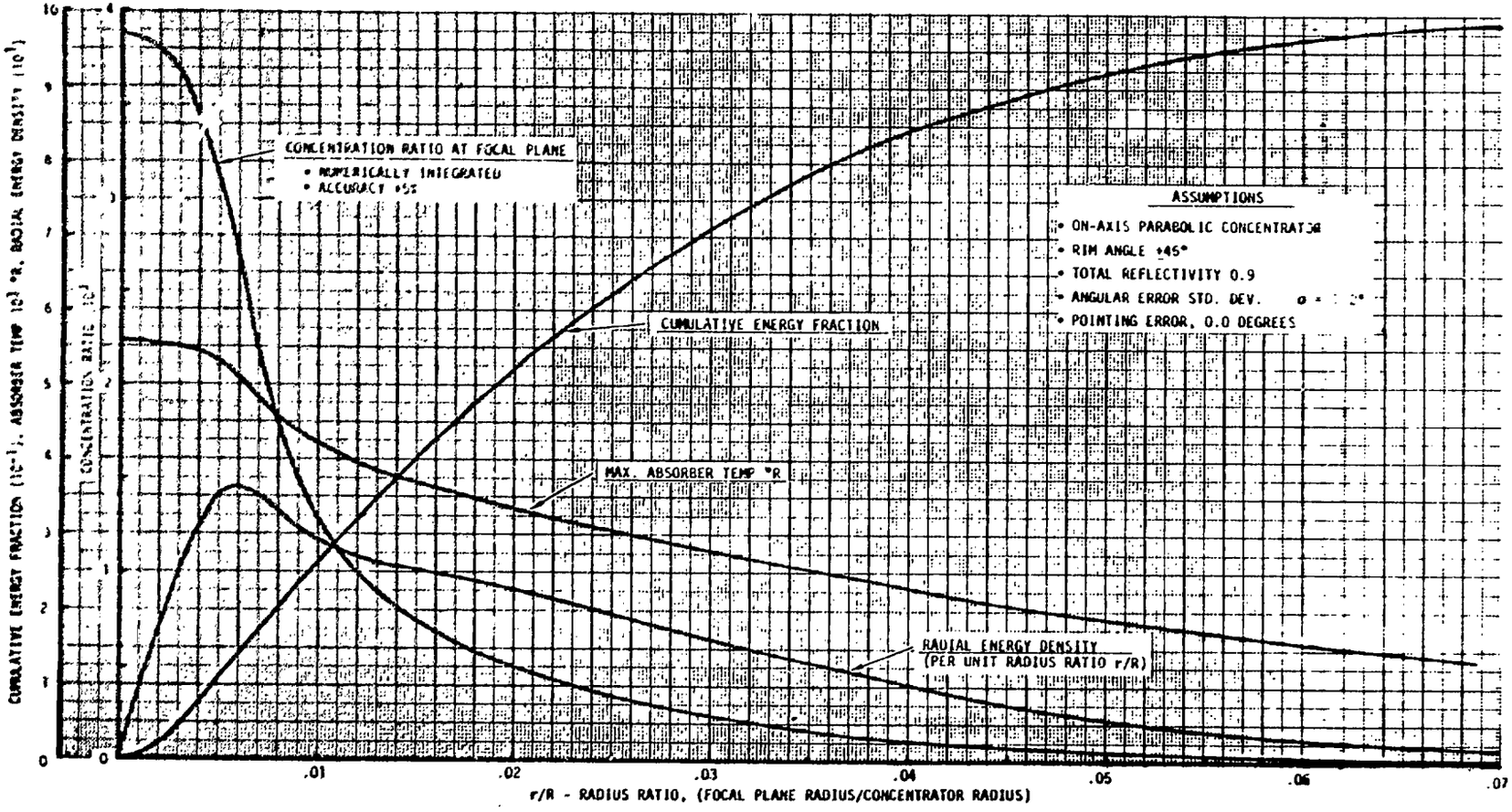

Figure 28. Solar Concentrator Energy Distribution for 1/2° Surface Error .

Energy and temperature distributions are given in Figure 28 for a concentrator surface error standard deviation (σ) of 0.5 degrees. This deviation includes the effects of surface finish, wrinkling, waviness, and contour errors. Pointing error was chosen to be 0.0 degrees since this provides the worst case (high) flux intensity for materials considerations. The effects of pointing errors will be accounted for by shifting the flux distribution off center by an amount equal to 0.05568 β, where β is the pointing error in degrees. A maximum pointing error of 0.1 degrees will be assumed. The effect of this error on peak flux intensity is negligible in the study. The accuracy of results obtained is considered to be within $\pm$ 5%. For purposes of this study, they can also be used for the case of an off-axis paraboloidal concentrator as long as the average rim angle is $\pm$ 45°. A reflector skirt will be used at the absorber to boost the peak concentration ratio.

COLLECTOR STATE OF THE ART

Sundstrand Corporation and Goodyear Aerospace Corporation were contacted regarding their experience with solar concentrators built for the Air Force ASTEC program in the early 1960's. References 1 and 9 describe the very extensive analysis, fabrication and testing effort involved. A rigidized design was chosen over a folding petal design as the result of competitive testing of 10 ft. diameter models. The rigidized designs were produced by Goodyear for Sundstrand. They were fabricated by laying up gores of 1 mil mylar on a paraboloidal tool, seaming the radial butt joints with tape, inflating to shape, and spraying the backside with a lacquer coat and polyurethane foam (Figure 29). The 44.5 ft. dia. mirror was supported by a tubular truss framework to facilitate handling and mounting on a solar tracker.

Three types of optical performance tests were used:

1. Optical ray tracing using a thin collimated light source.
2. Flux intensity mapping at the focal plane using a point sensing radiometer, with the mirror pointed at the sun.
3. Cumulative energy mapping at the focal plane using a cold cavity calorimeter and various aperture sizes, with the mirror pointed at the sun.

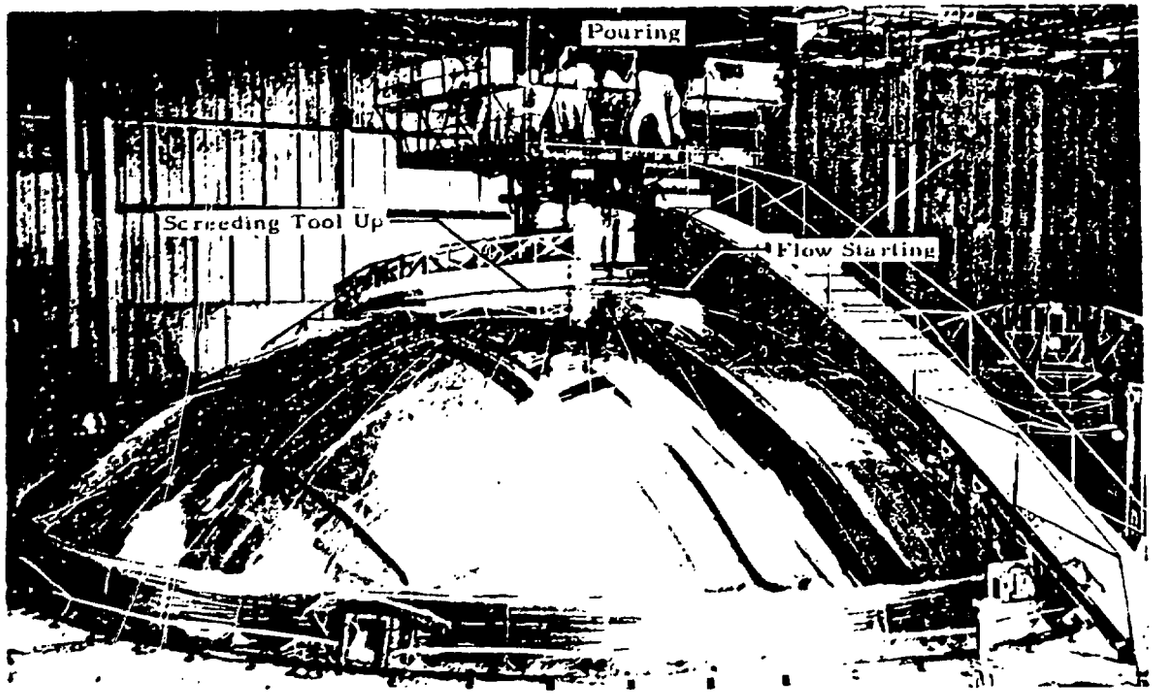

Figure 29. Foaming Operation Sequence - 44.5 Ft. Inflated Production Mirror

(Reproduced from Ref. 1)

The peak concentration ratio achieved by the 10 ft. diameter design was 3900:1. This agrees roughly with results of the optical ray tests which indicated an angular surface error of about 0.5^{o} standard deviation. Most of this error is believed to result from graininess or "orange peel" in the foam backing.

The profile of the 44.5 ft. diameter mirror was checked by template before and after rigidization. The surface error at selected points was within 0.2 inches from a true paraboloid and the corresponding error was on the order of 0.08^{o} standard deviation. "Orange peel" was avoided by spraying with a lacquer coat before applying the foam. The foaming process, however, introduced a spiral ripple in the mirror surface due to the pattern in which the foam was applied and the uneven stretching effects on the mylar from heat generated by the foaming reaction. The peak concentration ratio of the finished mirror was 3200:1 which corresponds to an angular surface error of about 0.6^{o} standard deviation, slightly worse than for the 10 ft. dia. mirror. Figure 30 presents a flux contour map obtained from solar testing of the 44.5 ft. dia. collector.

Sundstrand has indicated that the optical smoothness and quality of the mirror surface was far superior in the inflated unrigidized state. This was also evident in photographs of the paraboloid surface before and after rigidizing which showed marked difference (> 10:1) in the quality of reflected images. Conceivably this degradation from foaming could be reduced by use of a slow reacting foam mixture to reduce heating effects, but temperature gradients across the foam layer in service could still cause serious distortions of the overall paraboloidal contour. Sundstrand recommended the non-rigidized, inflated concept for large mirror surfaces in space.

ACHIEVABLE CONCENTRATOR PERFORMANCE

Based on concentrator development experience in the ASTEC Program, it appears that inflated paraboloidal contours can be fabricated with an angular surface error of $\pm 0.08^{o}$ standard deviation, and possibly $\pm 0.05^{o}$ with tooling and fabrication process refinements. Preliminary tests of the basic specular reflectance of aluminized films indicates that a dispersion error of $\pm 0.09^{o}$ can be achieved, with $\pm 0.06^{o}$ possible through pre-stretching or polishing of film. This equates to an overall (RSS) surface angular error of $\pm 0.12^{o}$ (searchlight quality) with a potential of achieving $\pm 0.08^{o}$.

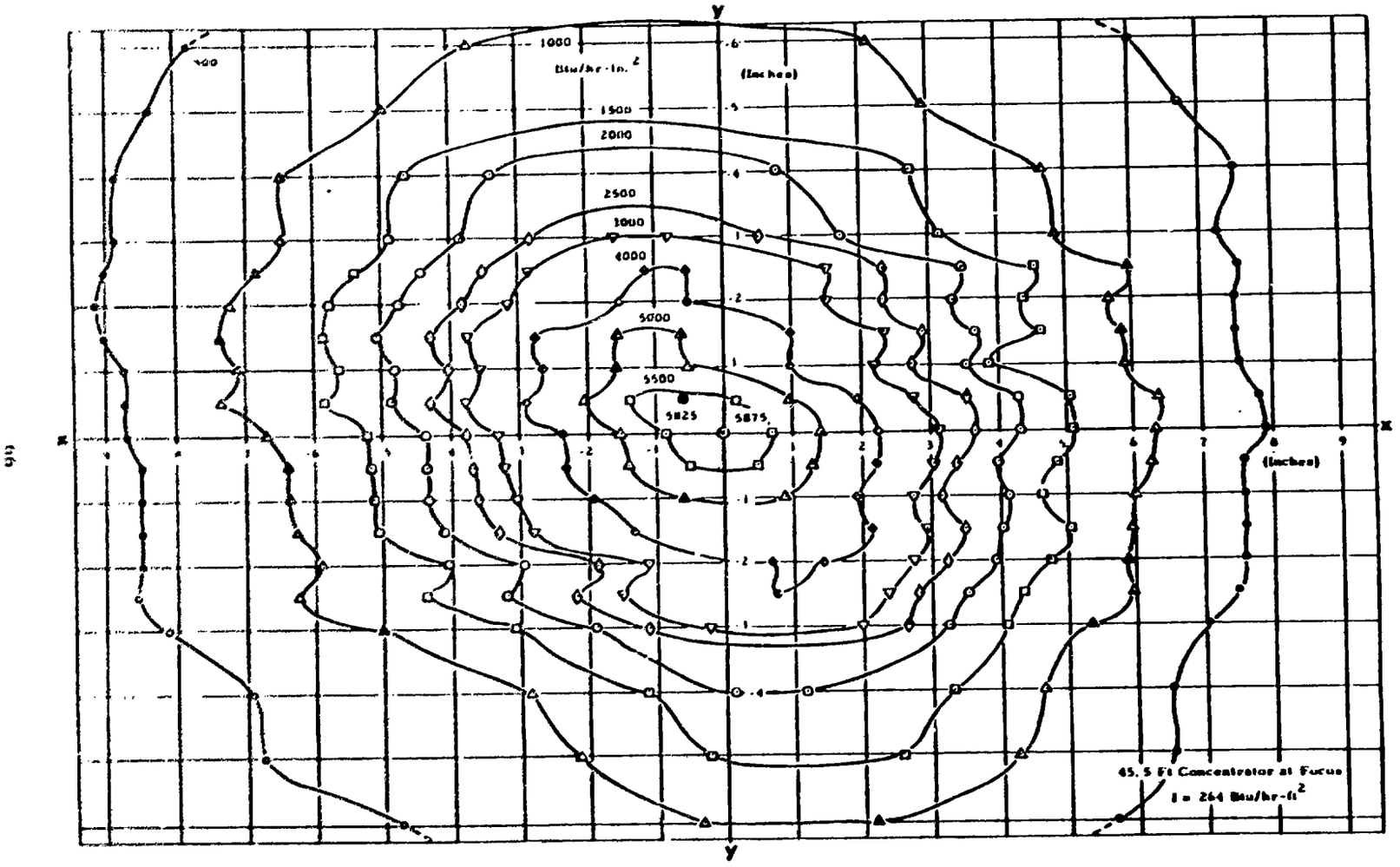

Figure 30. Sunstrand Test Results of Goodyear Concentrator - Flux Contour Map
(Reproduced from Ref.1)

Table 5 presents the assumed error budget for an overall collector pointing error of 0.1 degrees. These accuracy values are considered to be within the capabilities of state-of-the-art attitude control system hardware. Table 6 gives an achievable average concentration ratio of 14,328:1 at the exit of a Winston horn (compound parabolic reflector skirt) whose inlet aperture radius ratio (r/R) is 0.006. The exit of the horn would be located at the optical inlet of the absorber cavity. The maximum absorber temperature corresponding to this concentration ratio for an absorptivity/emissivity ratio of 1.0, is 7700°R, assuming zero absorber efficiency, or 100% reradiation losses. At 7000°R, the reradiation losses are reduced to 68.3%.

Table 5. Collector Pointing Accuracy Error Budget

ERROR SOURCE	REMARKS/BASIS	BUDGET (DEG.)
Attitude Determination	Stellar Aided Inertial System	.01 DEG.
Control Dynamics	Function of Disturbance Levels and Control Bandwidth	.05 DEG.
Structural Deformation Thermal Deformation	Function of Configuration, Structure Design, and Induced Loads	.086 DEG.

RSS = ± 0.100 DEG.

*3 Standard Deviations

Table 6. Achievable Concentration Ratio

ASSUMPTIONS

- Rim Angle $\pm 45^{\circ}$
- Surface Error 0.12° (Std. Dev.)
- Collector Efficiency 0.80
  (Reflectivity 0.9)
  (Canopy Transmission 0.89)

AVERAGE C.R. AT INLET TO WINSTON HORN = 9,800 (on-axis)

AVERAGE C.R. AT EXIT OF WINSTON HORN = 14,328 (off-axis)

- Winston Horn Concentration (Theor.) 2:1
- Off-Axis Correction Factor 0.95
- Pointing Error Correction Factor 0.95
- Window Transmission Factor 0.9
- Winston Horn Reflective Efficiency 0.9

5.0 THRUSTER/ABSORBER PERFORMANCE

To achieve a high performance propulsion system, a high delivered specific impulse is necessary. The specific impulse achieved by a rocket thruster is dependent on the propellant selected, the final propellant gas temperature attained and the thruster performance losses. Theoretically the vacuum specific impulse varies as

$$I_s \propto \sqrt{\frac{\text{Temperature}}{\text{Molecular Weight}}}$$

therefore a low propellant molecular weight is desirable and leads to the selection of a low molecular weight propellant. For conventional liquid bipropellants at a given chamber pressure, the gas temperature is only a function of the fuel and oxidizer mixture ratio. For the solar rocket the approach used is to use a monopropellant and achieve high gas temperature through solar heating. Final propellant gas temperatures exceeding that of conventional bipropellants are possible and are limited only by wall material temperature limits and/or the sun's temperature.

Two absorber/thruster concepts were evaluated in this study. One absorber/thruster concept utilizes a solar cavity heat exchanger configuration in which the propellant indirectly absorbs the solar radiation incident on the heat exchanger walls. The maximum propellant gas temperature for this concept is limited by the temperature limit of the wall material. The other absorber/thruster configuration incorporates direct solar radiation absorption through the use of absorbing molecules or solid particles. Since the absorber/thruster can be cooled with the propellant prior to entering the direct solar radiation absorber, a final gas temperature exceeding wall material temperature limits can be achieved and therefore this concept has a higher thruster performance potential than the cavity heat exchanger concept.

THEORETICAL PROPELLANT PERFORMANCE

Theoretical Vacuum Specific Impulse

To predict the potential delivered specific impulse for the solar rocket, parametric ODE* performance data were generated. The variation of theoretical equilibrium (shifting) vacuum specific impulse with gas temperature were determined for hydrogen (H_2), methane (CH_4), ammonia (NH_3), and hydrazine (N_2H_4)at a chamber pressure of 50 psia as shown in Figure 31. Data for thruster nozzle area ratios ranging from 100 to 400 are presented. For a given propellant gas temperature, hydrogen achieved a theoretical specific impulse a factor of two higher than that of ammonia or hydrazine and approximately 77-percent higher than that of methane. The increase in slope of specific impulse versus temperature with hydrogen at approximately 5000°R is the result of an increase in the amount of dissociated hydrogen. Methane specific impulse values for a given temperature were 14 to 24-percent higher than that of ammonia. As shown in Figure 31, the variation of theoretical specific impulse for an area ratio increase from 100 to 400 was approximately 6-percent at 7000°R gas temperature for hydrogen.

The desired high propellant temperatures represent a problem for methane. Above 1760°R methane starts to decompose and forms coke which deposits on coolant passage walls. This coking layer acts as an insulating layer and makes cooling of the heated surface difficult. Therefore methane was not considered a potentially attractive propellant for the solar rocket.

One approach to achieve a high specific impulse and low propellant volume is to utilize a combination of hydrogen and hydrazine. The theoretical vacuum specific impulse data for a gas temperature of 5000°R is presented in Figure 32 for various hydrazine mass fractions. The trend of specific impulse versus hydrazine mass fraction was roughly linear with specific impulse decreasing approximately 4-percent for each 10-percent of hydrazine added.

---

*One-dimensional equilibrium

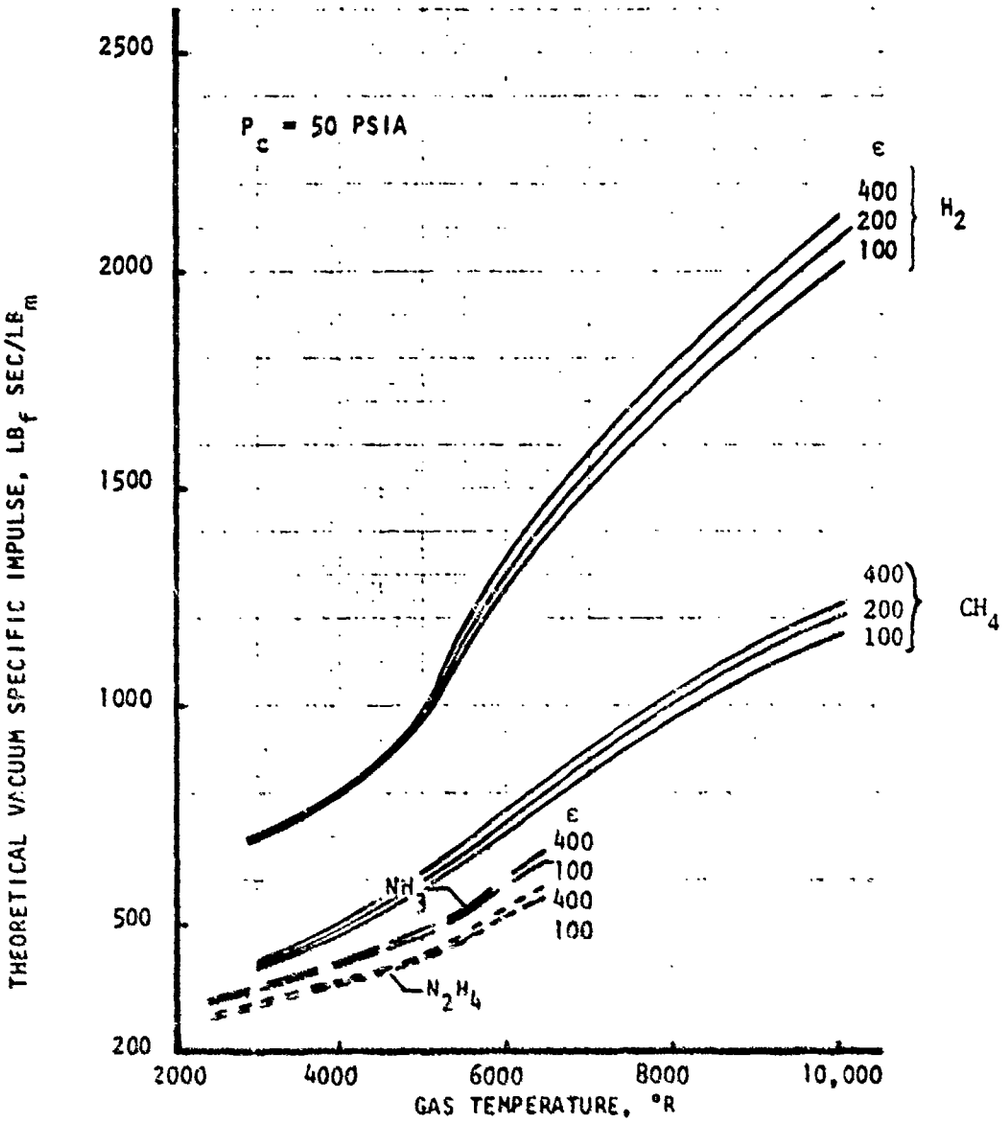

Figure 31. Theoretical Vacuum Specific Impulse Variation With Gas Temperature for Hydrogen, Hydrazine, Ammonia, and Methane

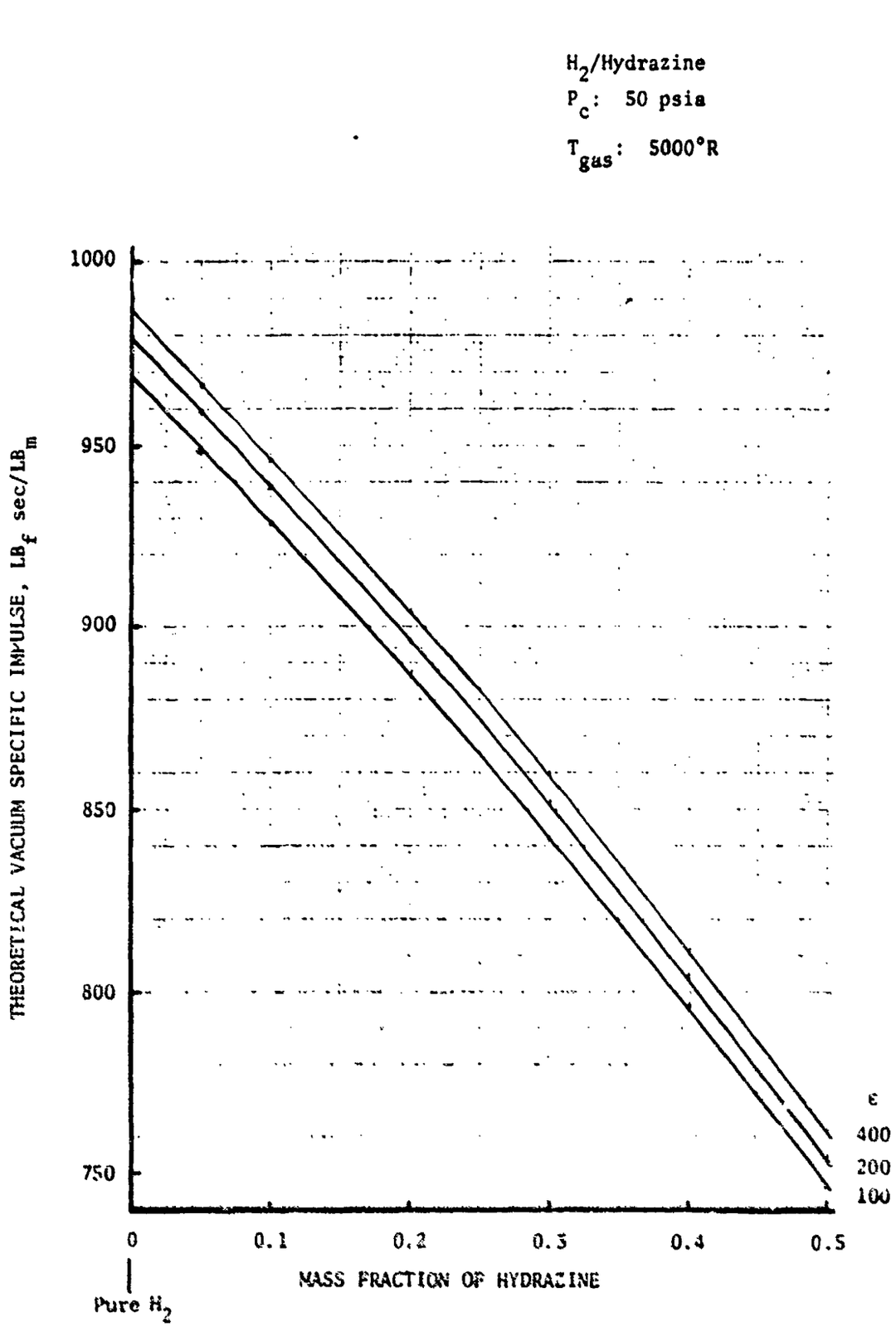

Figure 32. Hydrogen/Hydrazine Theoretical Specific Impulse at 5000°R

The influence of chamber pressure on the theoretical chemical equilibrium (shifting) vacuum specific impulse was determined for hydrogen and ammonia as shown in Figures 33 and 34, respectively. The variation with gas temperature and nozzle area ratio is also presented. For both hydrogen and ammonia the increase in the amount of dissociated hydrogen at the lower chamber pressures resulted in the higher specific impulses. Theoretical specific impulse increases as high as 16 percent were achieved. However, the increase in reaction kinetic efficiency at the lower chamber pressures was expected to negate the theoretical specific impulse increase. The reversal of this trend at the higher temperatures for hydrogen (Figure 33) is due to the influence of the increase in heat released in hydrogen recombination at the higher chamber pressure becoming dominate over the influence of the increase in dissociated hydrogen in the chamber at low chamber pressures.

For the particulate absorption thruster concept, one candidate propellant was a hydrogen-carbon mixture. Submicron carbon particles are used to directly absorb the incoming solar radiation. The variation of the theoretical specific impulse with carbon fraction and gas temperature was obtained for the hydrogen/carbon mixture at a chamber pressure of 50 psia and an area ratio of 100 to 1 (Figure 35). The addition of the higher molecular weight carbon degrades the specific impulse. At a fixed carbon fraction this degradation becomes greater at the higher gas temperatures.

The influence of nozzle area ratio for the hydrogen-carbon mixture is presented in Figure 36. For gas temperatures of 5000°R and lower, an increase in area ratio from 100 to 400 resulted in a 1.4 to 1.8 percent increase in the theoretical specific impulse. At gas temperatures of 7000° and 10,000°R, a specific impulse increase of 5.2 percent resulted for this same area ratio change.

Enthalpy Influences

One approach to rating the various candidate propellants from a thruster performance standpoint is to determine the achievable specific impulse for a given thrust level and solar radiation heat input. Pertinent relationships for a single fluid propellant are:

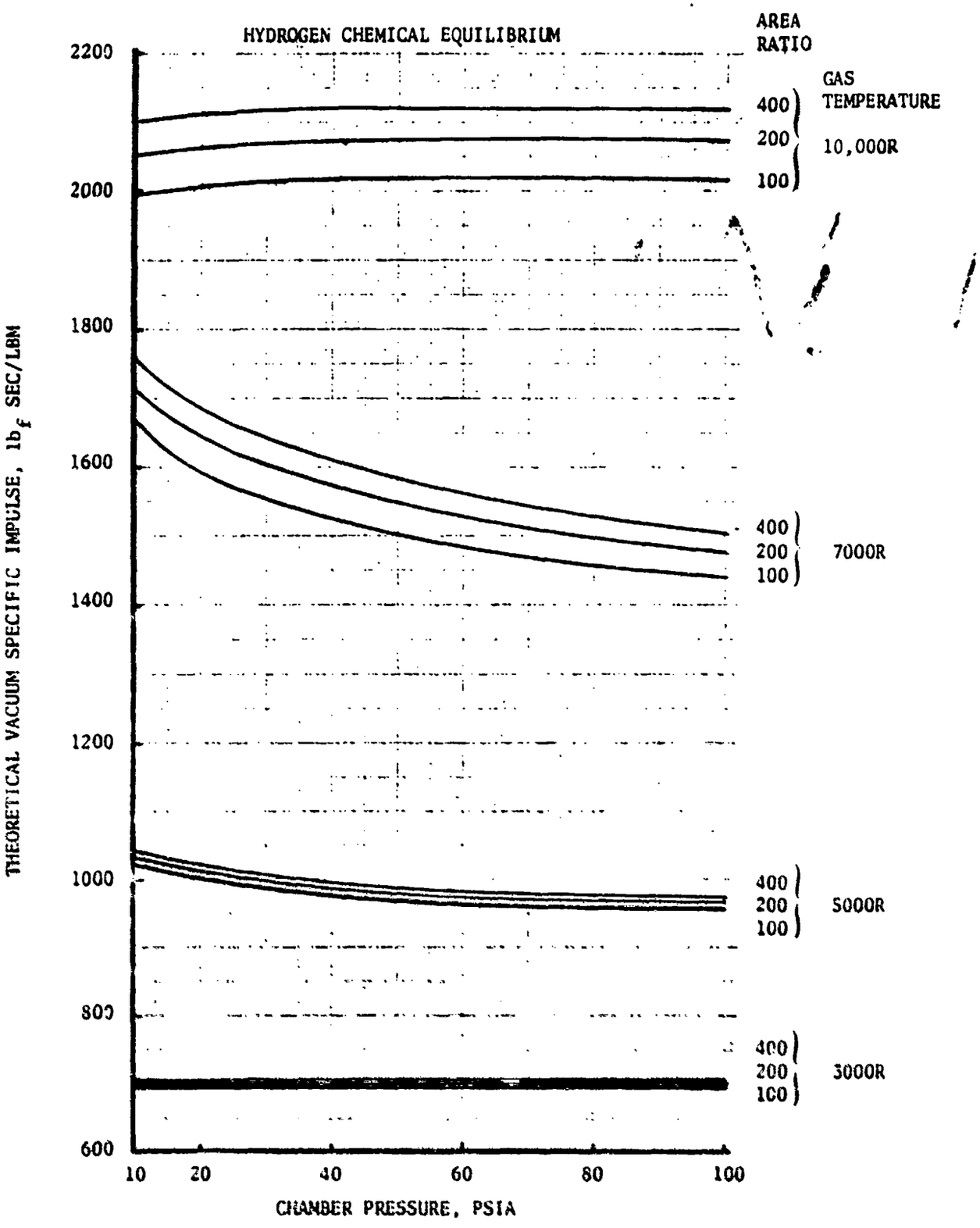

Figure 33. Theoretical Vacuum Specific Impulse Variation With Chamber Pressure, Area Ratio, and Temperature for Hydrogen

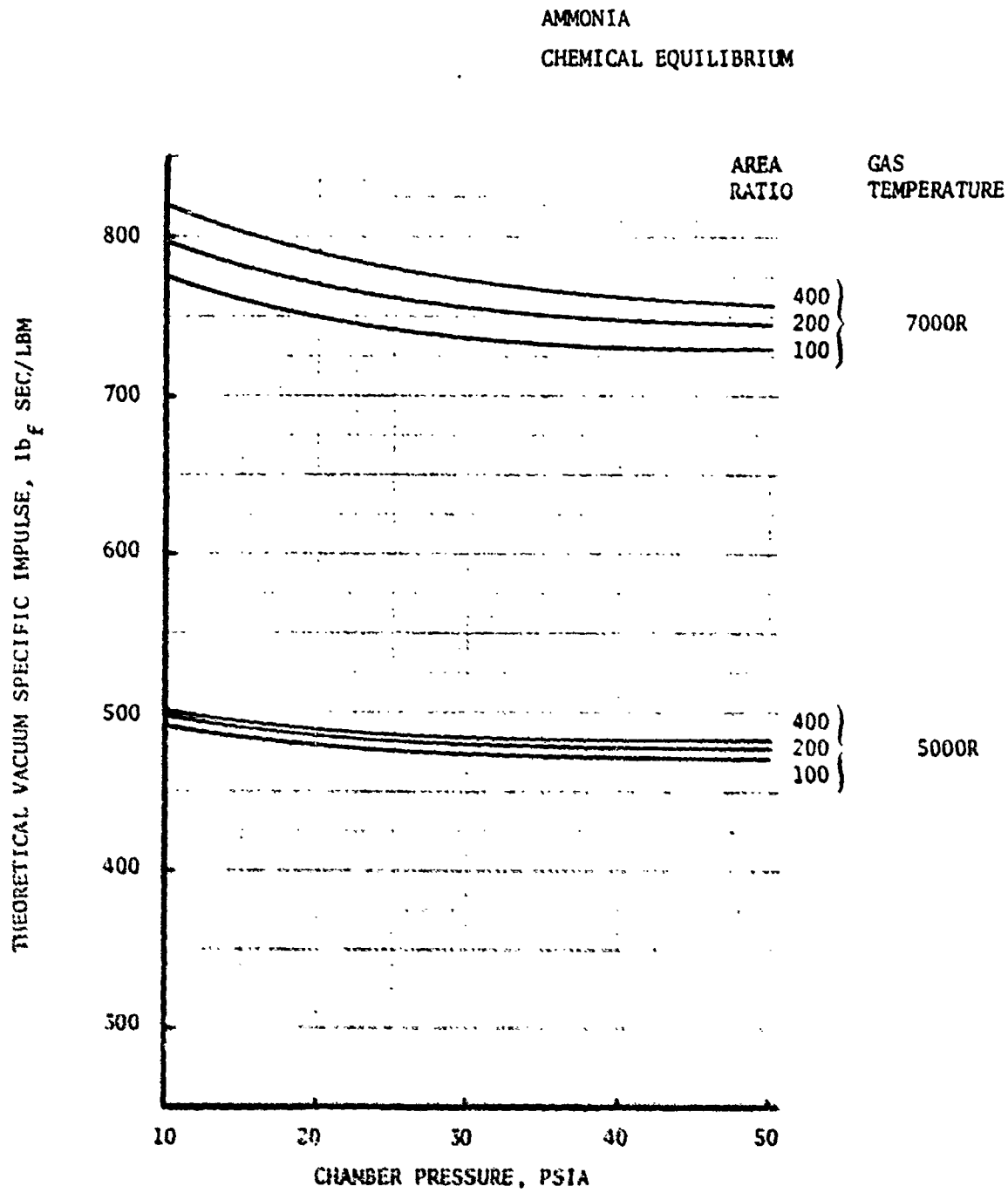

Figure 34. Theoretical Vacuum Specific Impulse Variation With Chamber Pressure, Area Ratio, and Temperature for Ammonia

HYDROGEN/CARBON
P_c = 50 PSIA
ε = 100:1
CHEMICAL EQUILIBRIUM

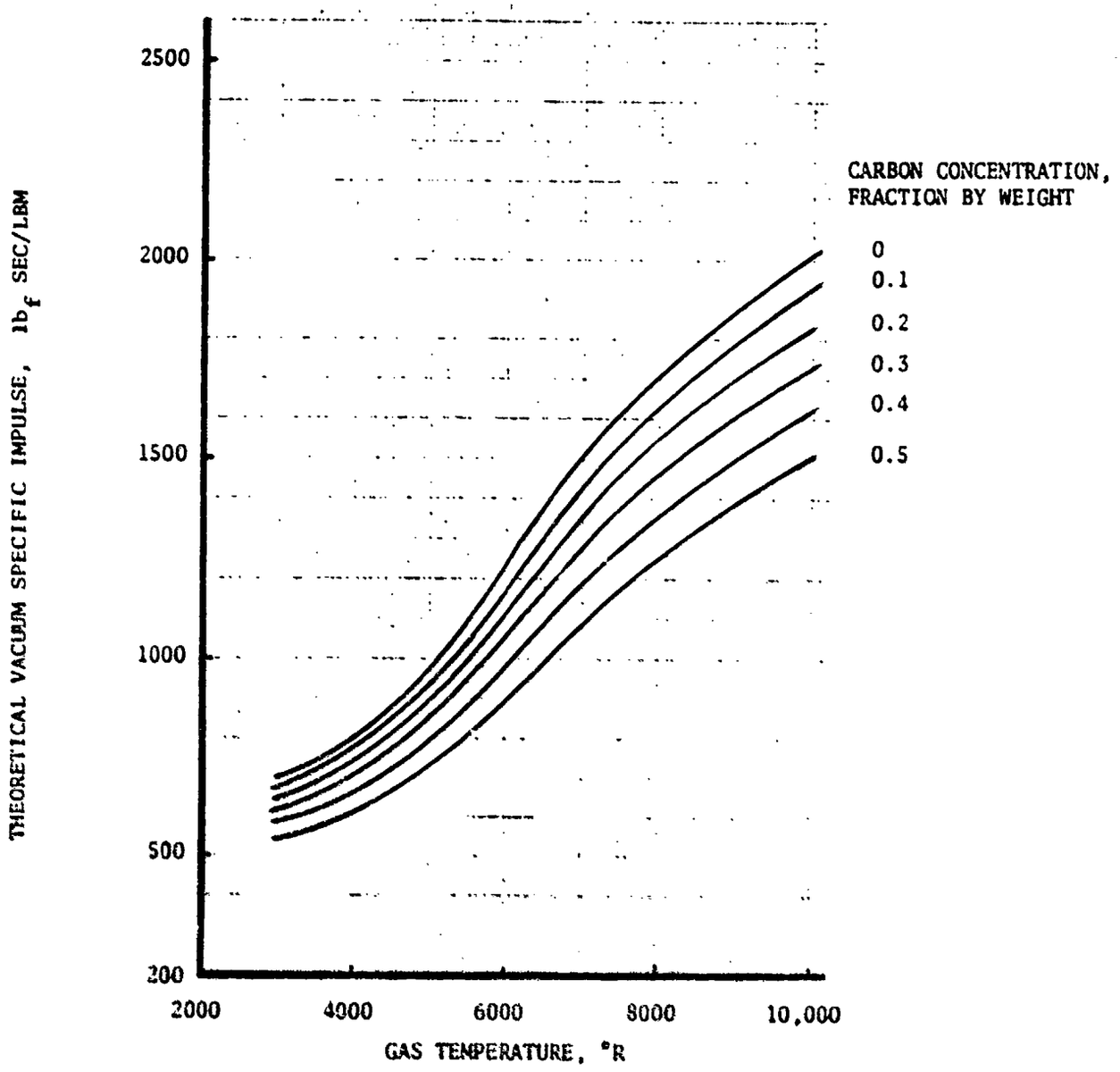

Figure 35. Theoretical Vacuum Specific Impulse Variation With Carbon Concentration and Gas Temperature for Hydrogen/Carbon

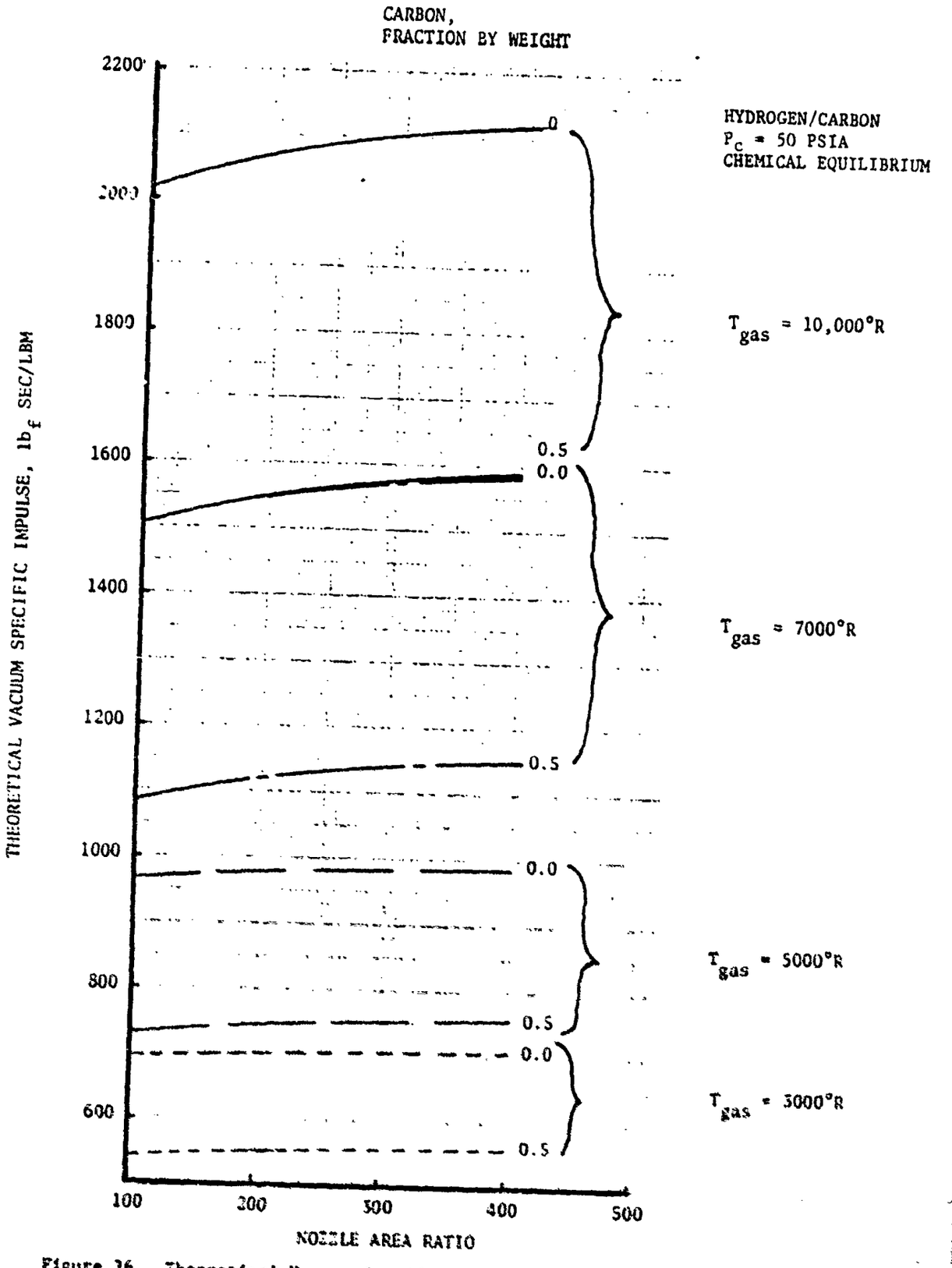

Figure 36. Theoretical Vacuum Specific Impulse Variation With Area Ratio, Carbon Concentration and Temperature for Hydrogen/Carbon

$$\text{Heat Input, } Q = \dot{m}_{Prop.} \Delta H_{Prop.}$$

and for a fixed thrust,

$$\dot{m}_{Prop.} \propto \frac{1}{I_s}$$

Combining the preceding two relationships,

$$Q \propto \frac{\Delta H_{Prop.}}{I_s}$$

A curve of specific impulse versus ΔH was plotted (Figure 37) and translated into a specific impulse versus $\Delta H_{Prop}/I_s$ curve as presented in Figure 38. As shown in Figure 38, hydrazine and H_2 resulted in approximately the same specific impulse for the same Q ($\Delta H_{Prop}/I_s$) but the ammonia specific impulse was approximately 14 percent lower for a given Q. However, to achieve the same specific impulse, the hydrogen only needs to be heated to less than one-half the temperature of the hydrazine which is desirable. The material temperature limitations and the limitation of not being able to exceed the effective sun temperature of approximately 11,000°R makes hydrogen an attractive propellant from an absorber/thruster performance standpoint.

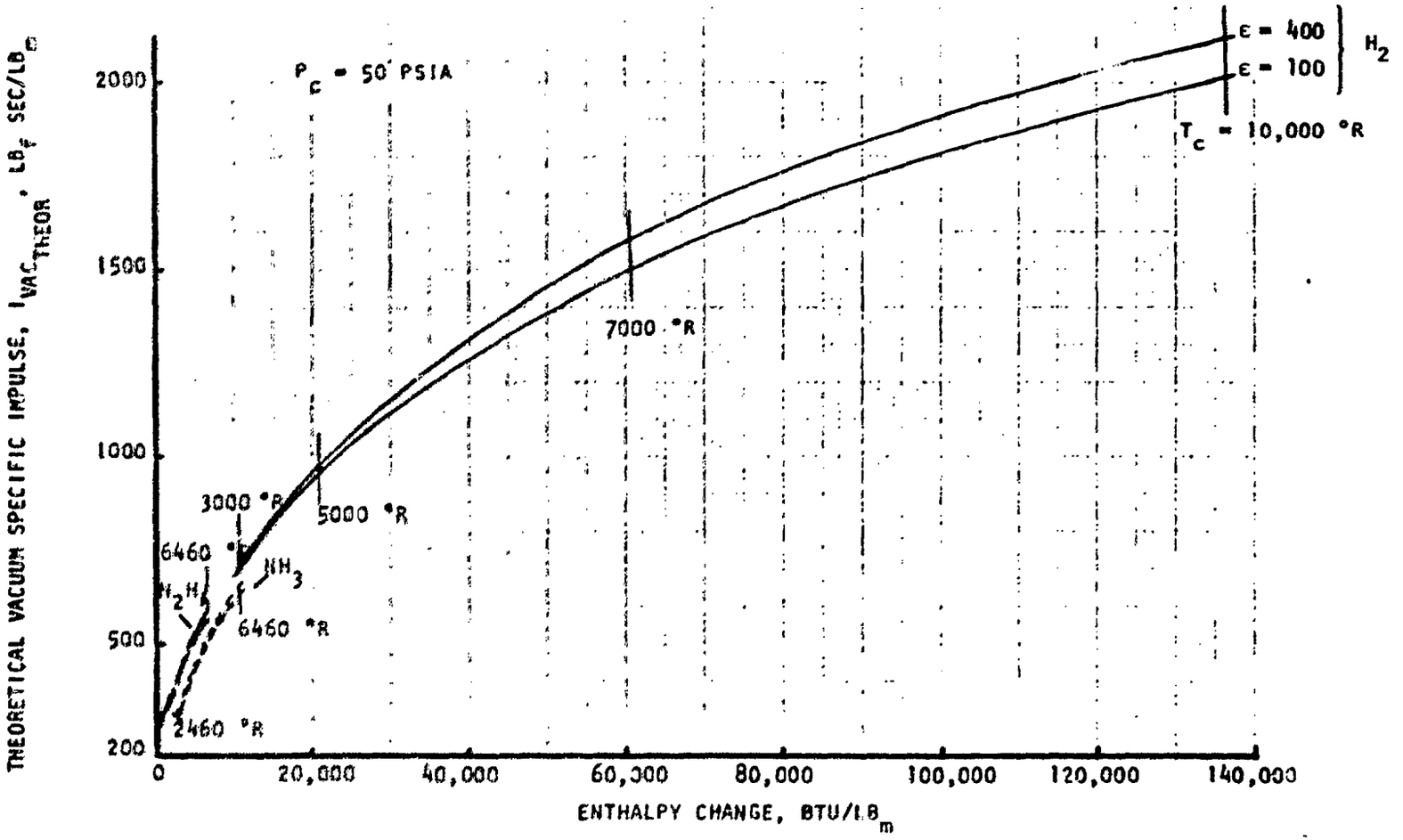

Figure 37. Theoretical Vacuum Specific Impulse Variation With Enthalpy Change for Hydrogen, Hydrazine, and Ammonia

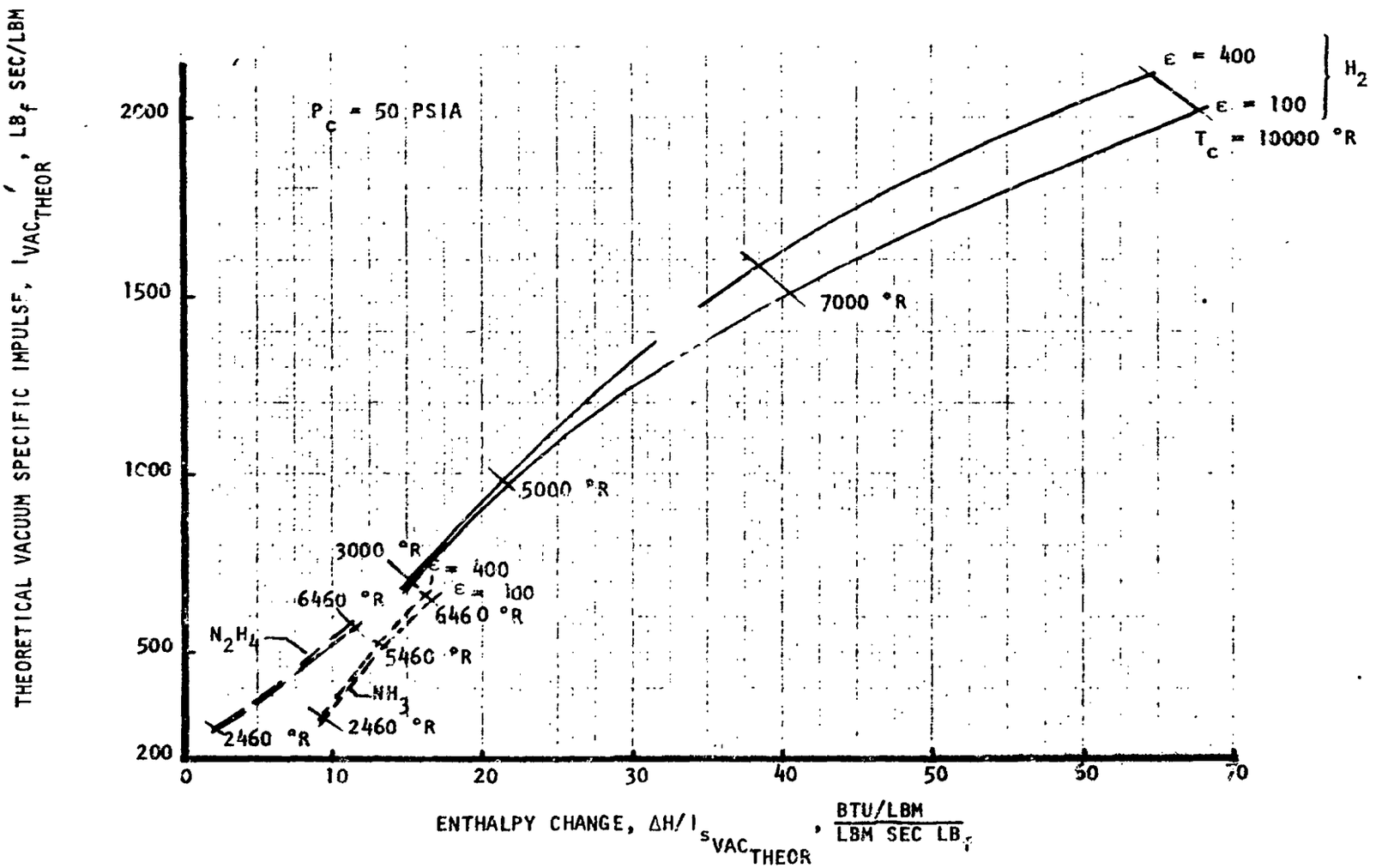

Figure 38. Theoretical Vacuum Specific Impulse Variation With $H/I_{s_{VAC}}$ for Hydrogen, Hydrazine and Ammonia

ABSORBER PERFORMANCE

Heat Exchanger Cavity Absorber

In determining the heat exchanger cavity concept, both spherical and flat disc absorber configurations were evaluated to obtain absorber efficiency trends. The spherical cavity represents the cavity with the lowest cavity shape factor which reduces cavity reradiation losses. The flat disc absorber represented the simplest concept.

The cavity absorber efficiency relationship was derived based on an extension of the work of Kreith (Ref. 10) and Stephens and Haire (Ref. 11). The cavity absorber efficiency was defined as:

$$\eta_{\substack{\text{Cavity}\\ \text{Absorber}}} = \frac{Q_s - (Q_{r_1} + Q_{r_2})}{Q}$$

Where

Q_s is the solar radiation absorbed by the cavity and working fluid

Q_{r_1} is the energy lost through reradiation through the opening

Q_{r_2} is the energy lost from the cavity external surface

Q is the incoming solar energy

$$\eta_{\substack{\text{Cavity}\\ \text{Absorber}}} = \frac{1}{1-(1-F_{12})(1-e_1)} \left[e_1 - \frac{3.9860465\text{x}10^{-12}}{C\ (A_2/A_1)} \right\{ e_1 e_2 F_{12} T_1^{\ 4} + e_w T_w^{\ 4} \left(1-(1-F_{12})(1-e_1) \right) \} \right]$$

Where

F_{12} = Shape factor

e_1 = Cavity internal surface emissivity

e_2 = Cavity opening emissivity

e_w = Cavity external surface emissitivy

C = Concentration ratio of energy entering cavity absorber

A_2/A_1 = Ratio of cavity opening area to internal area

T_1 = Cavity absorber internal surface temperatures, °R

T_w = Cavity absorber external surface temperature, °R

For the heat exchanger-type cavity, e_2 is equal to 1.0.

For the degenerate case of a flat disc, the above expression becomes:

$$\eta_{\substack{\text{Flat}\\ \text{Disc}\\ \text{Absorber}}} = e_1 - \frac{3.9860465 \times 10^{-12}}{C} \left[e_1 T_1^{\,4} + e_w T_w^{\,4} \right]$$

The efficiencies for a spherical heat exchanger type cavity and a flat disc absorber are presented in Figures 39 through 42 to illustrate the general efficiency trends.

For these cases an absorber surface emissivity of 0.3, an external surface emissivity of 0.05 and an external surface temperature of 960 °F were assumed. For the spherical cavity absorber, the efficiency increased with decrease in the ratio of cavity opening area to internal area (A_2/A_1) and with increase in concentration ratio. At 1000 °R spherical cavity internal surface temperature (Figure 42), an increase in concentration ratio did not significantly increase the cavity efficiency. However, at a cavity internal surface temperature of 4460 °R, a concentration ratio of 4000 to 6000 is required to achieve an efficiency of 60 percent (Figure 42). Due to the increase in reradiation with absorber internal surface temperature, the efficiency decreased significantly with increase in surface temperature for both the spherical cavity absorber and the flat disc absorber.

From Figures 39 through 41, the spherical cavity absorber has an efficiency greater than a factor of two higher than that of a flat disc absorber with an absorber surface emissivity of 0.3. As the flat disc absorber

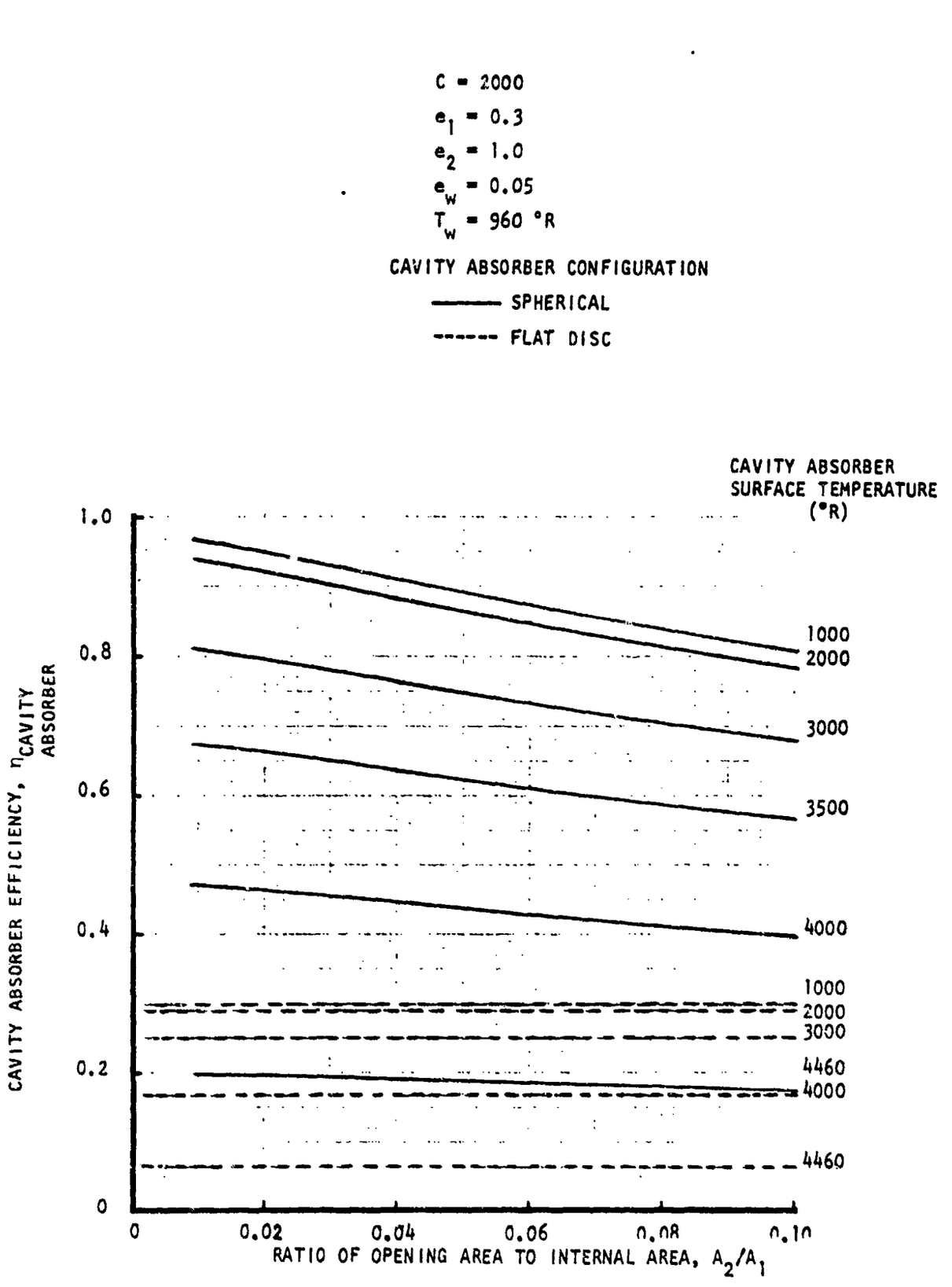

Figure 39. Heat Exchanger Type Cavity Absorber (Spherical and Flat Disc) Efficiency for Concentration Ratio of 2000

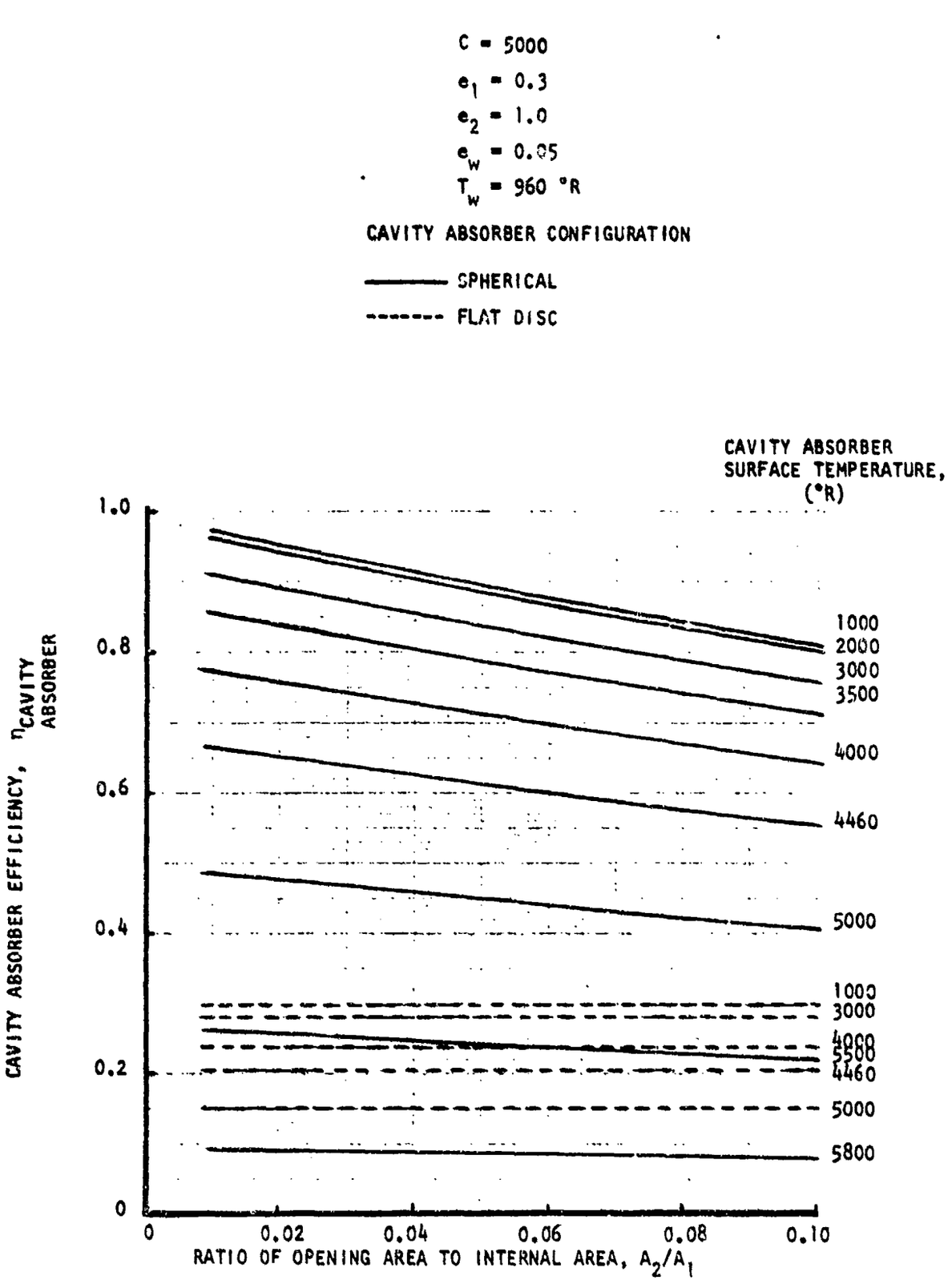

Figure 40. Heat Exchanger Type Cavity Absorber (Spherical and Flat Disc) Efficiency for Concentration Ratio of 5000

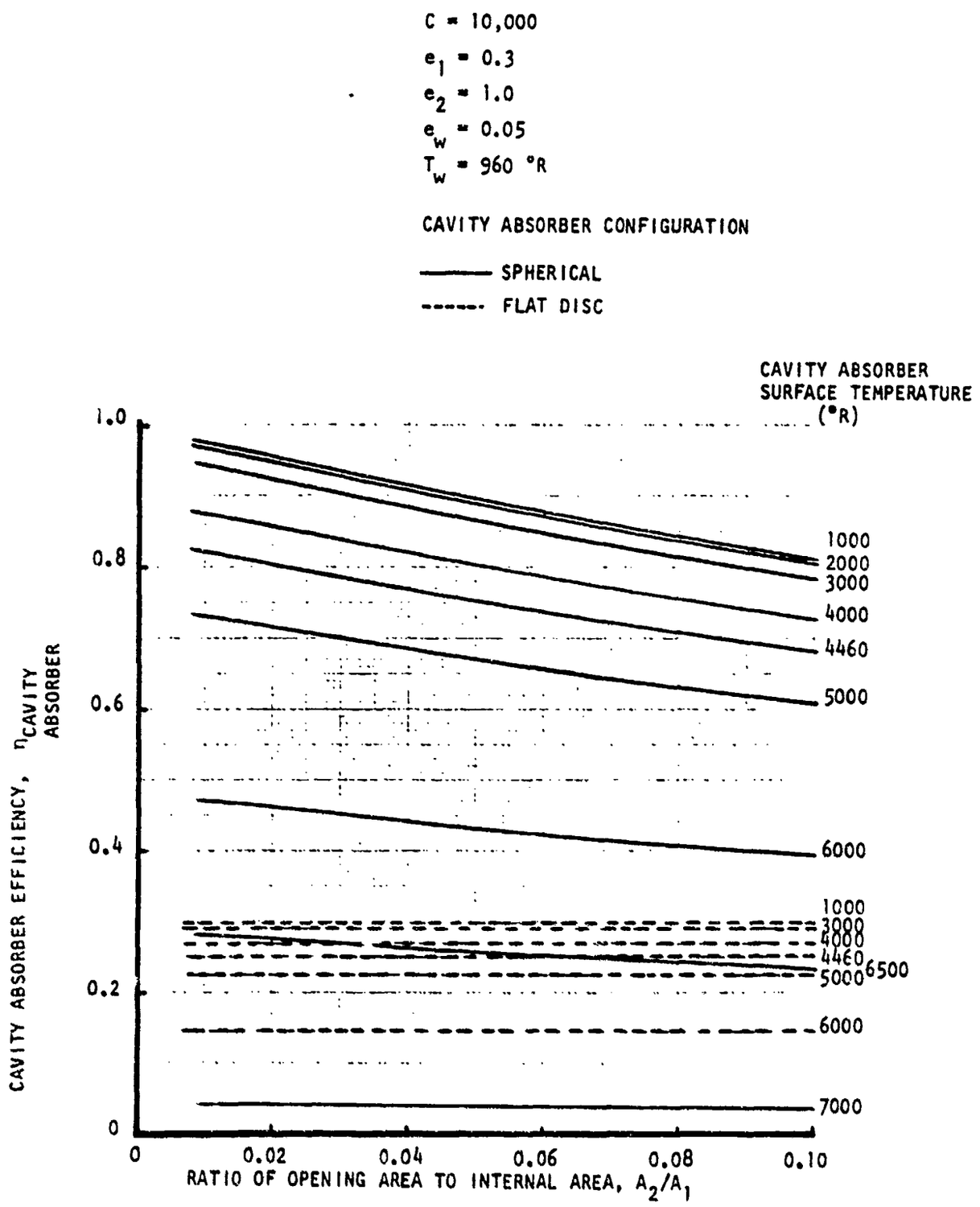

Figure 41. Heat Exchanger Type Cavity Absorber (Spherical and Flat Disc) Efficiency for Concentration Ratio of 10,000

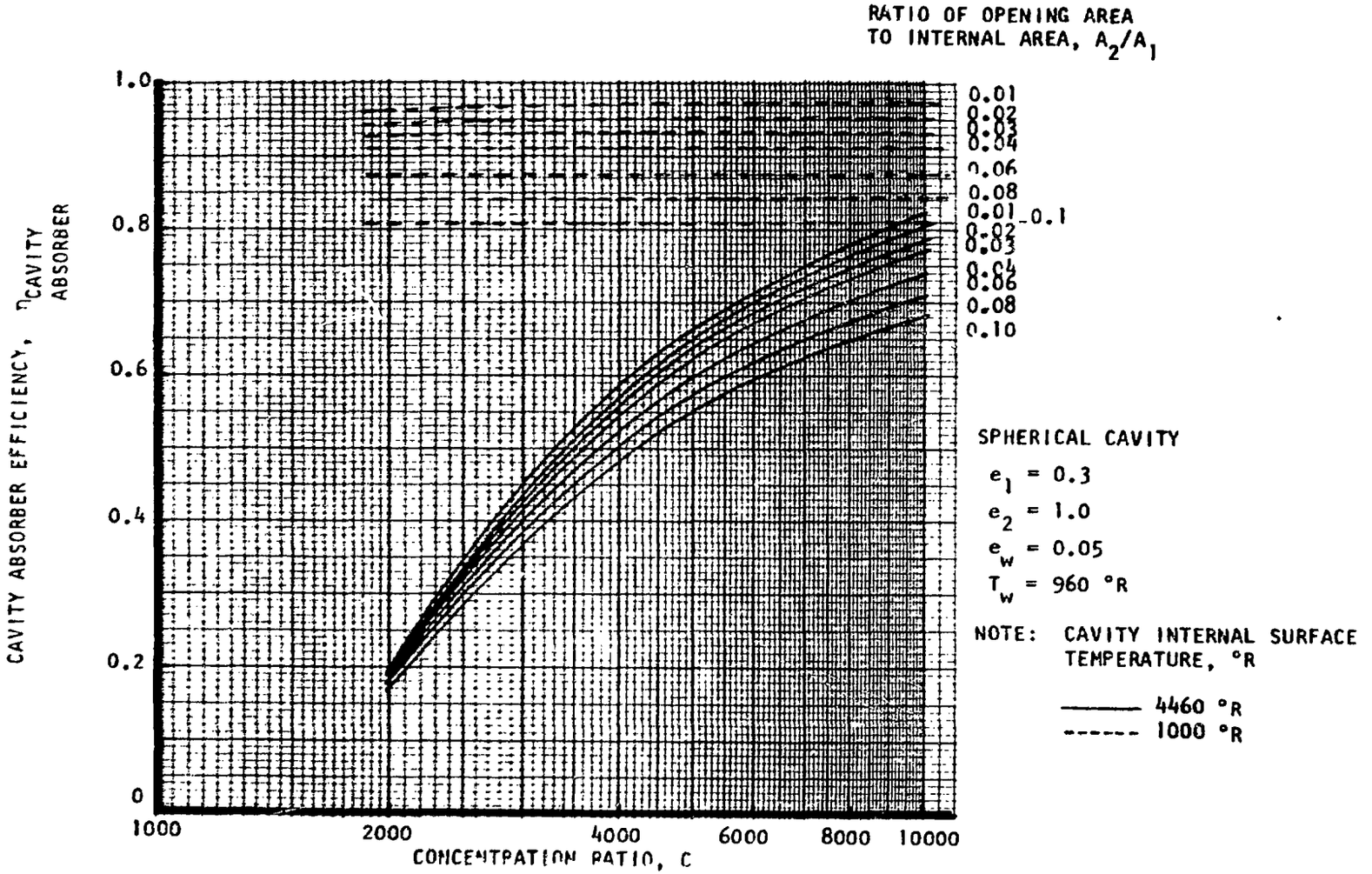

Figure 42. Heat Exchanger Type Cavity Absorber (Spherical) Efficiency Variation With Concentration Ratio and Cavity Area Ratio

emissivity is increased to 1.0, the absorber efficiency approaches that of the spherical cavity as shown in Figure 43. For the spherical cavity absorber (Figure 44), an increase in cavity internal surface emissivity did not significantly increase cavity efficiency for low opening area to internal area ratios (0.01), but did influence cavity efficiency at high opening area to internal area ratios (0.10).

The heat exchanger cavity concept selected consisted of a combination of a spherical cavity and a flat disc. As shown in Figure 45, the absorber cavity consists of a spherical absorber cavity, a reflector cone (Winston Horn), and a flat disc absorber. The spherical cavity permits the high concentration ratio (high heat flux) solar radiation to be spread over a large surface area to reduce the local surface heat flux. The right angle orientation of the incoming solar radiation (from the collectors) and the line of thrust necessitated separate components for the absorber and thruster.

To obtain a high absorber efficiency, low absorber surface temperatures and a high concentration ratio are required. For regions having low concentration ratios, low surfaces temperatures are especially important.

Analysis of the sphere-cone-disc absorber indicated that the absorber fluid conditioning circuit influences the overall absorber cavity efficiency. Absorber efficiency was determined using the 1/2 degree angular error-on-axis solar flux distribution and assuming hydrogen outlet temperature of 5000 °R and a collector diameter of 100 feet. The 5000 °R gas temperature represented the upper limit of the wall material (tungsten) or tungsten alloy being considered for the absorber/thruster. The four hydrogen flow circuits illustrated in Figure 46 were evaluated. The first circuit (two-pass disc circuit with the sphere and cone cooled first) resulted in the outer portion of the flat disc (r/R = 0.02 to 0.05) losing heat to the surroundings due to the high hydrogen bulk temperature and the low concentration ratio at the larger radii.

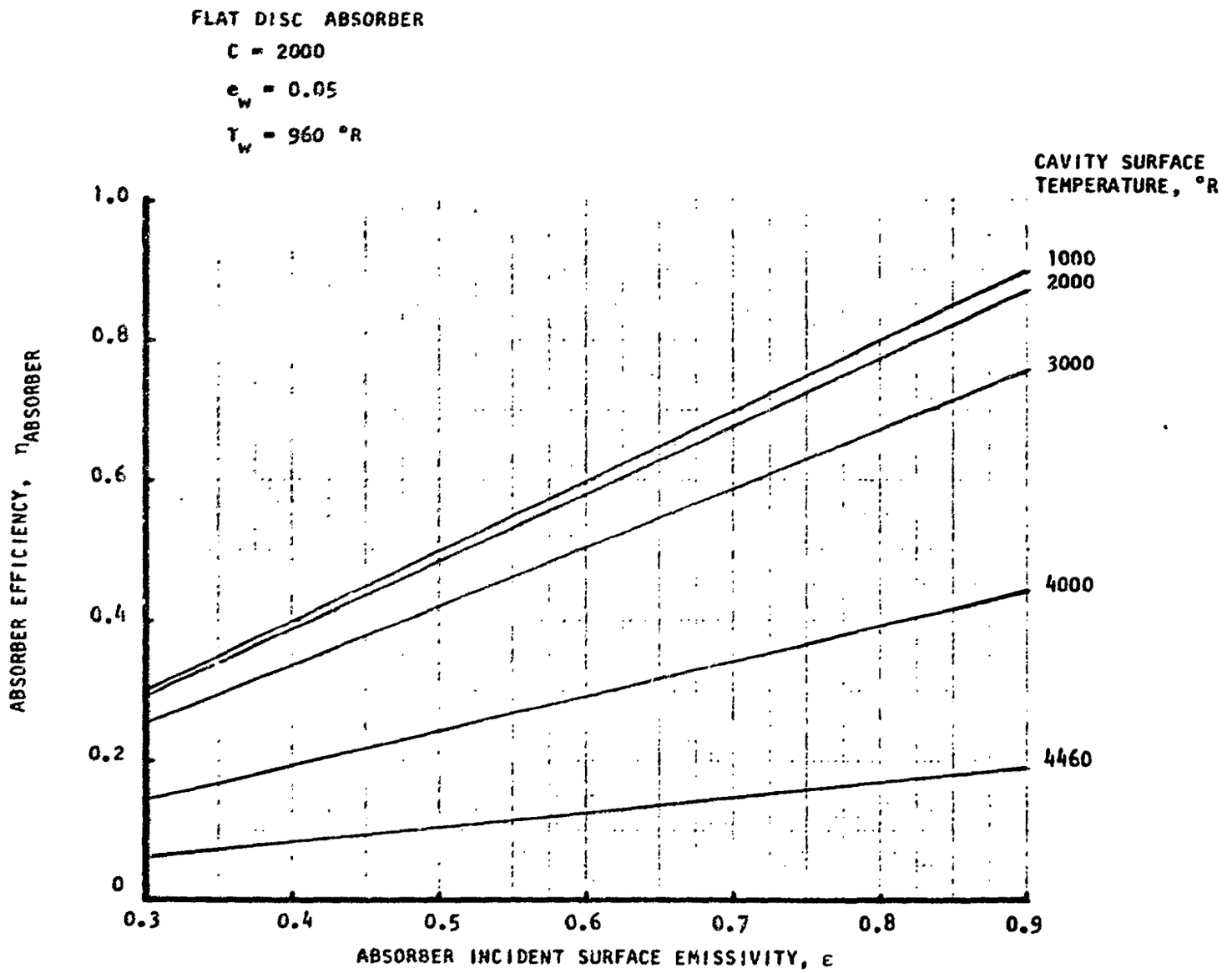

Figure 43. Heat Exchanger Type Flat Disc Absorber Efficiency With Absorber Surface Emissivity and Temperature

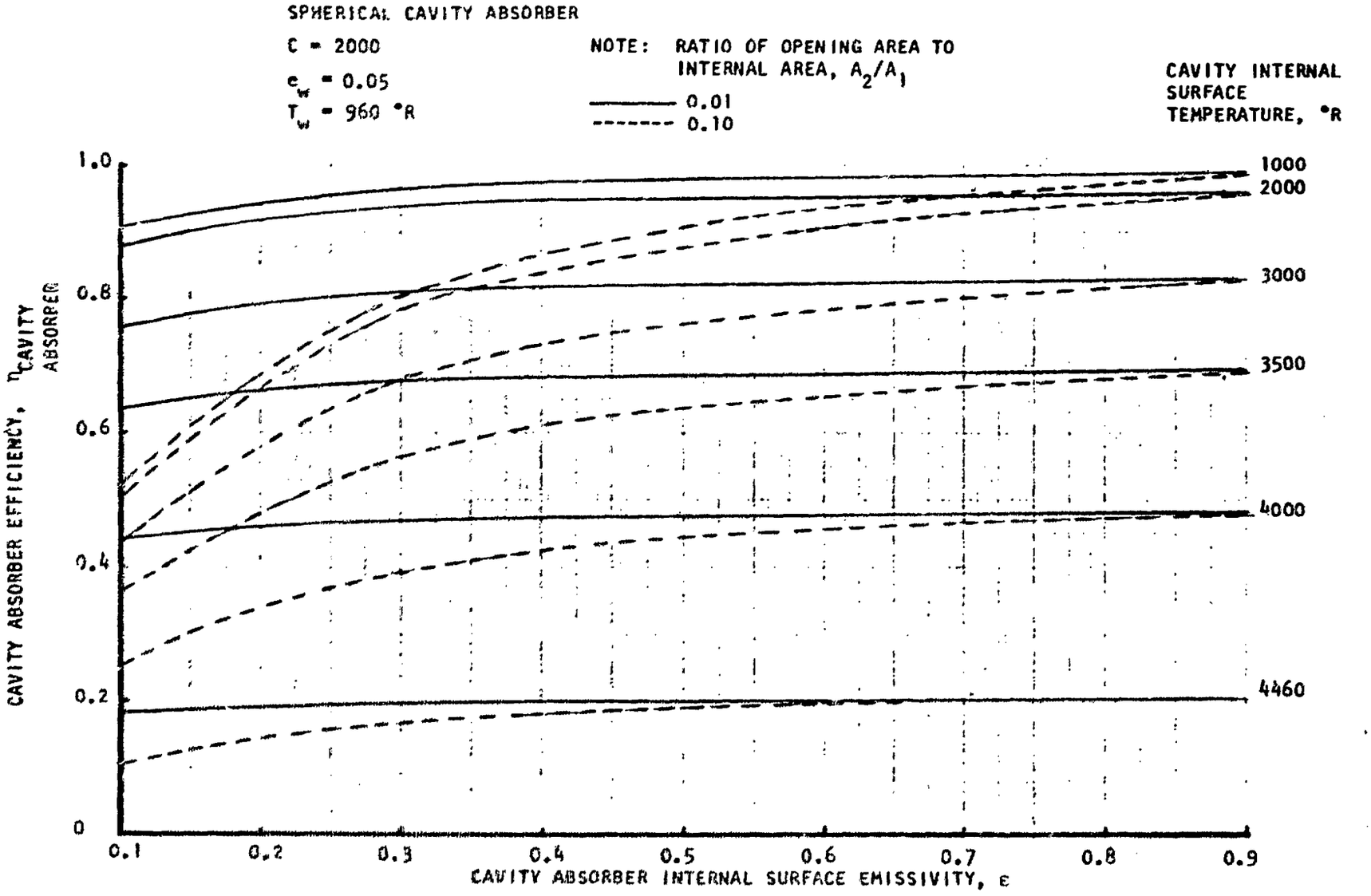

Figure 44. Heat Exchanger Type Cavity Absorber (Spherical Cavity) Efficiency With Absorber Surface Emissivity and Temperature

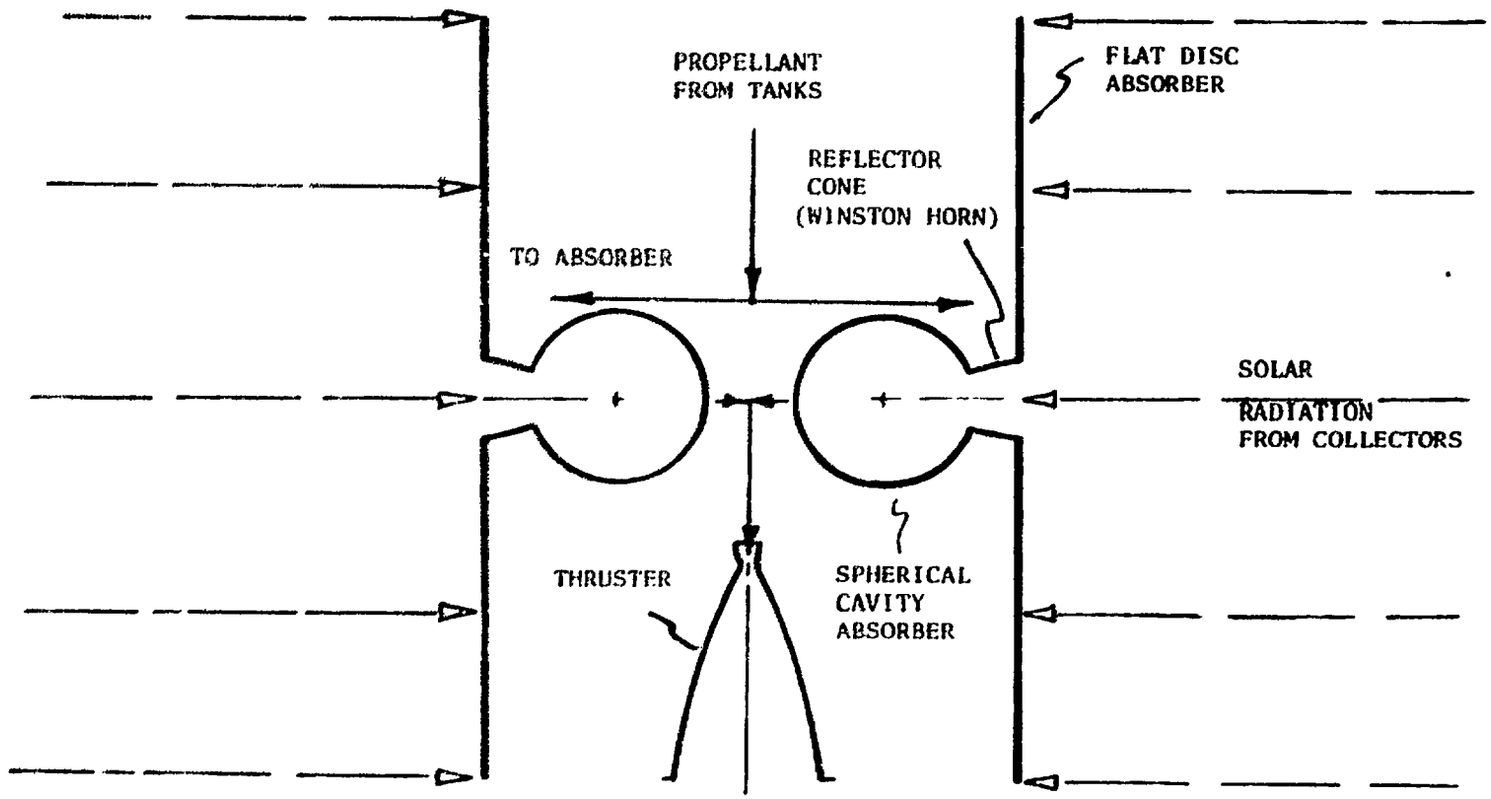

Figure 45. Heat Exchanger Absorber/Thruster Configuration

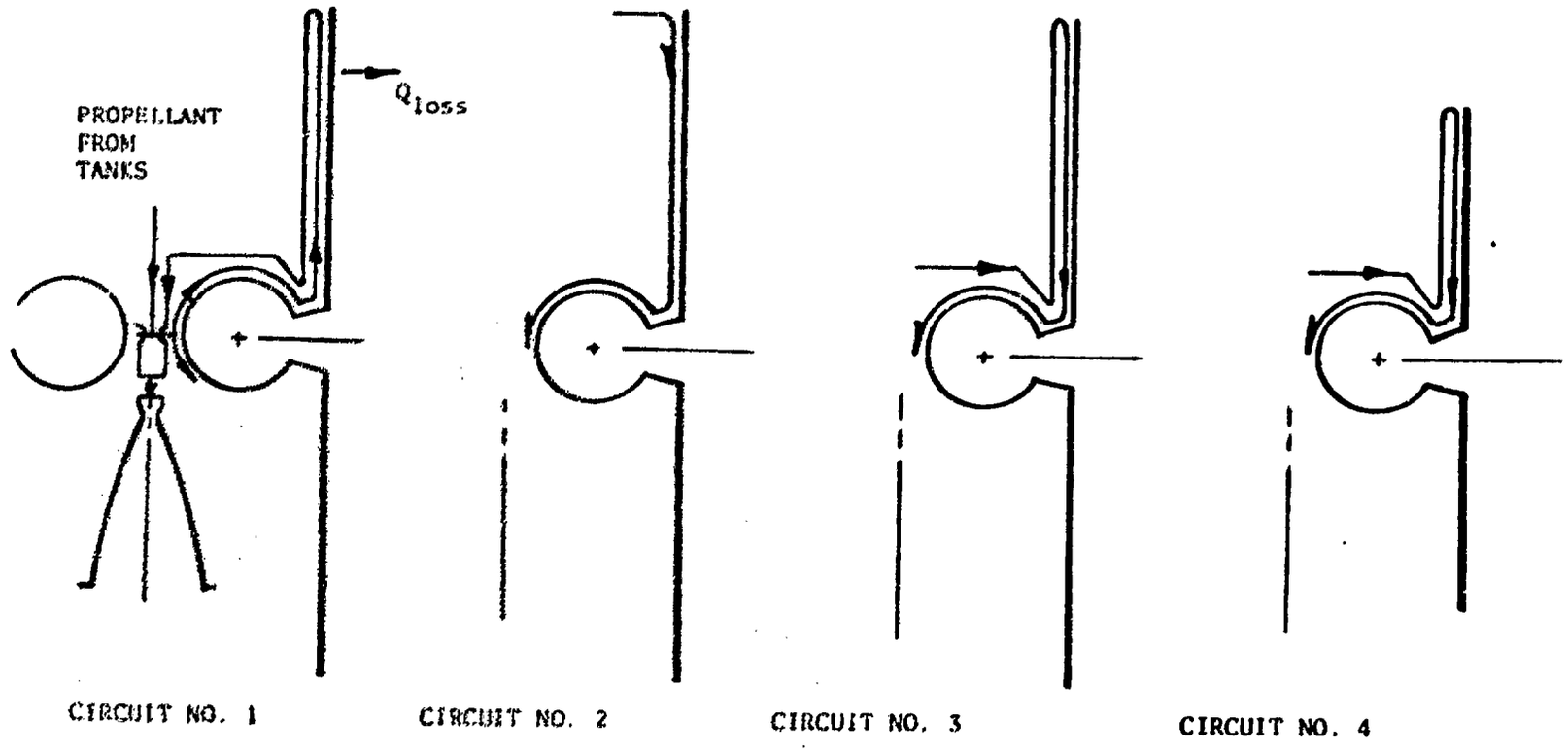

Figure 46. Typical Propellant Circuits

For a flat disc the minimum concentration ratio for a given absorber surface temperature is defined in Figure 47. The curve indicates those conditions which produce zero absorber efficiency (i.e., the heat absorbed is just equal to the heat lost by front-side and back-side re-radiation).

Due to the high hydrogen temperatures near the inner radius of the disc, the second configuration resulted in an overall absorber efficiency less than 50 percent. The third configuration (two-pass disc circuit with the disc cooled first) lost heat from 0.03 to 0.05 r/R. Therefore for the fourth configuration the disc outer radius was limited to a r/D of 0.13 (18 inches) and provided a satisfactory design. The two-pass circuit resulted in a more uniform surface temperature due to the balancing of the cold and hot fluid temperature influences.

A brief analysis of the cooling ability of the dissociated propellants was performed using a generalized coolant correlation. As shown in Figure 48. the cooling parameter (which is directly proportional to the coolant-side film coefficient at a fixed mass velocity) increases slightly with increase in fluid temperature. This trend indicates a slight improvement in cooling capability.

For the nominal collector surface angular error of 1/4-degree and a sphere/horn/disc cavity absorber, the influence of the absorber heat input and absorber efficiency with the reflector cone inlet radius ratio (cone or horn radius to collector radius) was determined using hydrogen as the propellant. As shown in Figure 49, the heat absorbed and the absorber efficiency leveled off at a radius ratio of 0.006 (a 3.6-inch radius for a 100-ft collector diameter). Therefore, this radius ratio value was selected as the nominal cone inlet radius ratio value.

The influence of the collector surface angular error was determined for the heat exchanger cavity absorber using hydrogen with an 8-inch diameter spherical cavity and a 36-inch diameter annular disc. As the surface angular error was increased the heat absorbed and the absorber efficiency

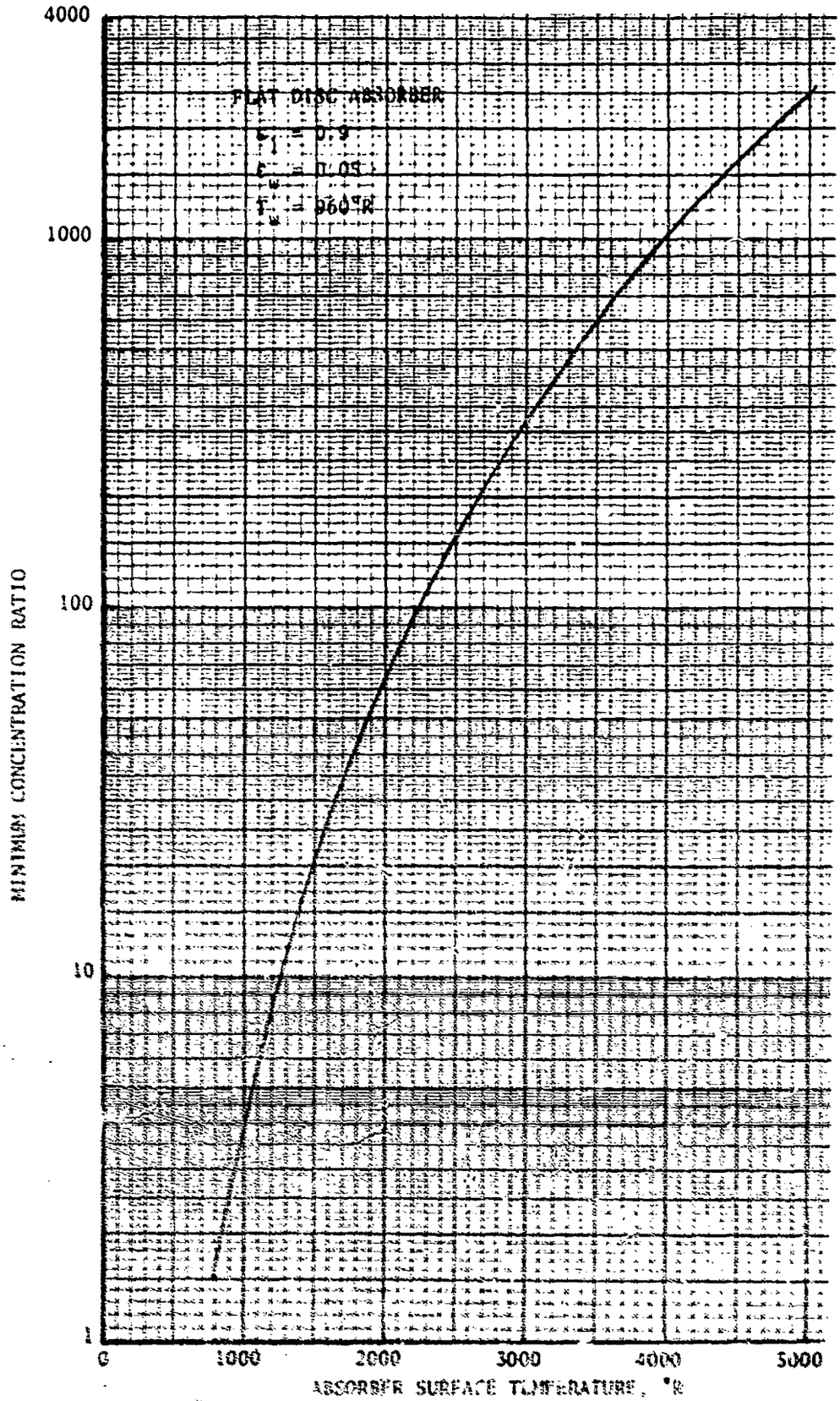

Figure 47. Minimum Requirement Concentration Ratio Variation With Absorber Surface Temperature for a Flat Disc

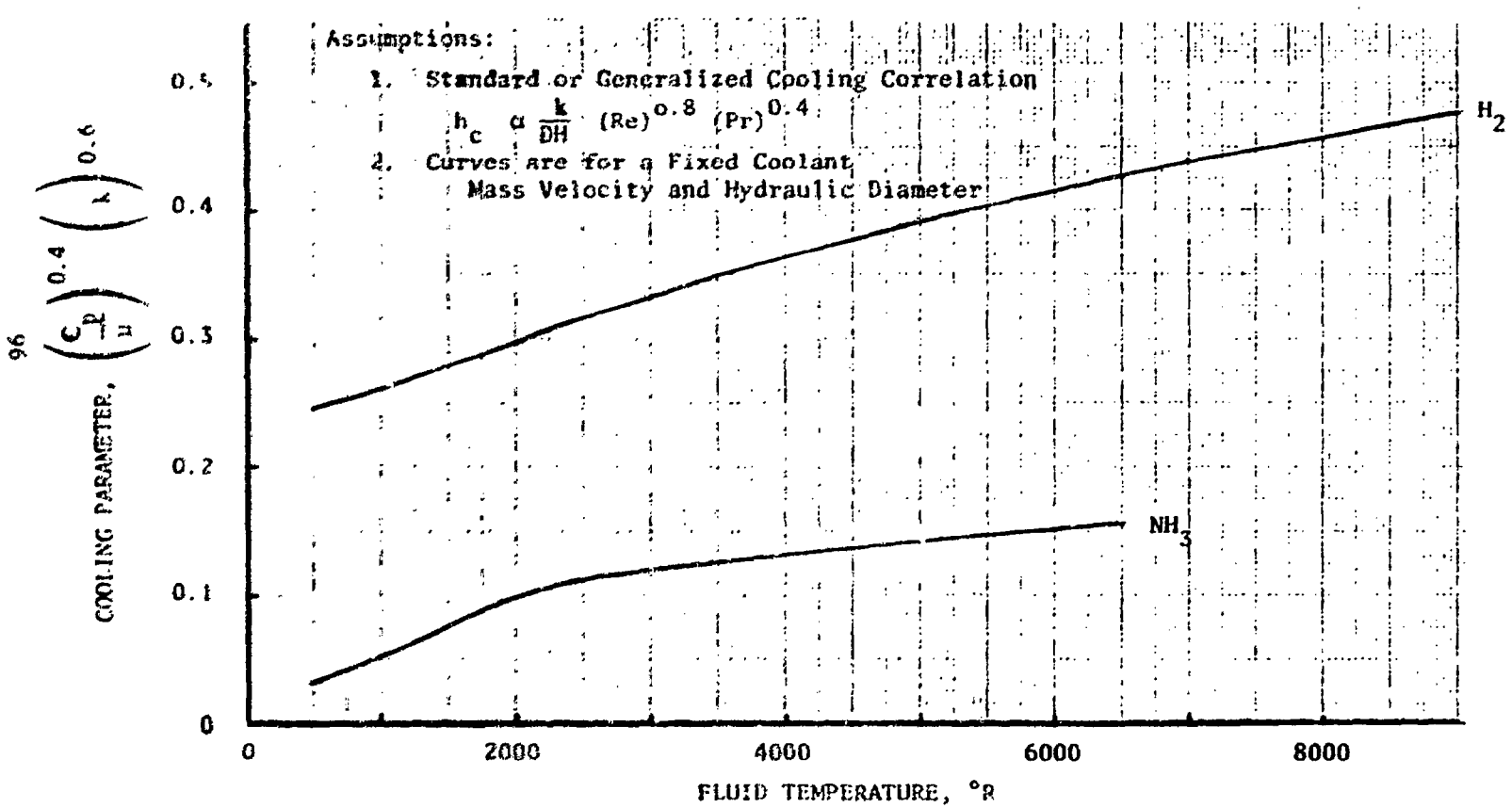

Figure 48. Cooling Parameter Variation With Temperature

Propellant: H_2
$T_{H_2\ outlet}$: 5000°R
Collector:
Diameter: 100 ft
Surface Angular Error: 1/4°
Collector Efficiency; 80-percent
Absorber:
Spherical/Horn/Disc
Disc Diameter: 36 in.

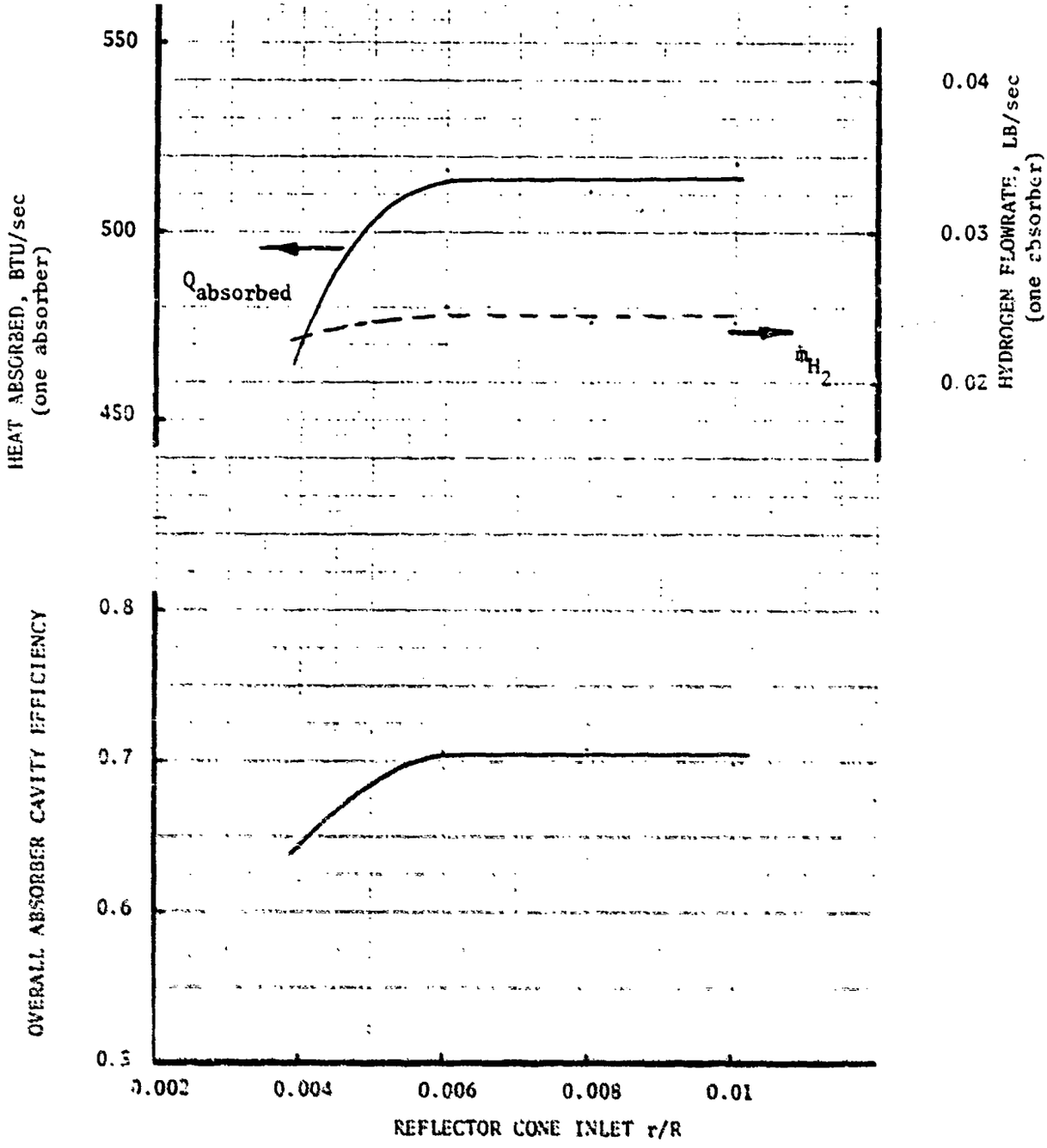

Figure 49. Absorber Cavity Efficiency, Heat Absorberd, and Propellant Flowrate Variation With Reflect Cone Inlet Location (Heat Exchanger Absorber With Hydrogen)

decreased, as shown in Figure 50. As a result to maintain the 5000°R hydrogen outlet temperature, the hydrogen flowrate decreased. The propellant temperature of 5000 °R was selected as a maximum for this absorber/thruster concept using tungsten and tungsten alloy materials.

The results of the heat exchanger cavity absorber analysis are presented in Figures 51 and 52 for ammonia and hydrogen, respectively. As shown in these figures, the absorber efficiency and the heat absorbed decreased with increase in propellant absorber outlet temperature. Efficiencies varied from 70-to 85 percent over the 3000 to 5000 °R propellant temperature range. The heat absorbed and efficiencies were similar for both ammonia and hydrogen; however, the hydrogen flowrate was approximately 1/4 that of the ammonia flowrate as a result of hydrogen's higher heat capacity.

Particulate Absorber

The basic concept of the particulate absorber/thruster involves the direct solar radiation absorption by the propellant as well as a heat exchanger. As shown in Figure 53, the solar radiation enters an enclosed absorber through a high transmittance solid window. The incoming solar radiation is absorbed by the particulates mixed with the primary propellant. Through conduction, convection and radiation the heat absorbed by the particulates is transferred to the primary propellant which is then exhausted through a conventional nozzle.

A number of particulate absorber/thruster configurations were qualitatively evaluated (Figure 54). With the incoming solar radiation oriented 90-degrees to the line of thrust, a one absorber/thruster system could absorb the radiation from both collectors (Concept A) or two absorber/thruster systems could be used (Concept C and D). Concepts C and D could provide a spacecraft roll control feature with two gimbaled thrusters. Concept D attempts to minimize reradiation losses to the absorber walls but most likely the reradiation losses through the absorber window will increase. The fourth concept has the incoming radiation and the thrust direction in-line and represents a more conventional thruster configuration. However, for the particulate absorber/thruster concept this approach could present a solar

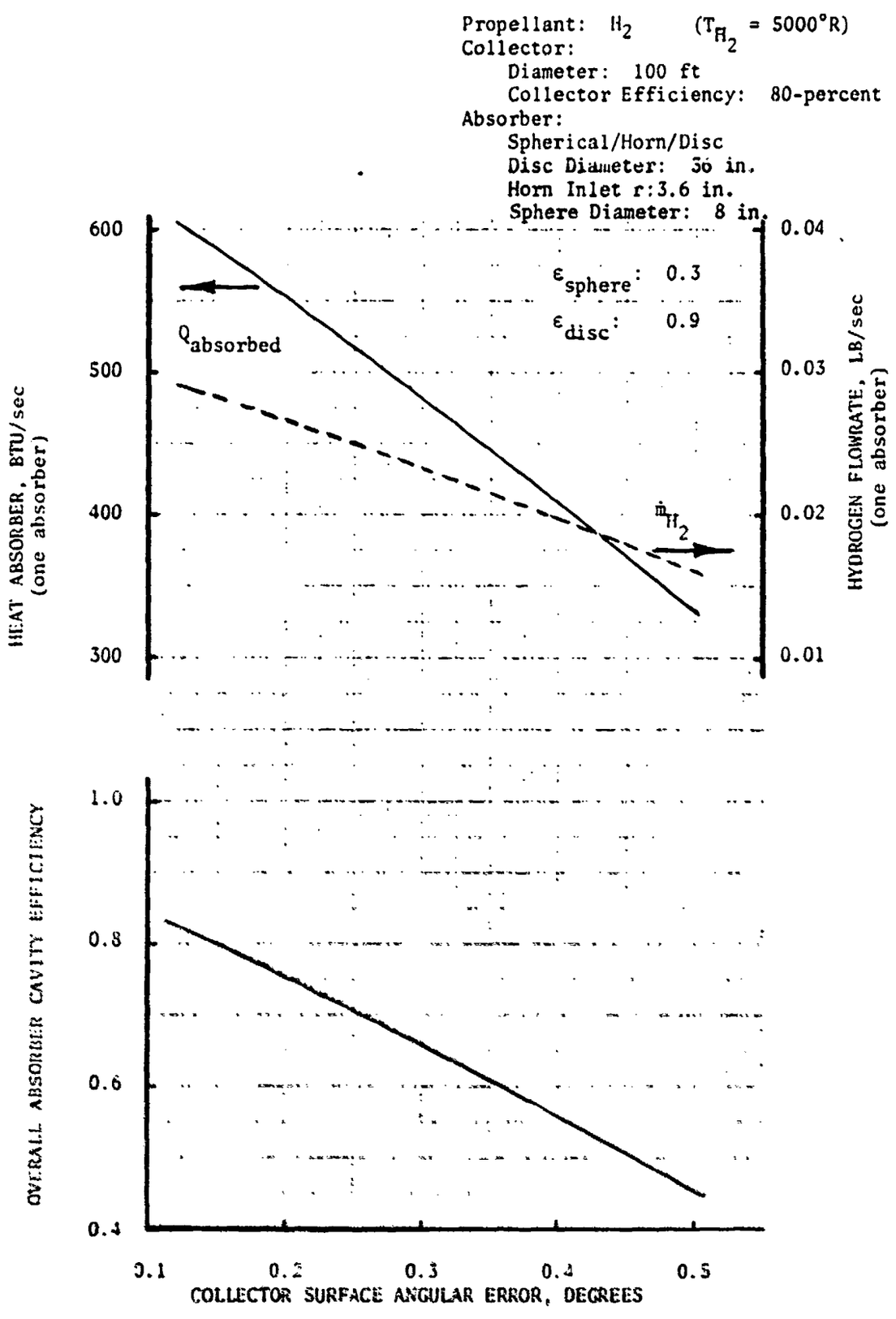

Figure 50. Absorber Cavity Efficiency, Heat Absorbed, and Propellant Flowrate Variation with Collector Surface Angular Error (Heat Exchanger Absorber With Hydrogen)

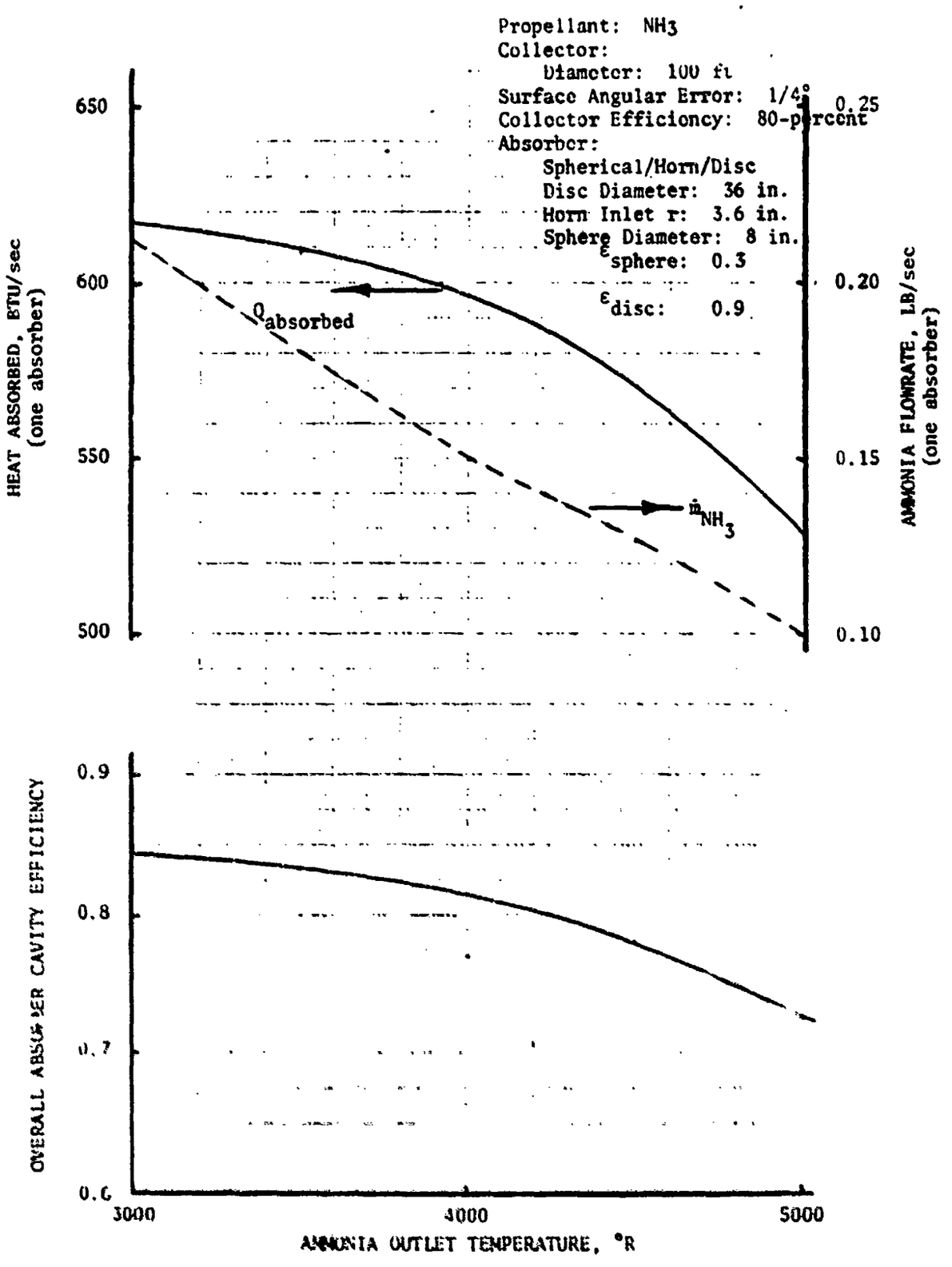

Figure 51. Absorber Cavity Efficiency, Heat Absorbed, and Propellant Flowrate Variation With Propellant Outlet Temperature (Heat Exchanger Absorber With Ammonia)

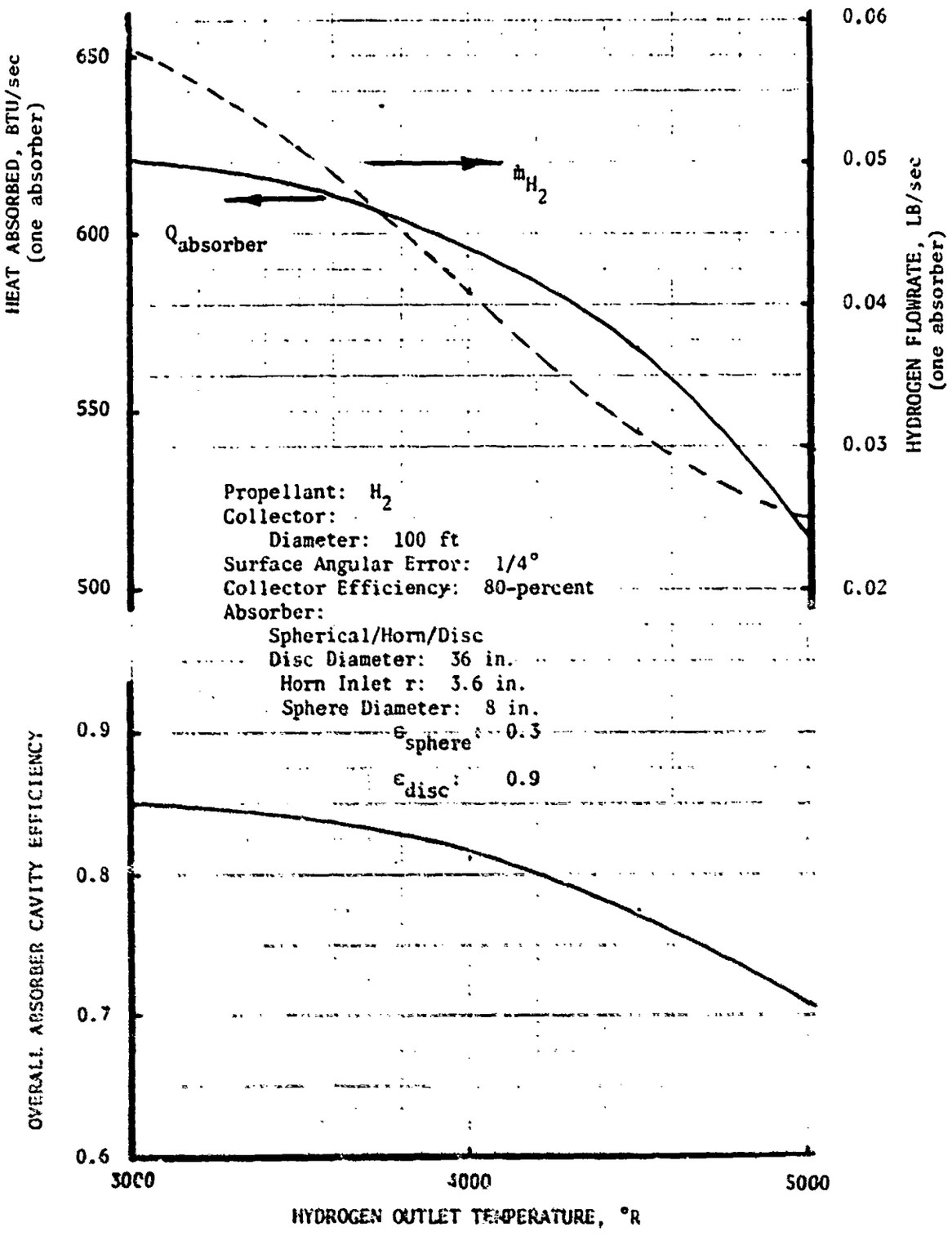

Figure 52. Absorber Cavity Efficiency, Heat Absorber, and Propellant Outlet Temperature (Heat Exchanger Absorber With Hydrogen)

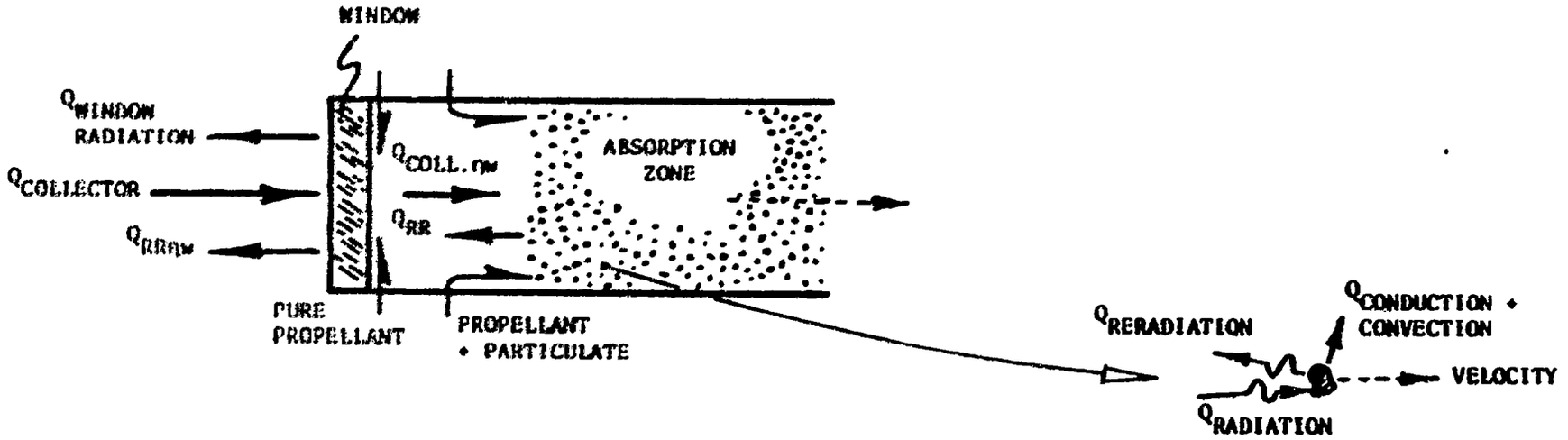

Figure 53. Particulate Absorber

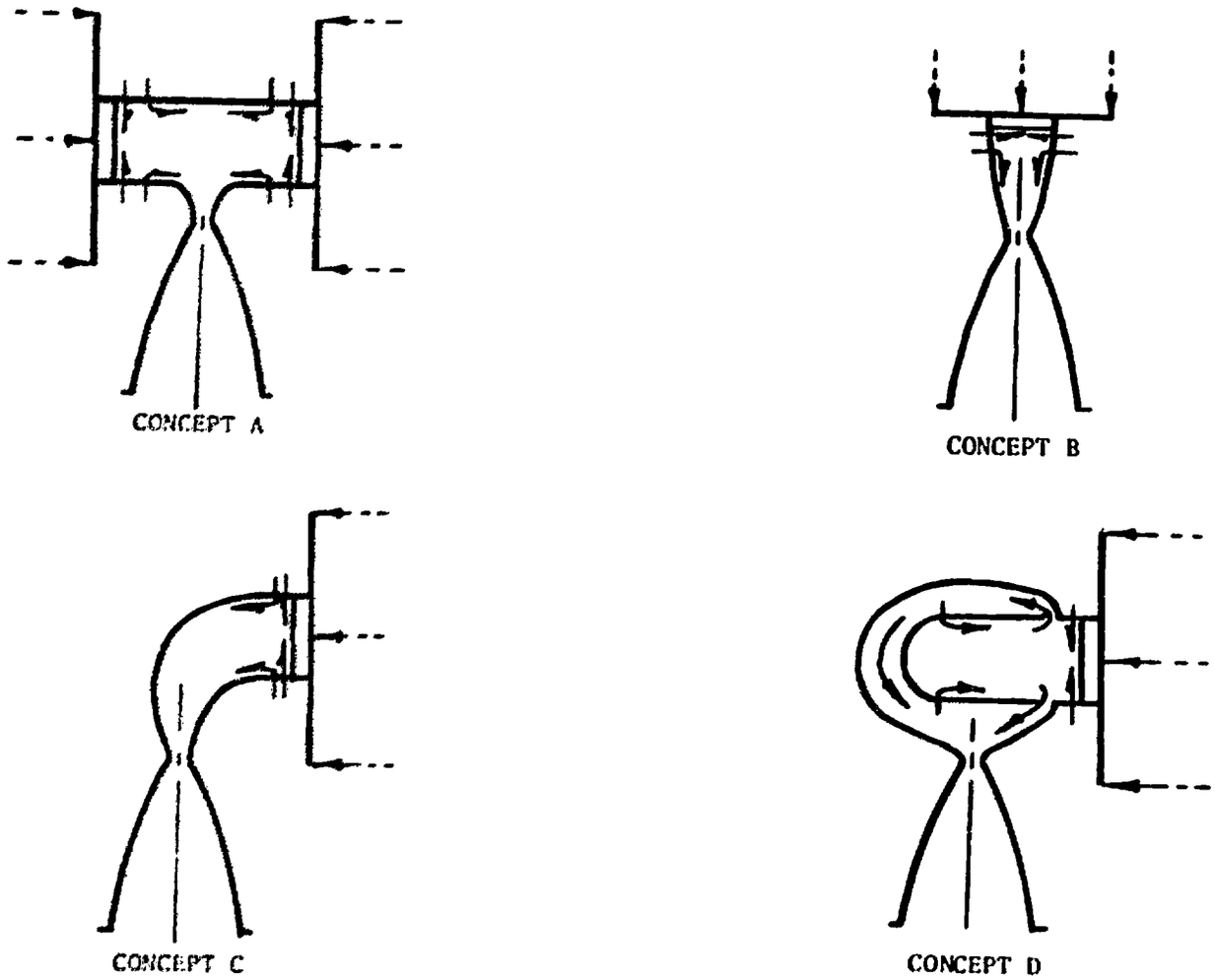

Figure 54. Particulate Absorber/Thruster Concept

radiation alignment problem during gimbaling as well as additional collector losses. Due to the disadvantages discussed and to provide a comparison of the two absorber/thruster concepts, Concept A and C were selected.

A survey of solar radiation absorbing media was conducted as shown in Table 7. The imaginary component of the material index of refraction provides an indication of the solar absorption efficiency of a particulate material. A value of approximately 0.50 is ideal. Silicon, selenium, and carbon have values close to this and therefore were the prime absorbing media candidates. Another important consideration in the selection of the absorbing media is the molecular weight of the material. A low molecular weight absorbing media is desired to result in a minimum degradation of the thruster specific impulse. Of the three prime material candidates, the carbon had the lowest molecular weight and therefore was selected. As shown in Figure 55, 80-percent of the solar radiation could be absorbed with a 5-cm absorption length and 0.5 micron carbon particles using only a 10-percent carbon mass fraction. In fact with a 10-cm absorption length, the incoming solar radiation is essentially 100-percent absorbed.

As shown in Figure 53, the actual mechanisms involved in the particulate absorber/thruster are extremely complex. A mixture of gas and solid particles is simultaneously flowing, absorbing solar radiation of varying intensity, and reradiating energy. The solar radiation absorbed by the solid particles is transferred to the gas through heat conduction and convection as the mixture flows toward the chamber throat. The process is further complicated by the solid/gas mixture initially experiencing the total incoming solar radiation heat flux but then as the flow moves away from the receiving window (parallel flow absorber configuration) the radiant heat flux would decrease due to a radiation flow blocking effect.

Table 7. Material Index of Refraction

$(n = n_1 - in_2)$

Material	Molecular Weight	Wavelength (μm)	n_1	n_2
Aluminum	27	0.24	0.16	2.53
		0.40	0.40	4.45
		0.8	1.99	7.05
		2.0	2.30	16.50
Cesium	133	0.436	0.425	0.438
		0.546	0.278	0.95
		0.578	0.264	1.123
Nickel	59	0.50	1.828	3.389
		0.54	1.925	3.627
		0.60	2.066	3.995
Potassium	39	0.546	0.091	1.42
		0.578	0.094	1.57
Silicon	28	0.50	4.3	0.74
		0.55	4.4	0.63
		0.60	4.35	0.59
Selenium	79	0.50	3.003	0.515
		0.55	3.051	0.282
		0.60	2.922	0.061
Soot	12	0.43	1.56	0.46
(H/C = 1/14, 7)		0.55	1.57	0.48
		0.80	1.57	0.46
(H/C = 1/4, 6)		0.43	1.57	0.46
		0.55	1.57	0.53
		0.80	1.57	0.49
Tungsten	184	0.472	2.99	2.26
		0.501	3.04	2.34
		0.561	3.28	2.52

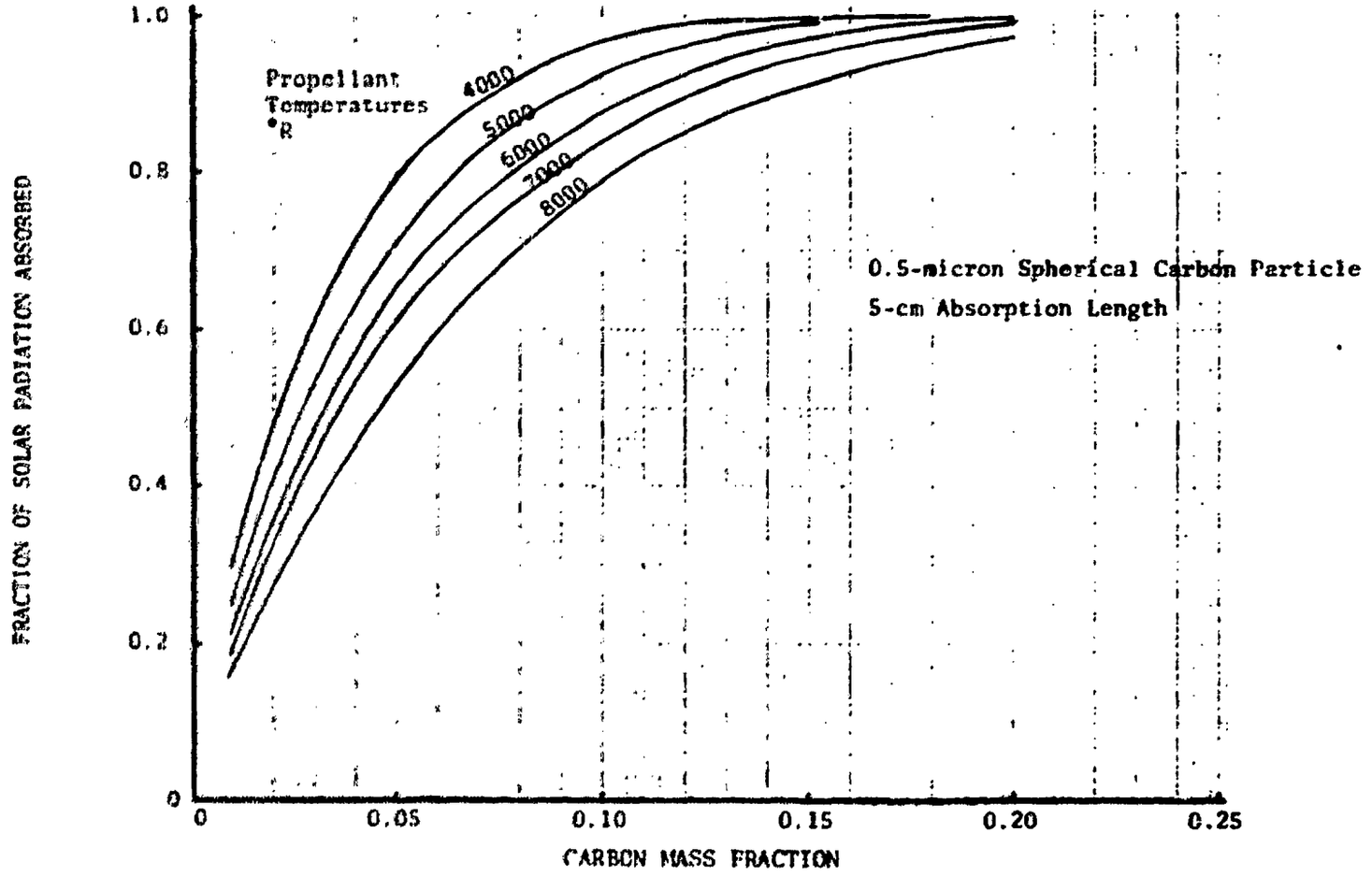

Figure 55. Carbon Particle Absorption

Simplified analyses of the particulate absorber resulted in an optimistic and conservative absorber performance evaluation approach. The equations regarding the major heat losses and the heat absorbed are:

$$Q_{reradiation} = e_{gas}\ \sigma\ AT_{gas}^{4}$$

$$Q_{\substack{window \\ radiation}} = e_{w}\ \sigma\ AT_{w}^{4}$$

$$Q_{\substack{particulate \\ absorption}} = Q_{collector}\ \eta_{w} - Q_{RR}\ \eta_{w} - Q_{\substack{window \\ radiation}}$$

As shown in Table 8, the analysis approaches differ in the temperature used for the reradiation heat loss. Since the radiant heating of the flowing particulate/propellant mixture will require a finite time increment, the gas reradiation was based on the absorber inlet propellant temperature for the optimistic approach. The conservative approach assumed a stationary column of particulate/propellant mixture with a reradiation temperature of approximately 90-percent of the final gas temperature. This latter approach would provide a minimum absorber efficiency value.

Using a 10-percent carbon mass fraction and a 7000 °R final gas temperature, the efficiency of the particulate absorber was determined for hydrogen/carbon using both analytical approaches. For the two thruster - two absorber configuration, absorber efficiencies of 37-percent and 15-percent resulted for the optimistic and conservative approaches, respectively. The difference in these results further indicated the need for a detailed analysis method for the particulate absorber.

Table 8. Particulate Absorber Efficiency

Optimistic Approach	Conservative Approach
Reradiation based on Inlet Temperature of Gas/Solid Mixture Two Collectors-one Absorber/Thrust	Effective Reradiation Temperature based on a Stationary Column of Gas/Solid Mixture
T_{gas}=7000°R $\eta_{absorber}$=0.51	
Two Collectors-two absorber/thrusters	Two Collectors-two absorber/thrusters
T_{gas}=7000°R $\eta_{absorber}$=0.37	T_{gas}=7000°R $\eta_{absorber}$=0.15

THRUSTER PERFORMANCE

Heat Exchanger Cavity Absorber/Thruster

For the solar rocket thruster, three thruster performance losses are encountered. These losses include the two-dimensional flow or divergence loss, the boundary layer loss and the chemical reaction kinetic loss.

The two-dimensional loss accounts for the nonaxial flow variations as well as the nonuniform nozzle flowfield. This loss was computed using the Rocketdyne computer program for analyzing bell nozzle flowfields which utilizes the method of characteristics for axisymmetric flow.

The boundary layer loss is the result of nozzle flow momentum deficit created by viscous drag and wall cooling. The Rocketdyne boundary layer computer program was used to calculate this loss. This computer program employs an integral solution to the momentum and energy equation.

The reaction kinetic loss is the result of the nozzle flow not being able to maintain chemical equilibrium due to the rapid flow expansion process occurring in the nozzle. This loss was computed using the JANNAF one dimensional kinetic (ODK) computer program.

All three of these analysis methods have and are being employed in determining the performance of existing chemical rocket thrust chambers.

The cycle life capability of the absorber/thruster was not evaluated in this study.

Heat Exchanger Cavity Absorber/Thruster

The results of the heat exchanger cavity absorber/thruster performance analysis are presented in Figure 56 and Figure 57 for a 100-to-1 area ratio, 90-percent length bell nozzle with two 100-ft diameter collectors having a 1/4-degree surface angular error. For the 3000 °R to 5000 °R propellant temperature range evaluated (fixed heat input) for the heat exchanger cavity absorber/thruster, the influence of delivered specific impulse and

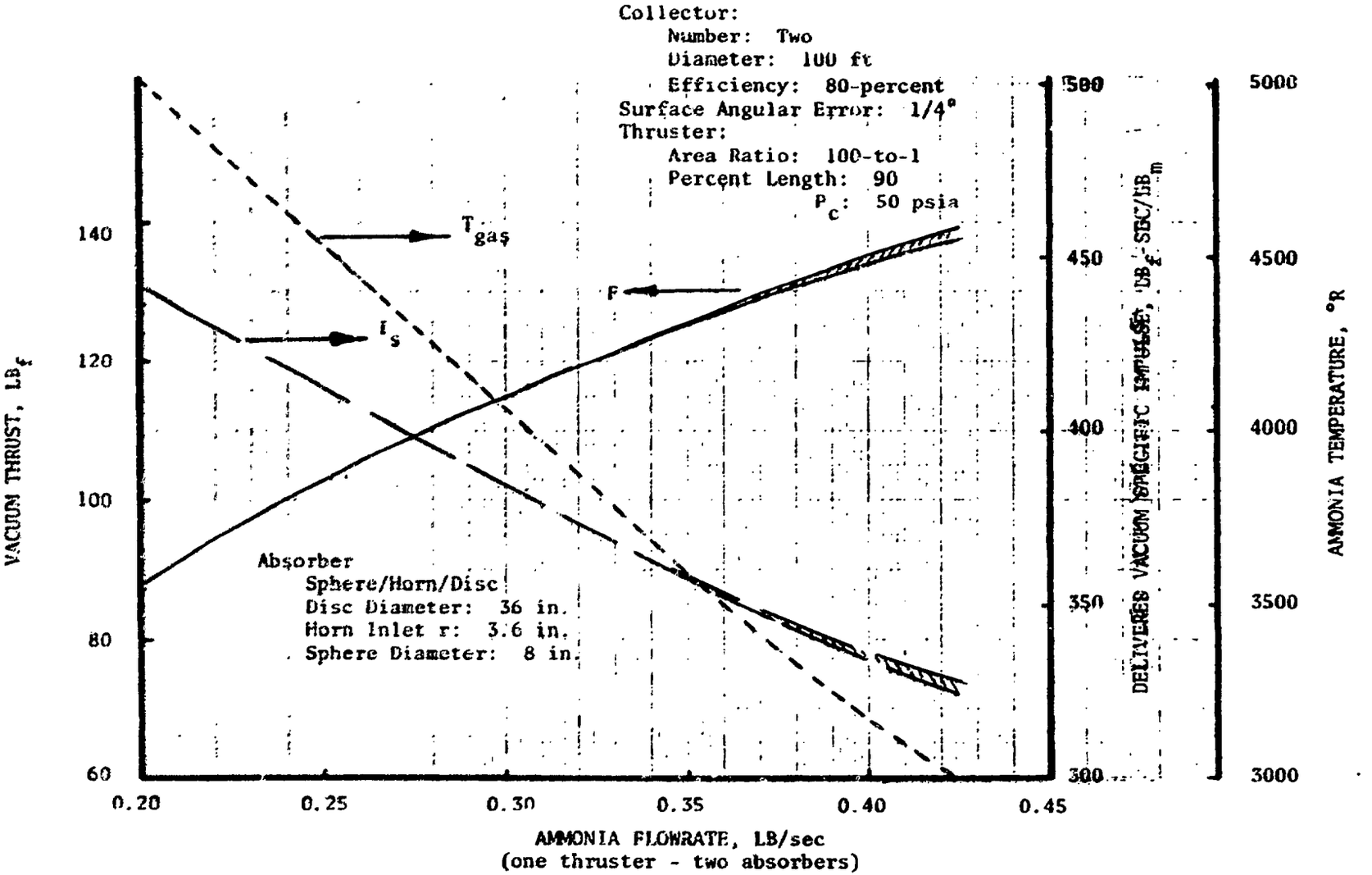

Figure 56. Ammonia Heat Exchanger Absorber/Thruster Performance

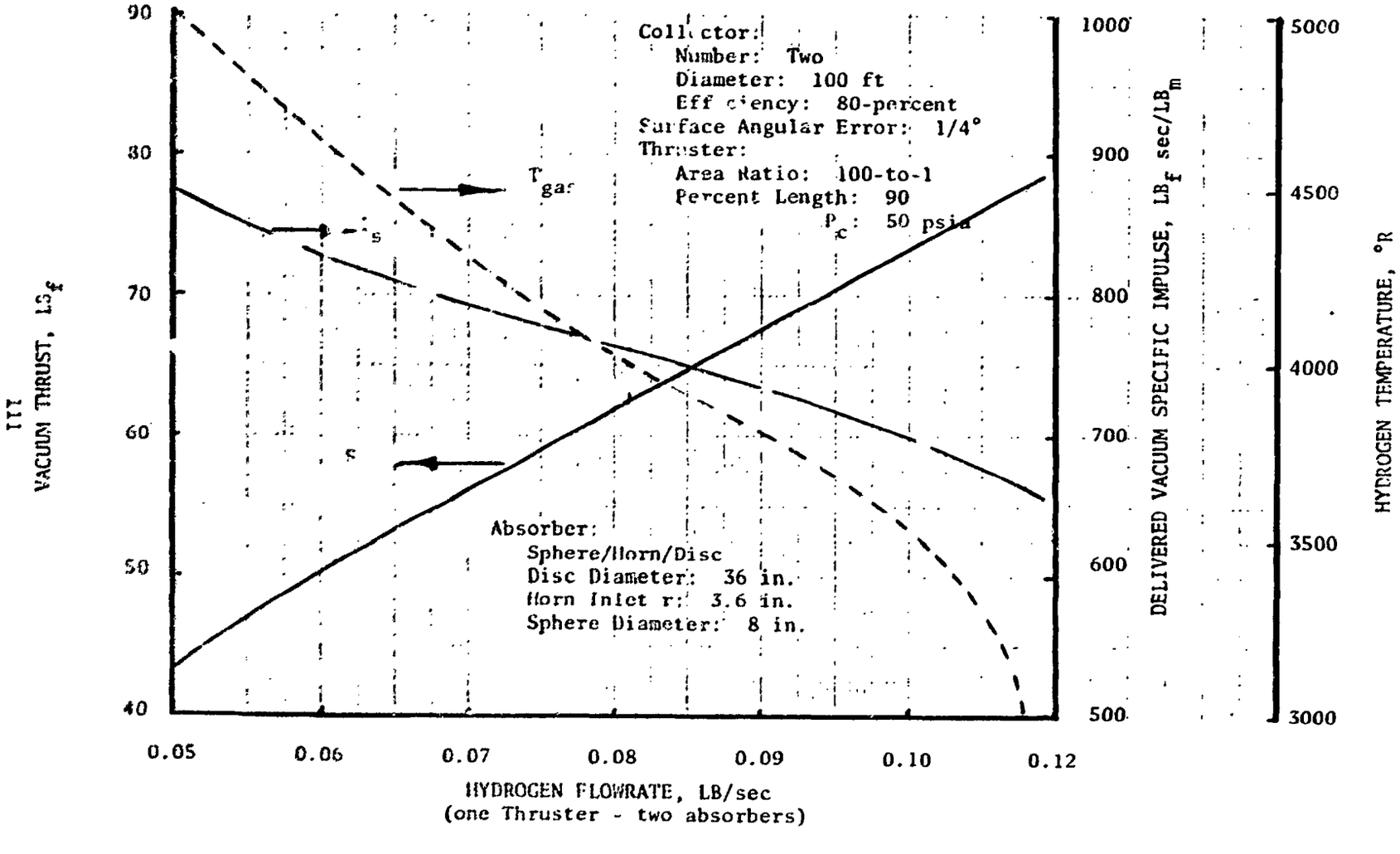

Figure 57. Hydrogen Heat Exchanger Absorber/Thruster Performance

thrust were determined. For ammonia as a propellant the delivered specific impulse varied from 330 to 440 lb_f sec/lb_m with thrust levels of 90 to 140 lb_f. As expected, hydrogen achieved significantly higher delivered specific impulses (650 to 880 lb_f sec/lb_m) and lower thrust levels (40 to 80 lb_f) as compared to ammonia.

A heat exchanger cavity absorber/thruster configuration with hydrogen at 5000°R (highest performance) is shown in Figure 58. Each absorber consists of a reflector cone (Winston Horn) with a 7.2-inch diameter inlet, an 8-inch diameter sphere to dissipate the reflector cone magnified heat flux, and a 36-inch diameter annular disc absorber. This sphere/horn/disc absorber configuration achieved a 71-percent overall efficiency. The single thruster at a chamber pressure of 50 psia delivered a specific impulse of 872 lb_f sec/lb_m and 44 lb_f thrust. As shown in Figure 28 the thruster has an 0.826-inch throat diameter, a 12.58-inch nozzle length and 8.26-inch exit diameter. The nozzle exit was placed at the same plane as the edge of the flat disc to prevent plume impingement on the disc absorber.

The two thruster-two absorber confguration (Figure 59) at the same conditions achieved a delivered specific impulse of 861 lb_f sec/lb and a thrust of 43 lb_f. The 1.3-percent lower specific impulse was primarily the result of an increased boundary layer loss due to the smaller chamber size. Using these results, the two thruster concept performance could be scaled from that of the one thruster concept by:

$$I_{s_{2\text{-thruster}}} = 0.987\ I_{s_{1\text{-thruster}}}$$

$$F_{2\text{-thruster}} = 0.977\ F_{1\text{-thruster}}$$

The influence of the collector surface angular error on delivered specific impulse is shown in Figure 60 for a one thruster-two absorber configuration using hydrogen at 5000 °R. The decrease in chamber size caused by a decrease in propellant flow with increase in angular error resulted in a 1-percent decrease in delivered specific impulse from 1/8 degree to 1/2 degree error. The thrust decreased with an increase in the angular error due to the decrease in heat absorbed.

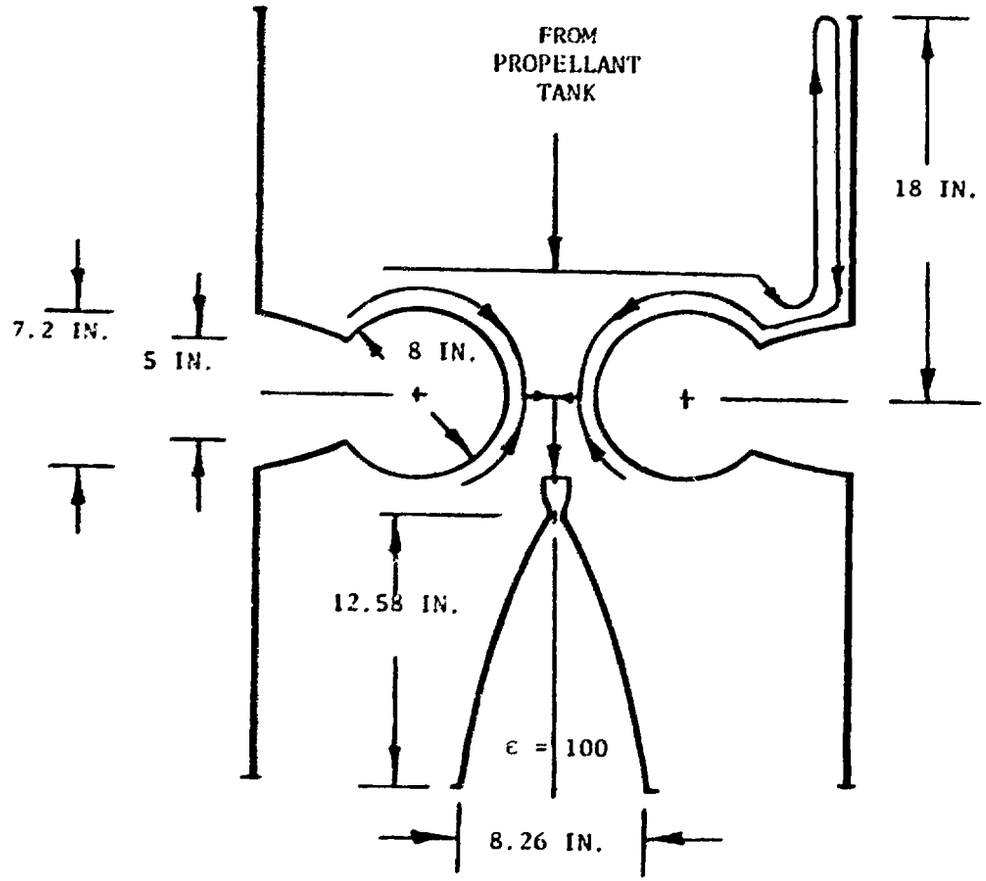

Collector:
- Number: Two
- Diameter: 100 ft
- Efficiency: 80-percent

Surface Angular Error: 1/4-degree

Absorber
- Spherical/Horn/Disc
- Disc Diameter: 36 in.
- Horn Inlet r: 3.6 in.
- Sphere Diameter: 8 in.

ϵ_{sphere}: 0.3

ϵ_{disc}: 0.9

- Efficiency: 71-percent

Thruster:
- Throat Diameter: 0.826 in.
- Area Ratio: 100-to-1
- Chamber Pressure: 50 psia
- Flowrate: 0.05 lb/sec
- Thrust: 44 lb_f
- Specific Impulse: 872 lb_f sec/lb_m

Figure 58. Heat Exchanger Absorber/Thruster (Hydrogen at 5000°R)

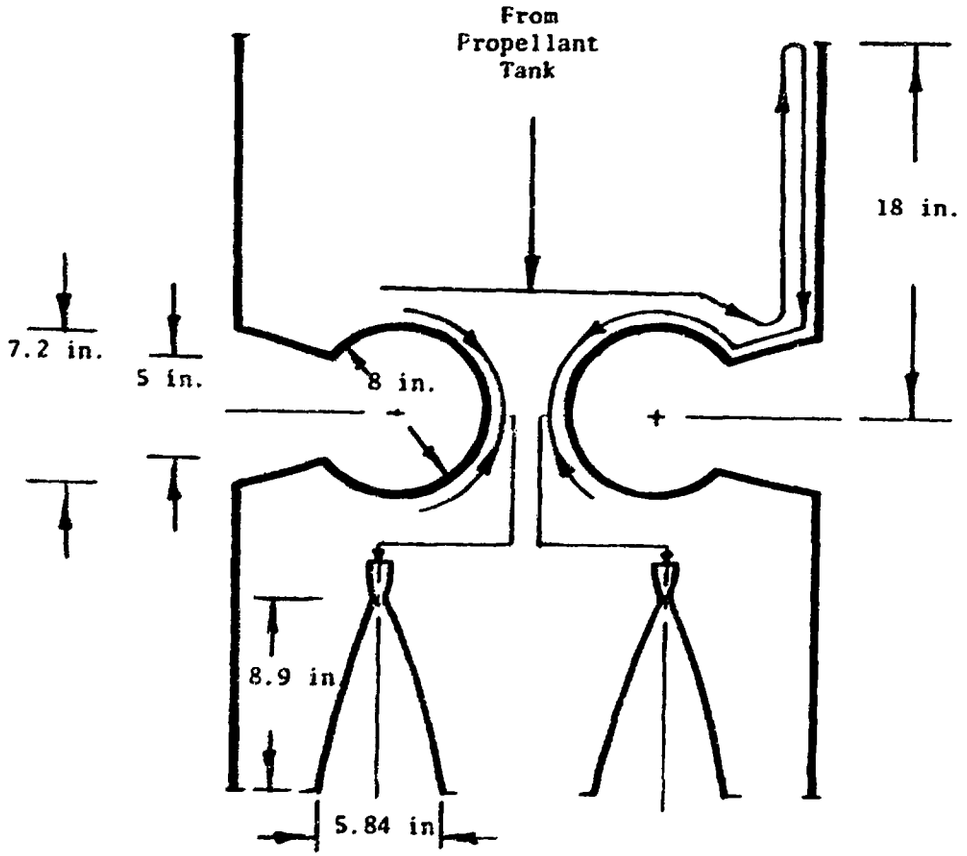

Collector:
- Number: Two
- Diameter: 100 ft
- Efficiency: 80-percent
- Surface Angular Error: 1/4-degree

Absorber:
- Spherical/ Horn/Disc
- Disc Diameter: 36-in.
- Horn Inlet r: 3.6-in.
- Sphere Diameter: 8-in.
- ϵ_{sphere}: 0.3
- ϵ_{disc}: 0.9
- Efficiency: 71-percent

Thruster:
- Throat Diameter: 0.584-in.
- Area Ratio: 100-to-1
- Chamber Pressure: 50 psia
- Flowrate: 0.025 lb/sec each
- Thrust: 21.5 lb_f each
- Special Impulse: 861 lb_f sec/lb_m

Figure 59. Heat Exchanger Cavity Absorber/Thruster (Two Thrusters)(Hydrogen at 5000°R)

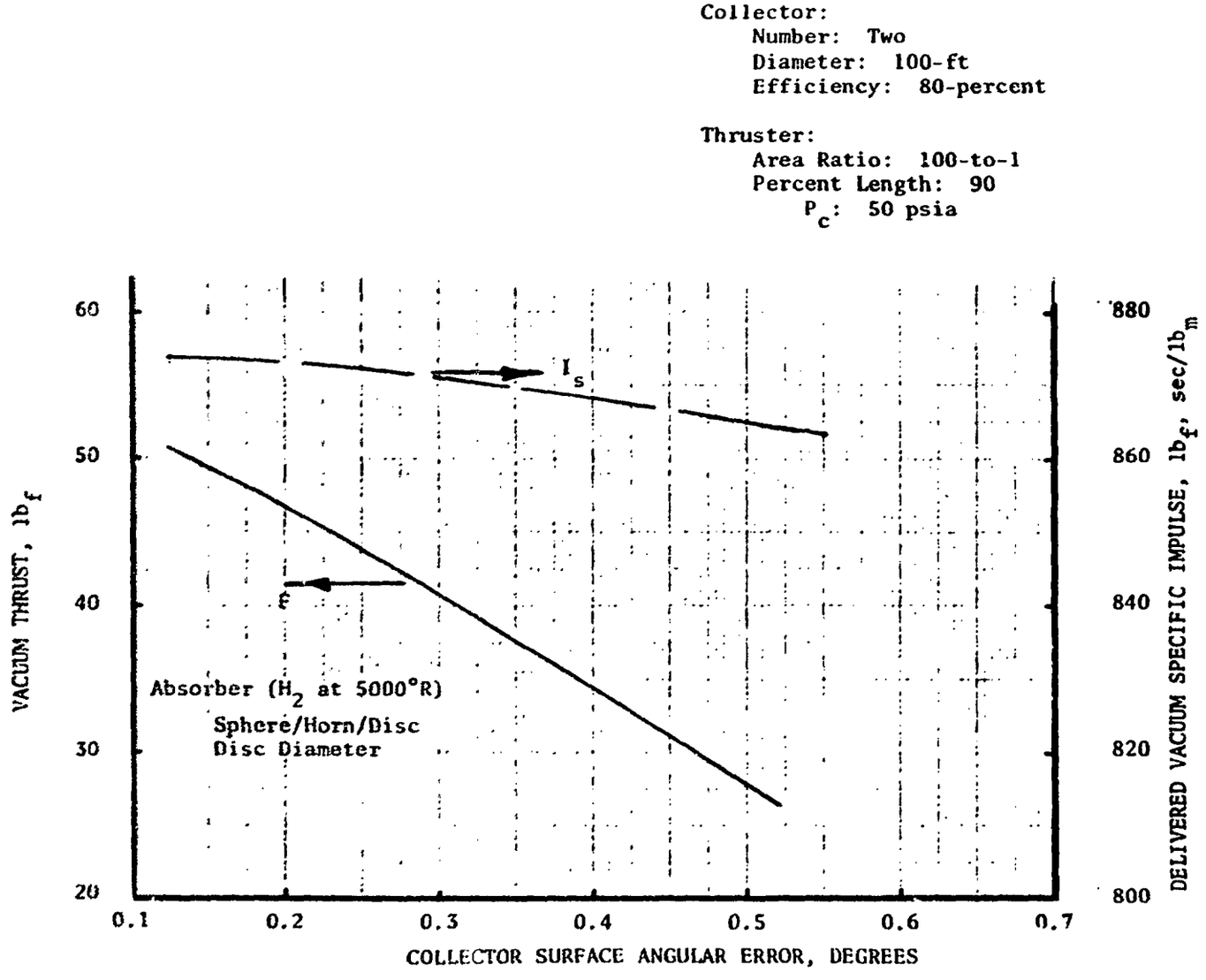

Figure 60. Influence of Collector Surface Angular Error for Heat Exchanger Cavity Absorber/Thruster (Hydrogen at 5000°R)

Estimates of the propellant pressure drop required to cool the heat exchanger cavity absorber using hydrogen and ammonia is presented in Figure 61. The ammonia pressure drop is higher than the hydrogen pressure drop since ammonia is a poorer coolant and therefore requires a higher coolant mass velocity to attain comparable wall temperatures.

The estimated heat exchanger cavity absorber/thruster weight using the two 100-ft diameter collectors varied from 63 lb at 5000 °R propellant temperature to 67 lb at 3000 °R. The increased weight at the low propellant temperature is due to the increase in thrust chamber size.

For the two thruster-two absorber configuration, a performance analysis was performed for a thrust chamber at a chamber pressure of 20 psia for hydrogen to determine the influence of chamber pressure. A comparison of the performance analysis results for 20 psia and 50 psia chamber pressures is shown in Table 9. The lower chamber pressure resulted in a thrust chamber approximately 1.5 times larger. For the same gas temperature (5000R) and nozzle area ratio (100-to-1), the lower chamber pressure has a 2.6 percent higher theoretical vacuum specific impulse. This is due to the increase in the amount of dissociated hydrogen at the lower chamber pressure.

The two-dimensional (geometric) nozzle efficiencies shown in Table 9 for the two chamber pressures are slightly different as a result of gas property variations. Typically, the reaction kinetic efficiency will decrease with decrease in chamber pressure due to the increase in dissociated species and increase with increase in chamber size. In this case (Table 9), the chamber pressure effect dominated and the reaction kinetic efficiency decreased for lower chamber pressure. The boundary layer loss increases with decrease in chamber pressure for a fixed chamber size. At a fixed chamber pressure, the boundary layer will slightly increase with decrease in chamber size. For the cases evaluated the chamber pressure was decreased and the chamber size increased. The result was an increase in boundary layer loss.

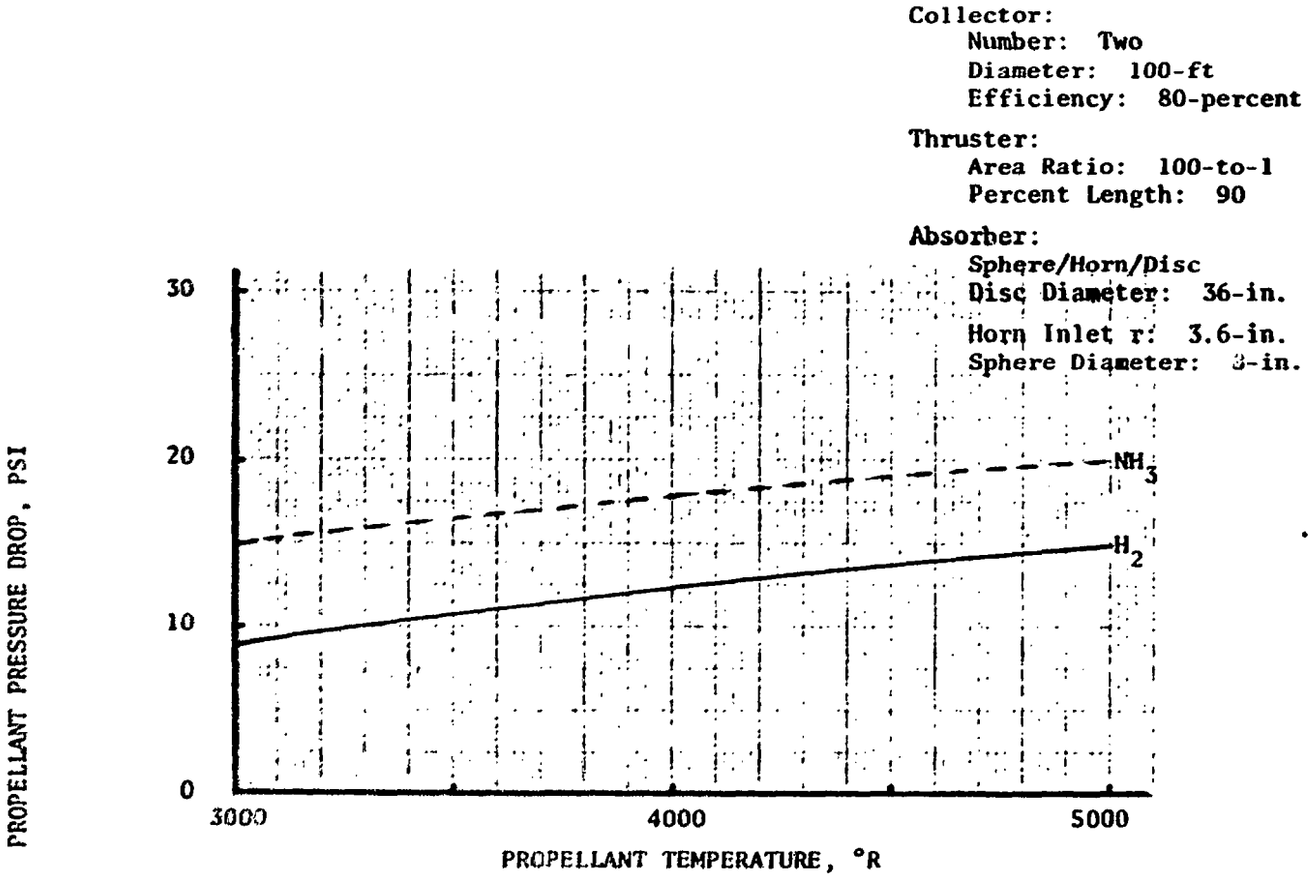

Figure 61. Estimated Coolant (Propellant) Pressure Drop - Heat Exchanger Cavity Absorber/Thruster

Table 9. Influence of Chamber Pressure on Heat Exchanger Cavity Absorber/Thruster (Two Absorbers - Two Thrusters)

Propellant: Hydrogen

Chamber Gas Temperature: 5000R

Nozzle Area Ratio: 100-to-1

Absorber/Thruster: Heat Exchanger Cavity Configuration (Two Absorber - Two Thrusters)

	P_c = 50 psia	P_c = 20 psia
Theoretical Vacuum Specific Impulse, lb_f sec/lbm	969.04	993.92
Throat Diameter, Inch	0.584	0.892
Nozzle Length, Inch	8.90	13.6
Two-dimensional (Geometric) Efficiency	0.9945	0.9962
Reaction Kinetic Efficiency	0.9613	0.9395
Boundary Layer Loss	0.0676	0.08134
Delivered Vacuum Specific Impulse, lb_f sec/lbm	860.9	849.4
Delivered Thrust, lb_f	21.5	19.5

The combined result as shown in Table 9 is a 1.3 precent lower delivered vacuum specific impulse for the 20 psia chamber pressure. The gain in the theoretical specific impulse for the lower chamber pressure became a deficit due to an increase in the reaction kinetic and boundary layer losses.

Particulate Absorber/Thruster

Using the optimistic absorber analysis result for a one thruster-two absorber configuration, the performance analysis for a 100-to-1 area ratio, 90-percent length bell nozzles with two 100 ft diameter collectors was performed. Hydrogen/carbon (10-percent) was used as the propellant. For the 6000 °R to 8000 °R propellant temperature range evaluated, the variation of delivered specific impulse and thrust were determined. As shown in Figure 62, the delivered specific impulse varied from 940 lb_f sec/lb_m to 1100 lb_f sec/lb_m for the hydrogen/carbon propellant with a carbon mass fraction of 0.1. The thrust decreased from 23.5 lb_f to 9 lb_f as the propellant temperature was increased from 6000 to 8000 °R.

A particulate absorber/thruster configuration with hydrogen/carbon at 7000°R is presented in Figure 63. The absorber consists of a 6-inch radius cylinder plus an annular disc. Hydrogen first cools the annular disc absorber then splits to: (1) cool the solid window and (2) cool the thruster and absorber body. Once the absorber body is cooled, the hydrogen enters a solid particle gas mixer and the hydrogen/carbon mixture is injected downstream of the window. The cylindrical particulate absorber/disc configuration achieved a 51-percent overall efficiency using the optimistic absorber analysis approach. The single thruster at a chamber pressure of 50 psia resulted in a delivered specific impulse of 1041 lb_f sec/lb_m and thrust of 14 lb_f. The conservative absorber analysis approach would result in the same thruster performance but would require a larger collector surface area to achieve the same heat input absorbed by the absorber/thruster.

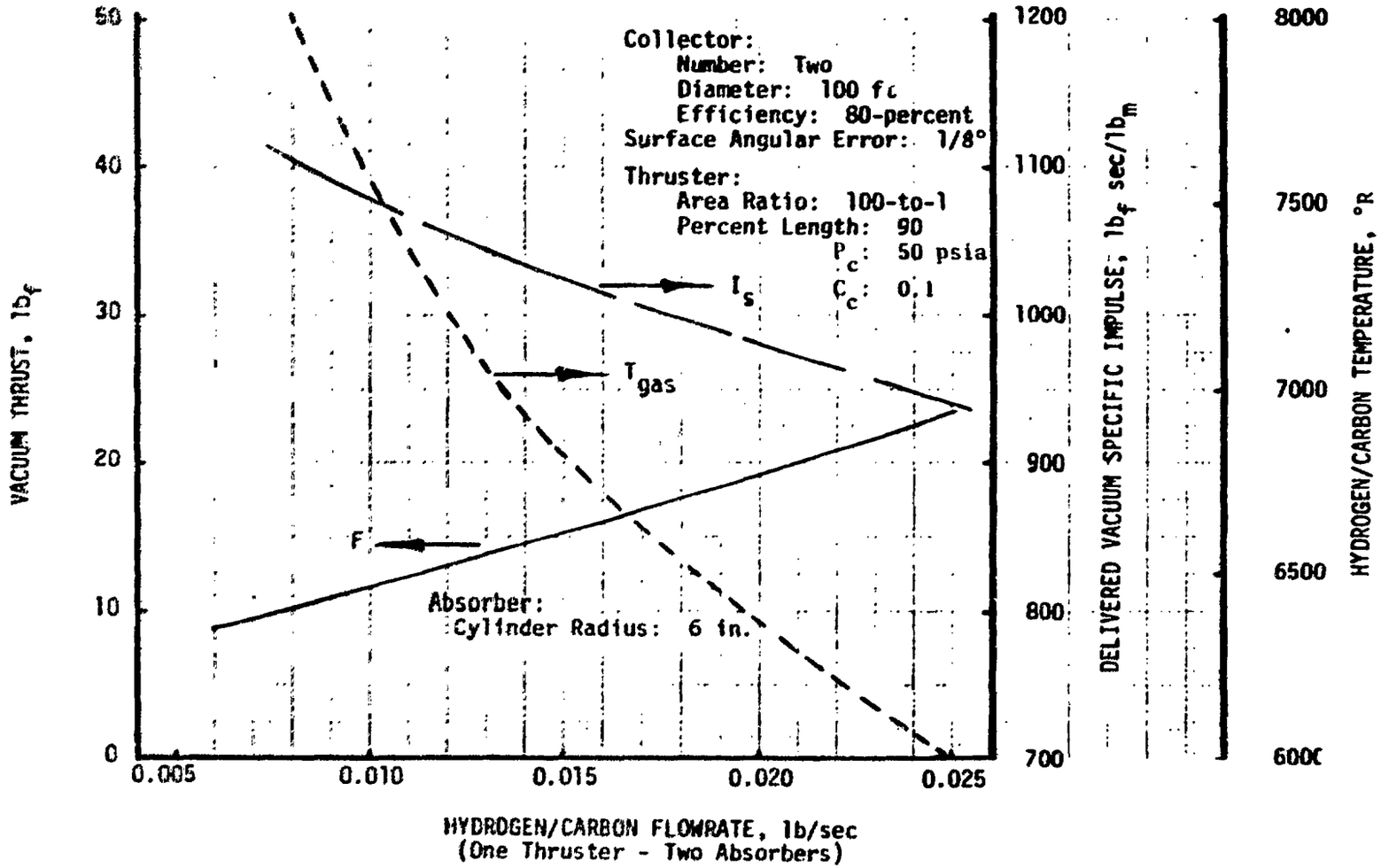

Figure 62. Hydrogen/Carbon Particulate Absorber/Thruster Performance

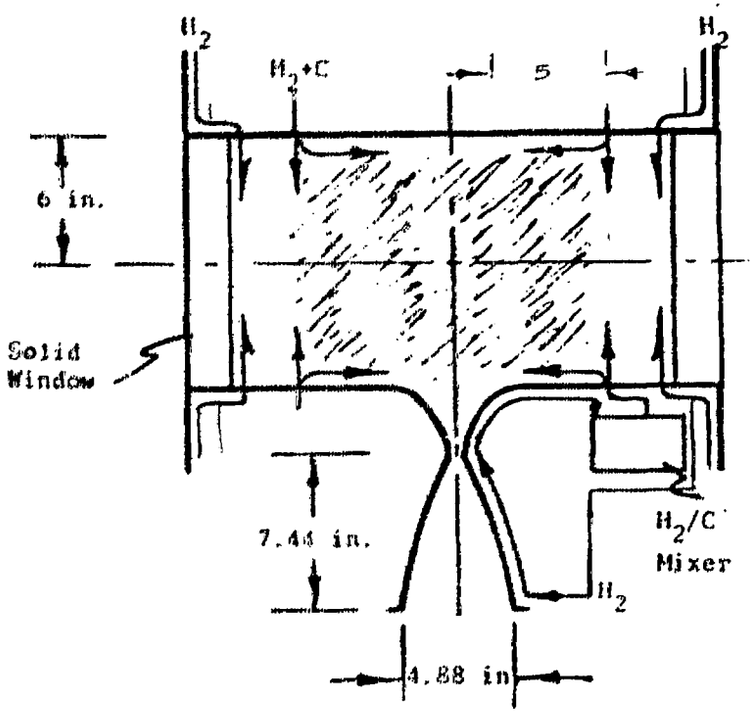

Collector:
- Number: Two
- Diameter: 100 ft
- Efficiency: 80-percent

Surface Angular Error: 1/8-degree

Absorber:
- Cylindrical Particulate/Thruster/Disc
  - ϵ_{gas}: 1.0
  - ϵ_w: 0.1
  - η_w: 0.9
- Efficiency: 51-percent

Thruster:
- Throat Diameter: 0.489 in.
- Area Ratio: 100-to-1
- Chamber Pressure: 50 psia
- C_c: 0.1
- Flowrate: 0.013 lb/sec
- Thrust: 14 lb_f
- Specific Impulse: 1041 lb_f sec/lb_m

Figure 63. Particulate Absorber/Thruster (Hydrogen/Carbon at 7000°R)

CONCLUSIONS AND RECOMMENDATIONS

Based on theoretical chemical equilibrium performance data generated during the program, hydrogen (H_2) provided the maximum vacuum specific impulse potential and hydrazine (N_2H_4) the lowest. For the particulate absorber/thruster, submicron carbon particles provided a highly efficient solar radiation absorption media and a low molecular weight particulate which would minimize the specific impulse degradation of hydrogen.

The heat exchanger cavity absorber/thruster achieved absorber efficiencies of 70 to 80-percent and was determined to be capable of delivering vacuum specific impulses of 650 to 880 lb_f sec/lb_m with hydrogen (H_2) and 330 to 440 lb_f sec/lb_m with ammonia (NH_3) for propellant temperatures of 3000 to 5000 °R. At these high gas temperatures, the concept requires a high temperature refractory metal (tungsten or tungsten alloys) for the absorber and thruster walls. A maximum temperature of 5000 °R was chosen as the wall temperature limit. The particulate absorber/thruster presented a complex analytical flow-heat transfer problem. Simplified analysis approaches resulted in a factor of two variation in absorber efficiency which for a fixed absorber heat input does not alter thruster performance but changes the required collector surface area. The particulate absorber/thruster resulted in delivered vacuum specific impulses of 900 to 1100 lb_f sec/lb_m with hydrogen/carbon at temperatures of 6000 to 8000 °R.

Recommendations for further absorber/thruster work include:

1. Experimental/analytical verification of hydrogen cooling capability at dissociated propellant temperatures.
2. Investigation of applicable fabrication techniques using refractory metals.
3. For the particulate absorber/thruster:
   (a) Detailed evaluation of the absorber analysis method
   (b) Particulate absorber flow pattern evaluation
   (c) Gas/solid particle mixer for space operation

4. Propulsion System

   (a) Pump versus pressure-fed; use of solar driven pumps

   (b) Use of propellant boiloff

   (c) Absorber/thruster mission operation as related to burn and coast periods with collector defocusing.

All these recommendations lead to a demonstrator absorber/thruster program with analysis, design, fabrication, and test to experimentally verify the solar rocket concept.

6.0 ORBIT MECHANICS

Mission velocity requirements as a function of vehicle thrust-to-weight ratio and orbit transfer techniques are analyzed in the section. Stabilization and attitude control requirements that will be imposed on the spacecraft systems for the baseline mission are established.

Alternate missions that would be feasible with the Solar Rocket are identified.

MISSION REQUIREMENTS

The principal characteristic mission requirements of a low thrust-to-weight orbital transfer vehicle are the mission velocity and trip time.

Baseline Mission

Transfer from a low altitude (160 - 220 n.mi) orbit inclined at 28.5 degrees to the equator to a Clarke (geosynchronous equatorial) orbit is the baseline mission to be used for the Solar Rocket performance analysis.

Depending on the thrust-to-weight ratio of the orbit transfer vehicle, the transfer maneuvers can be generally divided into three distinct types. These three types of transfer maneuvers are pictorially illustrated in Figure 64. The mission velocity requirements range from a low of 14,000 fps to a high of 19,200 fps depending on the vehicle thrust-to-weight ratio of the orbit transfer vehicle (Figure 65).

The classical two-impulse transfer, with one impulse at perigee and the second impulse at apogee is commonly associated with transfer vehicles having a thrust-to-weight ratio considerably above 0.1. The mission velocity for such a vehicle corresponds to approximately 14,000 fps and a trip time of 5.27 hours.

Lower thrust-to-weight vehicles may also fall into this two impulse transfer category as long as the corresponding burntime is generally shorter than the transfer time and the transfer trajectory still resembles an ellipse. The corresponding mission velocity would be considerably higher, and the trip time, although also increasing, would still be generally less than a day.

On the other end of the orbital transfer spectrum is the transfer maneuver associated with vehicles having thrust-to-weight ratios below 0.001. These

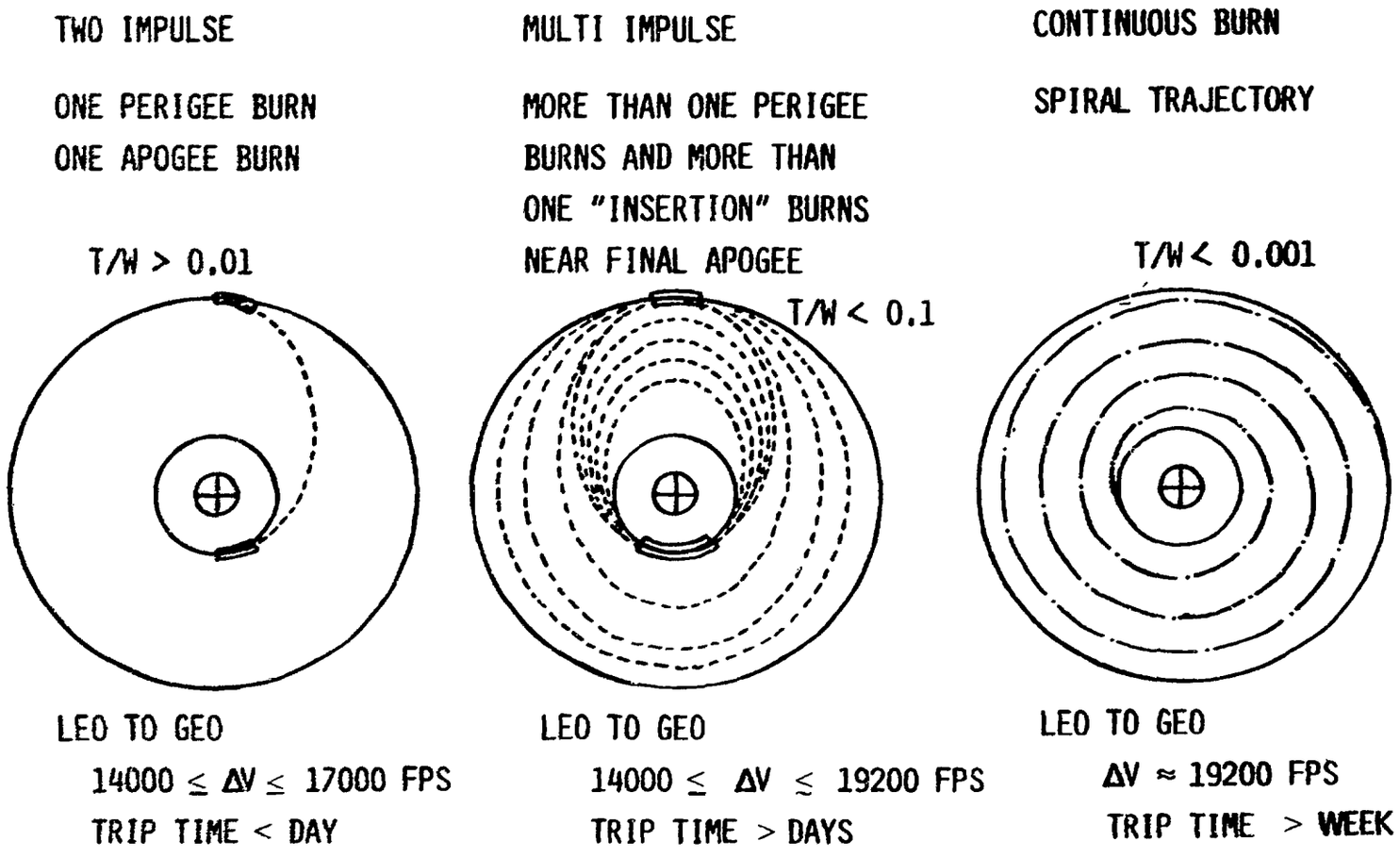

Figure 64. Types of Transfer Maneuvers

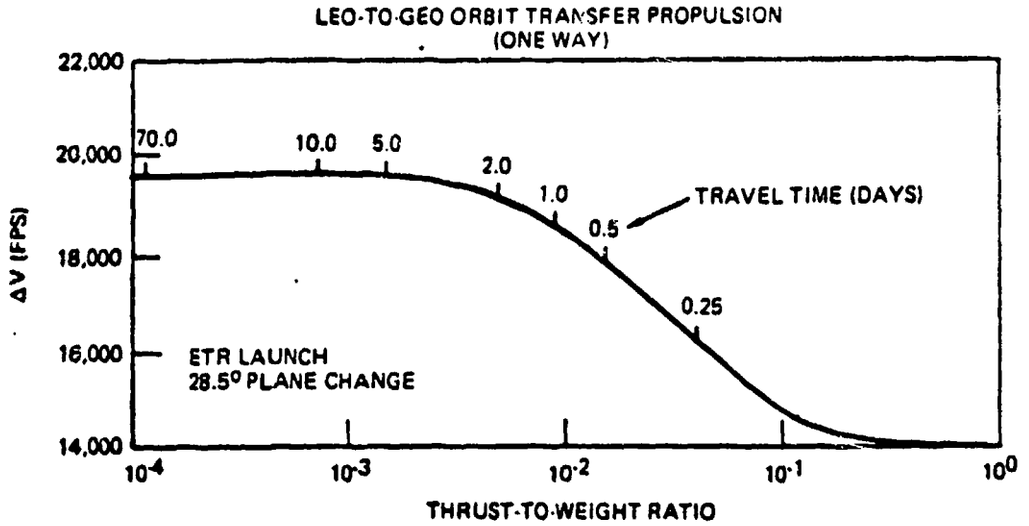

Figure 65. Mission Velocity Requirements - Continuous Burn Spiral

classical, extremely low thrust-to-weight orbit transfers are characterized by a continuous burn spiral trajectory. Although this type of trajectory represents the shortest trip time for low thrust-to-weight propulsion systems, it also demands the greatest energy expenditure. The mission velocity in this regime is 19,200 fps and the value remains essentially independent of vehicle thrust-to-weight ratio. The burntime equals the transfer time and as a first approximation it can be obtained by the following relationship

$$t = \frac{\Delta V}{(T/W)_{AV} g} = \frac{596.76}{(T/W)_{AV}} \quad \text{(seconds)}$$

where $(T/W)_{AV}$ is the average thrust-to-weight ratio for the mission. The trip time corresponding to the expected thrust-to-weight regime for the Solar Rocket is shown in Figure 66.

This trip time approximation does not take into account the time spent in Earth shadow with zero thrust. In previous studies (SEPS, etc.), it was found that the inclusion of the time spent traversing the Earth shadow results in a trip-time increase of approximately 10% at no increase in propellant expended.

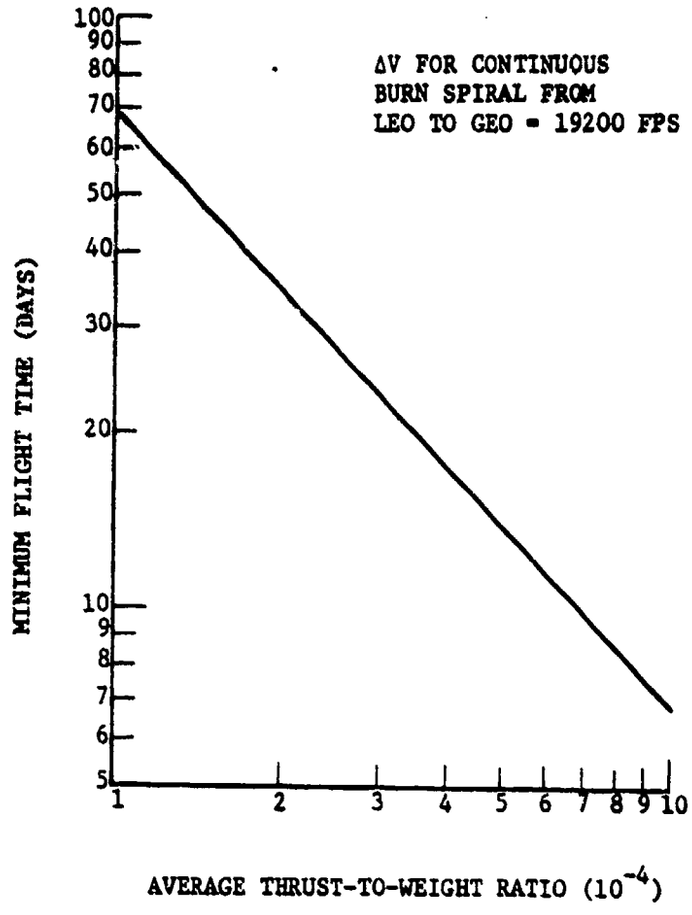

Figure 66. Minimum Flight Time - Continuous Burn Spiral Transfer

Qualitatively the shadowing effect can be illustrated by considering the maximum percentage of one orbital revolution that can be expected to be in Earth shadow (Figure 67) as a function of orbit altitude. In low orbit the percentage can be as high as 43%, while at geosynchronous altitude it is only 5%. With 50% of the spiral transfer being at altitudes greater than 4000 n.mi, it is reasonable to assume that approximately only 10% of the flight will be spent in Earth shadow. This would increase the minimum trip times shown by about 10%.

A viable alternative to the classical continuous burn spiral transfer method is to perform the burns only in the vicinity of perigee and/or apogee.

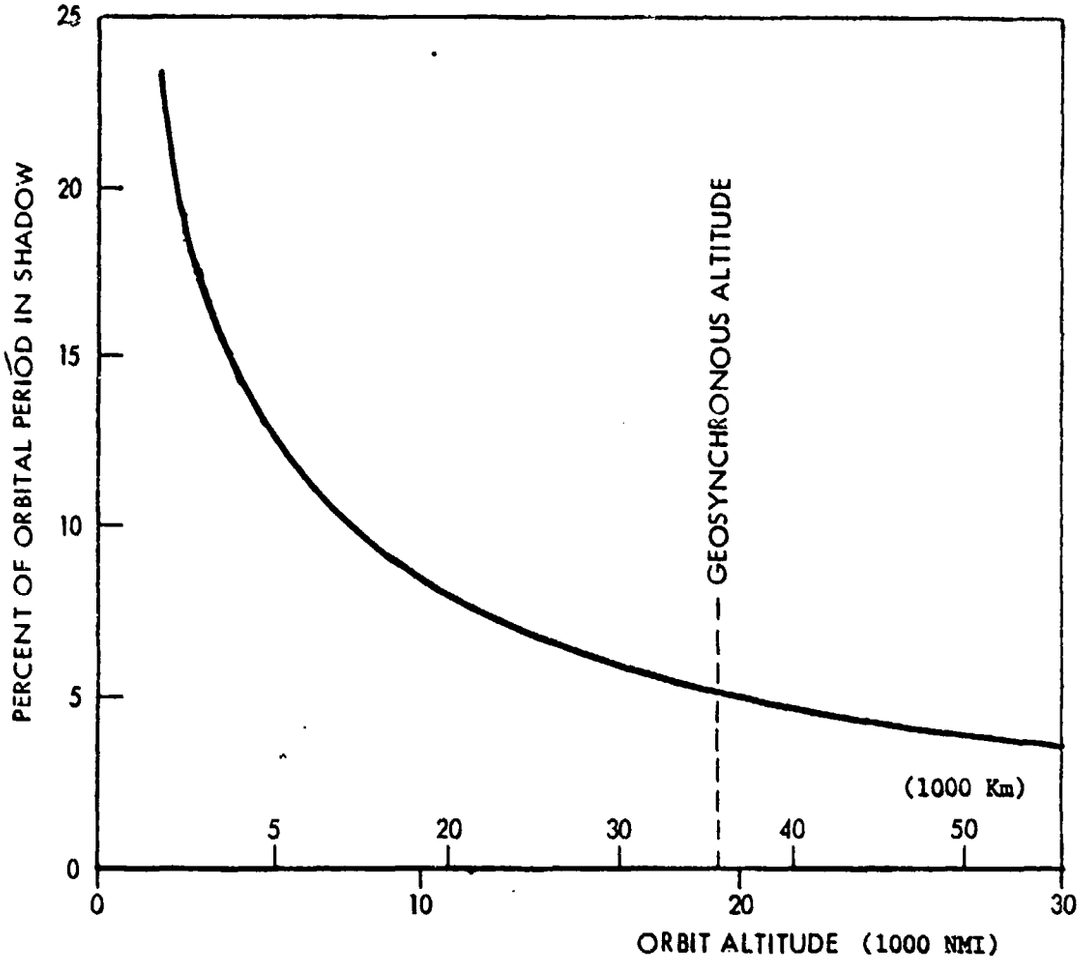

Figure 67. Maximum Time in Earth Shadow Circular Orbits

Theoretically, with an infinite number of such impulses, it should be possible to reduce the required mission velocity to that attained from purely impulsive burns. However, the flight time to achieve mission objectives would also be increased.

A Rockwell International-developed Geosynchronous Trajectory Optimization Program (GEOTOP) was used to investigate the multiple-burn, low thrust-to-weight transfer trajectories. With this program, it is possible to optimize the duration and sequencing of the perigee and/or apogee burn arcs to minimize the mission ΔV as a function of total trip time. It is feasible to use the

program in its high-speed orbit-averaging mode for most of the analysis, and only resort to the precision integration mode only when very detailed time histories are needed.

The relationship between the mission ΔV and corresponding trip time obtained by optimizing the multiburn transfer is illustrated in Figure 68 The example illustrated is for an initial thrust-to-weight of 0.3×10^{-3} g's $\left(\frac{F}{W} = \frac{20}{65000}\right)$ and two representative specific impulse values (872 and 1041 sec). Thus, for example, by extending the transfer from 14 days to 30 days, the mission ΔV can be reduced from 19,200 fps to 16,500 fps (Isp = 872 sec). These trip time increases should, however, be considered in relationship to the 180 + day trip times that are characteristic of the Solar Electric Ion Propulsion Systems.

The increase in the number of revolutions for the spiral ascent as the trip time is increased as the result of multi-impulse transfer technique is illustrated in Figure 69. The number of revolutions strongly affect the number of maneuvers required to maintain proper solar alignment. The pitch and roll angle histories are shown in Figures 70 and 71 respectively as a function of the fraction of an orbital revolution. Of particular concern are the "snap roll" maneuvers that would have to be performed twice per revolution when the sun vector is nearly coplanar with the orbit plane (β is small). Increasing the number of revolutions during the ascent mission results in a direct increase of propellant expended to perform these maneuvers.

The number of burn arcs for the mission also impose a design requirement, since the main thrusters will have to go through a number of start and shutdown cycles as a function of trip time (Figure 69).

Some of the pertinent transfer parameters for the 30 day multiple burn trajectory are presented in Figures 72 through 77. The sequence of the burn arcs starts with a number of "perigee" burns (Figure 72). These power-on arcs extend for more than half of the ellipse. Subsequently, a combination of perigee and apogee burns increases the altitude so that one of the apogees is nearly at mission altitude. Finally, a sequence of apogee burns circularizes the orbit. For the 30 day mission the number of revolutions in the spiral is 182 with 196 burn arcs. The larger number of burn arcs represent the revolutions in the spiral when both apogee and perigee impulses were utilized.

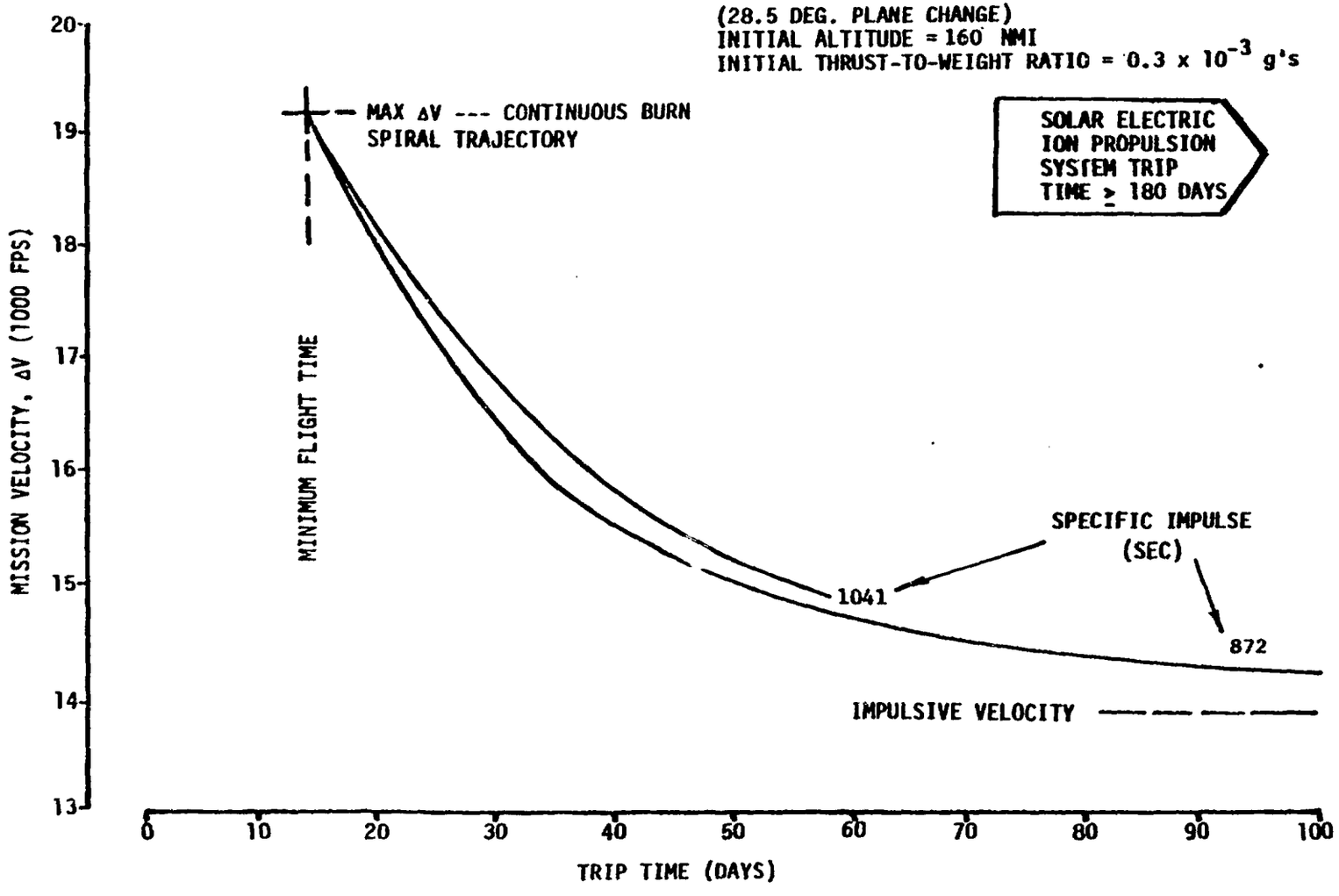

Figure 68. Specific Impulse Effect - Multiple Impulse Transfer

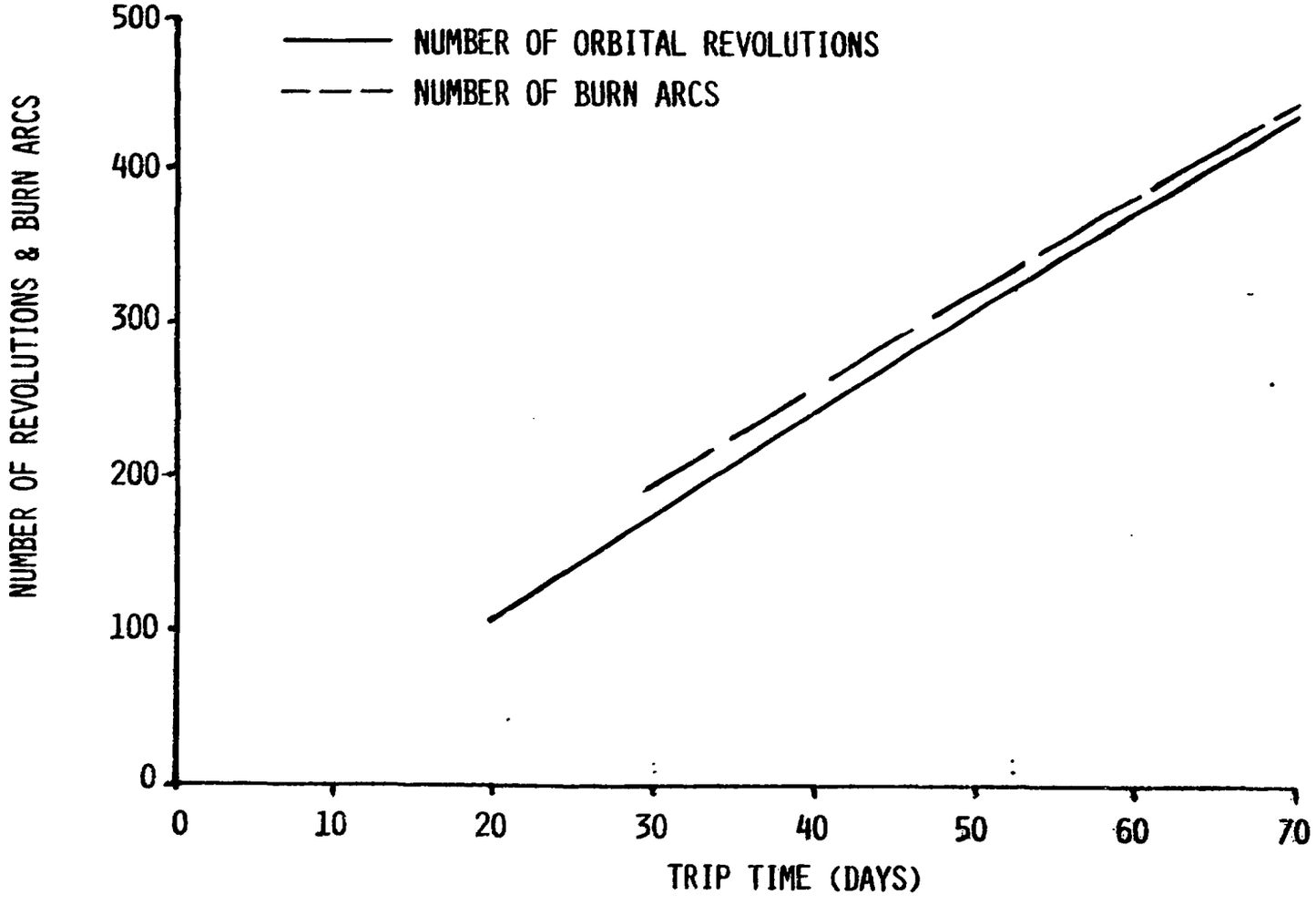

Figure 69. Number of Spirals - Multiple Impulse Transfer

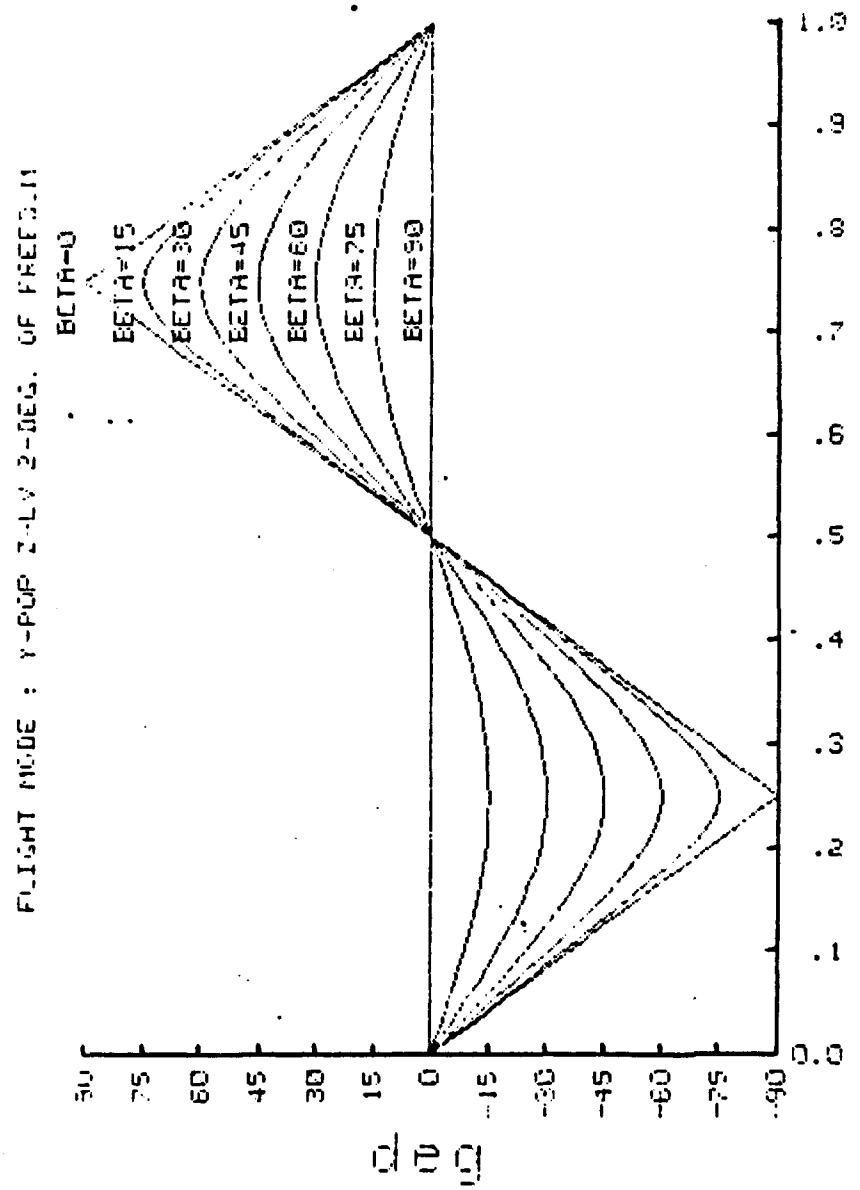

Figure 70. Solar Collector Pitch Angle

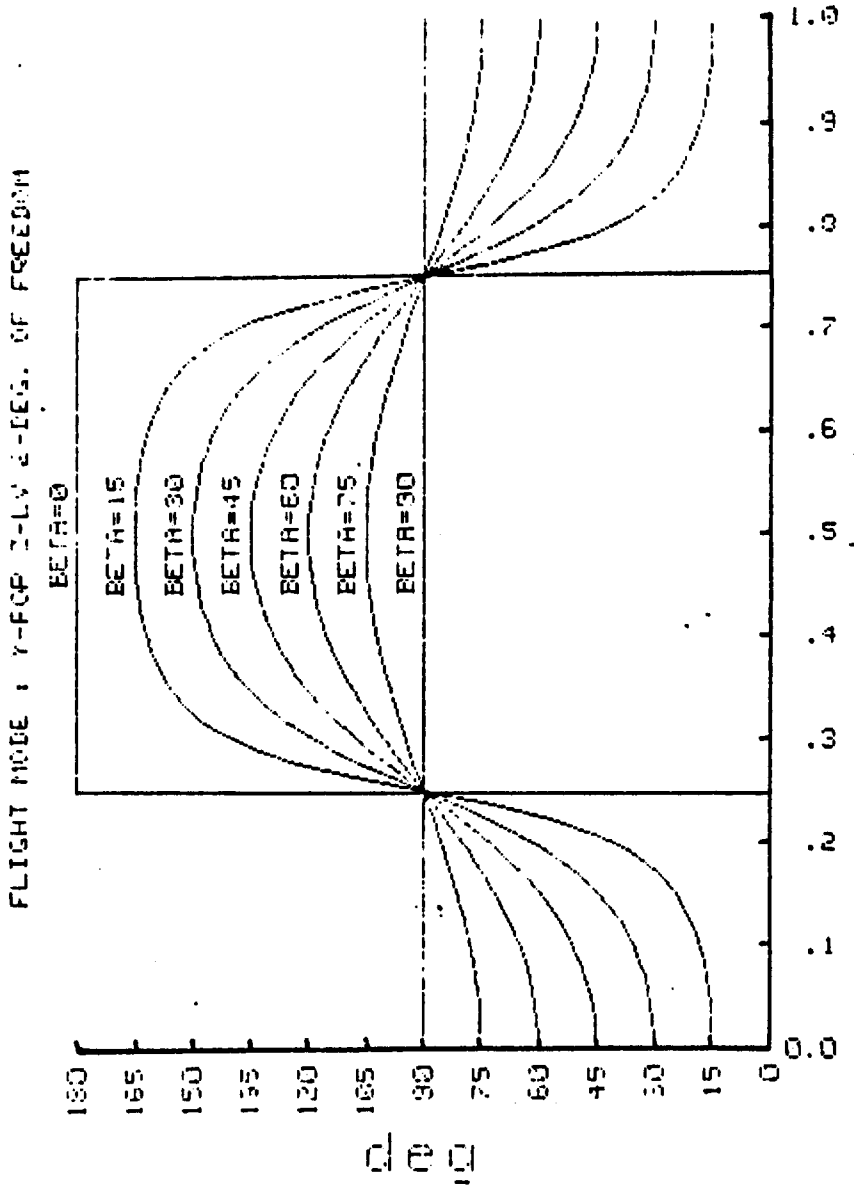

Figure 71. Solar Collector Roll Angle

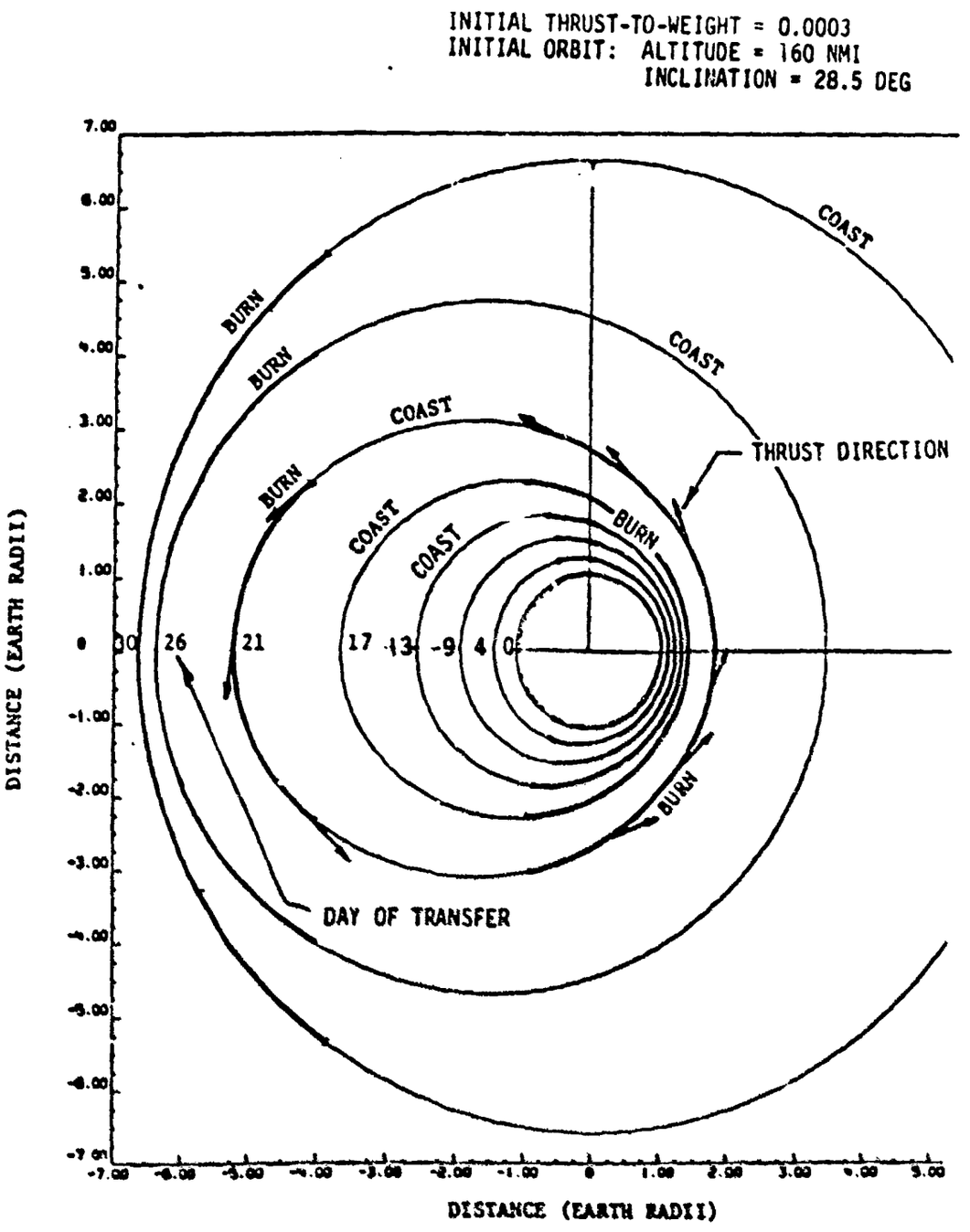

Figure 72. Multiple Impulse 30 Day Transfer Representative Ellipses

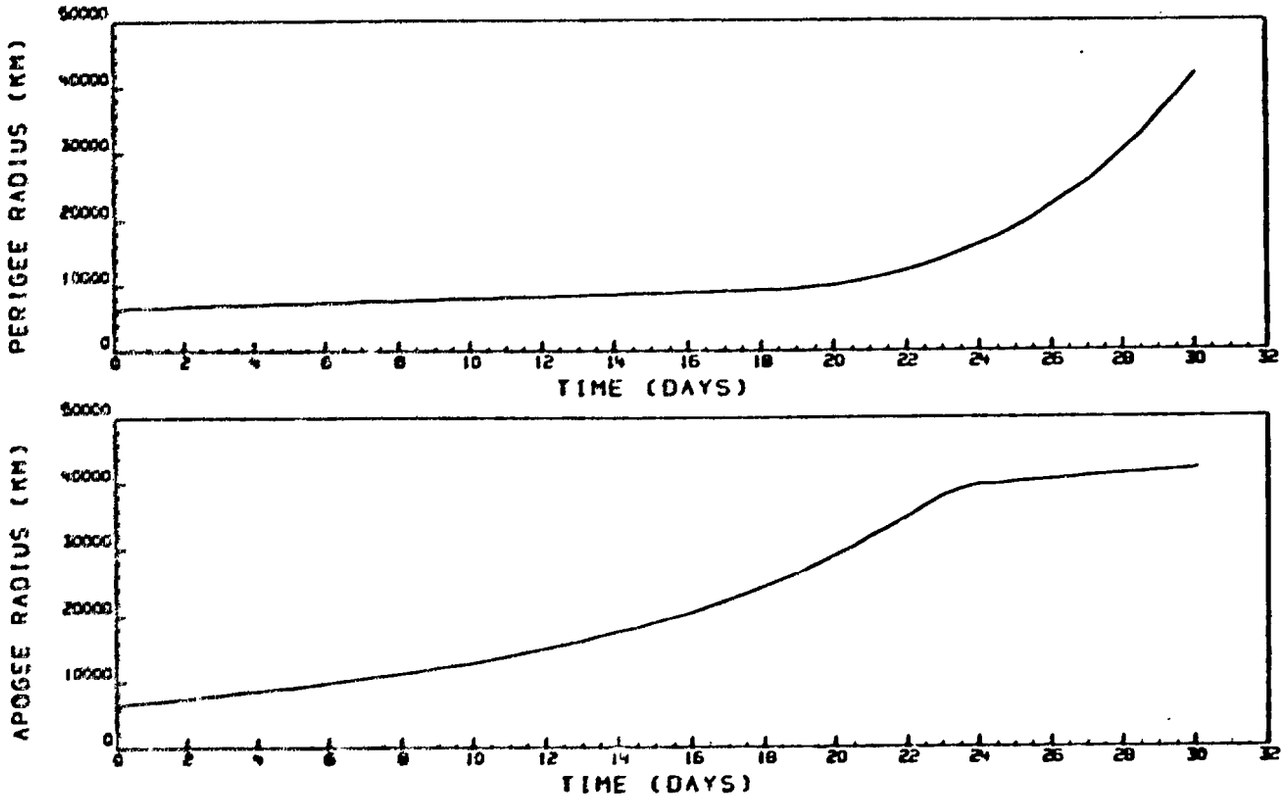

Figure 73. Perigee and Apogee Radius Time History - 30 Day Multi Impulse Transfer

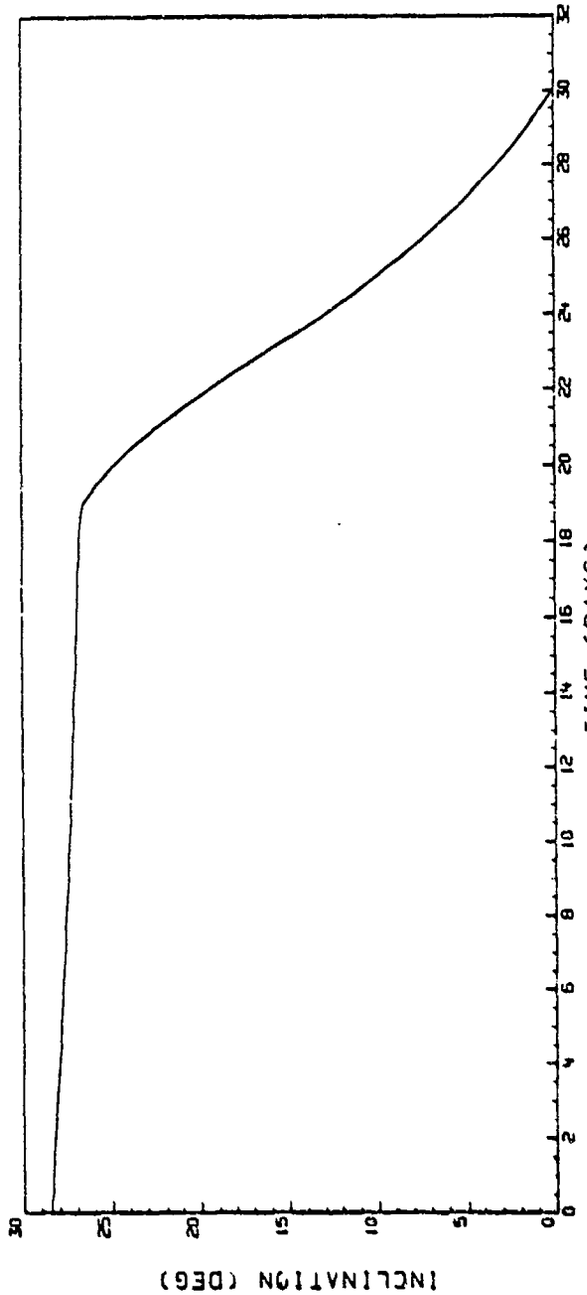

Figure 74. Inclination Time History - 30 Day Multi Impulse Transfer

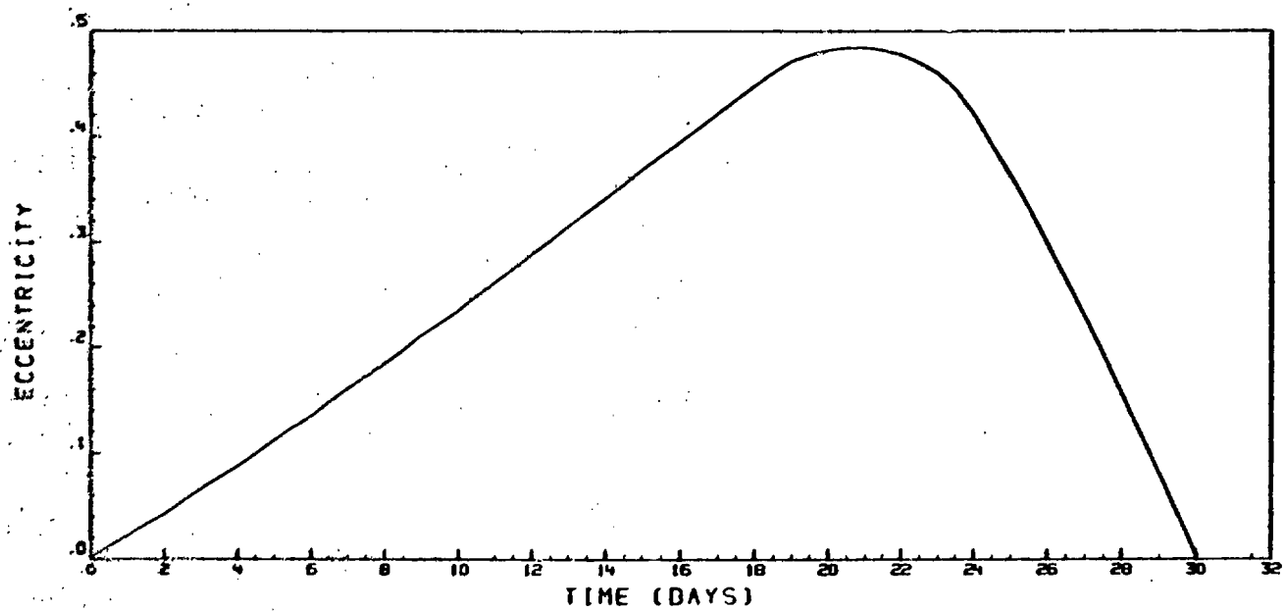

Figure 75. Eccentricity Time History - Multiple Impulse 30 Day Transfer

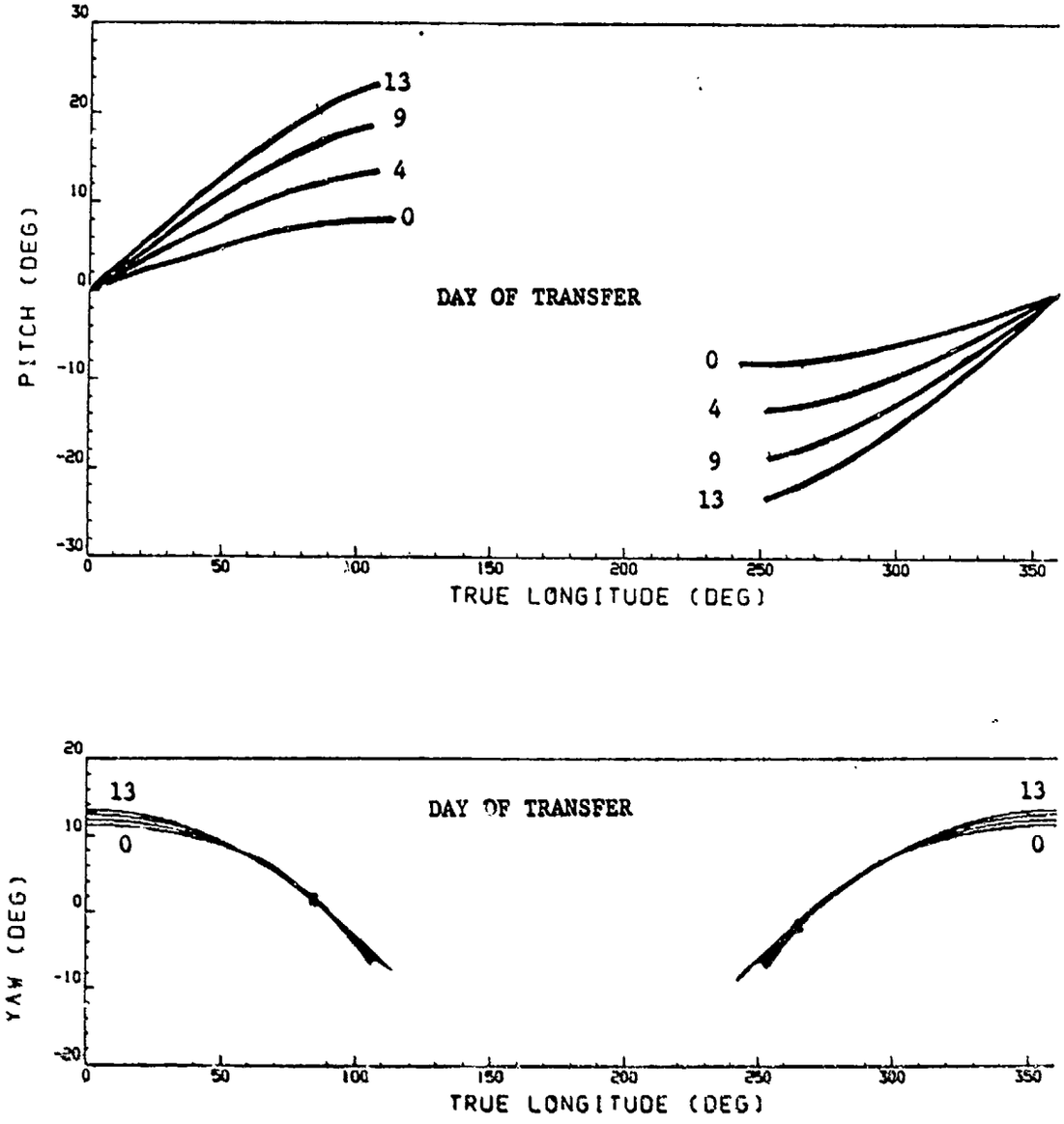

Figure 76. Representative Thrust Direction Histories Multiple Impulse 30 Day Transfer - First Half of Mission

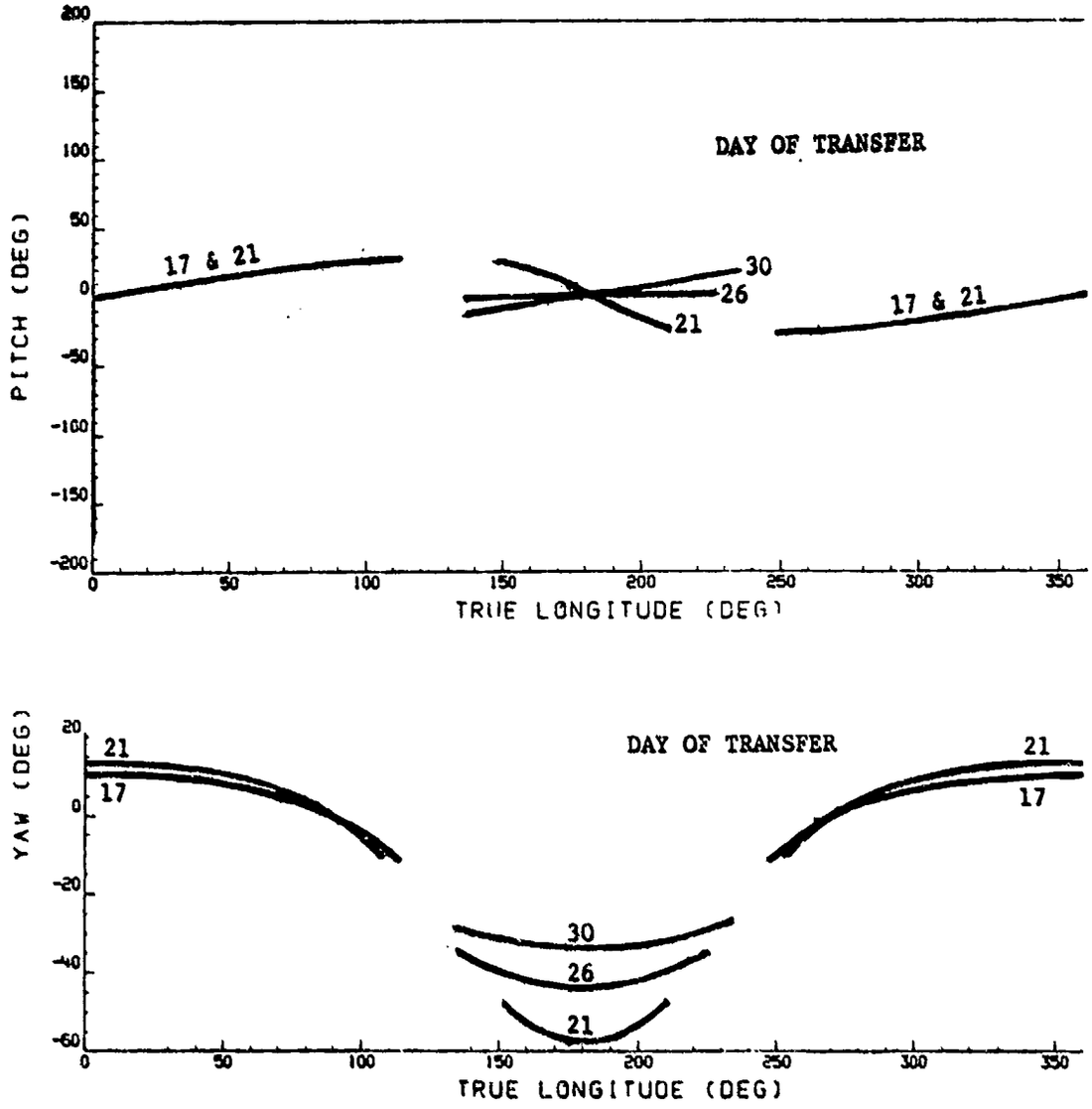

Figure 77. Representative Thrust Direction Histories Multiple Impulse 30 Day Transfer - Last Half of Mission

The effect on the other parameters of this type of transfer trajectory are seen in Figures 73 and 77. Of particular interest is the nearly fixed inclination flight during nearly two thirds of the trajectory, followed by a rapid change in inclination as apogee burns become dominating.

The thrust attitude history during representative burn arcs is shown in Figures 76 and 77. Consistent with the inclination time history the yaw steering is minimal for the perigee burns and increases considerably for the apogee burns during the later phases in the mission. Pitch steering remains consistently within $\pm$ 30 degrees throughout the flight. Limiting pitch steering to lower values, closer to tangential thrusting, at the expense of longer trip time remains a viable option.

The relationship of mission velocity, initial thrust-to-weight ratio, and trip time for multi impulse transfer is illustrated in Figure 78. For each initial thrust-to-weight the mission velocity corresponding to the respective minimum flight time remains unchanged at 19,200 fps. This flight mode corresponds to the continuous burn transfer trajectory.

The slope of the mission velocity with respect to the multi-impulse trip time becomes gentler as the initial thrust-to-weight ratio is decreased. The trip time thus increases more rapidly for the lower thrust-to-weight ratios. This is one of the reasons why for the usually lower thrust-to-weight ratio Solar Electric Ion Propulsion Systems the multi burn transfer technique has not been seriously considered. The higher thrust Solar Rocket system, however, ideally lends itself to the exploitation of the multi-impulse orbital transfer technique.

Upon close inspection of the data presented in Figure 78, the mission velocity -- trip time relationship can be generalized for a range of thrust-to-weight ratios. This is illustrated in Figure 79. Here the mission velocity is expressed as a function of the ratio of the flight time to the minimum flight time. The minimum flight time, corresponding to a continuous burn spiral, and can be easily expressed as a function of the average thrust-to-weight ratio (Figure 66) or related to the initial thrust-to-weight ratio. The mission velocity trip time relationship for multi burn transfers thus may be obtained for all thrust-to-weight ratio values of interest for the Solar Rocket System.

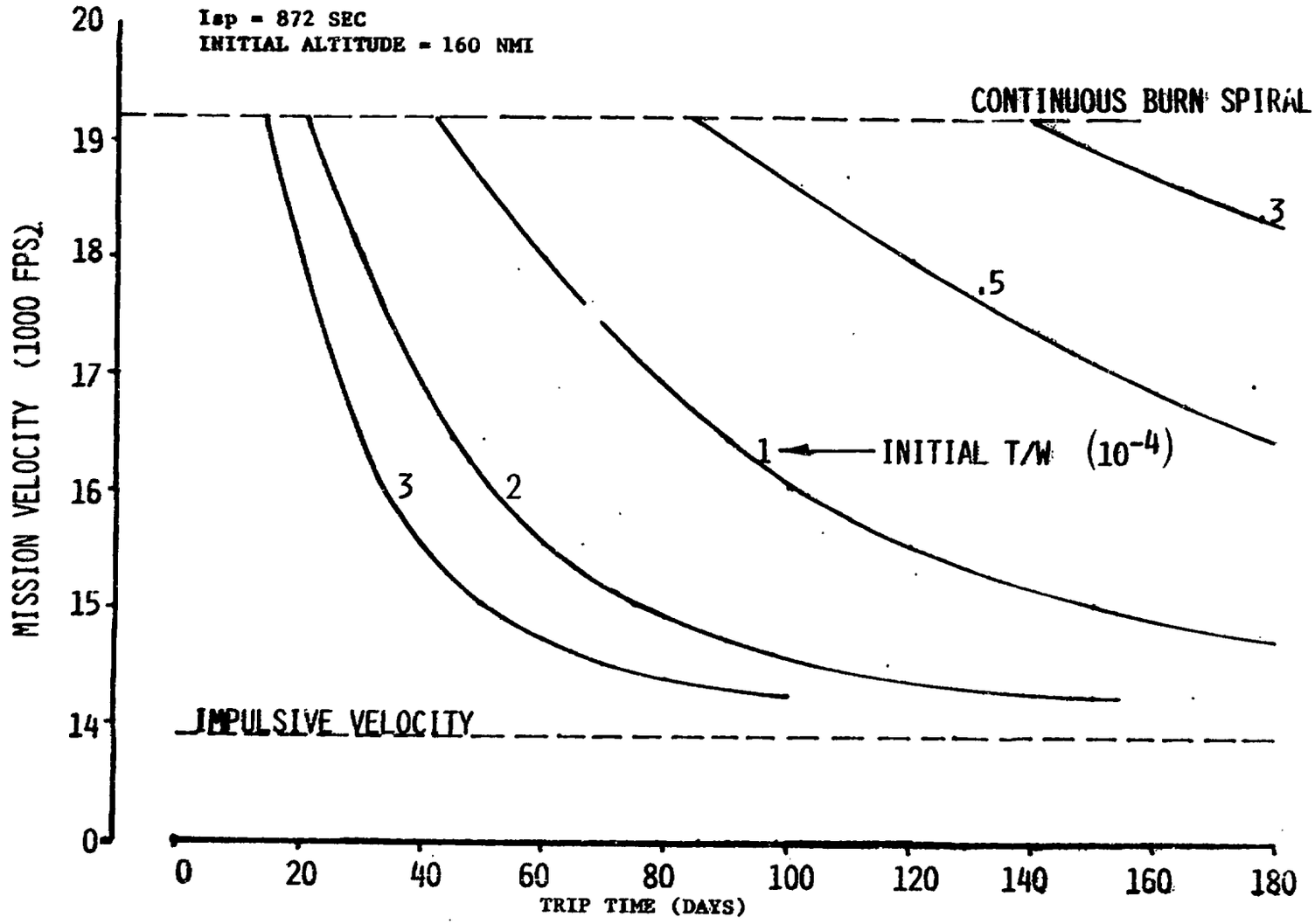

Figure 78. Thrust-to-Weight Ratio Effect - Multiple Impulse Transfer

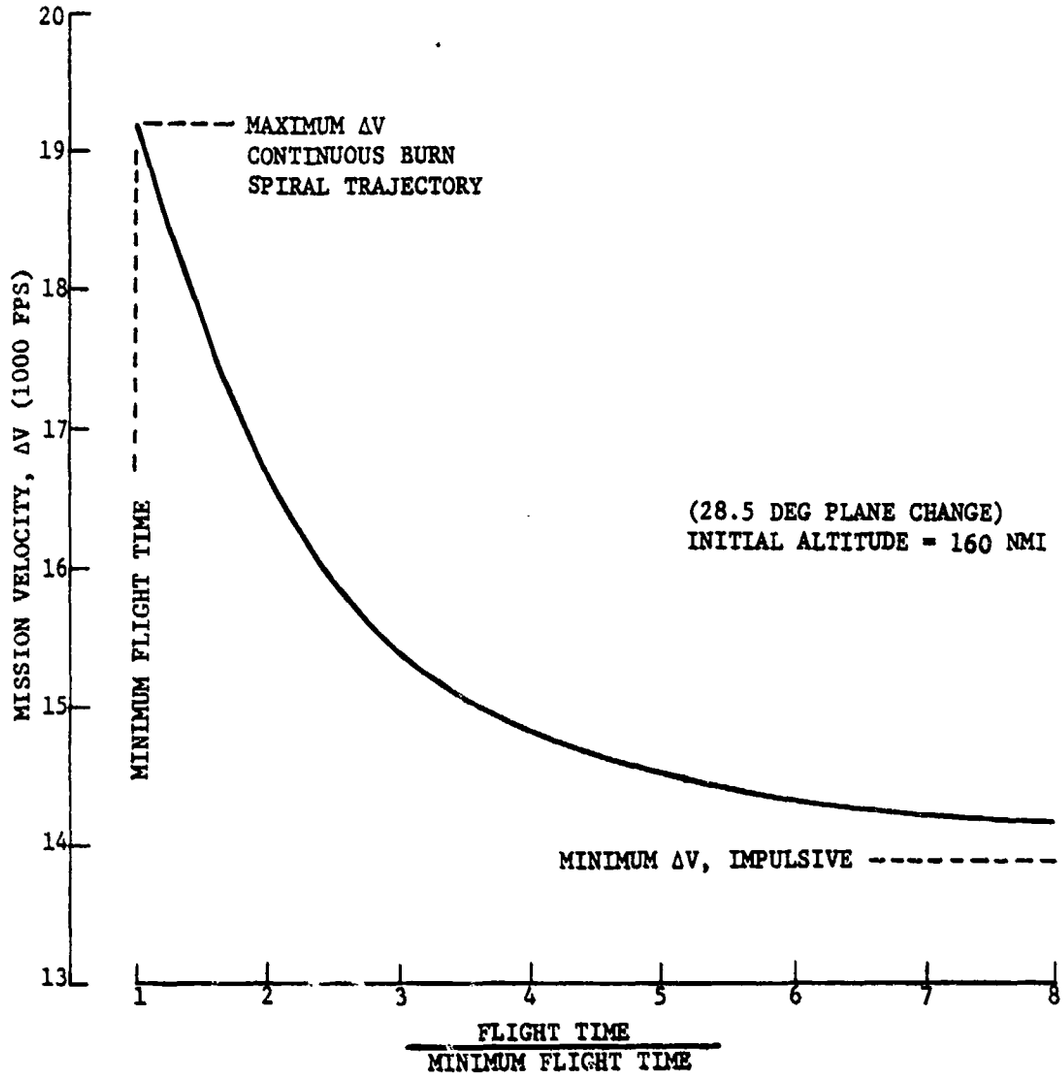

Figure 79. Generalized Mission Velocity Requirements - Multiple Impulse Transfer

Lower thrust-to-weight (< 0.05) chemical orbit transfer vehicles also may benefit from the multi-impulse technique. This is illustrated in Figure 80 for three values of thrust for which the single perigee and single apogee burn technique would result in mission velocity requirement from 15,350 fps to 16,600 fps. A transfer consisting of eight perigee burns and a single apogee burn would reduce the mission velocity requirement to less than 14,420 fps.

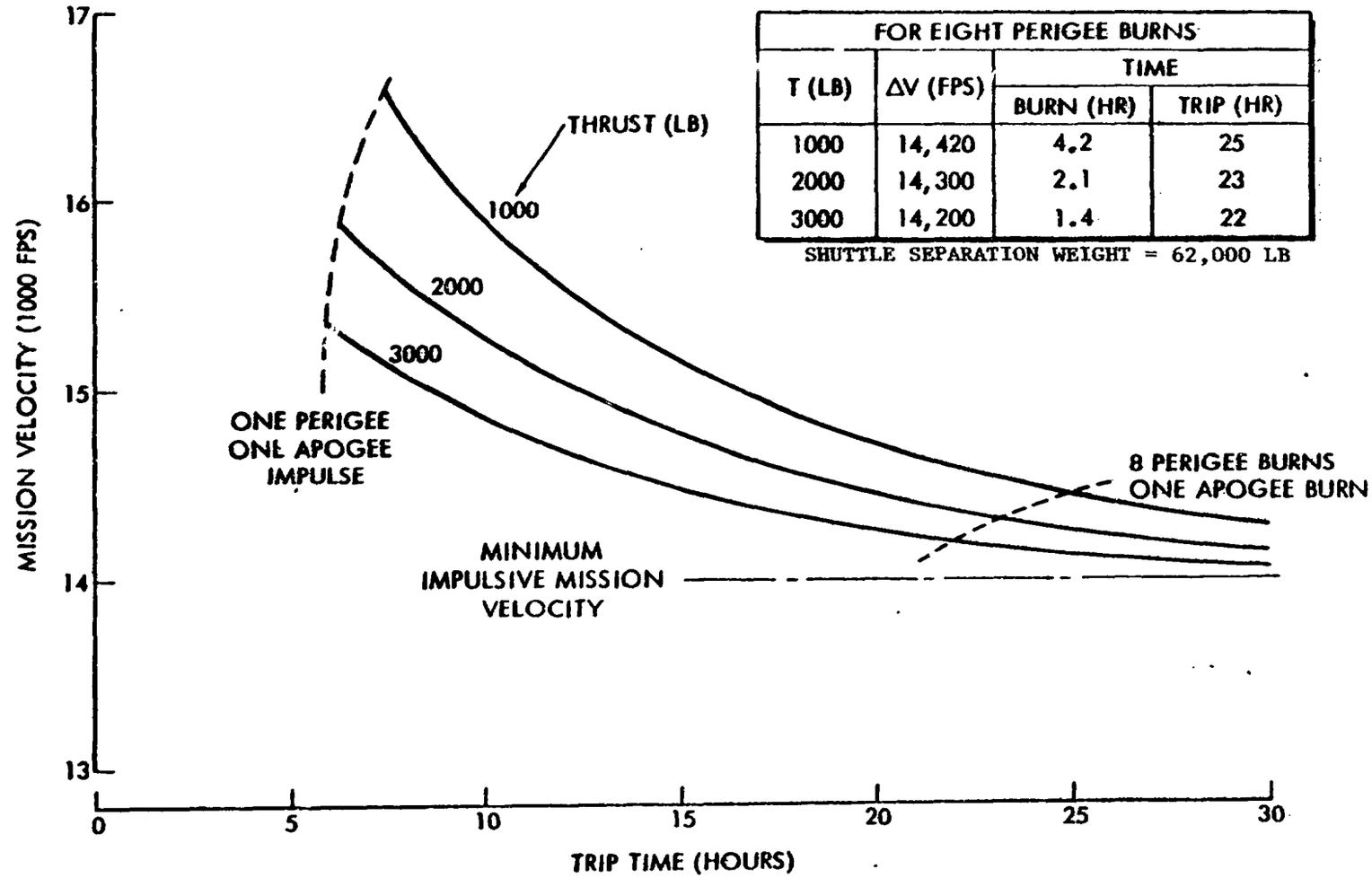

Figure 80. Mission Velocity for Chemical Stages - Multiple Impulse Transfer

Alternate Missions

Paragraph 4.5.2 of the SOW requires that other missions for the solar thermal rocket be identified. A number of Rockwell International in house studies were used as sources of some of the alternative missions. In addition, NASA JPL and Batelle Institute provided a number of potential mission descriptions that could be performed by the Solar Rocket.

The use of very low thrust-to-weight propulsion systems for other than LEO to GEO transfer were briefly analyzed. Of particular interest are the transfers from the low altitude (160 n.mi) parking orbit to orbits of higher altitudes. Plane change may or may not be required for such missions.

For these missions, the Edlebaum approximation for the low thrust-to-weight characteristic mission velocity was used for the ΔV data illustrated in Figure 81.

The relationship

$$\Delta V = \sqrt{V_o^2 - 2VV_o \cos \frac{\pi}{2} \Delta i + V^2}$$

gives the characteristic velocity directly in terms of the initial and final orbit velocities and the change in inclination. In its derivation, it is assumed that all intermediate orbits remain quasi-circular and that the thrust angle is held constant over each revolution. This is a characteristic of trajectories with thrust-to-weight ratios of less than 10^{-3}.

The transfer velocity for various inclination changes is presented as a function of final orbit altitude in the computer generated Figure 81. The initial orbit altitude was held constant at 150 n.mi. Information for ΔV 20,000 fps was not presented since it is believed that such velocity requirements would be outside the range of interest for propulsion systems other than those in the solar electric ion bombardment category. Such an upper velocity bound would limit orbit plane changes to slightly greater than 30 degrees. However, any change in altitude can be accommodated.

In order to estimate the trip times for these missions, average acceleration/trip time relationship was also included in the above figure. The trip time corresponds to that attained by using a continuous burn spiral for the transfer. As noted for LEO to GEO transfer, the velocity requirement can be reduced at the cost of extended trip time. Similar velocity reduction can also be achieved for all orbit transfer missions.

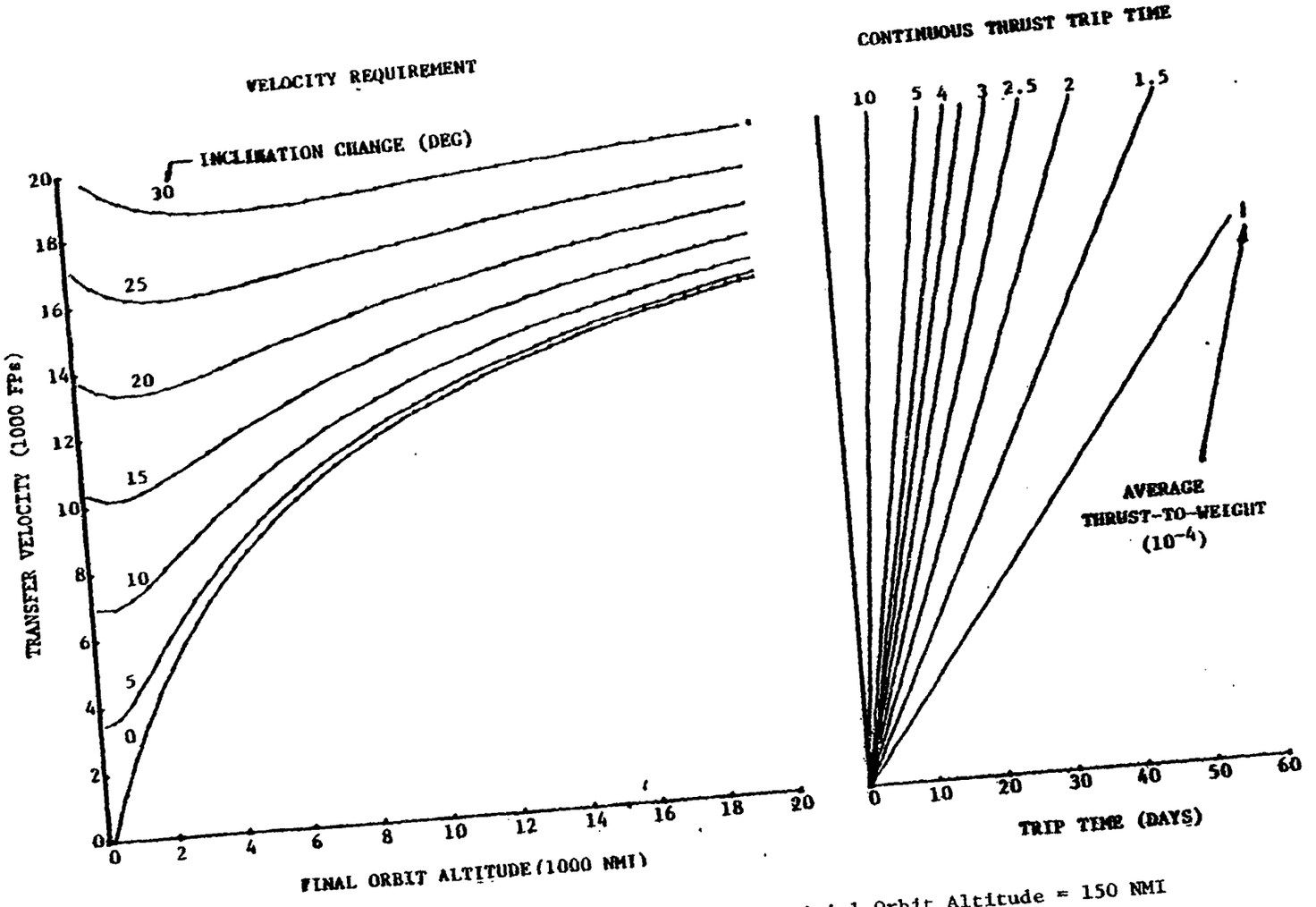

Figure 8[illegible]. Low Thrust-to-Weight Orbit Transfer Initial Orbit Altitude = 150 NMI

A series of Rockwell International in-house as well as contractual studies provided an insight of other potential missions for the Solar Rocket. Table 10 identifies some discrete high velocity missions that have been analyzed for other low thrust-to-weight orbit transfer vehicles. They are indicative of the type of orbit transfer missions that could be applicable for the Solar Rocket Propulsion System. Of particular interest could be the geosynchronous de-orbit missions for satellite removal operations. The mission velocity for this class of orbital transfer is illustrated in Figure 82. as a function of final orbit characteristics (apogee altitude and relative inclination). For example the mission velocity for a single in-plane de-orbit operations would be approximately 7000 fps.

Precision orbit maintenance or special orbit positioning missions can be performed by the Solar Rocket. Orbit maintenance can be performed either by a number of discrete impulses or by continuous thrust. For the later technique usually extremely low accelerations have to be used. Orbit positioning missions, however, may require much higher thrust-to-weight ratios. For example, as illustrated in Figure 83 for three elliptical orbits, the repositioning of the line of apsides could be readily performed by the Solar Rocket.

Table 10. Alternate Mission Options

INITIAL ORBIT		FINAL ORBIT		Continuous Burn Mission ΔV (FPS)
Altitude (NMI)	Inclination (DEG)	Altitude (NMI)	Inclination (DEG)	
160 CIRC	28.5	GEOSYNC	0	19,200
GEOSYNC	0	GEOSYNC	90	24,890* 18,615**
GEOSYNC	0	700 x 21100	63.4	17,630
GEOSYNC	0	160 CIRC	28.5	19,200
160 CIRC	28.5	700 x 21100	63.4	22,425

* Constant Altitude Transfer

** Optimized Transfer

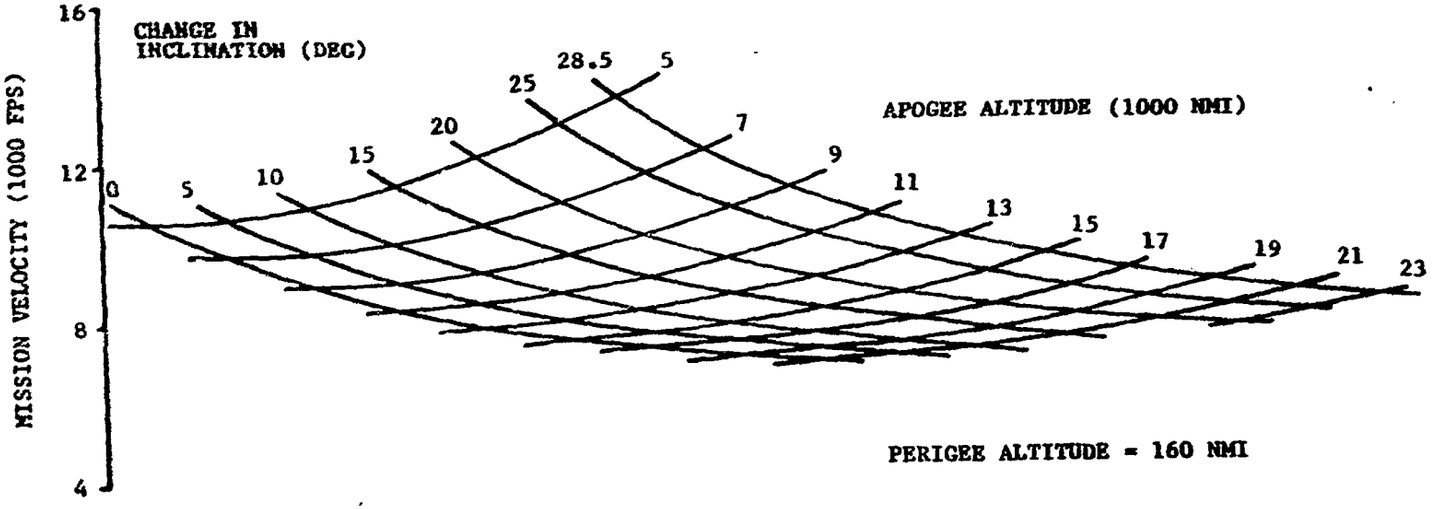

Figure 82. Mission Velocity Requirements for Transfer From Geosynchronous to Elliprical Orbits

	ORBIT CHARACTERISTICS		
	PERIOD (HR)	ECCENTRICITY	PERIGEE ALTITUDE KM (NMI)
A	24	0.5	14,705 (7940)
B	24	0.818	1296 (700)
C	12	0.7112	1296 (700)

(ACCELERATION DIRECTION REVERSED AT EACH CROSSING OF THE APSIS)

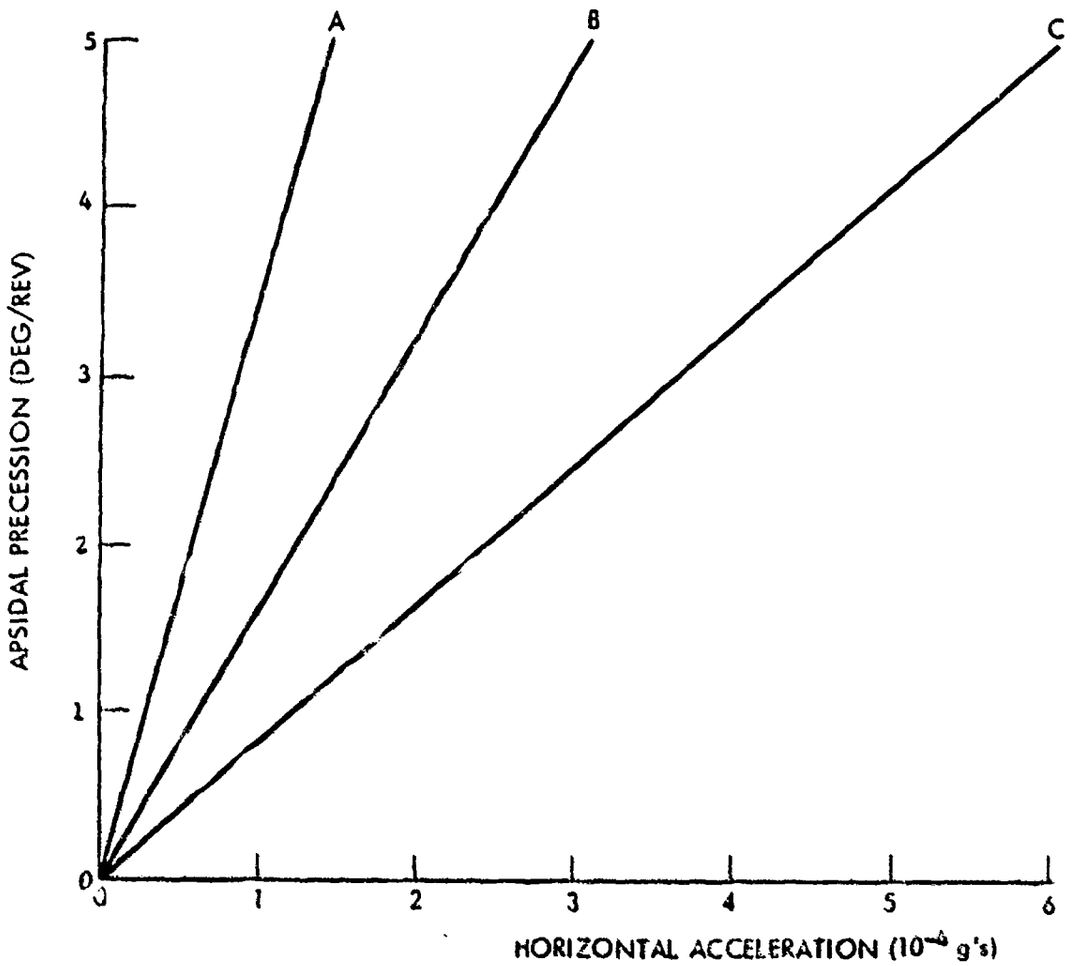

Figure 83. Apsidal Precession Control

The apsidal precession produced by thrusting is plotted here for the case of horizontal acceleration, ie.e, normal to the radius vector and in the orbit plane. The thrust direction is reversed twice per orbit at perigee and apogee. This requires either a snap-pitch or snap-yaw maneuver. The former is preferred.

Radial acceleration to overcome apsidal precession does not require reversal of the thrust vector. The acceleration to null a given procession rate, however, is approximately twice that needed with horizontal acceleration.

To evaluate the applicability of the Solar Rocket Concept for other than geocentric missions, a number of representative high energy (ΔV)/payload combinations have been selected (Table 11). These include JPL analyzed interplanetary vehicles as well as a nuclear waste disposal concept. The impulsive high thrust-to-weight vehicle mission velocity shown is usually that required to inject the payload on its transfer trajectory to the target. It does not include the velocity to perform the planetary capture maneuvers. Likewise, the payload is that package that would perform the end of the mission maneuvers plus the scientific payload.

The only exception to this being the nuclear waste disposal concept. Here all the velocities required to place the payload (nuclear waste plus shielding) into a 0.86 AU sun-centered circular orbit is given.

For low thrust-to-weight vehicles these mission velocities would be 35% - 40% higher.

Table 11. Alternate Mission Velocity Requirements

MISSION	IMPULSIVE ΔV (FPS)	MISSION PAYLOAD (LB)
HALLEY FLYBY TEMPEL 2 RENDEZVOUS	15,600	2020
VENUS ORBITAL IMAGING RADAR	11,750	1980
MERCURY ORBITER	16,500	1200-2700
SOLAR PROBE	25,500	1670
NUCLEAR WASTE DISPOSAL	16,050	6760
LEO TO GEO	14,000	--

STABILIZATION AND CONTROL

A summary assessment of a stabilization and control system was made to determine the requirements for offsetting disturbance torques and for generating maneuvers for proper solar collector pointing.

A representative vehicle configuration was selected for control system analysis. This is shown on Figure 84. This configuration has the following features:

- Weight = 36000 lb
- I_{xx} = 926,240 slug-ft^2
- I_{yy} = 1,143,050 slug-ft^2
- I_{zz} = 335,600 slug-ft^2
- The largest area which one collector can present to the airstream is 78,340 sq. ft.

Where trajectory data are required, it is assumed that the vehicle starts at 220 nmi altitude and takes 30 days and 200 orbits to get to geosynchronous altitude.

Disturbance Torques

For all low thrust-to-weight propulsion systems the relative magnitude of aerodynamic drag with respect to the thrust produced at low orbital altitudes is of major concern. For the Solar Rocket the influence of drag on the trajectory is negligible. As illustrated in Figure 85, the drag force at 160 n.mi. is but a small fraction of the estimated thrust of the solar rocket. It should be noted that the drag force decreases rapidly with altitude. For example, an order of magnitude decrease is realized by just increasing the altitude from 160 n.mi. to 225 n.mi.

The significant disturbance torques are aerodynamic and gravity gradient torques. Solar pressure torques are assumed to be negligible due to the symmetry of the collectors about the sun line. Aerodynamic torque was computed for an angle of attack of 25 deg. in the X-Z plane. (See Figure 84) The average torque as a function of time is shown on Figure 86.

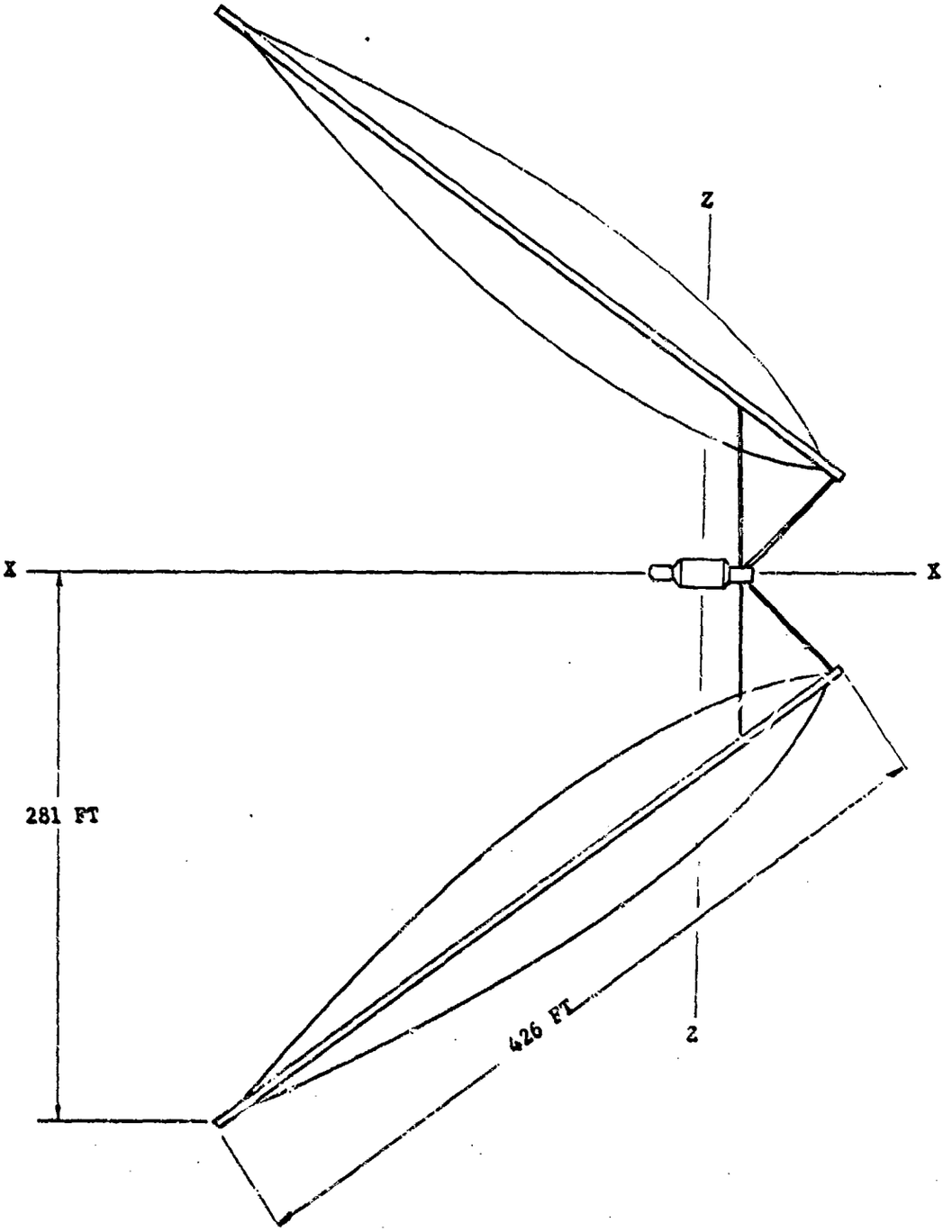

Figure 84. Inflatable Paraboloid Collector

ESTIMATED TOTAL ACHIEVABLE THRUST
USING HYDROGEN PROPELLANT
TEMPERATURE = 5000°R, SURFACE ERROR =
0.25°)

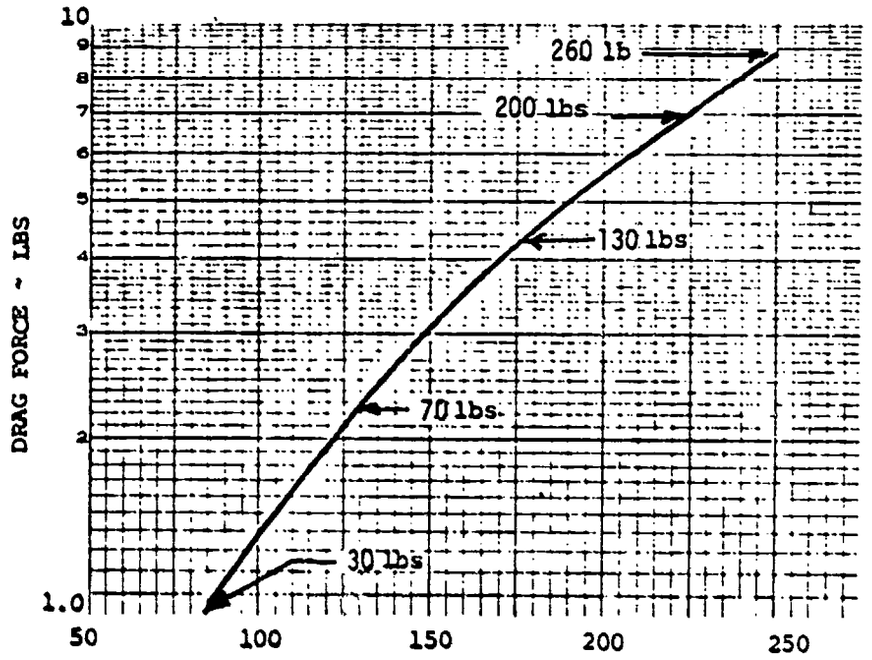

Figure 85. Maximum Drag Force on Two Concentrators (Altitude = 160 NMI)

The maximum gravity gradient torques, for the moments of inertia presented aobve, at 220 n.mi altitude are:

$$T = \begin{bmatrix} 0.72 \\ 0.75 \\ 0.27 \end{bmatrix} \text{ ft - lbs}$$

and at geosynchronous altitude are:

$$T = \begin{bmatrix} 0.0032 \\ 0.0033 \\ 0.0012 \end{bmatrix} \text{ ft - lbs}$$

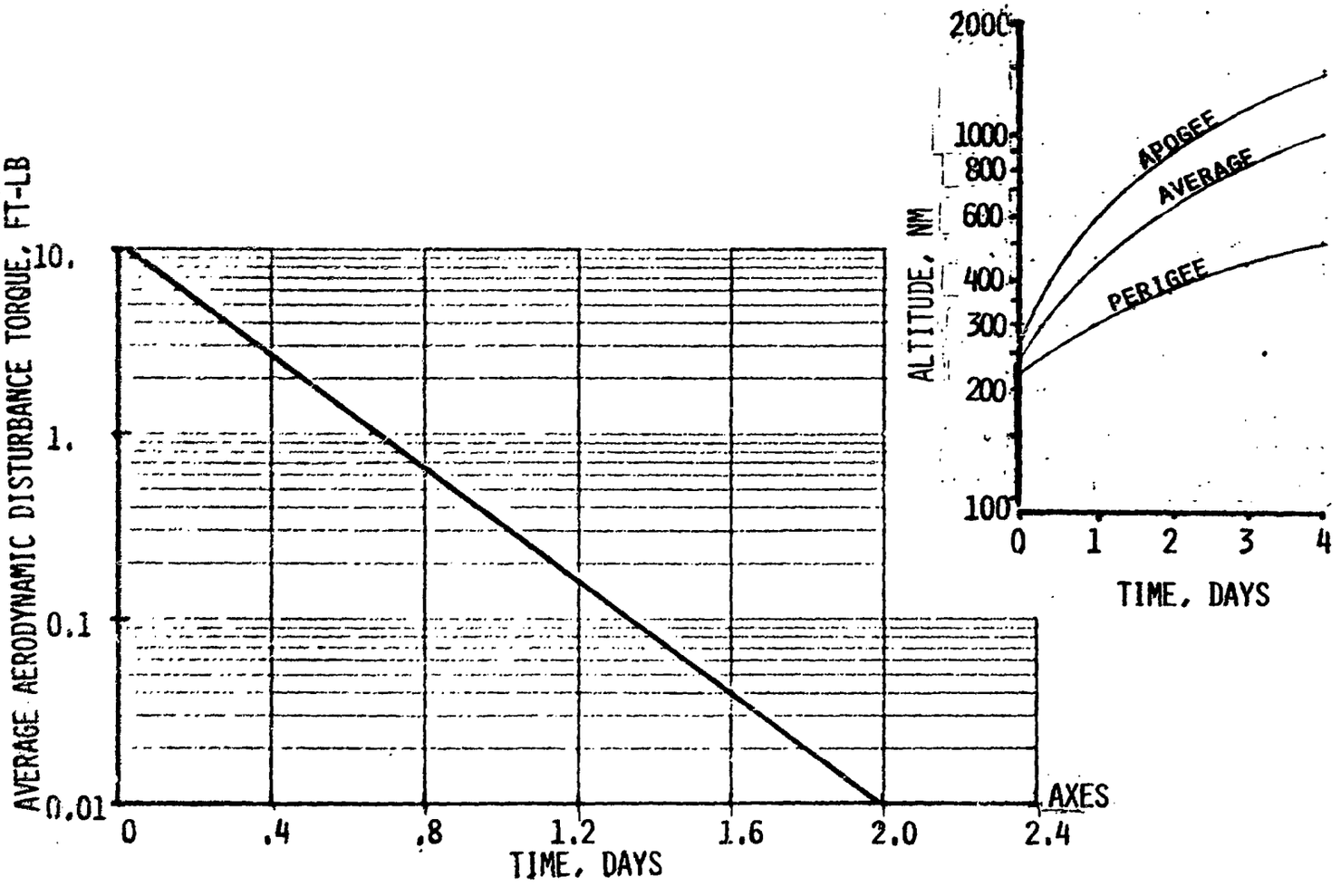

Figure 86. Aerodynamic Torque Versus Time

A constant application of control torque will be required during the transfer orbit to react against the disturbance torques. As the main thrusters are not always on, a reaction control system is required. Because of the large moments of inertia of the vehicle, it is desirable to locate the reaction control system jets as far from the center of rotation as possible in order to reduce propellant consumption. The consumption as a function of radial location of the jets is shown on Table 12 assuming a hydrazine system.

The radial location of 281 ft assumes jets located at the tips of the collectors; the 50 and 100 ft locations are intermediate locations. These are impractical because the collector structure would not support the loads. The practical location is for jets installed on the main body of the spacecraft, a 7.5 ft radial location. Such an installation is shown on Figure 87.

Steering Policies

When the component in the orbit plane of the angle between the vector normal to the solar collector and the roll axis of the vehicle passes near zero, a 180 degree roll is required to maintain accurate solar collector and thrust vector pointing. The optimum steering policy, optimum in the sense of zero error in collector and thrust vector pointing, requires a 180 degree snap roll. Definition and analysis of this policy requires roll attitude history data in order to determine torque requirements. As these data were not available sub-optimal steering policies, sub-optimal in the sense that collector pointing accuracy is not determined, were studied.

Table 12. Attitude Control Propellant Estimates

RADIAL LOCATION OF JETS, FT.	PROPELLANT CONSUMPTION		
	FOR AERO. TORQUES (LBS)	FOR GRAV. GRAD. TORQUES (LBS)	SUM (LB)
281.	2.1	4.2	6.3
100.	6.	12.	18.
50.	12.	24.	36.
7.5	80.	160.	240.

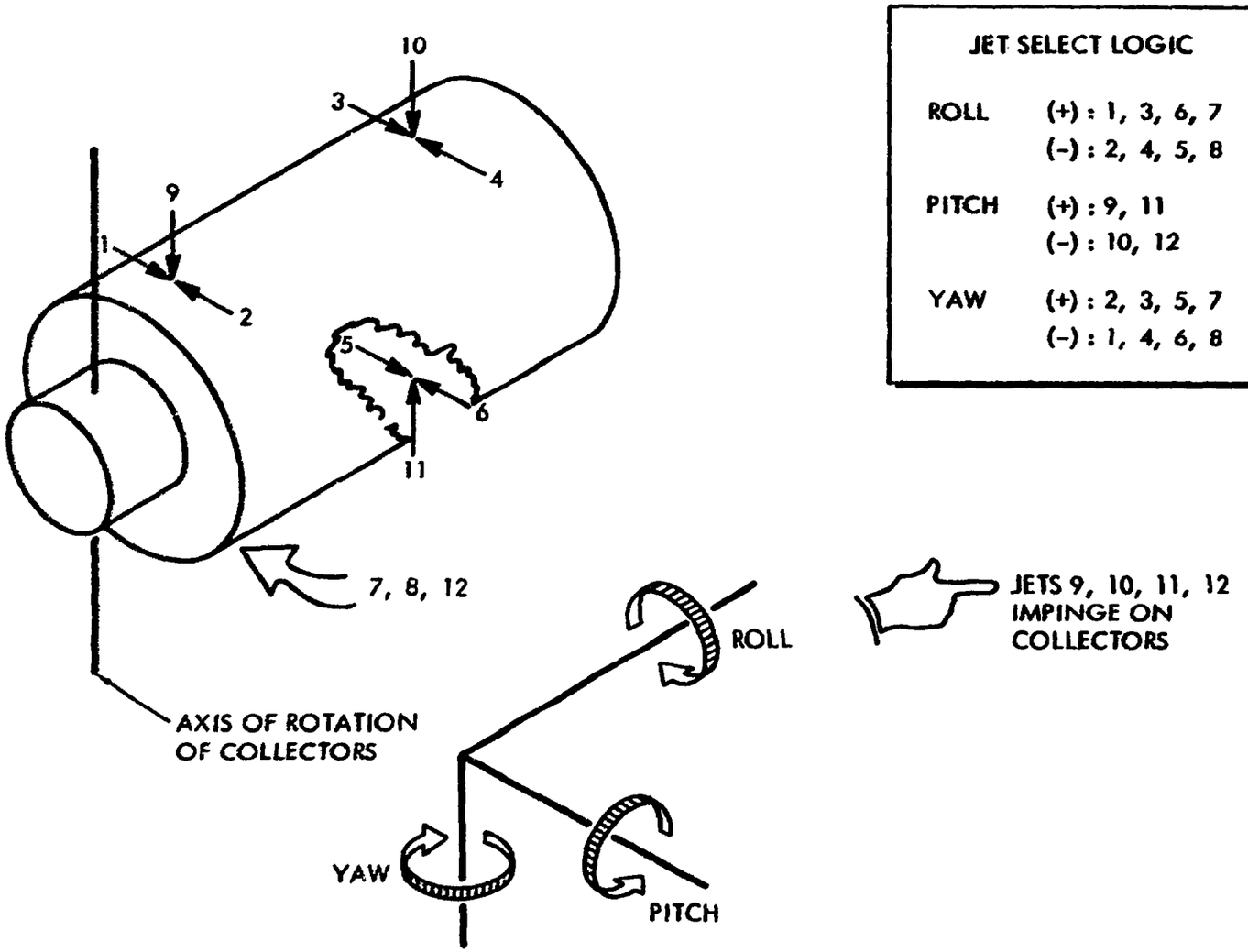

Figure 87. ACS Thruster Location

Steering Using a Reaction Control System

A sub-optimal steering policy would include a constant thrust to rotate the vehicle 90 deg. and then an immediately applied constant thrust in the opposite direction for 90 deg. to complete a 180 deg. rotation in minimum time. Assuming, for the representative configuration shown on Figure 84 and a specific impulse of 230 sec., the time to roll 180 deg. and the amount of propellant used are shown on Figure 88 as functions of the radial location of the jets and the thrust per jet. If the jets are located at the tips of the collectors, in this case 281 ft. a savings in fuel can be realized. Total consumption must take into account the number of orbits and the number of maneuvers per orbit. Assuming two maneuvers per orbit and 200 orbits for the trip, two one lb thrusters located on the main body, 7.5 ft. radius, would consume 3060 lbs of hydrazine. For 281 ft. radius, the consumption is 500 lbs.

A second sub-optimal steering policy would decrease propellant consumption at the expense of longer maneuver times by incorporating a coast period between the acceleration and deceleration period. The propellant consumption per roll maneuver is shown on Figure 89 versus maneuver time and coast time. For the above example with jets at a 7.5 ft. radius, 1192 lbs of hydrazine would be consumed if a 16 minute coast time were incorporated. This compares with 3060 lbs for zero coast.

Steering Using Gimbaled Main Thrusters

Using an RCS system for generating control torques requires a large amount of propellant. It is therefore desirable to gimbal the main thrusters to generate control torques. Gimbal angle freedom or control authority must be sufficient to balance a center of gravity offset in the yaw plane due to gimbaled collectors and at the same time, to generate roll and pitch torques.

For a collector rotation about the z axis of 90 deg. (See Figure 84.) and assuming the collector center of gravity is 100 ft from the xz plane and the main body center of gravity is 25 ft from the thrusters, the gimbal angle required is 18 deg. Each of the two thrusters would gimbal relative to this to produce roll torques. Figure 90 gives the gimbal angle requirement as a function of time to roll 180 deg. assuming the two thrusters are 10 ft apart. If, for example, the gimbal requirement for center of gravity balancing and yaw acceleration is $\theta = 20$ deg, the required time for rolling 180 deg. is ten minutes, and the third axis or pitch acceleration is ignored, then

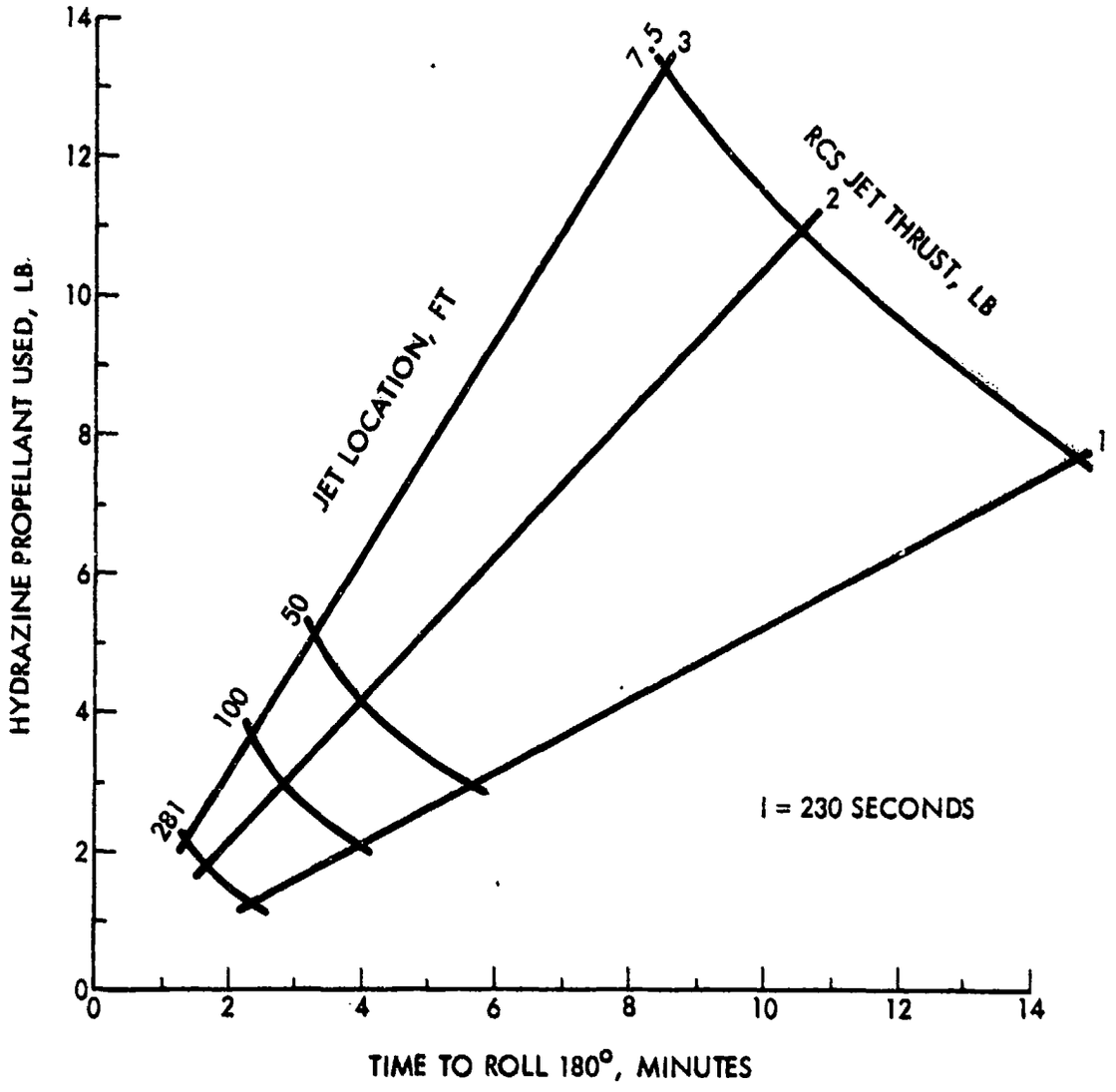

Figure 88. Propellant Used Per Maneuver Versus Maneuver Time

one thruster is gimbaled $\Theta + \alpha = 20 + 44 = 64$ deg. and the other is gimbaled $\Theta - \alpha = 20 - 44 = -22$ deg. In order to generate a pitch acceleration another component of gimbal angle would be required and would be normal to the plane containing α and Θ.

The time to complete the maneuver must be compared to the time requirements for accurate solar collector pointing in order to validate the control authority. As before, this requires roll attitude history data.

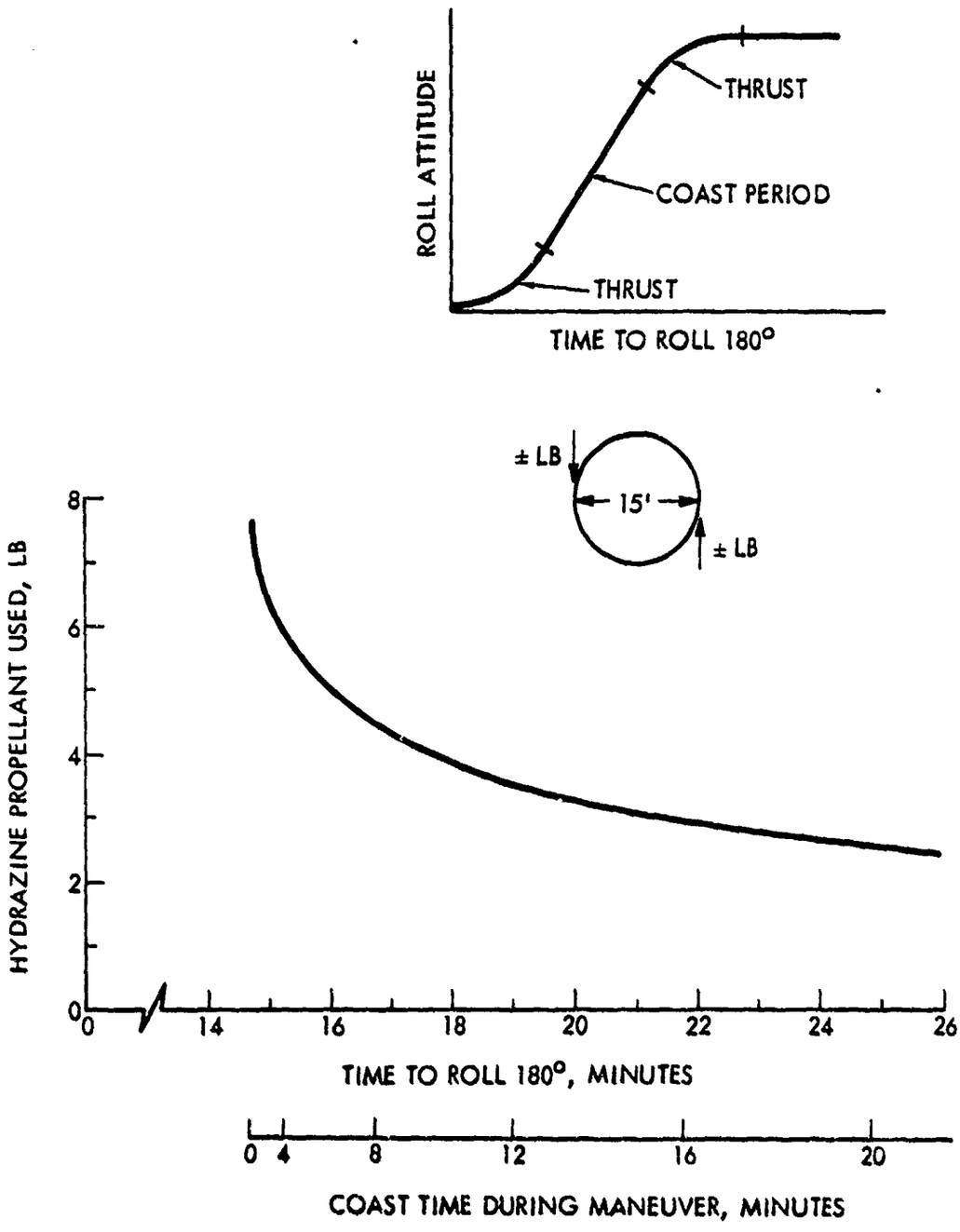

Figure 89. Propellant Used Per Maneuver For Maneuver With Coast Period

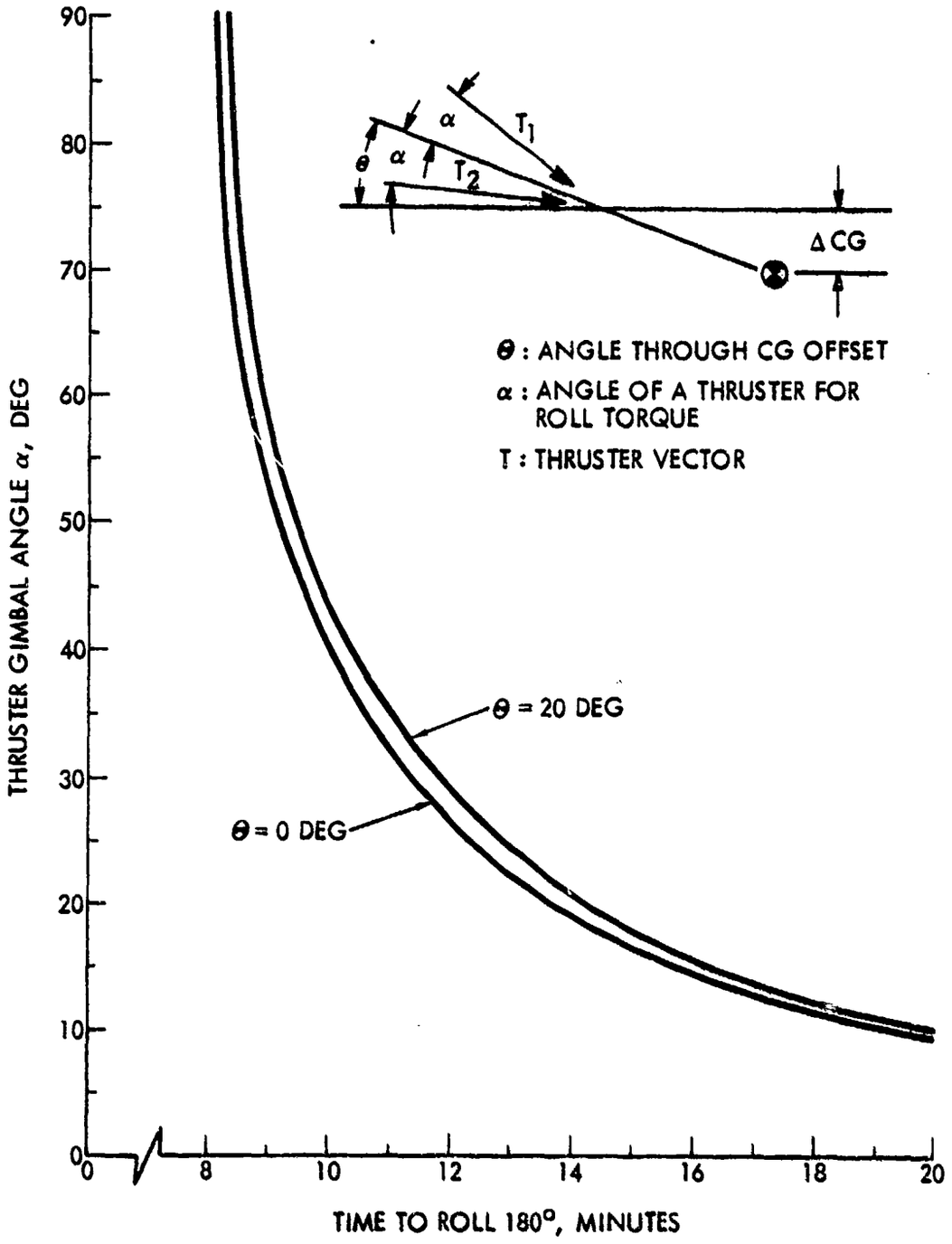

Figure 90. Gimbal Angle Versus Maneuver Time

Baseline Component Identification and Pointing Accuracy Budget

A baseline component identification is shown on Figure 91. This shows a flight computer and interface electronics as the central element of the system through which the remaining components relate to each other and derive their control. The main thruster gimbal drive positions the thrust line of action through the vehicle center of gravity. The collector gimbal drive orients the collectors to the sun. The reaction control system generates torque for altitude changes and to balance disturbance torques. A two-axis sun snesor and two star trackers would provide data to orient the collectors and update the inertial measurement unit, IMU. Tracking data for navigation, telemetry data to and from the vehicle, and commands are processed through the tracking, telemetry, and command, TT&C, component.

A pointing accuracy error budget is shown on Table 13. The budgets for altitude determination and control dynamics are reasonably obtainable values for steady state operation, i.e., maneuver dynamics are not included. The budget for structural and thermal deformation is based on a total pointing accuracy of 0.100 degrees.

Table 13. Pointing Accuracy Error Budget

ERROR SOURCE	REMARKS/BASIS	BUDGET (DEG.)
Attitude Determination	Stellar Aided Inertial System	.01 Deg.
Control Dynamics	Function of Disturbance Levels and Control Bandwidth	.05 Deg.
Structural Deformation Thermal Deformation	Function of Configuration, Structure Design, and Induced Loads	.086 Deg.

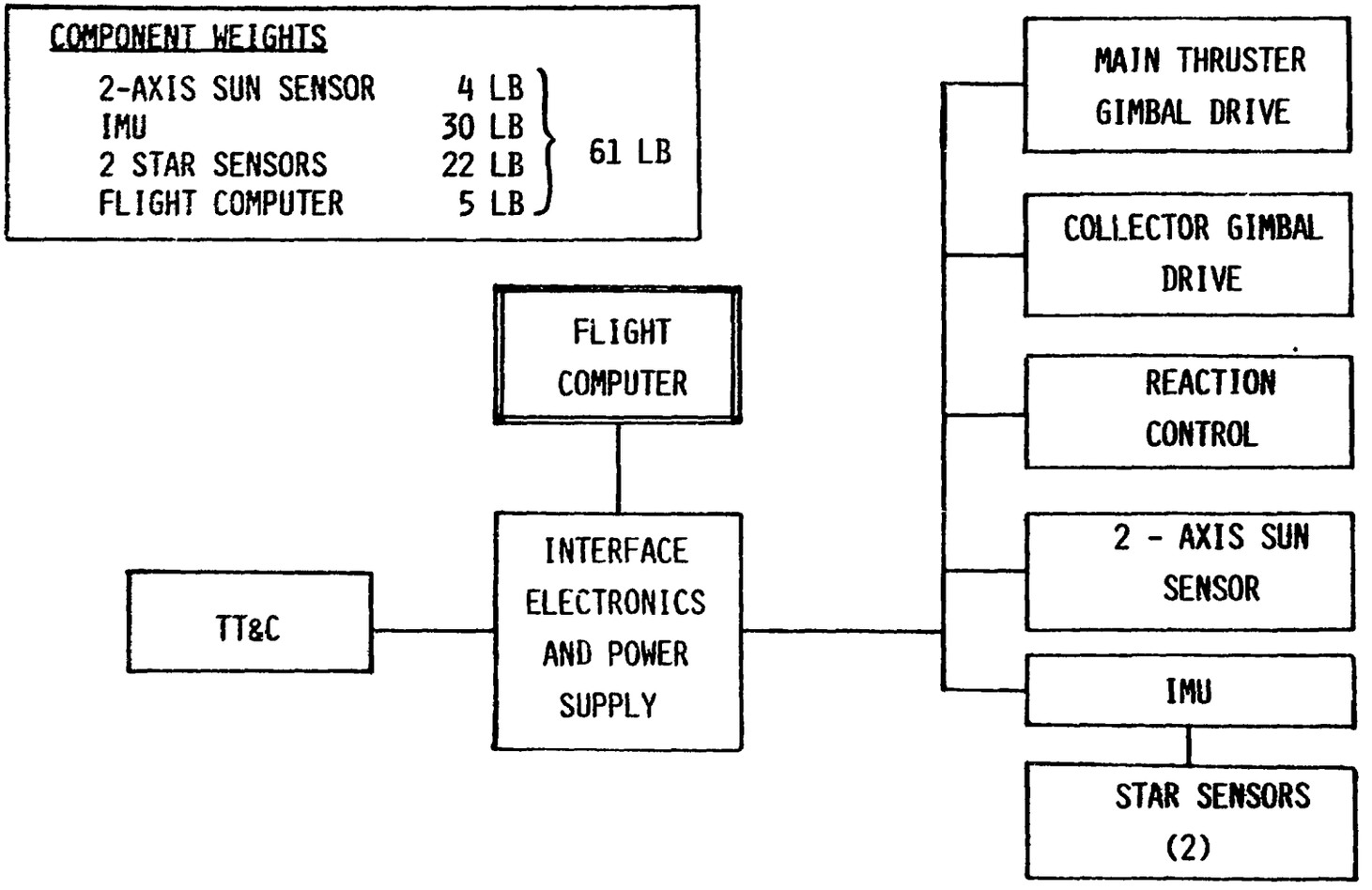

Figure 91. Attitude Control and Determination System

7.0 SPACECRAFT DESIGN

DESIGN CRITERIA

The Solar Rocket System (SRS) propellant tankage and useful payload are assumed to be a single integrated system capable of being launched into Low Earth Orbit (LEO) by Shuttle. Some of the major criteria used for sample system designs include the following:

- Space Shuttle System Payload accommodations, Level II Program Definition and Requirements, Vol. XIV, 3 July 1974 defines launch requirements.
- The representative payload is assumed to be the FLTSATCOM satellite with the apogee kick motor removed.
- Solar collector system to be capable of automatic deployment, being focused and defocused for intermittent or continuous propulsion, acquiring and maintaining accuracy sun pointing, protecting the payload and LH_2 propellant tankage from heat damage.
- Rocket engine thrust vector to have complete freedom of orientation in inertial space.
- Maximum rocket chamber pressure of 50 psia.
- Propellant tankage shall be designed to survive Shuttle emergency landing criteria using solar/electric powered pump feed system of low NPSH* (i.e., LH_2 ullage pressure at optimum value). Tankage shall be insulated and protected from micrometeor damage as required to complete assigned missions.
- Solar collector mass and solar pressure centroids should be coincident with rocket engine thrust vector.

USABLE SPACE SHUTTLE CARGO BAY LENGTH

The propellant volume available is a direct function of the portion of the Space Shuttle cargo bay available for tankage. Although the cargo bay has a nominal length of 60 ft., the Shuttle requires certain length

*Net positive suction head

allocations. Based on these factors, the overall length of the cargo bay available to the solar rocket system is 56.0 ft. This value was used in the preparation of the material presented in Section 8, Parametric Vehicle Synthesis. The rationale behind this selection is based on material found in NASA "Volume 14," parts of which are reproduced below.

"9.5 Reserved EVA Envelope Requirements. Shuttle/Orbiter EVA and rescue requirements dictate that portion of the payload envelope be reserved for EVA* usage, as indicated in Figure 92. Clarifications to these envelopes are as follows:

a. For the inside airlock configuration (area 1-A, Figure 92), the first 48 inches of the cargo bay is required to be clear for EVA access and operation. Payloads which are located in this area must be removable or jettisonable, so that this envelope is available prior to committing to an EVA."

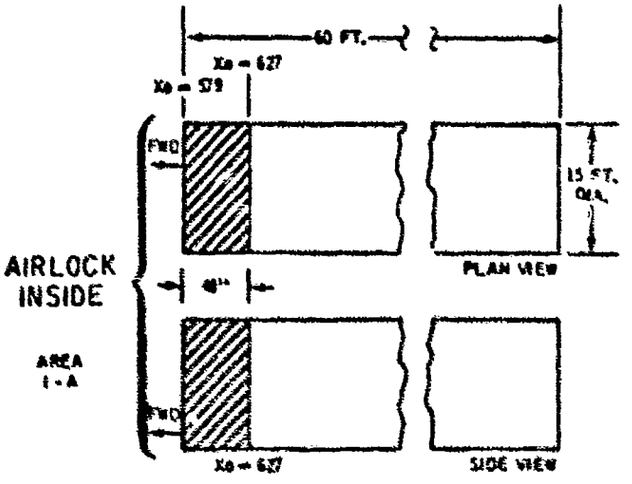

Figure 92. Reserved Envelopes for Forward Cargo Bay Area

*Extra-vehicular activity

As indicated above, a 56.0 ft. cargo bay limitation has been assumed for the solar rocket study. As operational experience with the Shuttle is accumulated, it is expected that changes in the usability guidelines will occur. Future solar rocket studies should monitor these developments with the objective of gaining additional tankage length. For a tank 14.5 ft. in diameter, a 1 ft. increase in the length of the cylindrical section of the tank permits an additional 693 lbs (ullage vol. incl.) of hydrogen to be carried.

A second length constraint is indicated in Figure 93, the c.g./length constraints of the Shuttle. Figure 93 was reproduced from Rockwell document SV79-10, Space Shuttle-Systems Capabilities and Constraints, Feb. 1979.

The center of gravity (c.g.) of all payloads carried in the Shuttle cargo must fall within the cross hatched area of Figure 93. It has been determined that the c.g. requirement is satisfied for all configurations utilizing the 40 ft hydrogen tank. For the high payload cases requiring multiple Shuttle launches, the c.g. for each launch must be checked for compliance with the Figure 93 criteria.

SHUTTLE LAUNCH ANALYSIS

Design criteria for a Shuttle launched solar powered rocket boosted/payload system into low earth orbit (LEO) is dominated by the Shuttle emergency landing criteria. Load factors are presented in Table 14.

Sign convention follows that of the Orbiter coordinate system in Figure 94.

Emergency landing load factors are ultimate. The longitudinal load factors are directed in all aftward azimuths within a cone of 20 degrees half-angle. The specified load factors shall operate separately.

For cargo weight between 32 Klb and 65 Klb, use a linear interpolation between the load factors given.

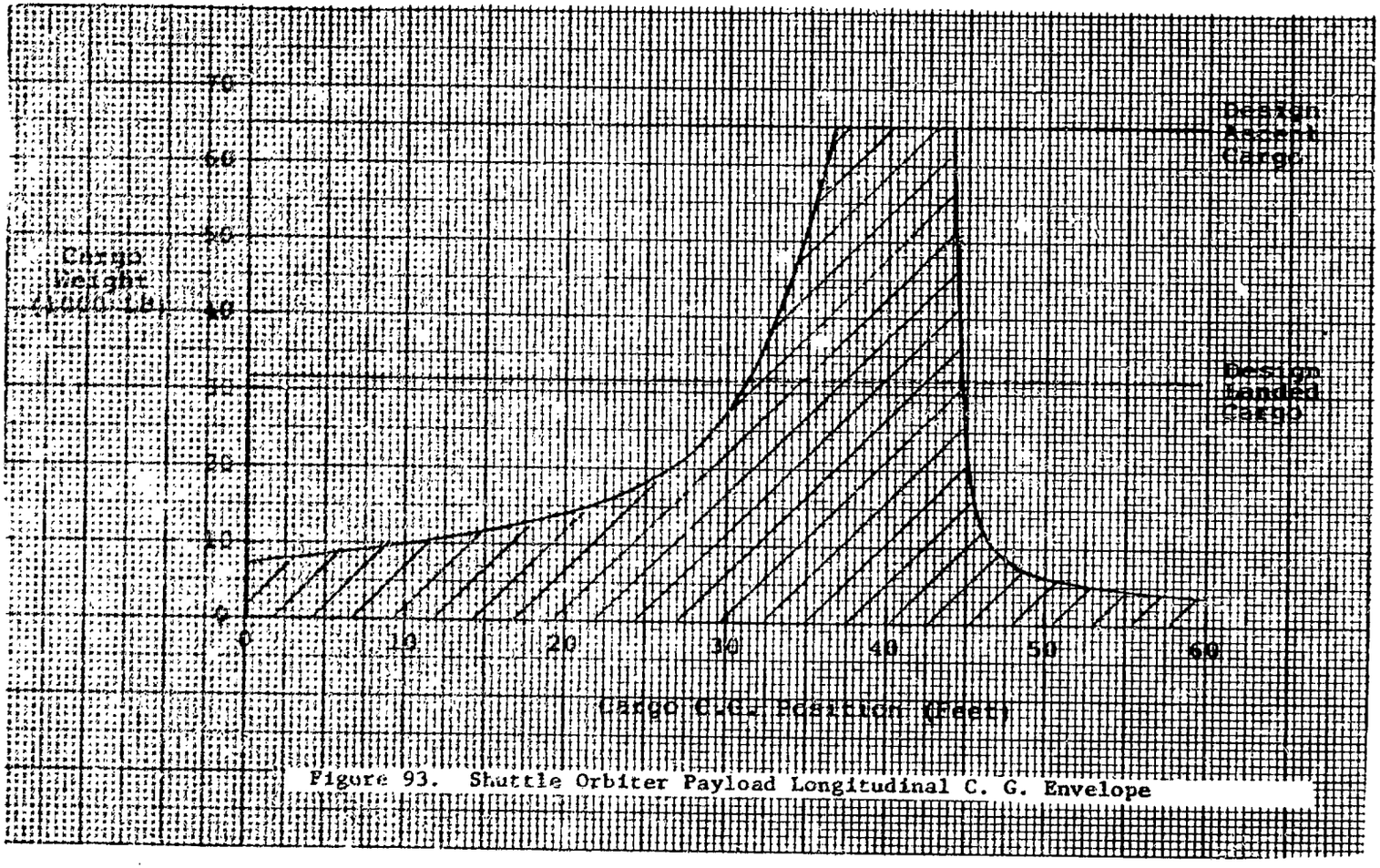

Figure 93. Shuttle Orbiter Payload Longitudinal C. G. Envelope

Table 14. Emergency Landing Design Load Factors

	Load Factor 65 Klb (29484 kg) Up 32 Klb (14515 kg) Down			Load Factor 65 Klb (29484 kg) Down		
CONDITION	X	Y	Z	X	Y	Z
Emergency Landing (Outside Crew Compartment)	+4.5 -1.5	+1.50 -1.50	+4.5 -2.0	+4.50 -0.738	+0.738 -0.738	+2.215 -0.985
Emergency Landing (Inside Crew Compartment)	+20.0 -3.3	+3.3 -3.3	+10.0 -4.4	—	—	—

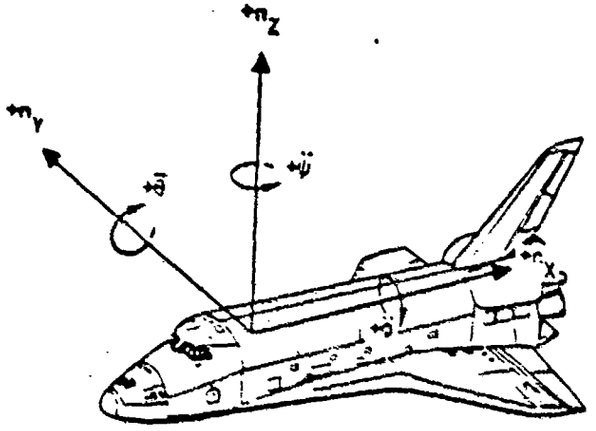

Figure 94. Sign Convention for Cargo Limit-Load Factors/Angular Accelerations

Figure 95 shows a FLTSATCOM and the solar rocket system in a "normal" method of installation on pallets in a Shuttle launch vehicle. As shown, the FLTSATCOM payload is cantelever attached to the LH_2 tank. The tank is then 5 point (redundant) mounted to Shuttle. Figure 96 shows the lg loads diagram.

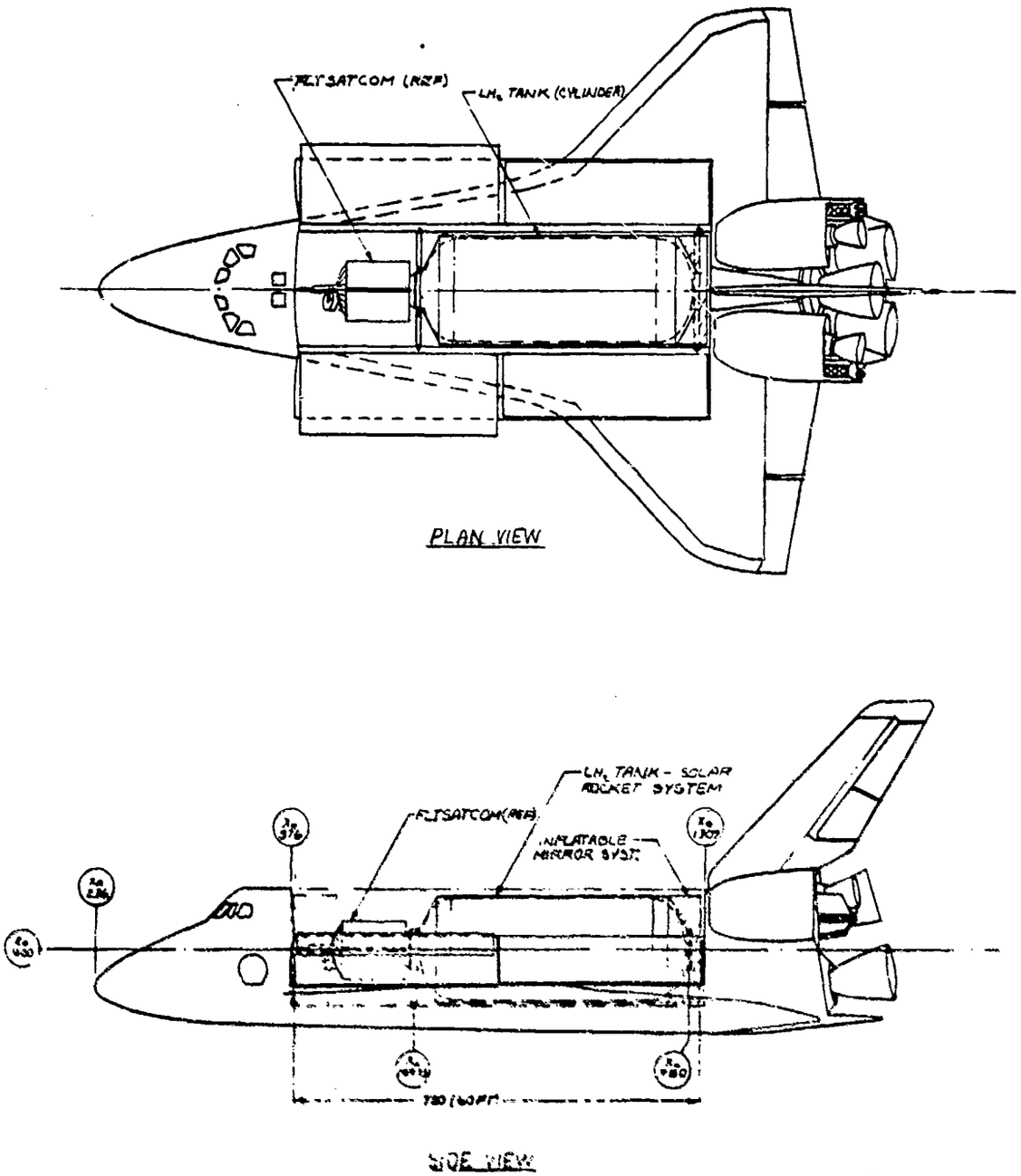

Figure 95. Solar Rocket and FLTSATCOM Installed in the Cargo Bay

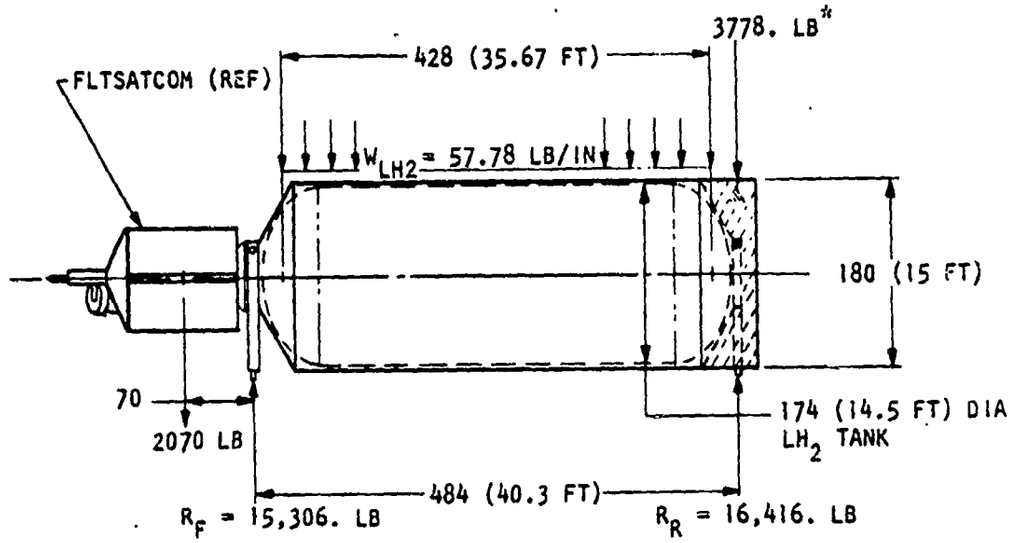

*SRS WEIGHT LESS TANKAGE AND PAYLOAD

Figure 96. 1g Load Diagram

Shear and moment diagrams for N_z = 4.5g emergency landing case are shown in Figures 97 and 98 respectively. A maximum moment of (-) 7,536,100 in-lb is located in X = 317 inch aft of FLTSATCOM MASS CENTROID. During emergency landing, the LH_2 tank will be subjected to the above bending moment plus internal pressure.

For a cylinder under pressure, the hoop stress is,

$\sigma_\theta = \frac{PR}{t}$, and the longitudinal stress is,

$\sigma_\phi = \frac{PR}{2t}$, which permits a bending stress of

$\sigma_M = \frac{MR}{I} = \frac{PR}{2t}$ to be applied.

Internal pressure increases the elastic buckling allowable of an unstiffened cylinder design.

Design allowables for 2219-T86 aluminum which is useful for LH_2 cryogenic tankage is,

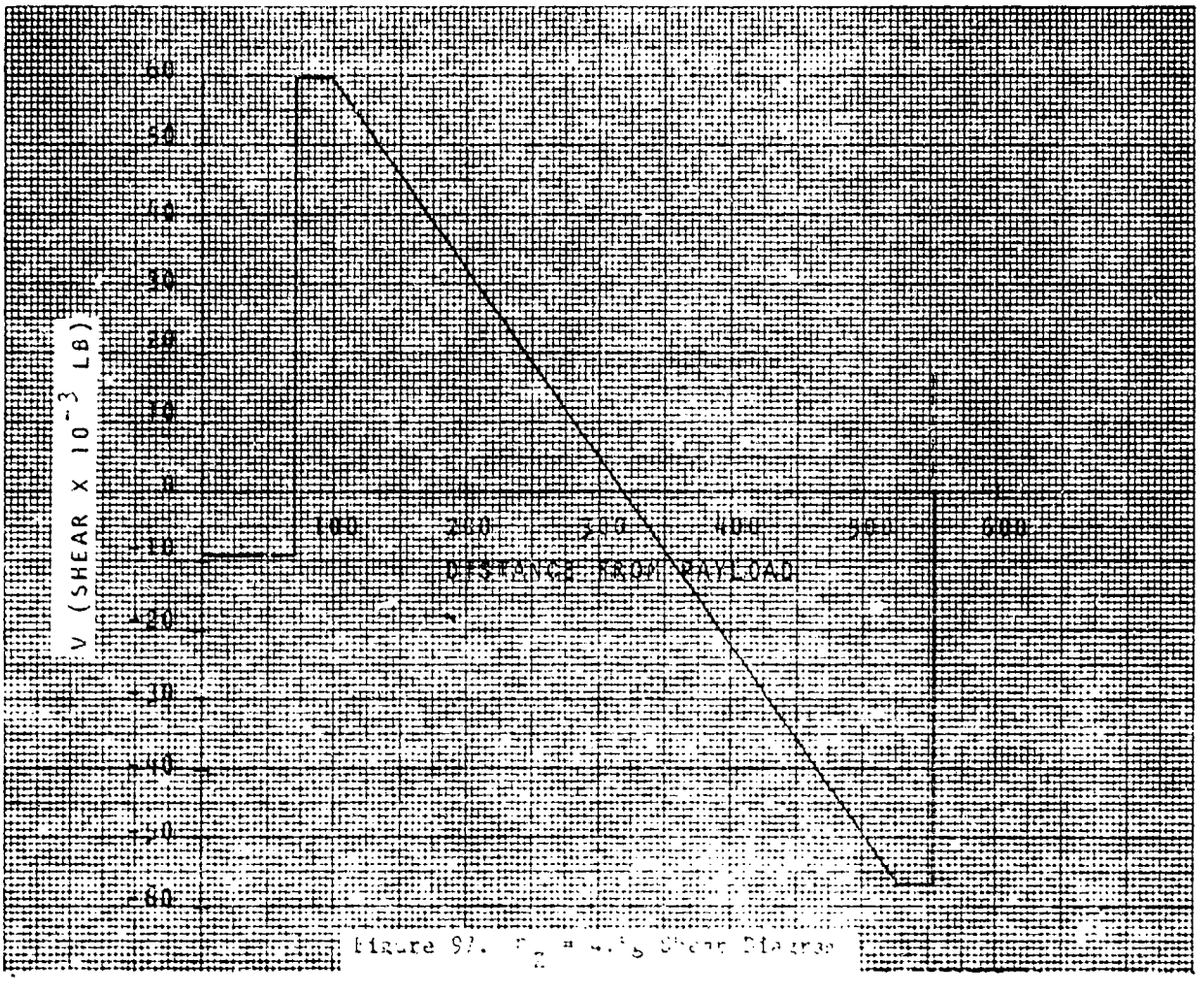

Figure 9?. [illegible] Shear Diagram

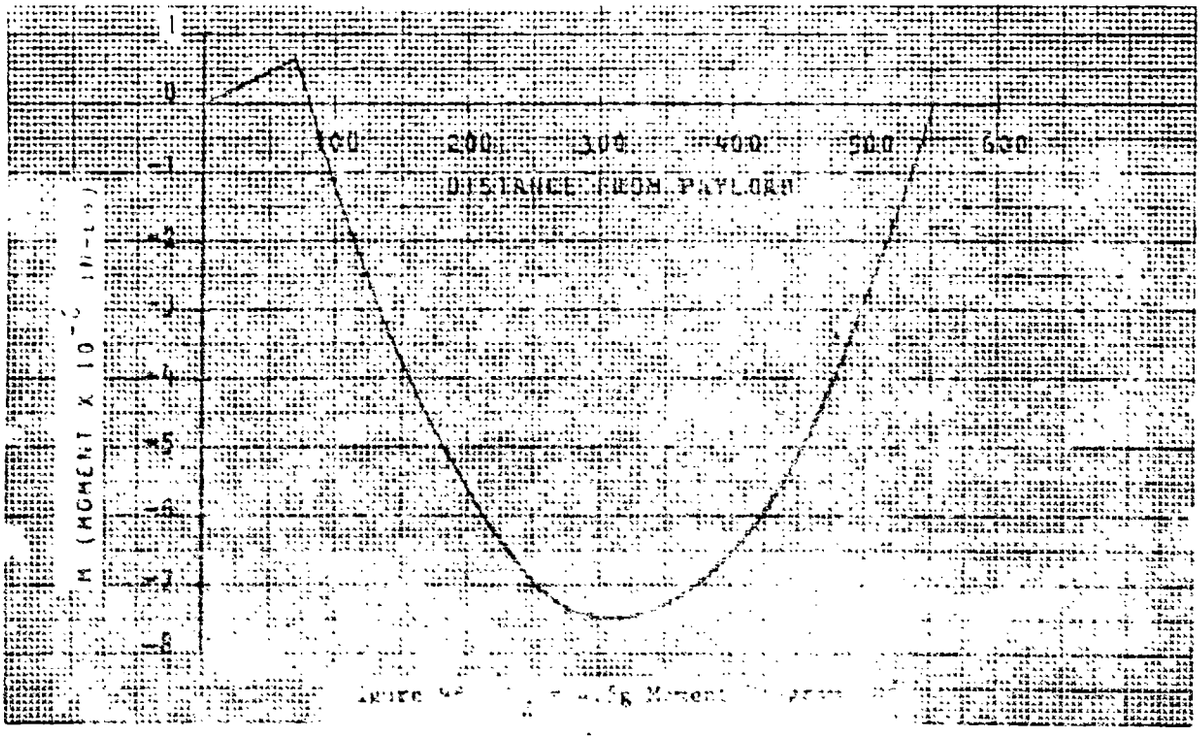

Figure [illegible] Moment Diagram

$$\left(\frac{\sigma}{N}\right)_{TY} \quad (-420^{\circ}F) = 68{,}000. \text{ PSI (TENSION)}$$

$$\left(\frac{\sigma}{N}\right)_{cr} \quad (C_b + \Delta C_b)E \left(\frac{t}{R}\right) \quad \text{(Compression*)}$$

The simultaneous solution of the following equations is required to find the optimum pressure in the LH_2 tank.

(A) $(\sigma_M + \sigma_\phi)$ (TENSILE YIELD) = 68,000. PSI ($-420^{\circ}F$)

(B) $(-\sigma_M + \sigma_\phi)$ (BUCKLING) = $(C_b + \Delta C_b)\ E \left(\frac{t}{R}\right)$

Since the solution of equations (A) and (B) is non-linear, curves of C_b vs. (R/T), Figure 99, and C_b vs. $\frac{P}{E}\left(\frac{R}{t}\right)^2$, Figure 100, from Rockwell Structures manual are included. Iterative solution produces the following results for pump-fed rocket system.

(A) $(\sigma_M + \sigma_\phi)$ = 68,000. PSI (tension)

(B) $(-\sigma_M + \sigma_\phi)$ = (-) 7,350. PSI (compression)

σ_M = 37,630. PSI

σ_ϕ = 30,370. PSI

t (shell thickness) = .0084 in.

P (internal pressure) = 5.878 Psig

For a pressure fed rocket system where the rocket chamber is 50 PSIA, an estimated 5 PSI system pressure drop requires that the LH_2 tank shell thickness becomes:

$$t = \frac{P\ (\text{Factor of Safety})\ R}{\sigma_{TY}}$$

$$t = \frac{55\ (1.5)\ 87}{68{,}000} = .1056 \text{ in.}$$

*Rockwell Structures Manual

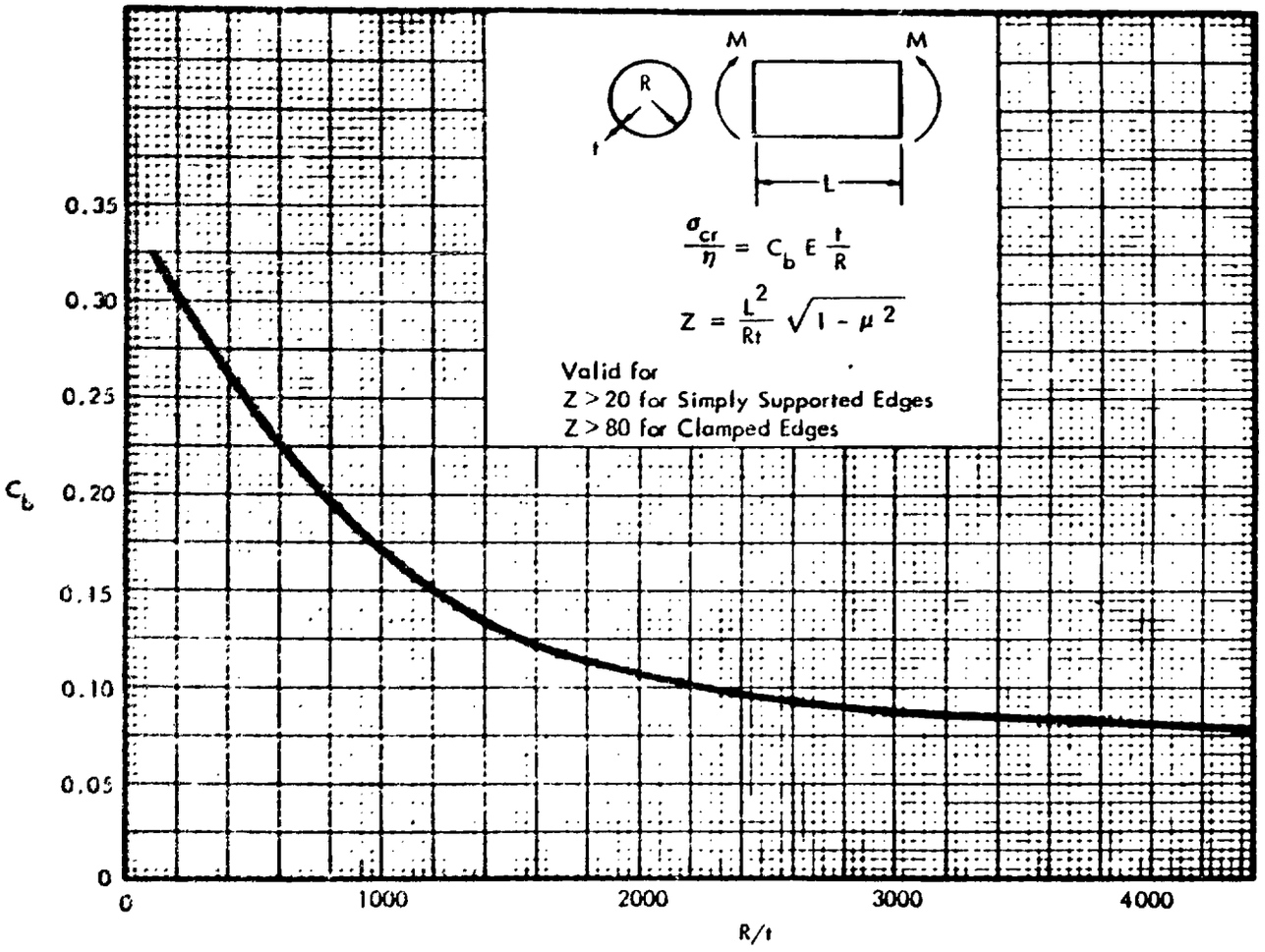

Figure 99. Buckling-Stress Coefficient, C_b, For Unstiffened Unpressurized Circular Cylinders Subjected to Bending

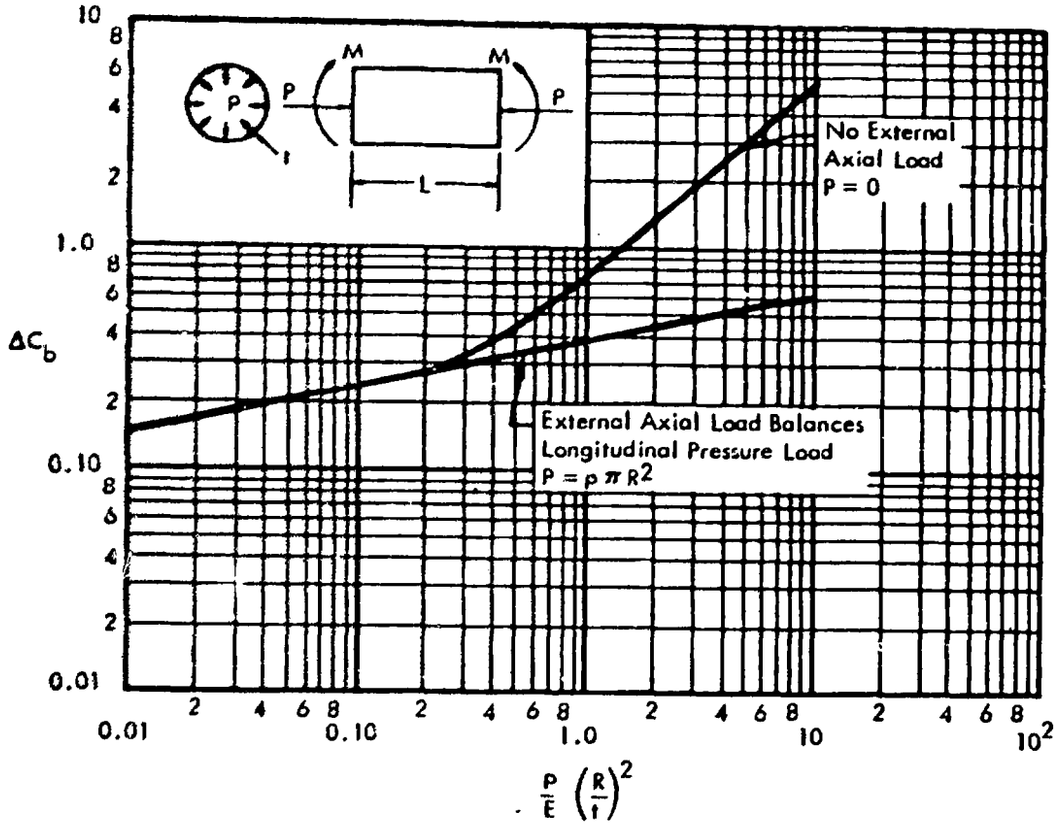

Figure 100. Increase in Bending Buckling-Stress Coefficient of Cylinders Due to Internal Pressure

The above analysis estimates the LH_2 tank design criteria. If a pressure fed rocket system is used, then pressure becomes the design driver. If a pump fed rocket system is used, the emergency landing constraints of Space Shuttle become the design driver.

MAJOR DESIGN CONSIDERATIONS

The long propulsive periods of the SRS requires that propellant tanks be protected against micrometeorites and superinsulated to minimize boiloff. Figure 101 shows a possible method for payload mounting to an LH_2 tank that utilizes insulation as a micrometeorite protection. Structural attachment of FLTSATCOM as a payload and a forward trunion mounting to Shuttle is also identified (FLTSATCOM has been used as a representative example of a SAMSO spacecraft). Fiberglass struts, filled with aluminized plastic microspheres are used to attach the trunion to the tank dome. The aluminized plastic spheres significantly reduce internal-to-strut, end-to-end radiant energy transfer.

COLLECTOR INTEGRATION

A basic requirement of the solar collector system is to maintain a high concentration of sunlight at the engine absorber surface. The concentration ratio achieved affects the temperature and efficiency of the absorber and consequently the size and mass of the collector system required for a given engine thrust.

Section 4.0, "Collector Concept and Performance," describes fully the major critical design factors and types of collector concepts applicable to SRS design. However, the design details of the off-axis, inflatable, non-rigidized collector is summarized in this section.

The initial off-axis collector design shown in Figure 22 utilizes a segment of a paraboloid with an optical angular symmetry of 45 degrees about a line in the latus rectum plane that passes through the Paraboloid focus. Two membranes per collector are used. A transparent membrane and a reflective metallized membrane are fastened together and inflated to form the paraboloidal reflector.

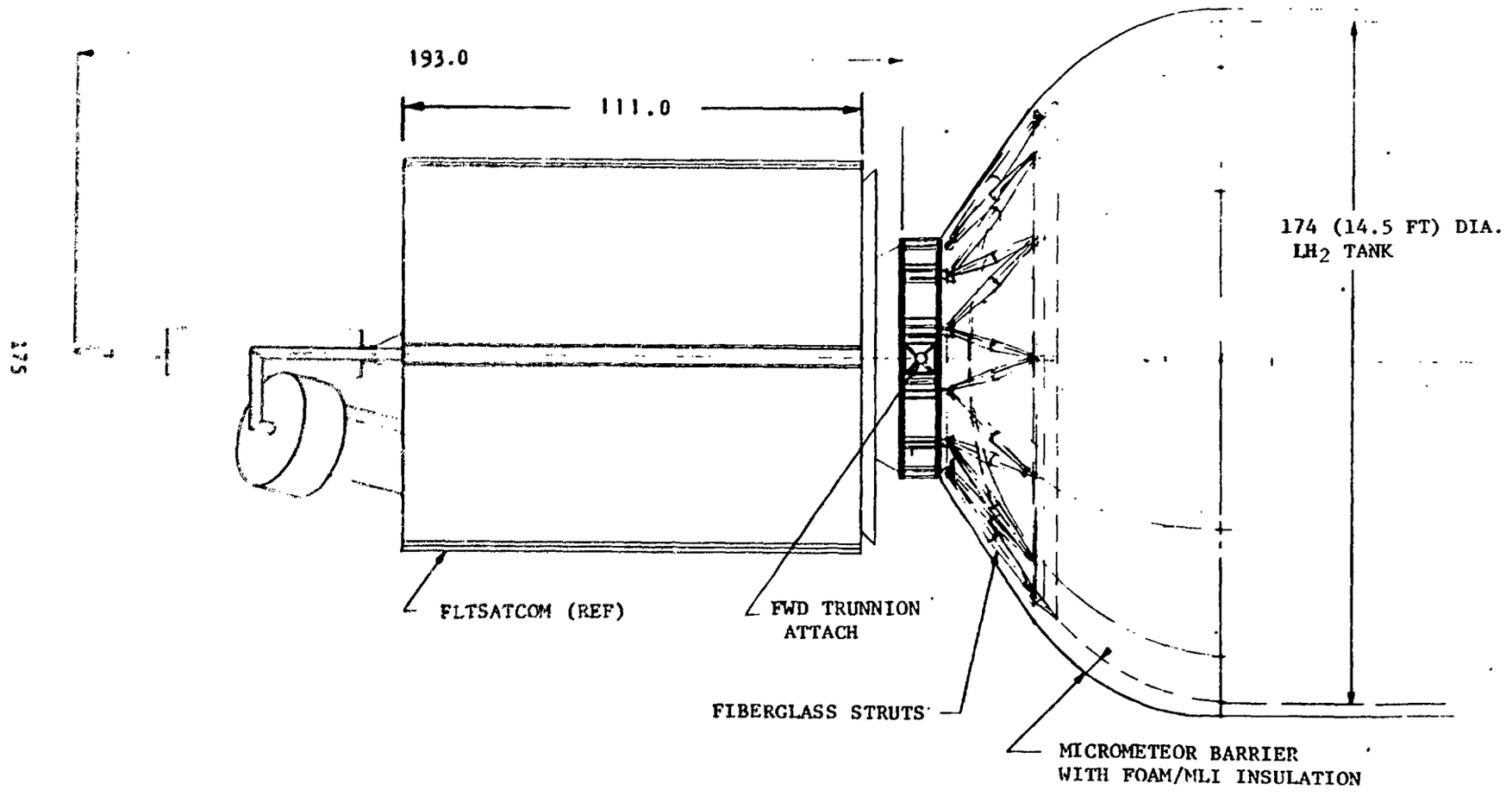

Figure 101. Solar Rocket System Forward Trunnion Attach Detail

The inflated membranes are shape-stabilized by an elliptical toroidal ring. Interior cross cabling (thread like) helps to maintain the elliptical shape. The elliptical boundary and pressure maintain the paraboloid reflector shape. The reason that uniform internal pressure may sustain a paraboloidal shape rather than a sphere is the presence of fixed boundary conditions for the membrane, and a non-uniform film thickness. Fortunately, a cylinder of light from the sun intercepts the paraboloid in a planar-ellipse and subsequently reflects the light to the focal point bounded by a right circular cone. Active figure control can be provided by adjustment of the cross cabling and/or internal pressure. Relative alignment between the two collectors can be accomplished by adjusting the mounting struts for one of the collectors. The collector shown in Figure 22 is connected to the collector gimbal ring located near the focal point with inflatable struts that are reflective coated to minimize thermal damage during solar acquisition. Note that the optical path penetrates the transparent membrane twice. Reflected light has small grazing angles to the transparent membrane which may produce total reflection losses over certain areas of the beam.

Acquiring the sun with a deployed high concentration ratio (CR) collector may prove to be the most difficult collector design problem. As the collector scans towards the sun and the solar image approaches the SRS absorber assembly, the high radiation intensity can destroy tankage insulation, gimbal structure, collector attachment structure, etc. Figure 102 shows one method of how it may be possible to avoid solar image and eliminate grazing reflection angles.

The paraboloid of revolution and right circular cone membranes are inflated, and stabilize by an elliptical torus at the plane of intersection. The paraboloid is reflective coated and functions as a collector. The cone is reflective coated in all areas that do not obscure the solar rays as shown in Figure 102. As the collector scans the sun, the reflected converging cone of light is intercepted before impinging on the spacecraft structure, and like an optical corner cube the light is reflected back out the entrance aperture of the collector. The apex of the cone will require reflective coatings to perform at over 99% efficiency to prevent solar heating

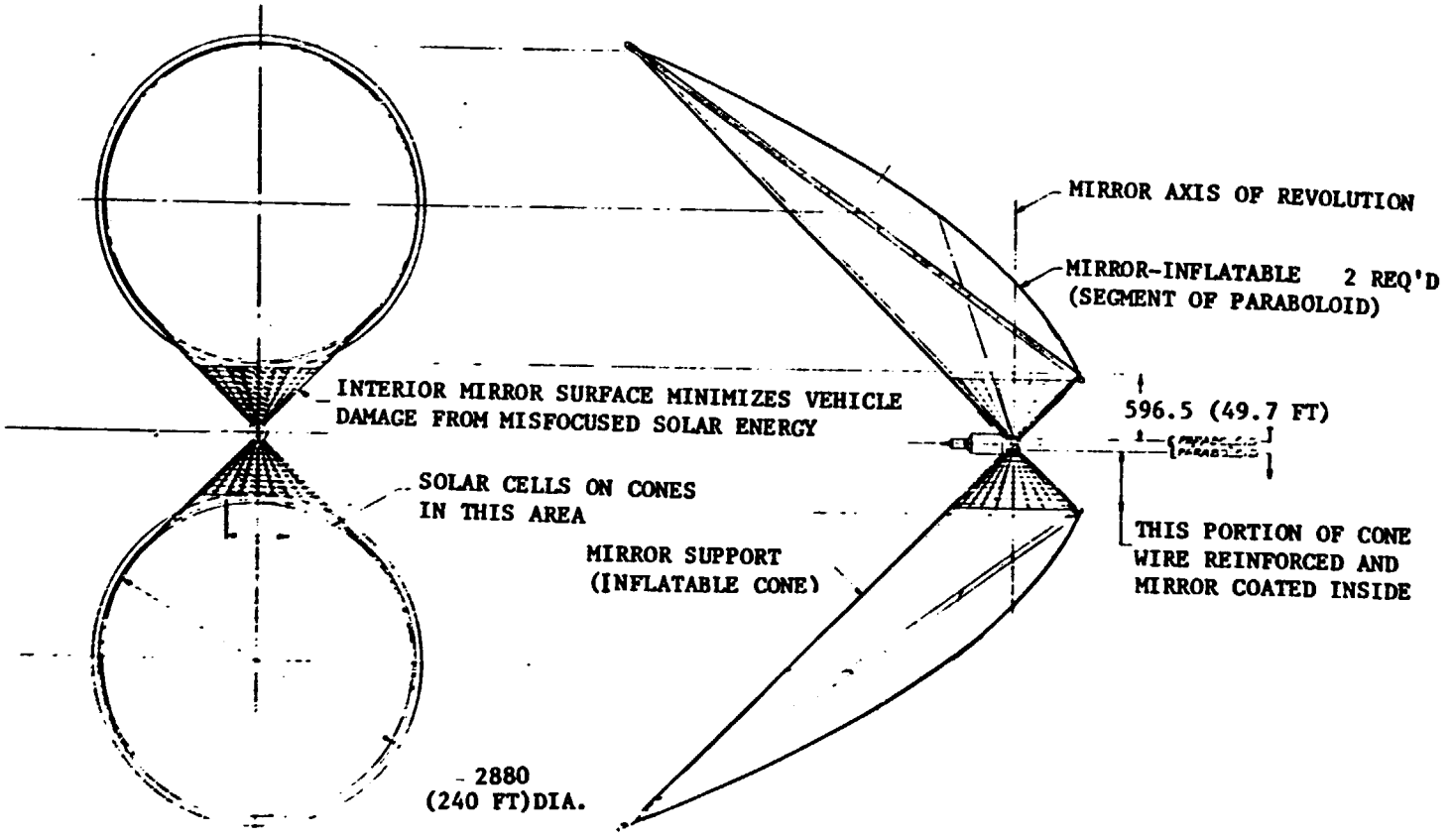

Figure 102. Inflatable Cone/Paraboloid Collector

damage near the absorber. The design of Figure 102 minimizes solar tracking but unfortunately does not have mass or solar pressure balance at all vectors of SRS engine thrust. Figure 103 is a modification of the principles embodied in Figure 102 wherein the mass and solar pressure centroids are located on the mirror axis of rotation. The intersection of the cone to the paraboloid is shifted toward the paraboloid apex until area and mass balance are achieved.

Perigee/apogee burn sequences require some method of diverting or refocusing the collector to prevent energy from reaching the absorber that heats the propellant. Also, a movable reflector or iris may be located several feet away from the absorber where out-of-focus rays are intercepted and reflected to the collector surface and thence into deep space.

The paraboloid figure may have to be closely approximated by spherical segments. If the true view ellipse of Figure 103 is subdivided into an array of circles of varying radii and each circle formed is sealed by a transparent membrane, it would be possible to reproduce the paraboloid closely (even in an optical sense). If, for each sphere formed, the ratio of focal length to segment diameter is greater than 8 to 1, classical optical quality of figure is obtained. The cone and spherical abberration of the sphere becomes insignificant and can be neglected for ratios greater than 8.

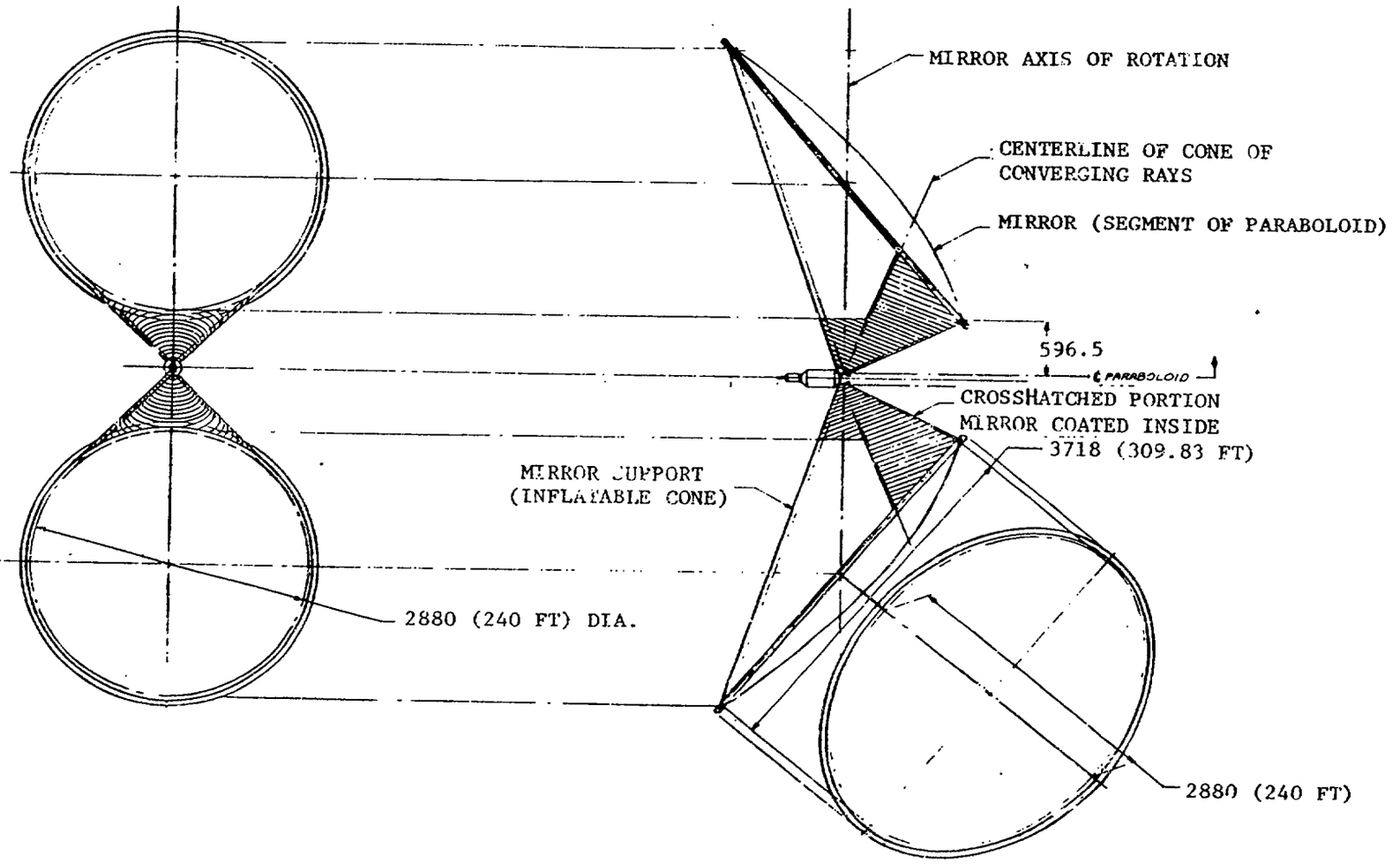

Figure 103. Inflatable Cone/Paraboloid Collector - Collector Mass Centroid on Rotation Axis

EXHAUST PLUME ANALYSIS

An analysis was performed to determine the plume impingement momentum forces and convective heating rates in the free molecular flow regime as a result of operating the hydrogen thruster. The objective of the analysis was to develop iso-pressure and iso-heating rate maps as a function of the spatial distance from the thruster. From these maps, the user may approximate the impingement force and convective heat flux onto a surface (e.g., the solar concentrator) as a result of gas impingement. The purpose of this section is to briefly state the assumptions and describe the method used to present the plume flow field results.

ASSUMPTIONS

1. Free-molecular gas flow, i.e., the Knudsen number >10.
2. The gas streamlines originate from a point source and travel in a straight line and radially outward, i.e., spherical source flow model.
3. The point source (origin) is the intersection of the thruster nozzle centerline and the thruster nozzle exit plane.
4. The exhaust plume mass flux distribution is the same as the one presented in reference 13.
5. The gas velocity is constant in the free molecular flow regime.
6. The mass flux, momentum flux, and convective heating rate flux along a streamline attenuate as the square of the distance from the point source.
7. Free molecular gas flow exists beyond a radius of five feet from the origin.

ANALYSIS

A. Input Parameters

(1) The gas is hydrogen

(2) Engine chamber pressure = 50 psia

(3) Engine chamber temperature = 5000°R

(4) Engine thrust = 10 lbf

(5) Maximum specific impulse is 1255.3 lbf-sec/lbm

B. Determination of Free Molecular Flow Regime Thruster Exhaust Gas Limiting Velocity

$$V_{lim} = \sqrt{2\, g_c\, C_p T_c\, 778} \qquad (1)$$

From reference 14, the specific heat at constant pressure (C_p) is 8.304 BTU/lbm-°R for shifting equilibrium and 4.345 BTU/lbm-°R for frozen equilibrium for hydrogen at 50 psia and 5000°R. A specific heat value of 8.304 BTU/lbm-°R was selected to be conservative in the impingement pressure and heat flux results. Consequently,

$$V_{lim} = \sqrt{2(32.17)(8.304)(5000)(778)}$$

$$V_{lim} = 45588.9 \text{ ft/sec } (13895.5 \text{ m/sec})$$

C. Determination of Thruster Mass Rate

$$\dot{m} = \frac{F}{Isp} = \frac{10}{1255.3} = 7.9664 \times 10^{-3} \text{ lbm/sec} (3.6135 \times 10^{-3} \text{ Kg/sec}) \qquad (2)$$

D. Free Molecular Exhaust Plume Mass Flux Distribution

From reference 1, the mass flux per steradian is:

$$\frac{d\dot{m}}{d\Omega} = r^2 \rho V = e^D \qquad (3)$$

where $D = ([A_4\theta + A_3]\theta + A_2)\theta^2 + A_o \qquad (4)$

The coefficients A were considered functions of chamber pressure and the streamline angle, θ, measured from the nozzle centerline. With the engine chamber pressure assumed to be 50 psia (3.4023 atmospheres) and a thruster flow rate of 7.9664×10^{-3} lbm/sec (3.6135×10^{-3} Kg/sec), the resulting coefficients were:

$$A_o = 1.123 \ln P_c - 6.0338 \quad (5)$$

$$A_2 = -1.715 \ln P_c - 12.69 \quad (6)$$

$$A_3 = 1.327 \ln P_c + 13.24 \quad (7)$$

$$A_4 = -0.234 \ln P_c - 4.201 \quad (8)$$

For other mass flow rates, only the constant in the "A_o" term changes. The constant is obtained by integrating equation (3) from 0 to π radians and varying the A_o constant until the desired mass rate is obtained, i.e.,

$$\dot{m} = \int_o^{\pi} \left(\frac{d\dot{m}}{d\Omega}\right) d\Omega = \int_o^{\pi} \left(\frac{d\dot{m}}{d\Omega}\right) 2\pi \sin\theta \, d\theta \quad (9)$$

For example, $\dot{m} = 7.0565 \times 10^{-3}$ lbm/sec (3.2008×10^{-3} Kg/sec) at an engine chamber pressure of 50 psia (3.4023 atmospheres), $A_o = 1.123 \ln P_c - 6.1578$ or $A_o = -4.7827$

E. Momentum Flux Determination

The momentum flux is another way of describing the total impingement pressure available to a surface. Thus:

$$P = \rho V^2 = V_{lim} \frac{e^D}{r^2} \quad (10)$$

Equation 10 has no correction factor for true angle of incidence (true gas streamline impingement angle) or energy accommodation coefficient. It is the correct form of impingement pressure on a flat plate whose surface is normal to the streamline in question and whose energy accommodation coefficient is unity. For infor-

mation on gas streamline true impingement angle and accommodation coefficients, refer to Reference 13.

A map of curves of constant-momentum forces per unit area can be generated as shown in Figure 104. With the use of Equation 10, the product of impingement pressure (P) and the radius distance squared (r^2) can be obtained, i.e., $Pr^2 = V_{lim}\, e^D$. Note that the mass flux (Eq. 3) is in metric units (radians, atmospheres, and Kg/sec) and the resulting force will be in Newtons per steradian if the velocity is in meters/sec. Table 15 presents the values used in the development of Figures 104 and 105. However, the parameters were converted into English units.

Table 15. Momentum and Energy Flux per Steradian

Streamline Angle (Degrees)	$P\ r^2$ (lbf Per Steradian)	$\dot{Q}\ r^2$ (BTU per Steradian - sec)
10	20.3364	1191.6623
20	8.5984	503.8473
30	3.0952	181.3714
40	1.1872	69.5650
50	0.5494	32.1953
60	0.3144	18.4245
70	0.2063	12.0900
80	0.1303	7.6331
90	0.0601	3.5207

By selecting the desired impingement pressure, the distance from the point source (see assumption No. 3) on the streamline will be determined, thus:

$$r = \sqrt{\frac{P\ r^2}{p}}\ , \text{ feet}$$

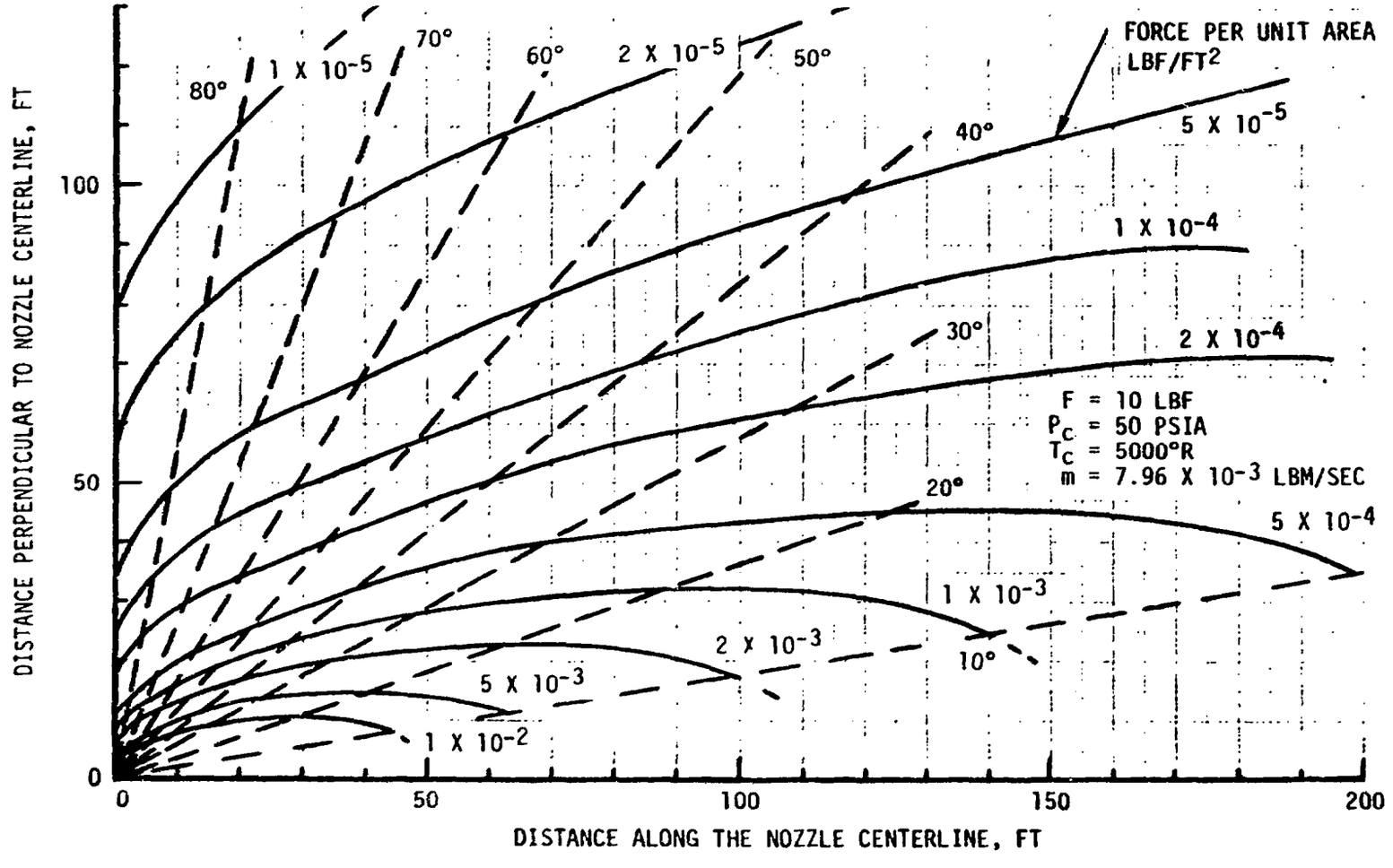

Figure 104. Hydrogen Thruster Exhaust Plume Impingement Momentum Force Per Unit Area Isobars

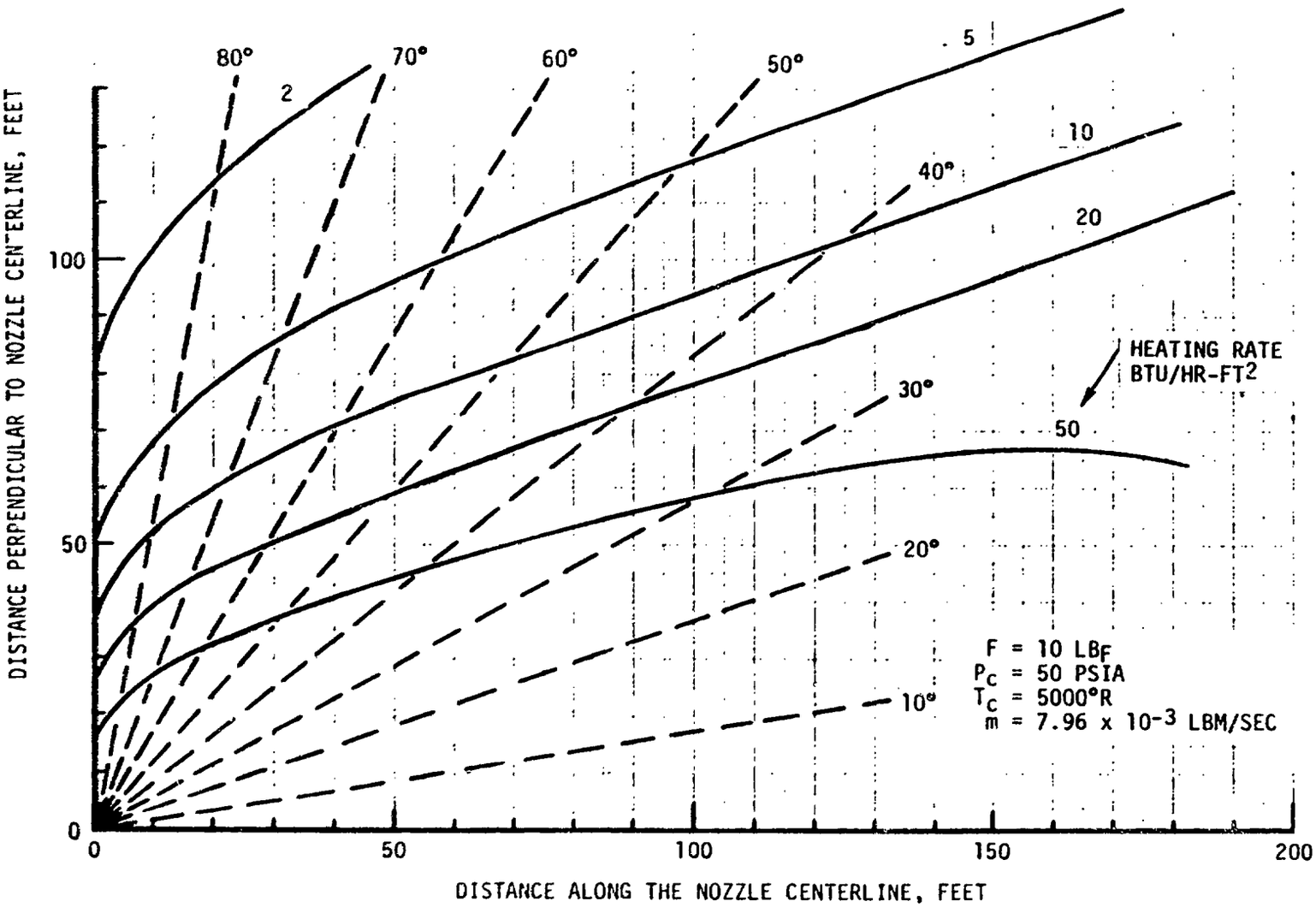

Figure 105. Hydrogen Thruster Exhaust Plume Impingement Heating Rate Isobars

and

$$X = r \cos\theta$$

$$Y = r \sin\theta$$

Example:

$P = 1 \times 10^{-4}$ lbf/ft^2 on the streamline where

$\theta = 40^\circ$

$$\therefore r = \sqrt{\frac{1.1872}{1 \times 10^{-4}}} = 108.96 \text{ feet}$$

and $X = 108.96 \cos 40^\circ = 83.47$ feet

$Y = 108.96 \sin 40^\circ = 70.04$ feet

The point should be 108.96 ft. from the origin on a line whose angle is 40 degrees from the nozzle centerline (x-axis), i.e., 83.47 feet in the x-direction (along the nozzle centerline) and 70.04 feet in the y-direction (distance perpendicular to the nozzle centerline). By repeating this process for different streamline angles, a loci of points for $P = 1 \times 10^{-4}$ lbf/ft^2 will be generated. Thus, the curve of constant pressure is generated. The process is repeated for other impingement pressures.

F. Convective Heat Transfer

The heat flux onto a surface can be approximated by the total energy available in the thruster exhaust plume:

$$\dot{Q} = \rho V^3 = V_{lim}^2 \left(\frac{e^D}{r^2}\right) = PV_{lim}/778 \qquad (11)$$

The discussion in Section E about the true impingement angle and energy accommodation coefficient presented for the momentum flux applies to the energy flux.

A map of curves of constant energy flux per unit area is shown in Figure 105. The method used to develop Figure 105 is the same as Figure 104 ($\dot{Q}r^2 = V_{lim}^2 e^D$). From Table 15, obtain $\dot{Q}r^2$.

Thus:

$$r = \sqrt{\frac{V_{lim}^2 e^D}{\dot{Q}}} \qquad (12)$$

G. Nomenclature

Symbol	Description	Units
A_o	Term in mass flux Equation, (see Eq. 5)	-
A_2	Term in mass flux Equation, (see Eq. 6)	-
A_3	Term in mass flux Equation, (see Eq. 7)	-
A_4	Term in mass flux Equation, (see Eq. 8)	-
D	See Equation (4)	-
Cp	Specific heat at constant pressure	cal/gm-^oK or BTU/lb-^oR
F	Force	Newton or lbf
g_c	Gravitational constant = 32.17	lbm-ft/lbf-sec^2
Isp	Specific impulse	lbf-sec/lbm
$\dot{m}$	Gas Mass Flow Rate	Kg/sec or lbm/sec
P	Gas Pressure	Newton/m^2 or lbf/ft^2
P_c	Engine Chamber Pressure	Atmospheres or psia
$\dot{Q}$	Convective Heat Flux	BTU/sec-ft^2
r	Distance from origin to impingement point	meters or feet
T_c	Engine Chamber Gas temperature	^oR
V	Gas velocity in free molecular flow	m/sec or ft/sec
V_{lim}	Limiting gas velocity in free molecular flow	m/sec or ft/sec
X	Distance along the nozzle centerline	feet
Y	Distance perpendicular to nozzle centerline	feet
θ	Streamline Gas flow angle	radians or degrees
ρ	Gas density	Kg/m^3 or lbm/ft^3
Ω	Solid angle	steradian
$\frac{d\dot{m}}{d\Omega}$	Mass flux per steradian	Kg/sec-steradian

8.0 VEHICLE SYNTHESIS AND PERFORMANCE

The parametric analysis of the solar rocket system was achieved using the "Solar Thermal Orbital Propulsion-Computerized Unmanned Spacecraft Synthesis" program (STOP CUSS). This program allows the investigation of various design and subsystem parameters and how these parameters affect the overall vehicle performance. Several algorithms were developed which adequately describe the size, weight and performance of the major subsystems affecting vehicle performance.

A subsystem synthesis approach provided a determination of the requirements of each subsystem consistent with the overall vehicle characteristics and mission requirements. Since there is no closed form solution, an iterative method was adopted. The iterative logic and its elements are shown in Figure 106.

The major structural elements of the propulsion stage are the propellant tankage, the solar collector components and the thruster system. Weight allowances must be assigned to each of these major elements to account statistically for the secondary structure and ancillary equipment. Each of the structural components is divided into its element models, each element is defined analytically, and a preliminary design synthesis is conducted on the individual elements to identify minimum weights for feasible designs. An appropriate set of scaling laws were derived for each element. Combination of these scaling laws will provide a relationship for the major components. A correlation factor (non-optimum weight, etc.) is applied to these laws based on historical data pertinent to the type of material, construction, and complexity of the component.

The synthesis approach starts with the sizing of the tanks to contain the propellant used for propulsive changes in the vehicle's orbits, (LEO-to-GEO, etc.) and the propellant that will boil-off during the longer trip times. The heating rate and total heat input throughout the various mission trajectory segments will influence the propellant boiled-off.

The quantity of propellant boil-off is a function of the vehicle's thrust-to-weight (hence trip time), the surface area of the tank(s) exposed to the thermal environment and the tank insulation concepts.

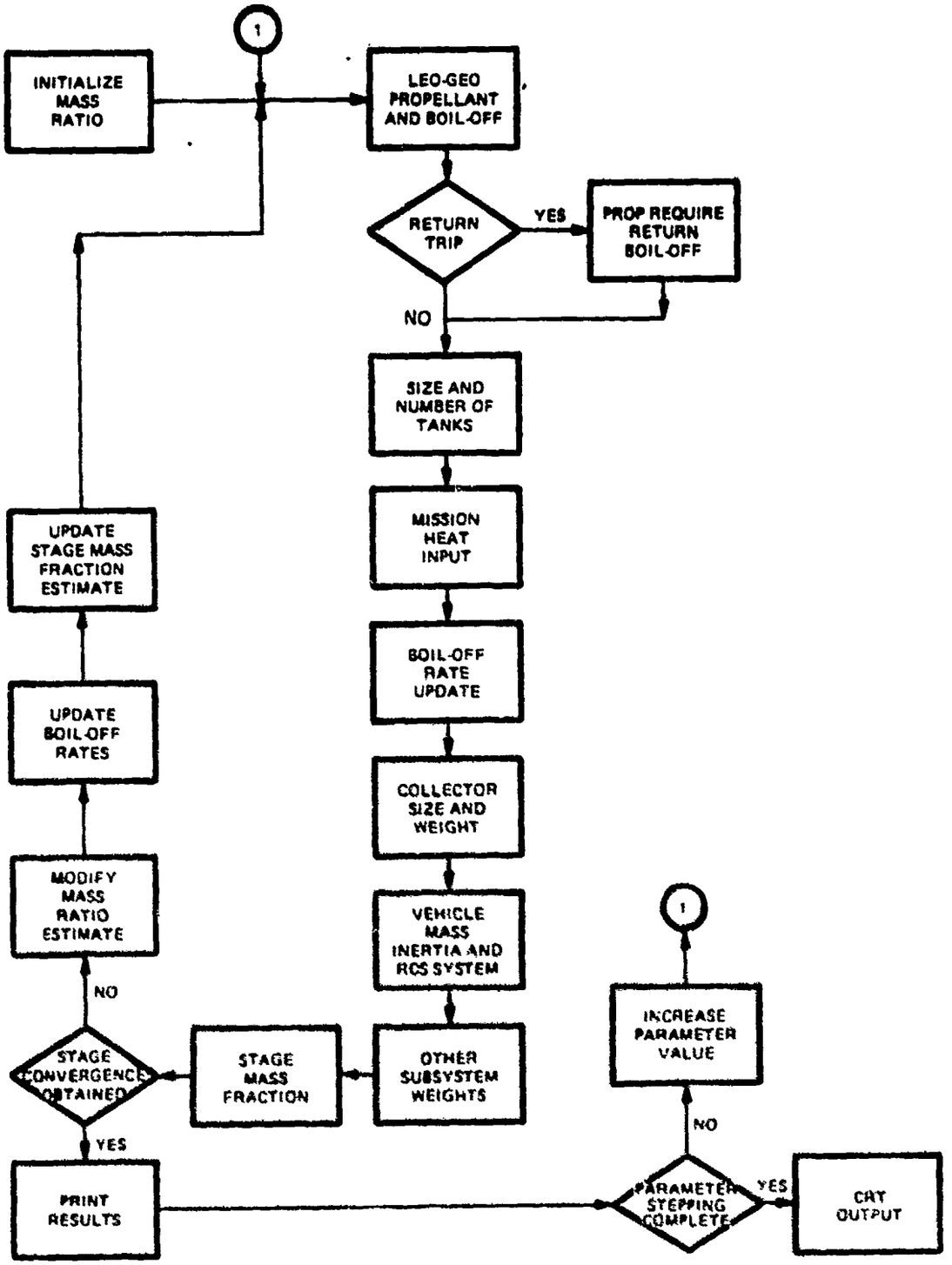

Figure 106. Subsystem Synthesis Logic

Sizing and number of propellant tanks employed for the large payload designs are dictated by the Shuttle Orbiter's cargo bay physical limitations.

The weight modeling consists of the derivation of the parametric equations that describe the structural weight of the stage in terms of its various components for a range of propellant combinations, loading environments, and for specific geometries.

The components investigated included:

1. Bulkheads
2. Cylindrical Tank Wall
3. Solar Collectors
4. Thruster System
5. Reaction Control System

The structural shells of the propulsion stage are a major contributor to the stage's inert weight. Improved weight-scaling laws defining the structural contribution must differentiate between the effects of stage diameter, loading environment, types of construction and materials. Weight data for the structural shells were obtained from Reference 15.

The solar collectors are described with respect to the engine thrust load and the type of thruster concept. The size of the collectors will contribute significantly to the vehicles inertia. The propellant requirements and weight algorithm for the reaction control system is a function of the vehicle's inertial, frontal projected area and mission duration.

The vehicle's remaining subsystems were considered with simplified weight algorithms in order to compute the stage mass fraction. The synthesis program systematically updates the mass fraction estimate with its computed value to derive a stage description which is consistant with the mission performance and environment requirements, Figure 106.

The STOP CUSS program output provided a summary weight statement for the vehicle's subsystems and propellant masses as shown in Figure 107. Also provided were pertinent descripture characteristics relating to the vehicle and the type of mission. Figure 107 shows these characteristics in five groupings. The first group being mission data, describing the velocity requirement, the LEO-to-GEO flight duration, and the amount of payload returned if the mission was a two-way trip. There were three types of missions

Summary Weight Statement

STRUCTURE AND MECHANISMS
PROPULSION SYSTEM
  THRUSTER
  SOLAR COLLECTION SYSTEM
    CONCENTRATOR
    ABSORBER
    HEAT TRANSFER SYSTEM
    INSULATION
  PROPELLANT SYSTEM
    TANK(S)
    INSULATION
THERMAL CONTROL
ATTITUDE CONTROL
  RCS
  ATTITUDE REF DETERMINATION
ELECTRICAL POWER AND DISTRIBUTION
  PHOTOVOLTAIC ARRAY
  ORIENTATION AND ACTUATION
  BATTERY AND STORAGE SYSTEM
  POWER TRANSMISSION AND CONDITIONING
NAVIGATION
T & C
INFORMATION MANAGEMENT & CONTROL
    TOTAL,SPACECRAFT DRY LESS GROWTH
      GROWTH
    TOTAL,SPACECRAFT DRY WITH GROWTH
RESIDUAL PROPELLANT
    STAGE BURN OUT
PROPELLANT-USABLE
    STAGE LAUNCH
PAYLOAD
VEHICLE IGNITION

STAGE MASS FRACTION(LESS P/L)

Vehicle System Characteristics

NUMBER OF STAGES	
PAYLOAD FRACTION RETURNED	
FLIGHT TIME	DAYS
VELOCITY REQUIREMENTS	FT/SEC
ENGINE	
THRUST LEVEL	LBF
WEIGHT	LBS
THRUST TO WEIGHT	
COLLECTOR DIAMETER	FT
TANK CHARACTERISTICS	
RADIUS	FT
WALL LENGTH	FT
OVERALL LENGTH	FT
SURFACE AREA	SQ FT
BULKHEAD ASPECT RATIO	
NUMBER OF TANK SETS	
TANK ENVIRONMENT	
MINIMUM PRESSURE	LB/SQ FT
OPERATING PRESSURE	LB/SQ FT
PRESSURE BURST FACTOR	
LATERAL ACCELERATION	
LONGITUDINAL ACCELERATION	
THERMAL DATA	
ABSORPTIVITY RATIO	
REFLECTIVITY RATIO	
EQUILIBRIUM WALL TEMPERATURE	R
UNIT HEAT FLUX	BTU/HR/FT2
TOTAL HEAT FLUX	BTH
INSULATION THICKNESS	FT
INSULATION WEIGHT	LB

Figure 107. STOP CUSS Program - Typical Output Data

considered, these being a one way trip from LEO to GEO (i.e., expendable vehicle), two way trip return empty (recoverable vehicle with expendable payload) and a fully recoverable mission (vehicle and payload).

Other grouping of vehicle data shown on Figure 107 are related to the engine system, tank geometry, tank design loading environment and the thermal data causing propellant boil-off.

SUBSYSTEM SYNTHESIS

The following will be a short description of the sizing and weight algorithms employed in the STOP CUSS program. The coefficients of some models were dependant on actual design concepts and were adjusted during the program execution.

Structural Tank Modeling

The tank units are constrained to fit within the Shuttle Orbiter cargo bay. Therefore, maximum tank size is limited to 14.5 ft diameter and 55 ft long. These tank sets are arranged in modular form (when required) to provide the tankage for the heavy payload vehicles for mission from low earth orbit (LEO) to geosynchronous earth orbit (GEO) and return. For the vehicle concept with smaller payloads which require a single Shuttle flight, the tank length is limited to 40 ft. This allows sufficient space in the cargo bay to carry the payload, engine subsystem and the packaged collectors in the single Shuttle flight.

The tanks are sized to allow for an ullage volume of 5% and a 3/4% for residual propellant and gases. The skin thickness for the tanks withstand the stresses induced by the launch loads and the tank operating pressures of 22.0 psi. The orbiter limit loading conditions considered were the landing loads of 3.0g lateral and 1.5g longitudinal and the tank being suspended from either end using the cargo bay's bridge fittings for a three point loading condition with one end floating to allow for fore and aft differential expansion.

Design loading for the tank structural elements are considered for earth launch conditions. Compressive load intensities are due to:

1. Axial loads caused by maximum longitudinal acceleration during earth launch when the stage is carried into orbit by the Shuttle.

2. Body bending if the stage is subjected to lateral accelerations during ascent. The Orbiter transportation to orbit will influence the lateral forces; reaction loads from support cradles if carried in the cargo bay of the reusable space shuttle vehicle.
3. Engine thrust loads during space operation of the stage or parent vehicle system. These thrust loads will be negligible when compared to the Shuttle ascent conditions.

Tank pressure loading conditions will be traded-off for the best consideration to preclude buckling, restrain boil-off while at the same time provide optimum stage performance.

Exacting data from design synthesis programs considered the structural strength and stiffness requirements resulting from compressive and pressure design criteria. Instability failure modes considered are panel buckling of the skin and stiffener elements, and column buckling and general shell instability. Information is available for several different types of construction for a range of shell diameters, internal pressures and design loading environments. Figure 108 shows structural weight data for a typical aluminum skin-stringer tank wall for a range of loading intensities and internal tank pressure. The resulting weight scaling data derived from this structural weight data is as follows:

The unit weight for pressurized tank walls is

$$W_{tank} = \frac{K_1 P R}{\sigma} + K_2 N_x^{K_3} R^{K_4} P^{K_5} \left(\frac{E}{10^6}\right)^{K_6}$$

where

N_x = compressive load intensity
σ = material working stress
E = Young's Modulus of the material
R = shell radius

Values of the coefficients for aluminum tanks and different types of construction are shown in the table below:

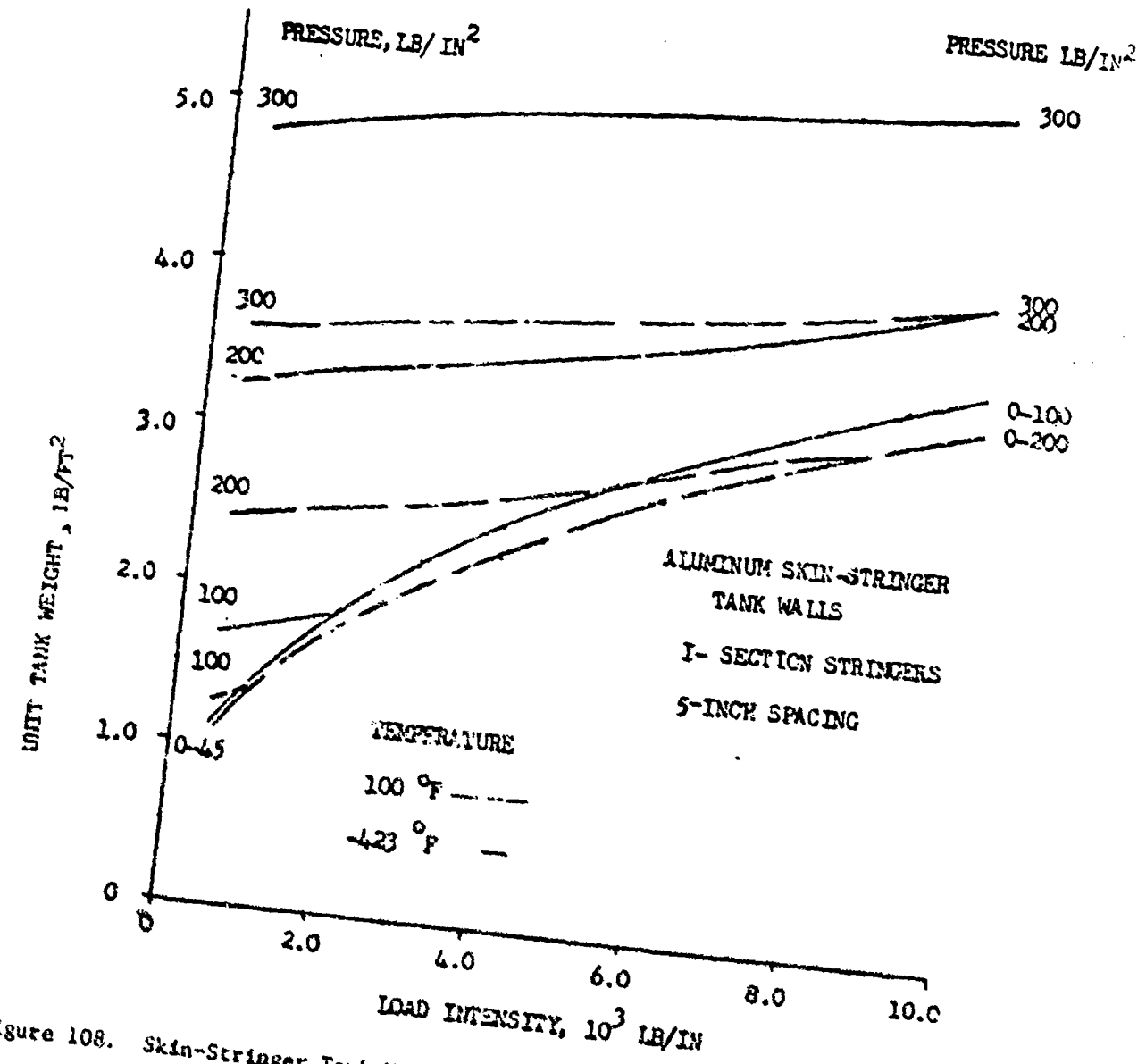

Figure 108. Skin-Stringer Tank Wall Unit Weight for Pressurized Aluminum Tanks

Construction	K_1	K_2	K_3	K_4	K_5	K_6
I Skin Stringer	10.40	0.332	0.533	0.778	0	-3.00
Hat Skin Stringer	10.40	0.350	0.533	0.778	0	-3.00
Waffle	10.40	0.0216	0.650	0.778	0	-3.00

The working stress is obtained from the material's ultimate stress Ft_u and yield stress Ft_y.

$$\sigma = \text{Min} \left[\frac{Ft_u}{FS_u} , \frac{Ft_y}{FS_y} \right]$$

where FS_u = the ultimate or burst factor of safety and FS_y = yield factor of safety.

The ellipsoidal bulkheads for the propellant tanks have been designed as minimum weight membranes subjected to internal pressures (ullage for the forward bulkhead and ullage plus hydrostatic head for the aft bulkhead). Aspect ratios less than 0.707 produce compressive stresses in the bulknead and have been considered for shell stability. Typical bulkhead weights are shown in Figure 109. Separate scaling relationships were determined for bulkhead aspect ratios on either side of the discontinuity value of b/a = 0.707. The following relationship was used for the bulkhead weight:

$$W = 3.12 \left(\frac{b}{a}\right)^{0.2} R^3 P \sigma^{-1} \quad \text{(1b)}$$

for the following aspect ratio range: $0.707 \leq \frac{b}{a} \leq 1.0$ which will allow the bulkheads to be treated as tension membranes and hence lighweight elements. Weight variation between scaled and design data did not exceed three percent. The aluminum allowable working stresses are a function of the operating temperature as shown in the table below.

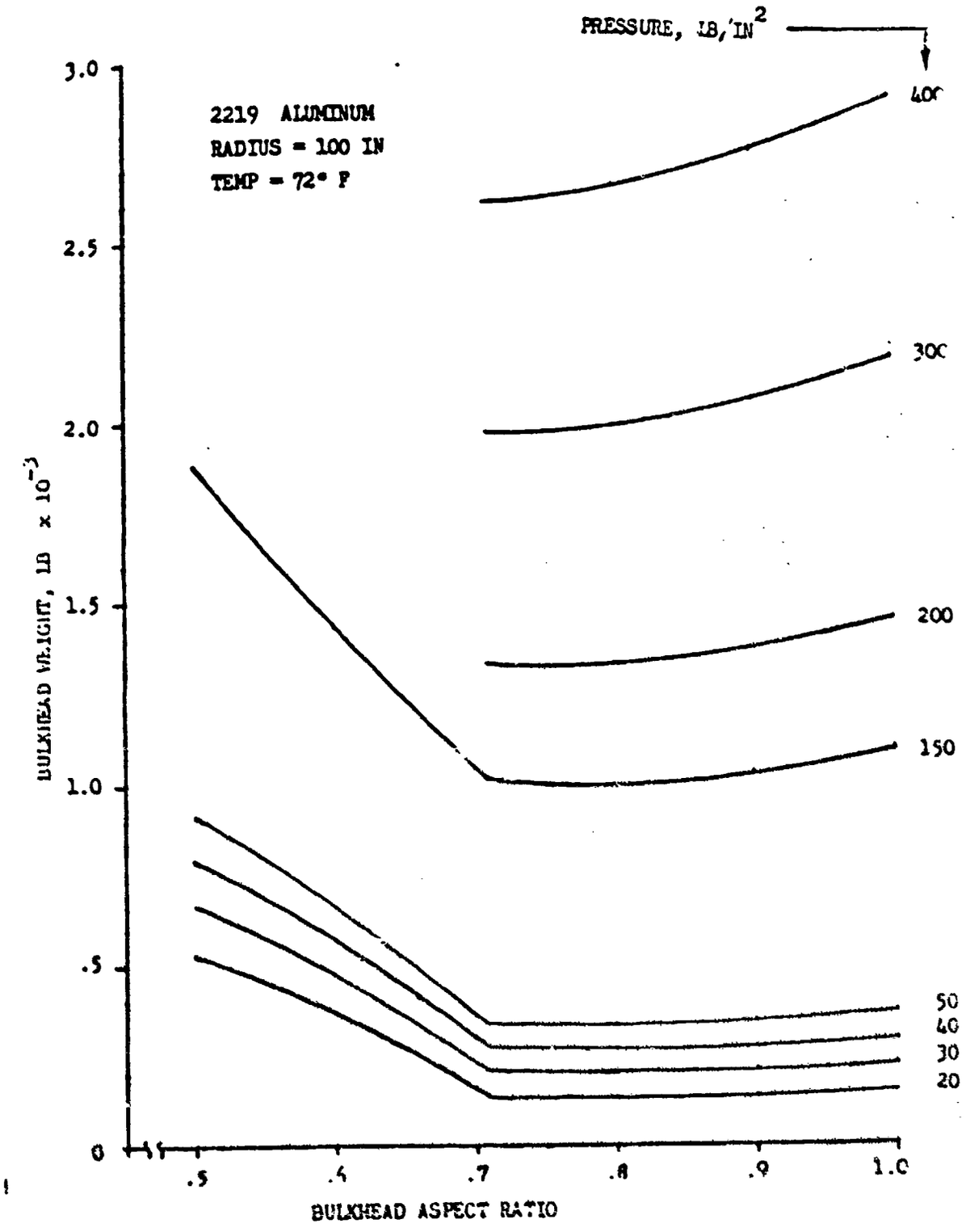

Figure 109. Effect of Pressure and Aspect Ratio on the Weight of Ellipsoidal Dome Bulkheads with Fixed Radii - Aluminum Al 2219

Temperature °C (°F)	$Ft_y \times 10^{-3}$ kg/cm^2 (lb/in^2)	$Ft_u \times 10^{-3}$ kg/cm^2 (lb/in^2)	$\times 10^{-3}$ kg/cm^2 (lb/in^2)	$E \times 10^{-6}$ kg/cm^2 (lb/in^2)
22.2 (72)	3.5 (49.8)	4.36 (62.0)	3.11 (44.3)	0.74 (10.50)
-73.3 (-100)	3.73 (53.0)	4.61 (65.6)	3.30 (46.9)	0.77 (10.95)
-178.9 (-290)	4.08 (58.0)	5.14 (73.1)	3.62 (52.2)	0.82 (11.70)
-240.0 (-400)	4.50 (64.0)	6.21 (88.3)	4.09 (58.2)	0.86 (12.20)
	ALUMINUM			

Solar Collector

The collector size and weight are a function of the vehicles thrust level and the engine performance characteristics. Two thruster systems were considered for the parametric studies. The lower temperature system has a specific impulse of 872 secs while the higher temperature system using "doped" hydrogen produced specific impulses of 1041 secs. The latter system requires considerably more energy and therefore the collectors required were larger and heavier. One of the trades conducted was to determine the benefits of the higher Isp thrusters.

The projected diameter for the parabolic collectors is expressed as a function of the thrust level, Figure 23.

$$D_{coll} = 15.4F^{0.5}; \ (5000^{\circ} \text{ R. Thruster})$$
$$50.0F^{0.5}; \ (7000^{\circ} \text{ R. Thruster})$$

where F = engine thrust level - lbf

D_{coll} = Projected diameter of collector - ft.

Based on available weight data for advanced inflated structures the solar collector weight is represented by

$$W_{coll} = 0.044 D^2_{coll} \quad \text{(Figure 26)}$$

where W_{coll} = weight (lb) of two solar collectors. This weight was for a light weight concept. One of the parametric trades considered the weight sensitivity effects of the solar collector unit weights.

Engine Thruster Systems

The engine system weight included weights for the absorber, thruster, insulation, plumbing and fittings. The weight scaling relation was based on the weight breakdown for the 25 lbf thruster with a single nozzle.

$$W_{ENG} = 1.53\ F^{1.15}$$

This relationship was considered to be adequate for both the 5000°R and 7000°R thruster design concepts. The engine system weight is only a small percentage of the stage dry weight.

Thermal Insulation

Due to the low thrust of the solar thermal rocket, the mission duration will be measured in days. The propellant employed is liquid hydrogen which as a cryogenic is very susceptable to boil-off during the mission. In order to restrain the amount of propellant boil-off, the tanks must be insulated with an efficient lightweight multi-layer insulation concept.

A simplified approach is used to determine the equilibrium wall temperature at the departure and arrival points for the mission. This approach considers an average surface temperature throughout the entire mission leg. The surface temperature (T_{WALL}) is assumed to be equal to the equilibrium wall temperature, which is given by

$$T_{WALL} = \left[\frac{\alpha_s}{\varepsilon} \frac{A_A}{A_\varepsilon} \frac{S_{ABS}}{\sigma} \right]^{1/4}$$

where

- α_s = the surface coating absorptivity (0.3)
- ε = the surface coating emissivity (0.8)
- A_A = the effective absorbing area
- A_ε = the effective emitting area
- S_{ABS} = the solar constant plus earth contribution
- σ = the Stefan-Boltzmann constant

For the tankage arrangement and the orbital rotational aspect of the vehicle the (A_A/A_E) ratio was assumed to be 0.5.

The presence of the earth will affect the heating flux experienced by the spacecraft. In addition to the solar flux, there are earth reflected and emitted heating fluxes. The total heat flux, S_{ABS}, is given by

$$S_{ABS} = \alpha_s S_\theta \left[1 + \left(\frac{S_R}{S}\right) + \left(\frac{\epsilon_R}{\alpha_s}\right)\left(\frac{S_E}{S}\right)\right]$$

S_R = earth reflected heating rate

S_E = earth emitted heating rate

S_θ = solar heat flux at 1 AU

The albedo of the earth is the sum of the reflected and scattered solar radiation and can be conservatively approximated by

$$Beff = 0.39g$$

where the altitude function, g, for a simple sphere is

$$g = 1 - \frac{\sqrt{h\,(2r_p + h)}}{r_p + h}$$

where r_p is the radius of the earth

h is a weighted average of the mission altitude

The heat emitted from the earth is assumed to be constant over its surface, where the average surface temperature is $T_p = 600^\circ R$ and the planet emitted radiation E_{ff}, can be expressed as

$$E_{ff} = ZgT_p^4$$

The view factor, Z, is 1.0 and 0.5 for single and clustered tanks, respectively; the equilibrium wall temperature is given by

$$T_{WALL} = \left[\left(\frac{\alpha_s}{\epsilon}\right)\left(\frac{A_A}{A_E}\right)\left(\frac{S(1+B_{eff})}{\sigma} + E_{ff}\right)\right]^{1/4} {}^\circ K$$

The insulation concepts considered were multi-layer, typical properties for DAM-NH insulation is shown in Figure 110. Since the tanks will contain liquid hydrogen, the lower thermal conductivity curves were used at the near

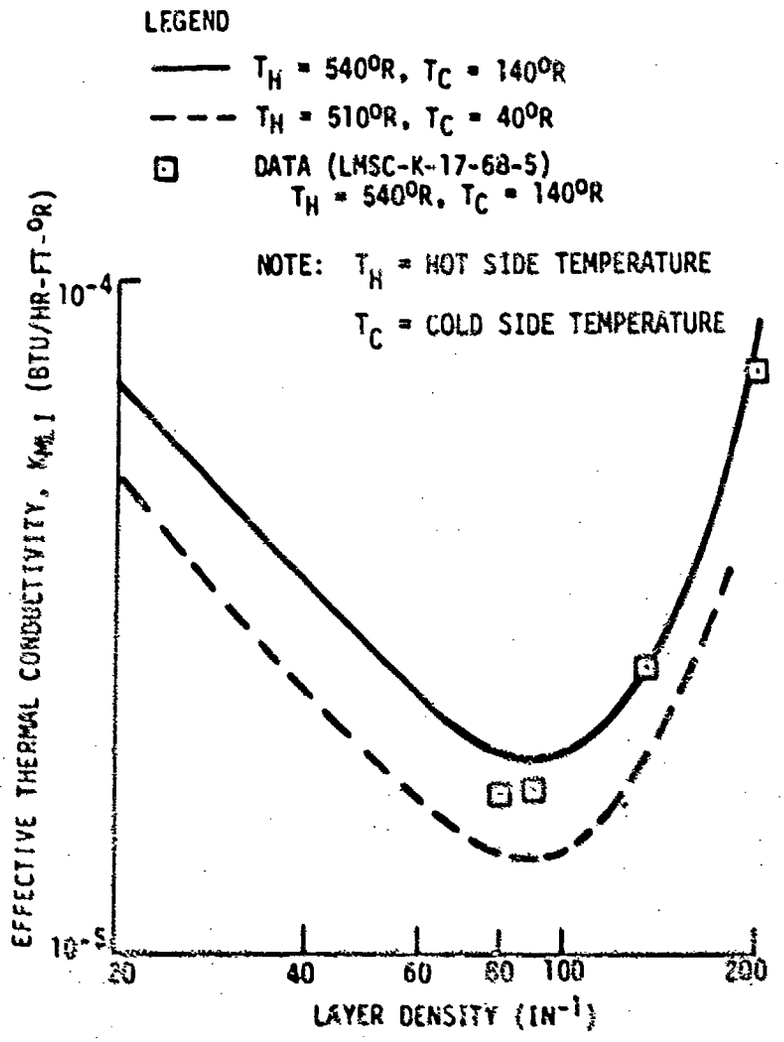

Figure 110. Thermal Conductivity of DAM-NM MLI (Reference 16)

optimum point of about 60 - 80 layers per inch. The heat flux (Q) equation used for the vehicle synthesis is

$$Q = \frac{2.5 \times 10^{-5}}{\ell_{ins}} \left(\frac{T_{WALL}}{540}\right)^4 \frac{BTU}{4R\text{-}FT^2}$$

where ℓ_{ins} - insulation thickness (ft)

The total heat input throughout the mission is given by

$$H_{in} = Q \times A_{TANK} \times T_{MISS}$$

where A_{TANK} is total surface area of all propellant tanks and T_{MISS} is the total mission time including stay time in geosynchronous orbit before return. The time for the outbound and return trajectory segment are a function of the initial thrust to weight and the number of burn cycles required to produce the velocity increment requirements, see Section 6.0.

The latent heat of vaporization (L_H) for liquid hydrogen is 190 BTU/lb. Therefore, amount of propellant boil-off is given by

$$W_{PROP\ B\text{-}O} = H_{in}/L_H$$

The boil-off rate is considered to be constant throughout the total mission duration. Therefore, during the long thrusting periods, the stage mass depletion rate must include the propellant boil-off rate. The propellant required to impart the required velocity increment ΔV is given by

$$W_{PROP} = W_{BO} \left(e^{\Delta V/Ig} - 1\right)$$

where W_{BO} = vehicle weight at end of mission leg

I = specific impulse of vehicle (secs)

A weighed average between no boil-off and full boil-off prior to start of mission segment is computed to account for gradual boil-off throughout the mission.

Prior to start of the orbital transfer mission, whether the vehicle consisted of a single tank or a multiple cluster of tanks, each tank is assumed to be filled to a uniform level of 95% which allowed a 5% ullage factor.

The unit weight scaling relationship for the multi-layer insulation includes an outer sheet which acts as a bumper to reduce penetration by micrometeoroids

$$W_{ins} = 2\ell_{ins} + 0.0362 \quad lb/ft^2$$

A 5 mil mylar scuff layer over 1/2 inch thick MLI insulation will give 99% survival probability for a 40 foot long and 15 ft diameter LH_2 tank throughout a 40 day mission.

Reaction Control Propellant Requirements

The reaction control propellant is required to stabilize the vehicle due to external disturbing torques. These torques are due to aerodynamic drag and gravity gradient. Section 6.0 showed an example of the fuel required for a thirty day mission and a particular size vehicle.

The aerodynamic torque on the vehicle results from the large projected frontal area of the solar collectors and their lever arm with respect to the vehicle's center of mass. Scaling from known reference points, the propellant required to overcome this torque is given by

$$W_{RCS-AERO} = 2.2 \times 10^{-7} D^3_{coll} T$$

where T is trip time in days.

The gravity gradient disturbances are a function of the inertia characteristics of the vehicle. Therefore for a constant thrust-to-weight the propellant is given by

$$W_{RCS-GG} = 1.9 \times 10^{-9} D^4_{coll} T$$

The tank weight to contain the RCS propellant is assumed to be 25% of the propellant weight plus 50 lb for nozzle and fittings.

Other Subsystems

The other subsystems included in the stage inertia weight are not strongly dependant of the vehicle size or mission duration. Typical system weights are based on current state-of-the-art technology. A listing of these weights is shown in the table below.

Constant Subsystem Weights

Subsystem	Weight Budget (lbs)
Thermal Control	79
Heat Transfer System & Insulation	112
Electrical Power and Distribution	354
Navigation	75
Telemetry, Tracking & Communication	62
Information Management & Control	50
Structure and Mechanism	200
Total Constant Weight	(932)

An allowance of 15% of the spacecraft dry weight has been added to account for vehicle growth.

PARAMETRIC TRADE STUDIES

A series of trade studies were conducted to determine the importance of several design parameters and the size limitation imposed by the Orbiter's cargo bay. The range of payload was 10,000 lb to 100,000 lb., the lighter payloads can be packaged within the Orbiter cargo bay together with the propellant tanks, collector and thruster systems. The larger payloads are composed of nested propellant tanks assembled in orbit from separate Orbiter flights.

Insulation Study

There are numerous choices of vehicle parameters for display via the CRT plotting routine of the STOP CUSS Program. For the initial run which varied the payload weight and the insulation thickness, a typical selection of plots are seen in Figures 111 through 115. The results shown are for the one way trip from LEO to GEO, with an initial thrust-to-weight-ratio of 0.0003 and using the lower temperature engine system whose performance is 872 secs specific impulse.

Figure 111 indicates the weight of the total vehicle plus payload at beginning of the mission at LEO (vehicle ignition weight). It is recognized that most of these vehicles exceed Orbiter delivery capability to LEO. Therefore, the vehicles shown are composed of a series of tank sets (maximum

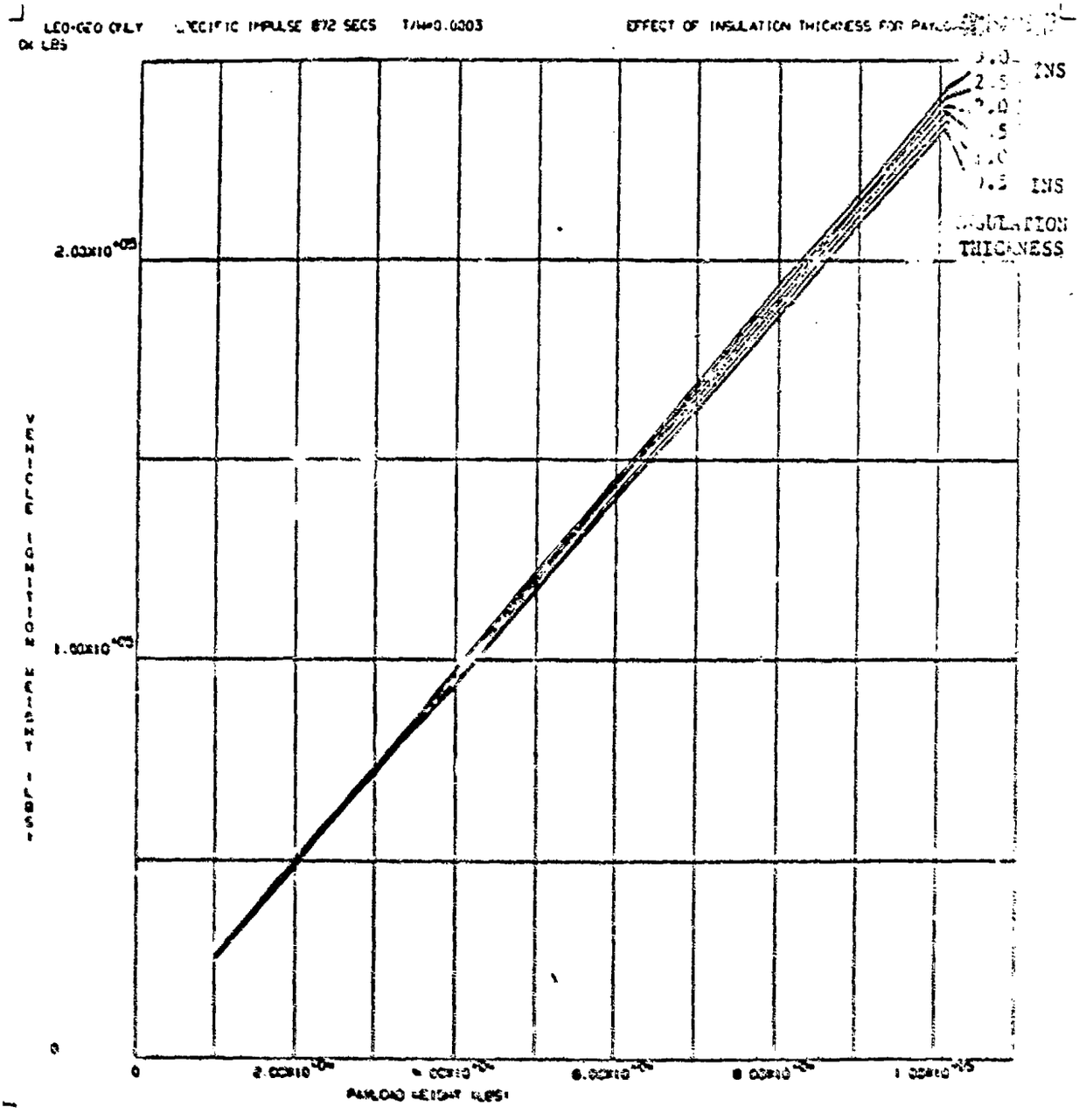

Figure III. Variation of Vehicle Weight With Payload and Insulation Thickness

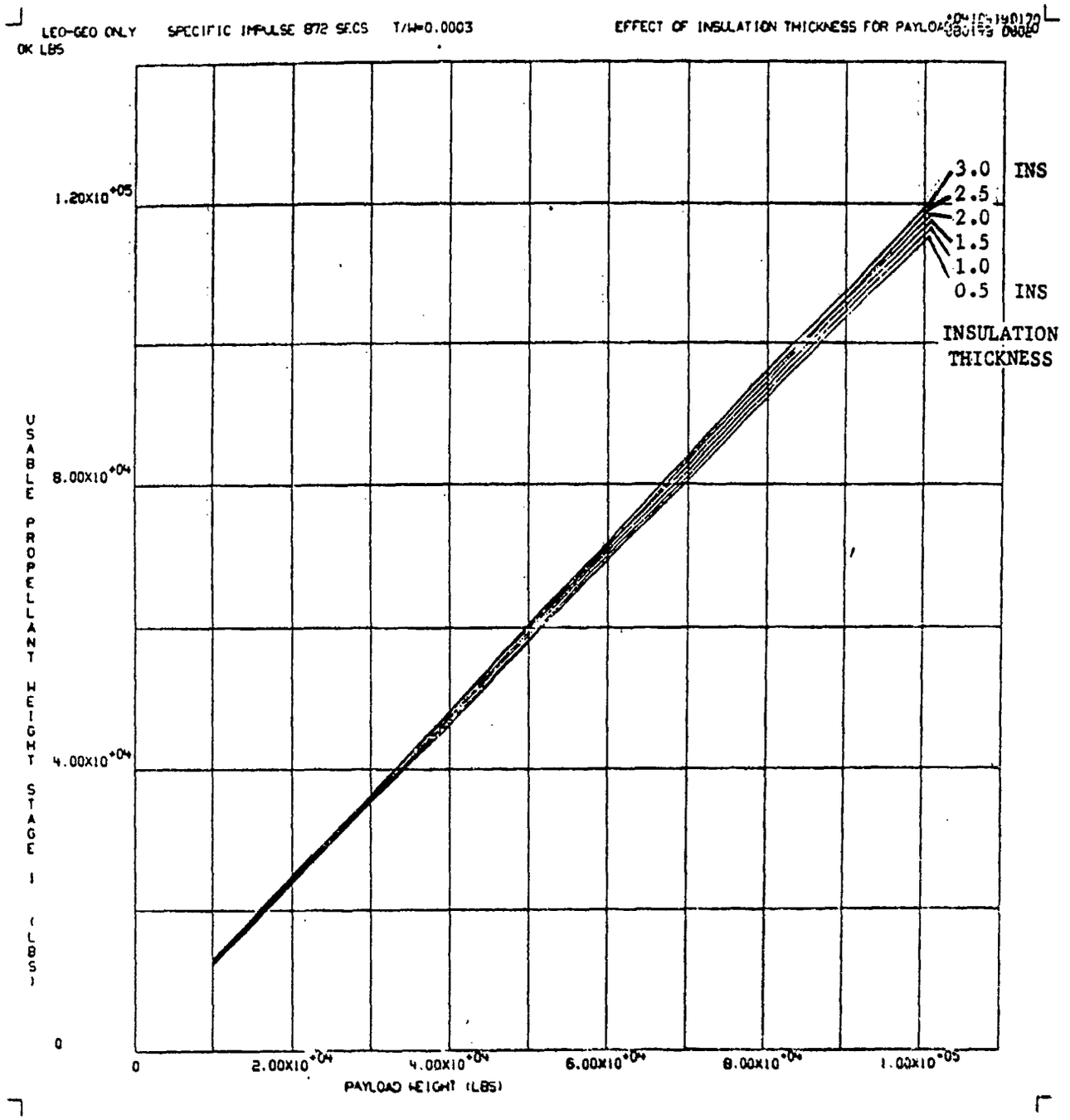

Figure 112. Usable Propellant Required for Various Insulation Thicknesses and Payload Weights

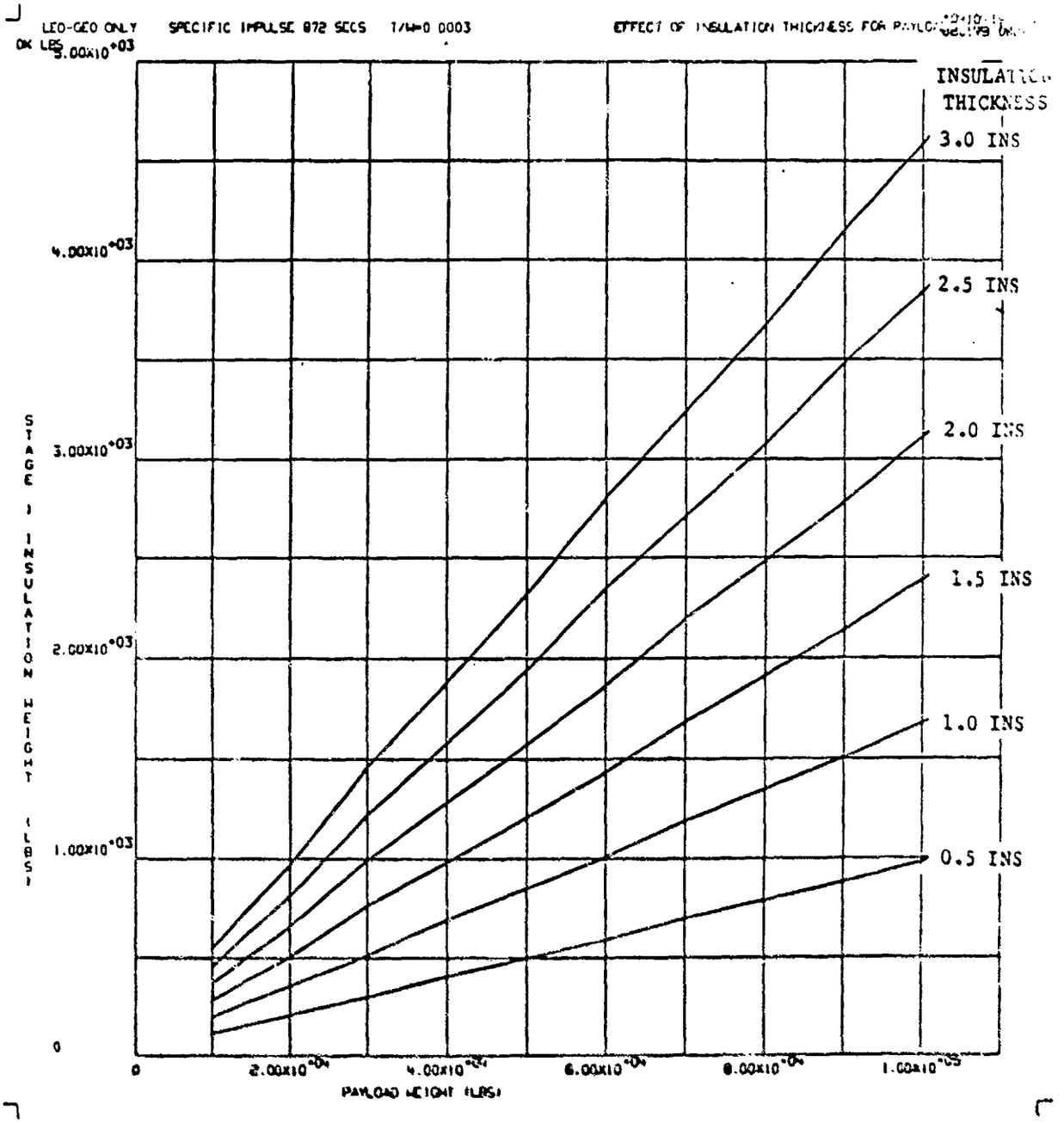

Figure 113. Insulation Weight Variation With Payload Weight

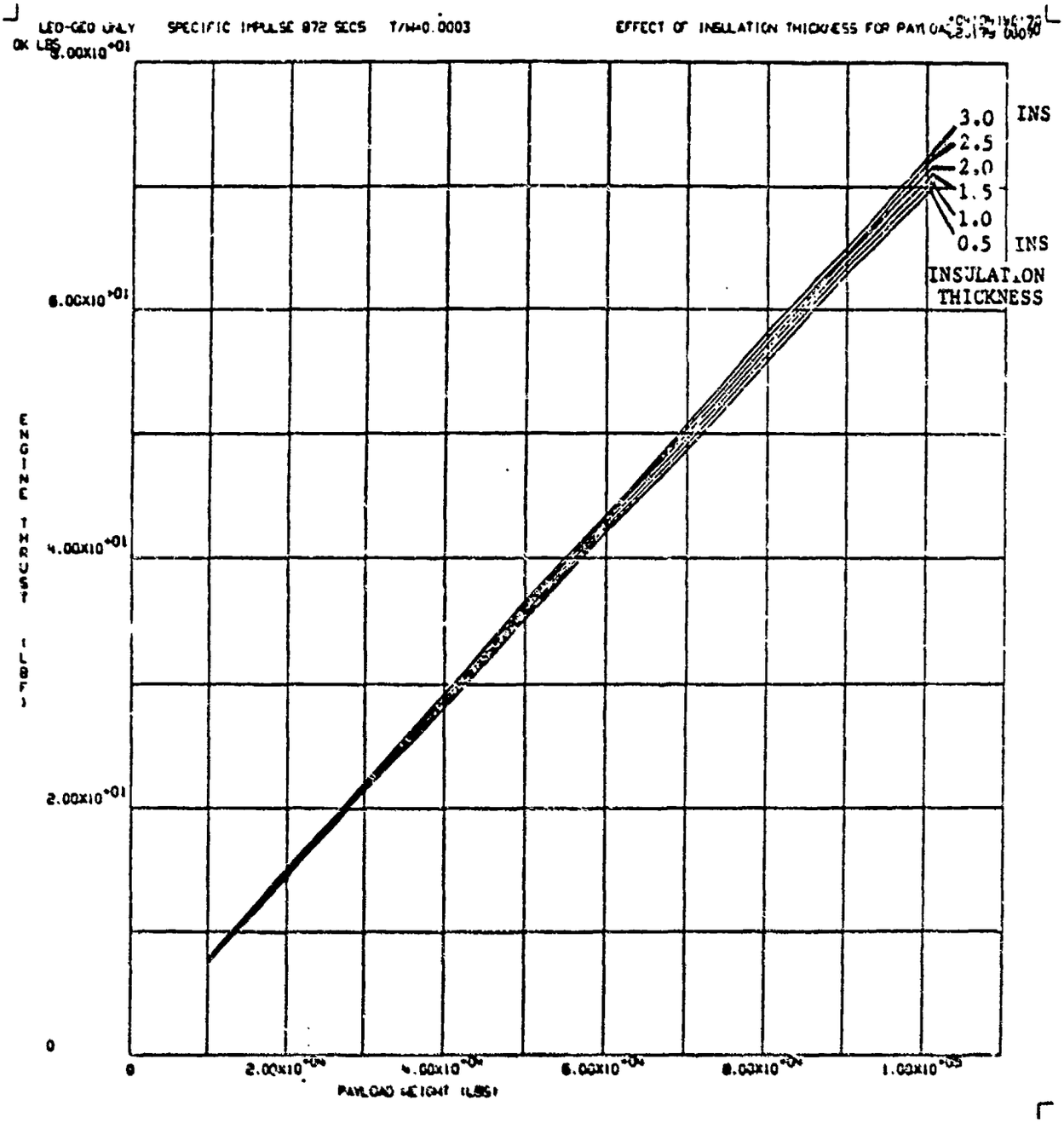

Figure 114. Engine Thrust Levels Required for Vehicles With Constant Thrust-to-Weight

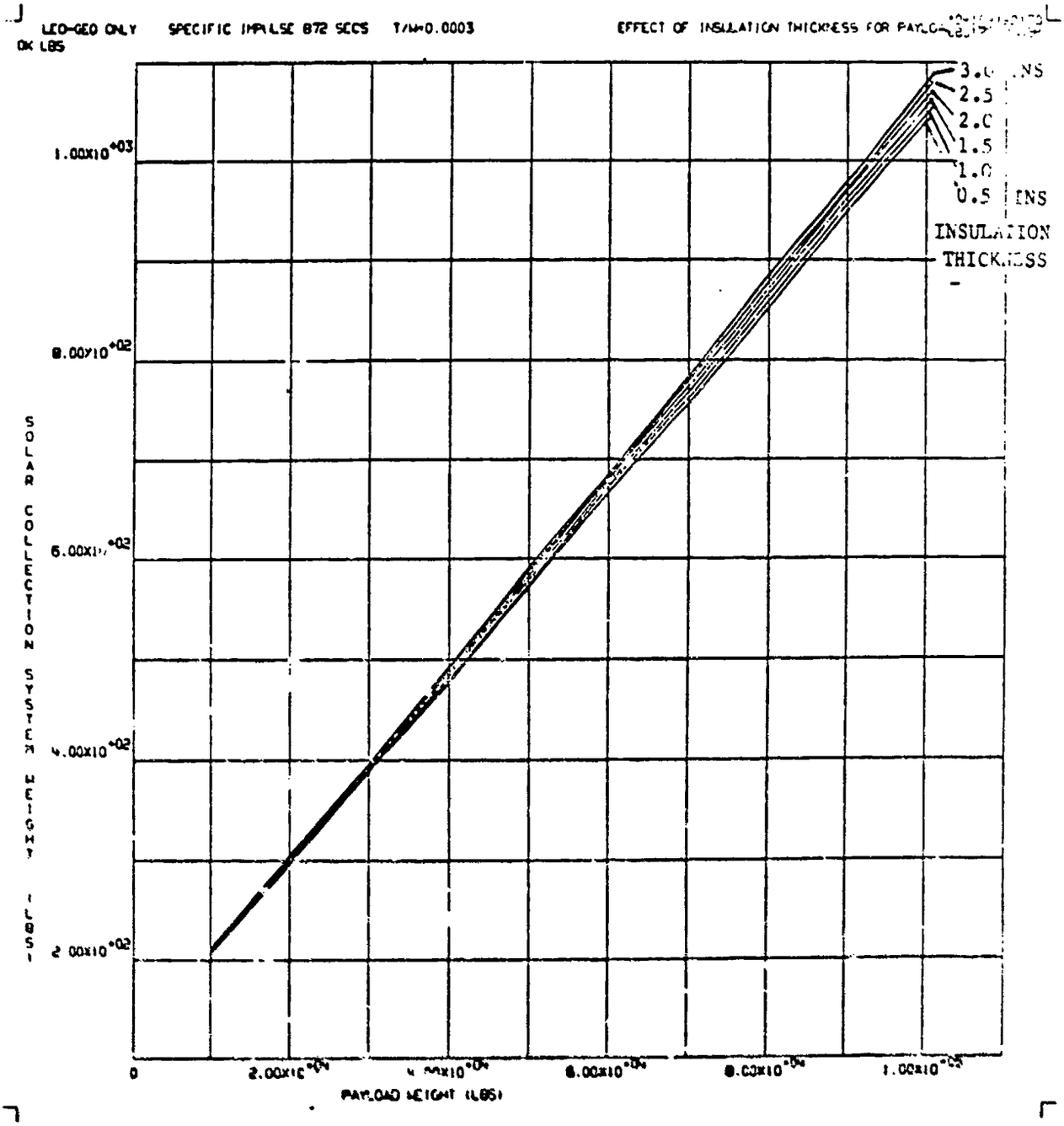

Figure 115. Solar Collector Weight Variation With Vehicle Payload Weight

length 55 ft) assembled together prior to departure from LEO. The tank sets are topped up with propellant to allow only a 5% ullage factor prior to departure. From this figure, the inference is that for the range and performance of insulation considered ($0.5 < t_{ins} < 3.0$ ins), the change in vehicle launch weight is less than 5%. In fact, the thicker insulation is a weight penalty to the vehicle performance. This is possibly due to the relative short trip time involved with the one way mission and the high thrust to weight ratio of 0.0003. The total time involved is approximately 14 days and hence the boil-off percentage is rather small compared with the amount of insulation involved.

Figure 112 shows the amount of usable propellant for each vehicle. The definition of usable propellant is the propellant used by the solar thermal thruster and the propellant that is boiled-off. The propellant boil-off could be used by a modified engine pump. The engine system will be more complex and heavier, since it is required to handle both fluid flow and the vented gas flow from the boil-off.

Figure 113 shows how the insulation weight varies with the payload and hence tank size and the insulation thickness. Each tank set is assumed to be covered with a constant insulation thickness on the tank wall and the tank ellipsoidal bulkheads.

The larger launch vehicles will require a corresponding larger and hence heavier thermal rocket engine if the vehicles T/W is held constant at 0.0003. The variation of engine thrust for the range of payloads considered is seen in Figure 114. For a given engine thrust, there is a corresponding amount of solar heat required. This solar heat is obtained from two parabolic collectors whose weight variations are shown in Figure 115.

The effect of insulation was considered also for the longer duration missions where the thrust to weight T/W is reduced to 0.00003. The engines used for the next three figures were the high temperature systems capable of specific impulse of 1041 secs. Figure 116 shows the vehicle weights required for a range of insulation thicknesses from 1.0 to 3.0 ins. It is apparent that the 1.0 inch insulation results in a weight increase of less than 8% for the largest payload system. Any further insulation thickness

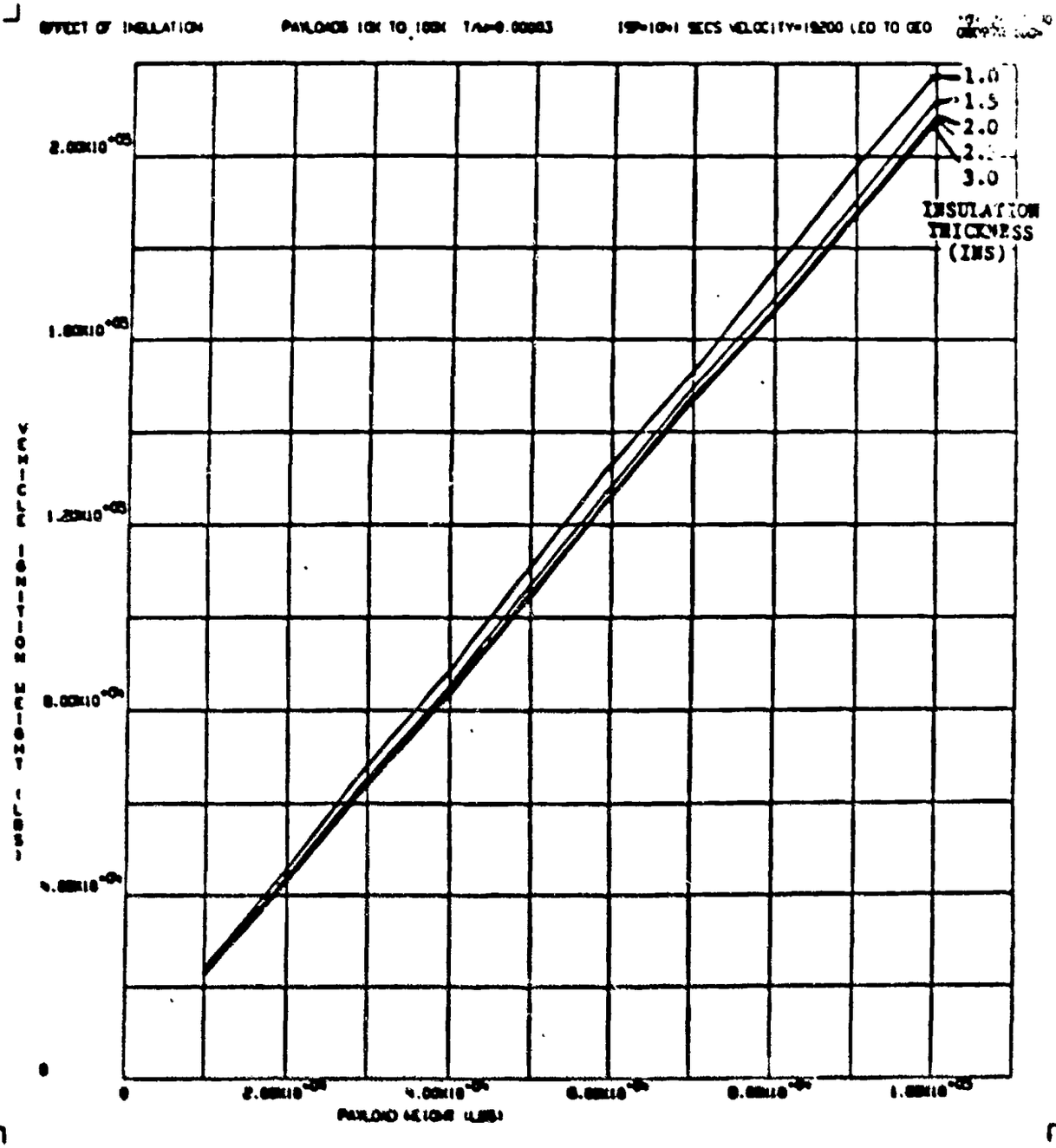

Figure 116. Insulation Performance, I_{sp} = 1041 sec, LEO-to-GEO Mission

reduction would begin to significantly impact the vehicle's performance. The return empty mission (Figure 117) and the two-way return mission (Figure 118) indicate similar trends. Therefore, it appears that 1.0 inch insulation will be adequate for those vehicle systems that have T/W 0.00003 for both the low (5000^{0}F) and high temperature (7000^{0}R) engine systems.

Thrust-to-Weight Variations

The thrust-to-weight ratio of the vehicle will directly affect the engine size and more significantly, the collector diameter and weight. The low temperature thrusters results are shown in Figure 119 (LEO-GEO mission) and 120 (LEO-GEO and return mission). They indicate that the overall vehicle weight can be reduced by increasing the T/W ratio. Although the engine and collector system weights increase, the trip times are reduced and there will be less propellant boil-off. There is no appreciable weight reduction when the T/W >1.0 x 10^{-4}.

The high temperature thruster results (Figures 121 and 122) show the direct opposite effects. When the T/W is increased, the overall vehicle weight increases. This is due to the significantly larger collectors required for the higher temperature thrusters. The collectors are becoming a predominant weight item and their size induces major disturbance torques both aerodynamic and gravity gradient. The return mission with the 100K lb payload, Figure 122, shows the vehicle weight increases about 75% when the T/W goes from 0.5 x 10^{-4} to 3.0 x 10^{-4}. The trip time for the continuous thrusting mission varies from 84 days outbound for the lowest T/W to 14 days outbound for the highest T/W shown. If the trip time is not important, then the T/W should not exceed 1.0 x 10^{-4} for the large payload vehicles.

When the vehicle payloads are 20,000 lbs and less, the T/W variation between 0.5 and 3.0 x 10^{-4} does not noticeably change the vehicle's launch weight. Then it will be better to consider the use of the lowest mission duration acceptable.

Engine Performance

The improvements in performance using the high temperature thrusters are shown in Figure 123. A T/W = 0.00010 is held constant for both thruster

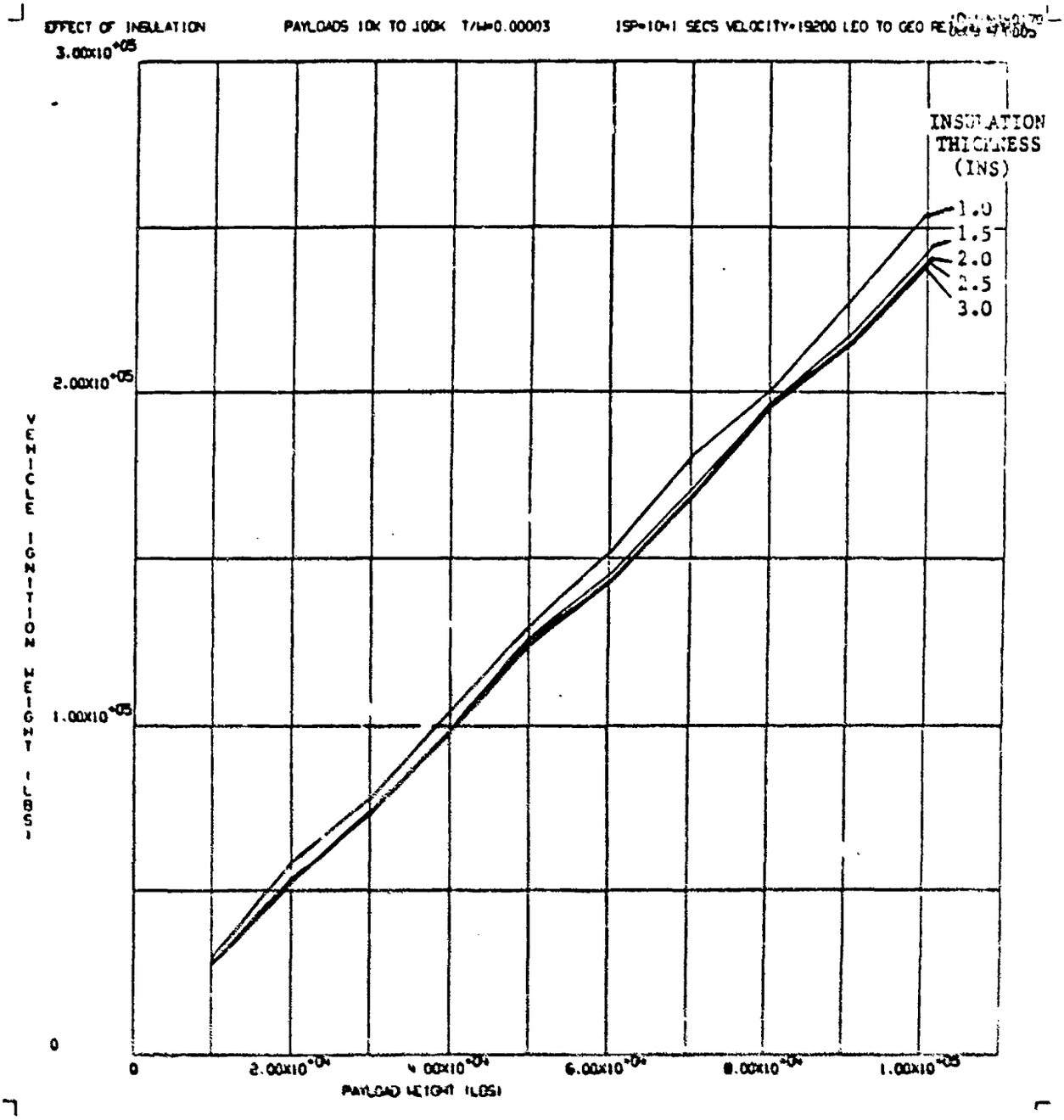

Figure 117. Insulation Performance, I_{sp} = 1041 secs, LEO-to-GEO and Return Empty Mission

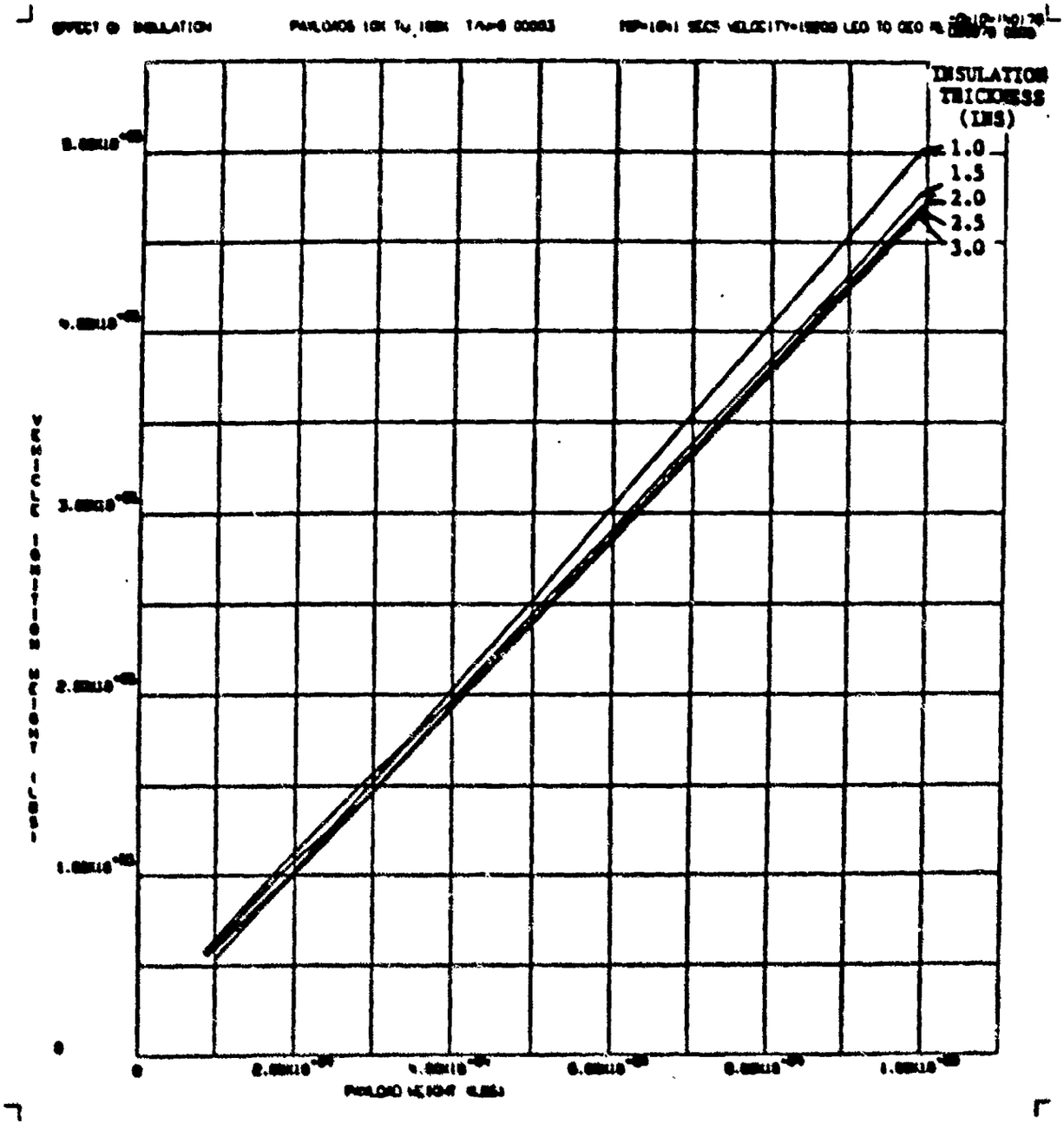

Figure 118. Insulation Performance, I_{sp} = 1941 secs, LEO-to-GEO and Return Mission

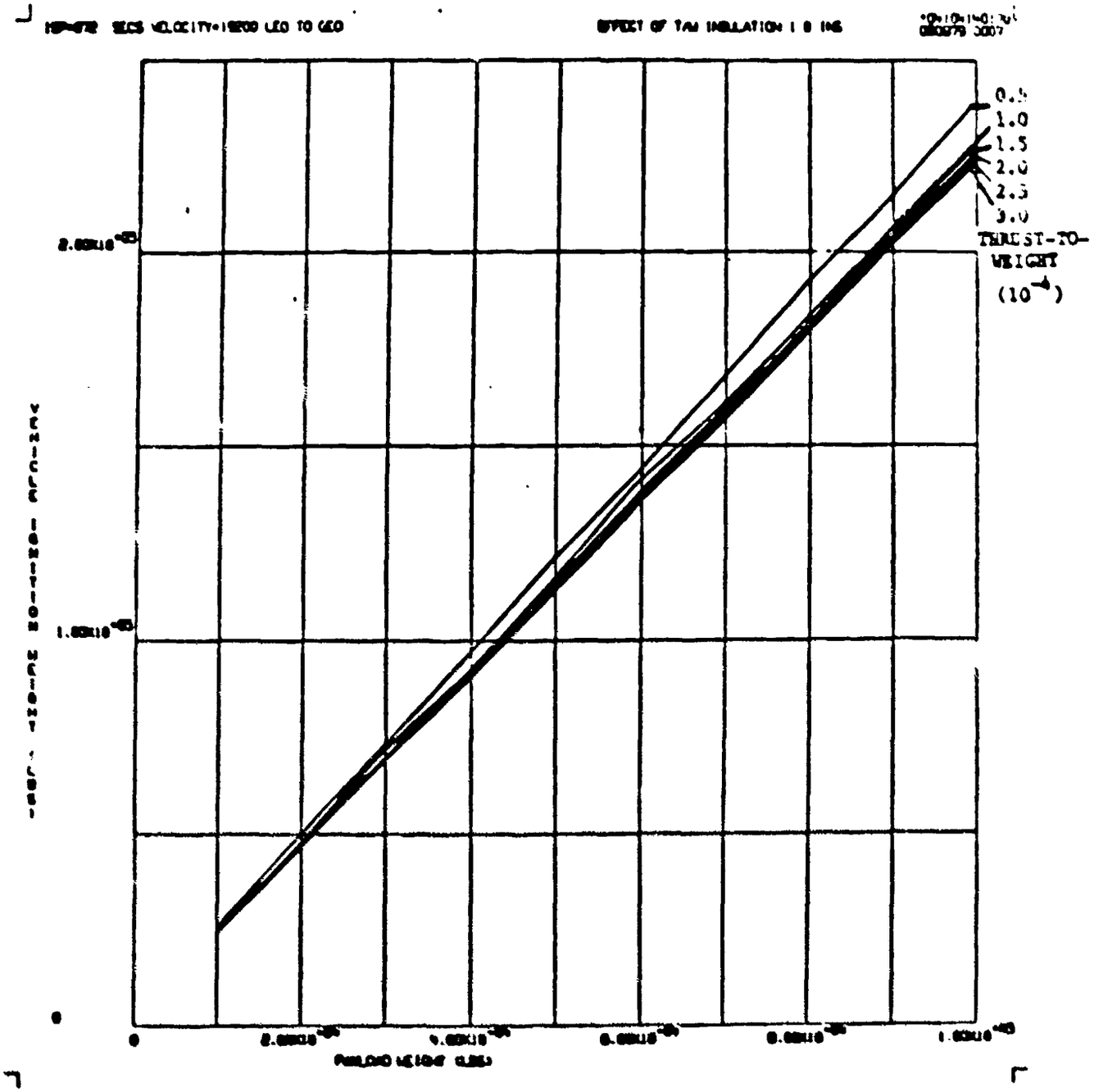

Figure 119. T/W Variation, I_{sp} = 872 Secs, LEO-to-GEO Mission

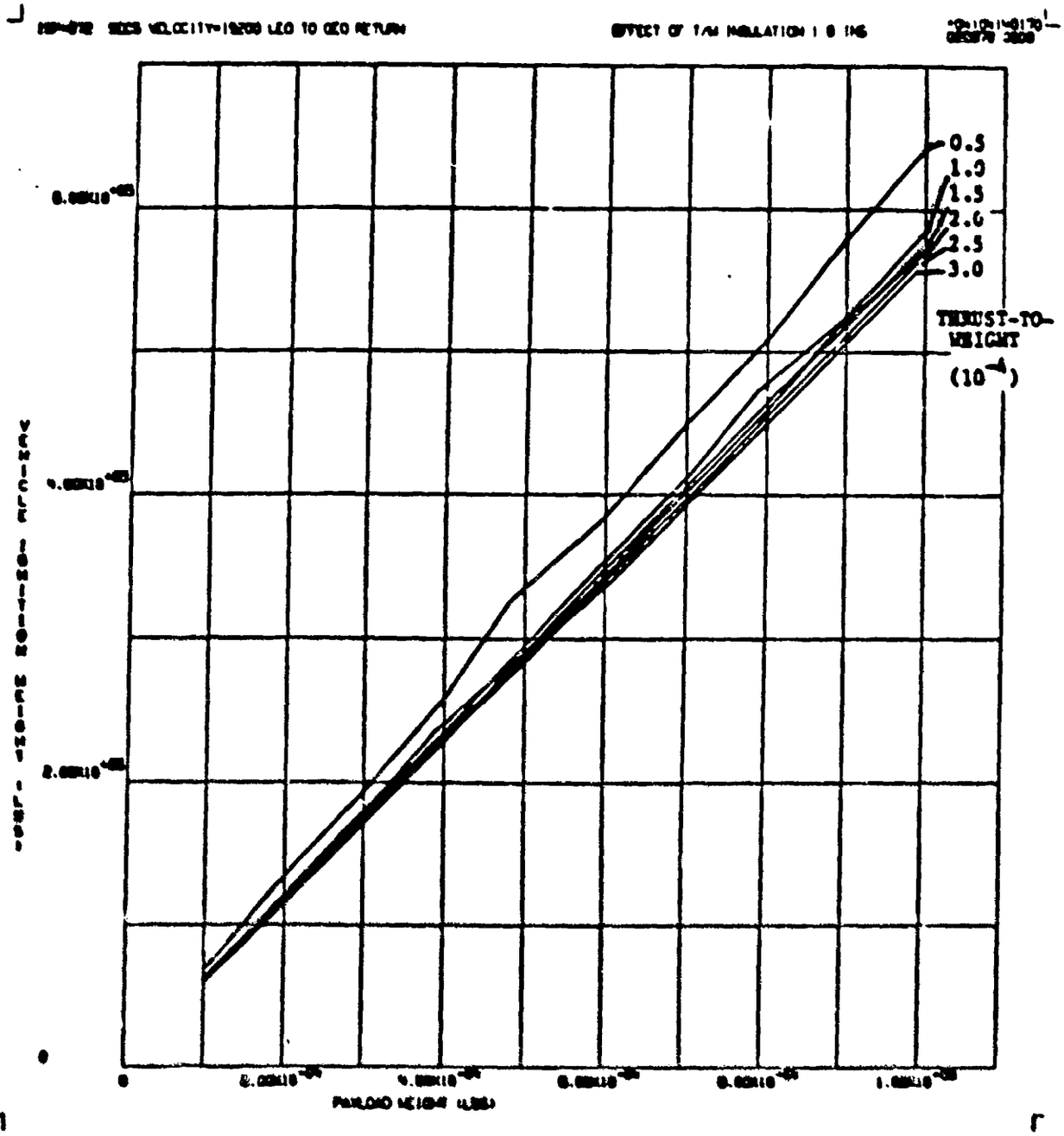

Figure 120. T/W Variation, I_{sp} = 872 Secs, LEO-GEO and Return Mission

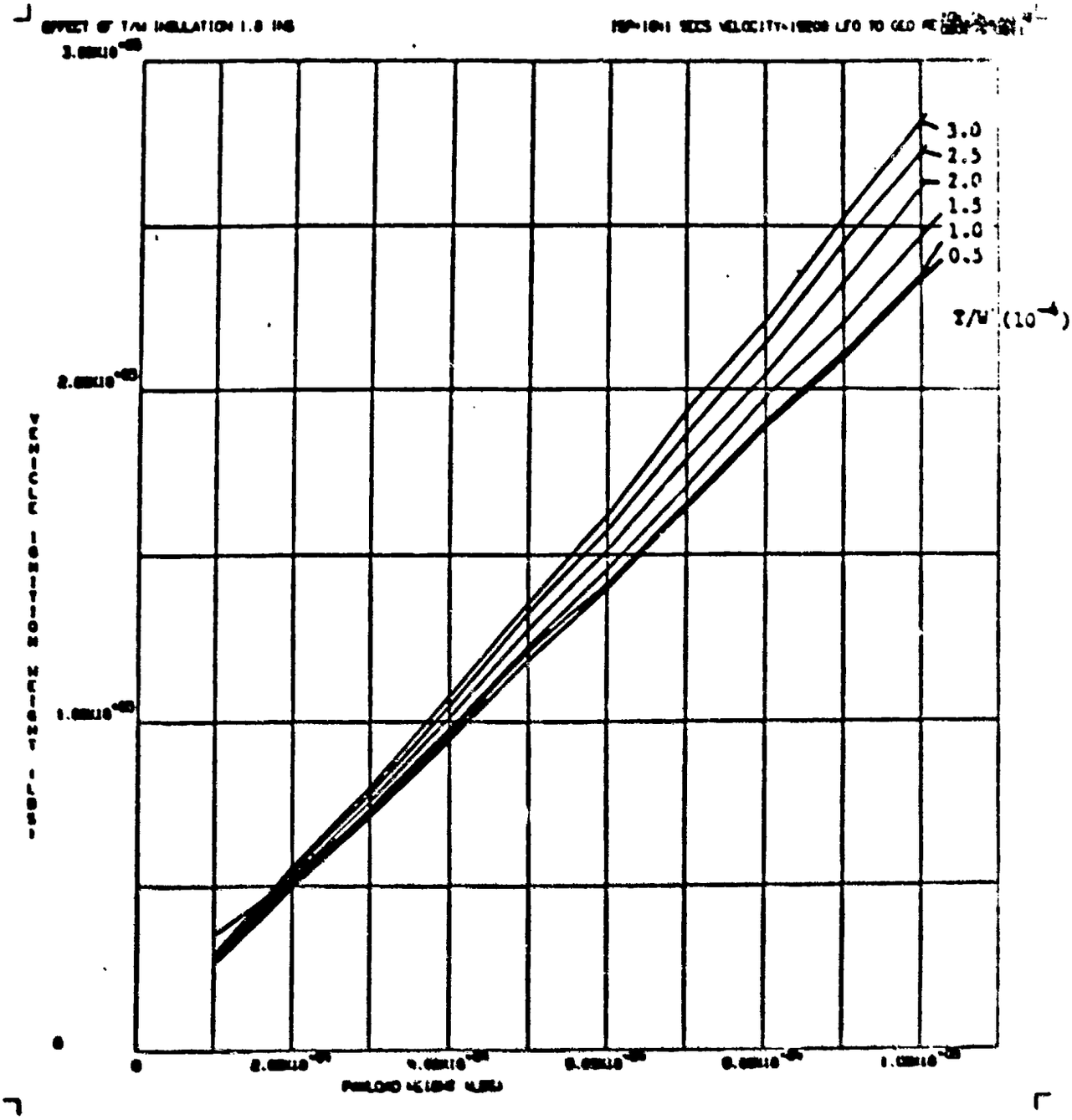

Figure 121. T/W Variation, I_{sp} = 1041 Secs, LEO-GEO Return Empty Mission

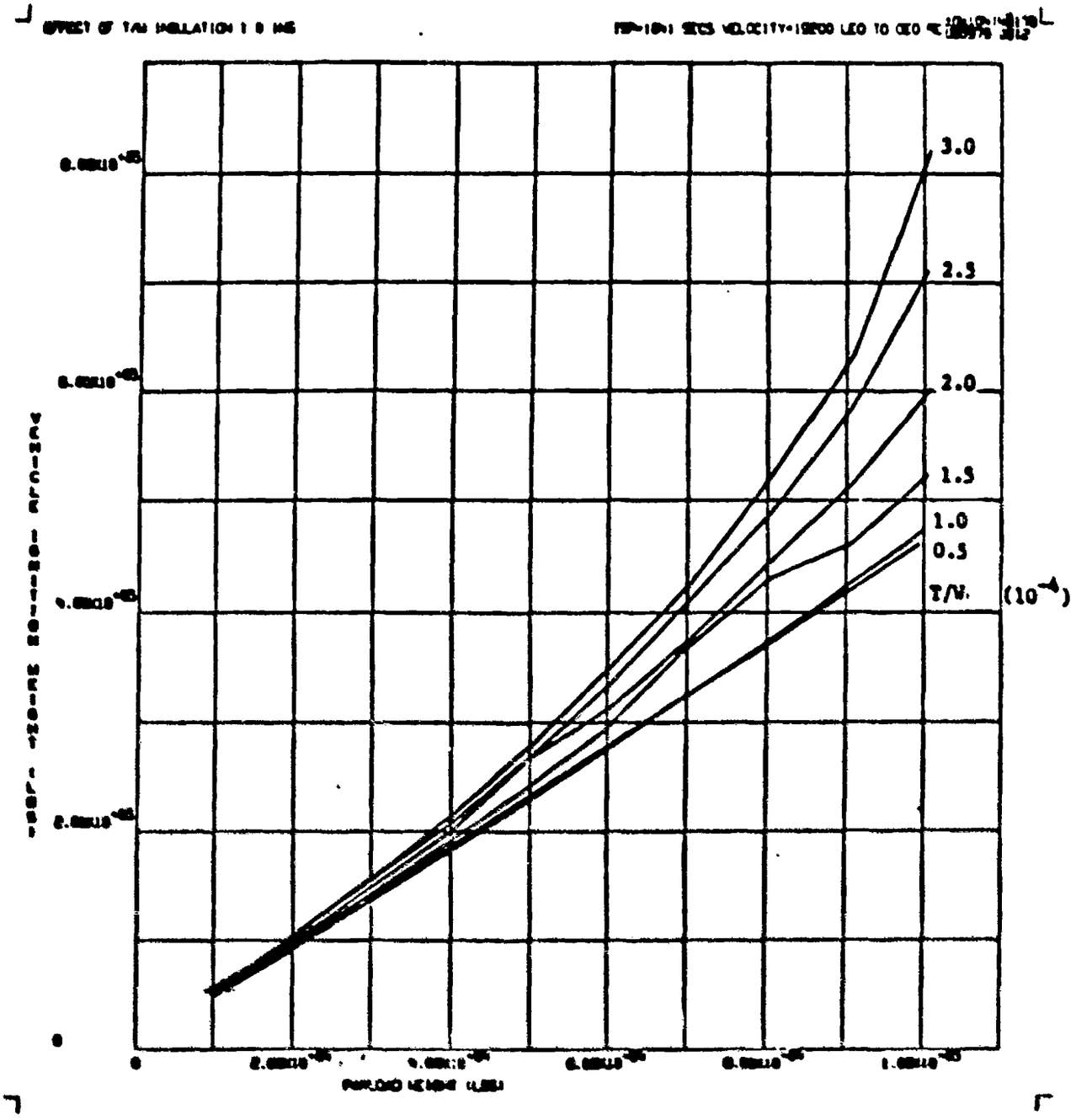

Figure 122. T/W Variation, I_{sp} = 1041 Secs, LEO-GEO Return Mission

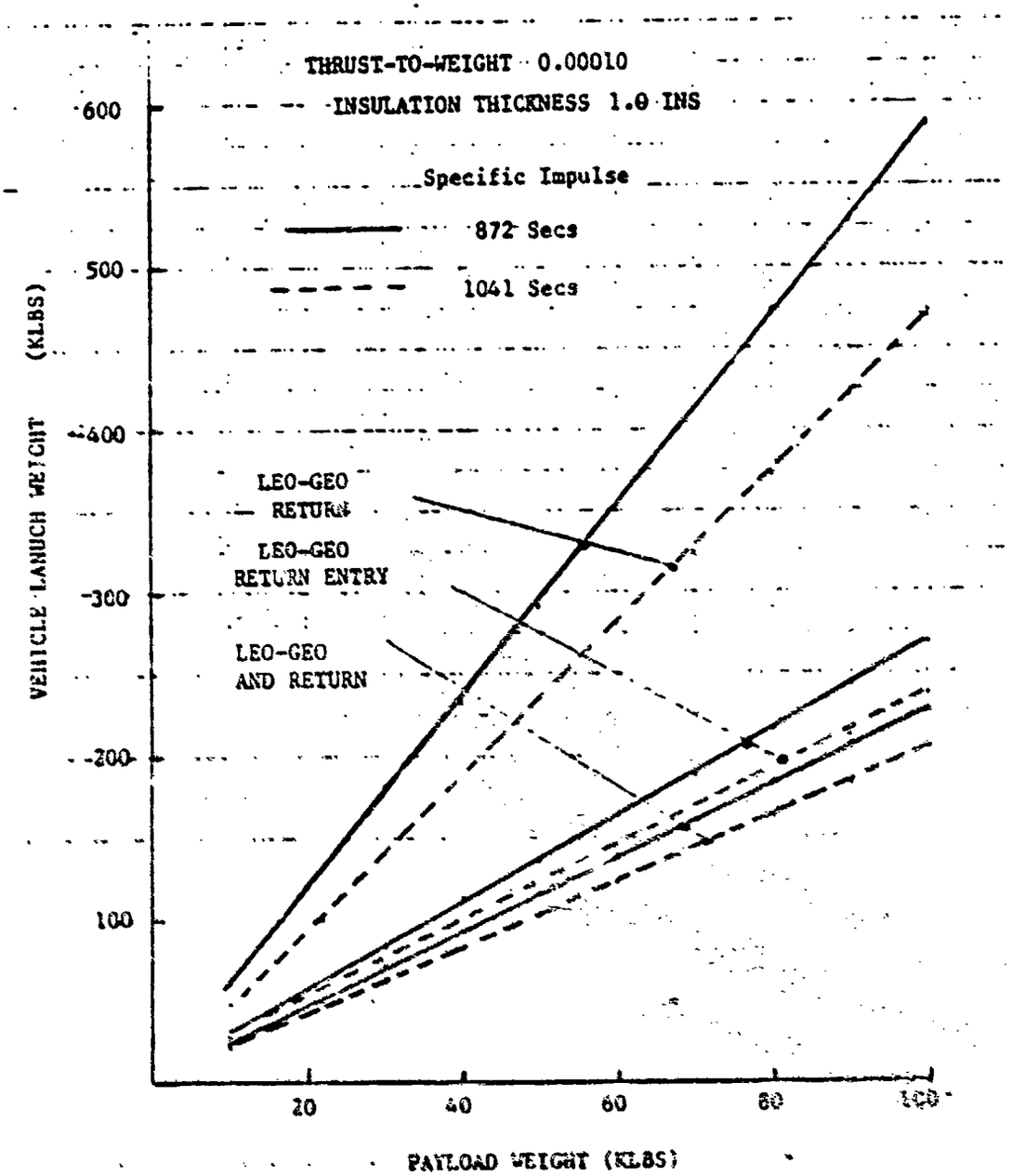

Figure 123. Effect of Improved Engine Performance

systems, and the thermal insulation was 1.0 inch for all three types of mission. Figure 123 shows that the high temperature thrusters can improve vehicle performance by at least 10% for the one-way mission and 20% for the round trip missions. It should be recognized that the results shown would result in an outbound trip time of 42 days. The weight of the engine thruster is considered constant between the high and low specific impulse, thruster weight is only a function of thrust level.

The engine performance is more beneficial at the higher payload ranges and the 2-way return trip missions.

Tank Pressure

There have been thruster design basepoints with chamber pressures ranging from 20 psi to 50 psi. Although there is a slight weight variation in the thrust assembly, there is a significantly larger weight variation in the propellant tank. Figure 124 shows how the vehicle's gross weight and stage mass fractions are affected by the tank pressure. For a constant launch vehicle weight, the payload capability is improved about 8% by decreasing the tank's pressure from 50 to 20 psi. The specific impulse for both pressures is assumed to be 872 seconds; there being no account for improved thruster performance at the higher operating pressures.

Single Orbiter Launch Capability

The previous results were concerned with the effects of various design and performance parameters with vehicles using 55 ft. long tanks. Most of the vehicles for the payloads of 20,000 lb. to 100,000 lbs. required multiple propellant tanks clustered together at low earth orbit. Each tank is brought up separately by the Orbiter and therefore the tank lengths were 55 ft. For the lighter payload vehicle systems it is possible to transport, payload, tankage, engine system and collectors in a single orbiter flight. For this single orbiter flight arrangement, the tank length is constrained to 40 ft to allow for packaging of the remainder of the vehicle within the cargo bay.

The vehicles considered for the single shuttle launch all had an initial thrust to weight ratio of 0.0003 and an insulation thickness of 1.0 in.

Figure 125 shows the payload capability for the single Shuttle launch for the two engine systems (specific impulse 872 and 1041 seconds). The payload capability increases as the trip duration from LEO-to-GEO increases. The

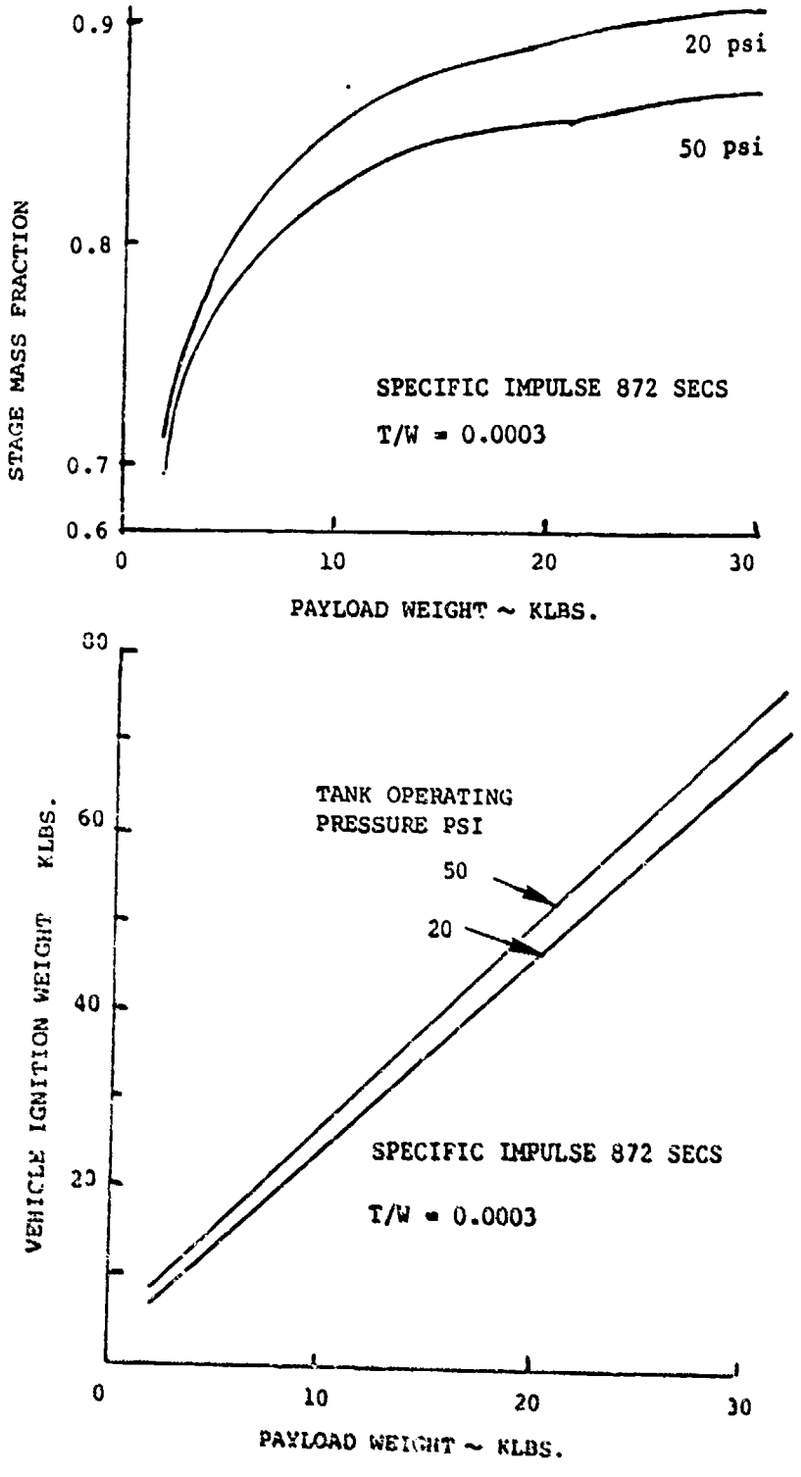

Figure 124. Effect of Tank Pressure

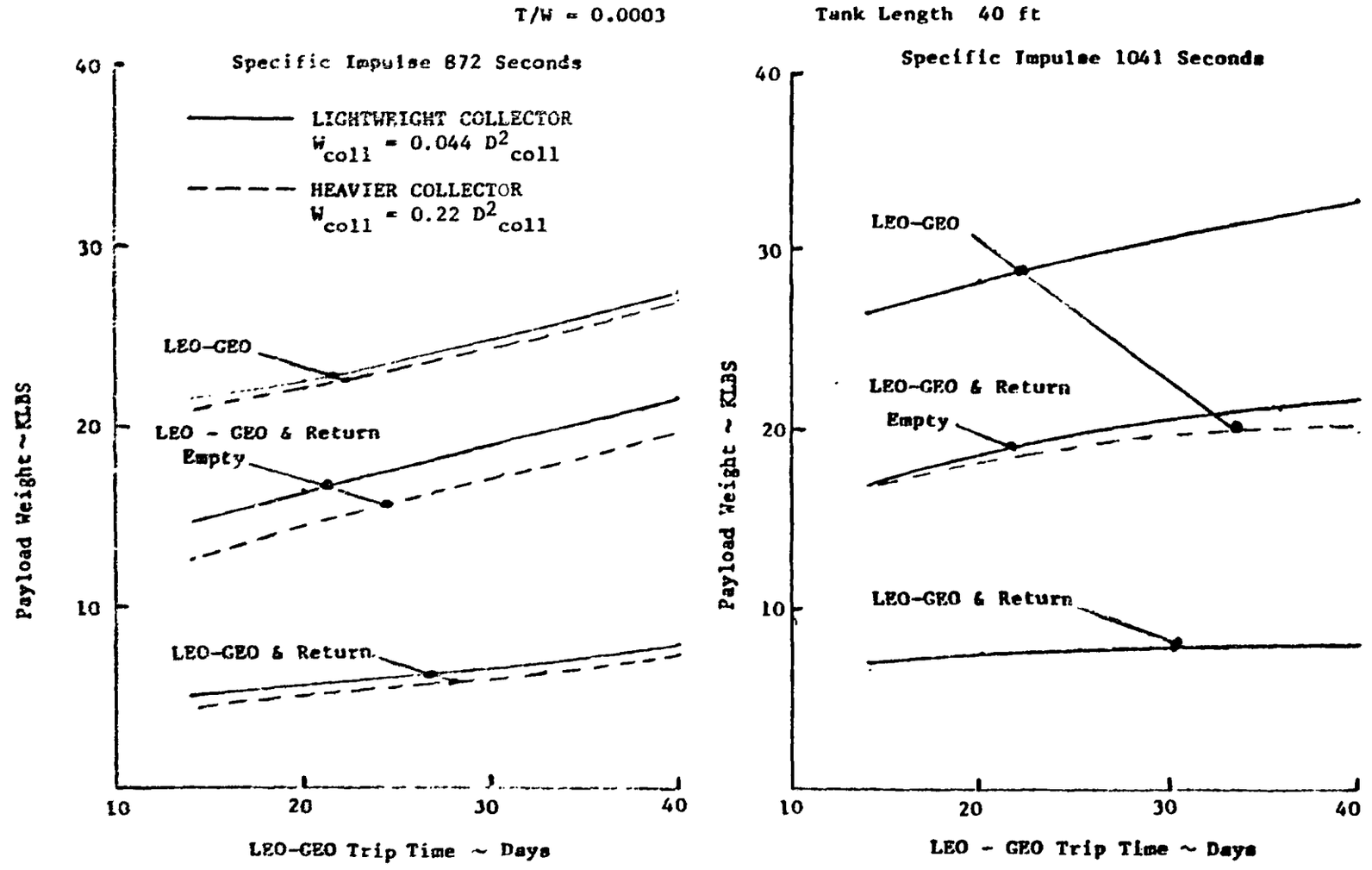

Figure 125. Single Orbiter Launch - Payload Capability

trajectories considered for these increased flight times are for the apogee/perigee burn flight modes which significantly reduced the total velocity requirements. The velocity required is 19,200 ft/sec at the 14-day trip time reducing to 15,750 ft/sec for the 40-day duration. The extended mission duration has the effect of increasing the amount of propellant boiled-off, which negates some of the benefits of the reduction in velocity requirements.

For the LEO-to-GEO mission, the orbiter capability ranges from 22,000 to 27,000 lbs. for the low temperature (5000°R) thruster system. This payload can be increased by 20% if the high temperature (7000°R) thruster is used for the propulsion system.

Missions which return the vehicle but leave the payload at GEO can place payloads from 15,000 lb to 20,000 lb into the geosynchronous orbit. This type of mission does not benefit from the improved thruster performance of the high temperature system. The payload is very sensitive to the returned stage inert weight. The collector weight for the high temperature system constitutes a significant percentage of the stage inert weight and negates the gains from the higher specific impulse.

Figure 125 also shows that the Orbiter can transport to LEO a solar thermal rocket system capable of placing and returning from GEO payloads ranging from 5000 - 7500 lbs. There does not appear to be any payload performance increases by employing the higher temperature thrusters.

The weight for the inflatable solar collector is based on very light-weight, perhaps optimistic design concepts with respect to the collector weight budgets. All the previous results are based on a weight algorithm of

$$W_{COLL} = 0.044\ D^2_{COLL}$$

If the collector weight model is increased 5 times the resulting single orbit launch payloads are shown as dotted lines on Figure 125. For the low temperature thrusters the payloads are reduced 5 - 10% for all three missions. The high temperature engine system with its much larger collectors has the payload reduce by 30% for the one-way mission. The other two missions have no payload capability. The increased collector weight, plus the large increases in inertias resulting in additional RCS propellant, completely erase the payload.

Figure 126 shows the vehicle launch weight for the corresponding vehicles on Figure 125. Most of the vehicles remain within the Orbiter's weight carrying capacity. If 3000 lb weight allowance is made for the support cradle, the Orbiter useful payload capability is 62,000 lb into the low inclination-low earth orbit.

The collector diameters are shown in Figure 127. The low temperature engine system requires collectors ranging from 50 ft to 65 ft, while the high temperature thruster needs collectors at least three times as large. The collector diameter increase with the extended trip time (Figure 127) is due to the constraints of a fixed volume propellant tank, increasing payload capability and a constant thrust to weight at initial launch.

Other Missions

Several other types of missions were considered to determine the solar thermal rocket systems performance. Three low earth orbit missions are shown in Figures 128 through 130. The first is the dispersal of space debris mission where the vehicle performs a small ΔV maneuver rendezvous to pick up a payload and imparts a similar ΔV to the payload debris before releasing the debris. These maneuvers are repeated until all the vehicles propellant has been expended.

Figure 128 shows the number of maneuvers that can be accomplished using a single orbit launch of a 55 ft. tank and engine system. For example, six maneuvers with ΔV = 4000 ft/sec could disperse 6 payloads of 8400 lb. each payload.

A similar type of mission would be to employ a fully fueled vehicle and gradually collect space debris. Figure 129 shows the number of maneuvers that can be accomplished with the 55 ft. tank vehicle system. The figure shows for example that 6 payloads of 3400 each can be picked up with ΔV = 5000 ft/sec between each maneuver. The dotted line superimposed on the curve is the payload down limitation of 32,000 lb for the Orbiter. This 32,000 lb. would include the payload's collected, the empty solar thermal vehicle and 3000 lb. for support cradle. The example of the 6 payloads is within this down weight limit.

A final type of mission is the sequential deployment of payload (sensors, etc.) with velocity maneuvers between each deployment (Figure 130). Since the vehicle and payloads are carried in a single orbiter launch, a 40 ft propellant tank has been used for the solar thermal rocket vehicle. An example shows that

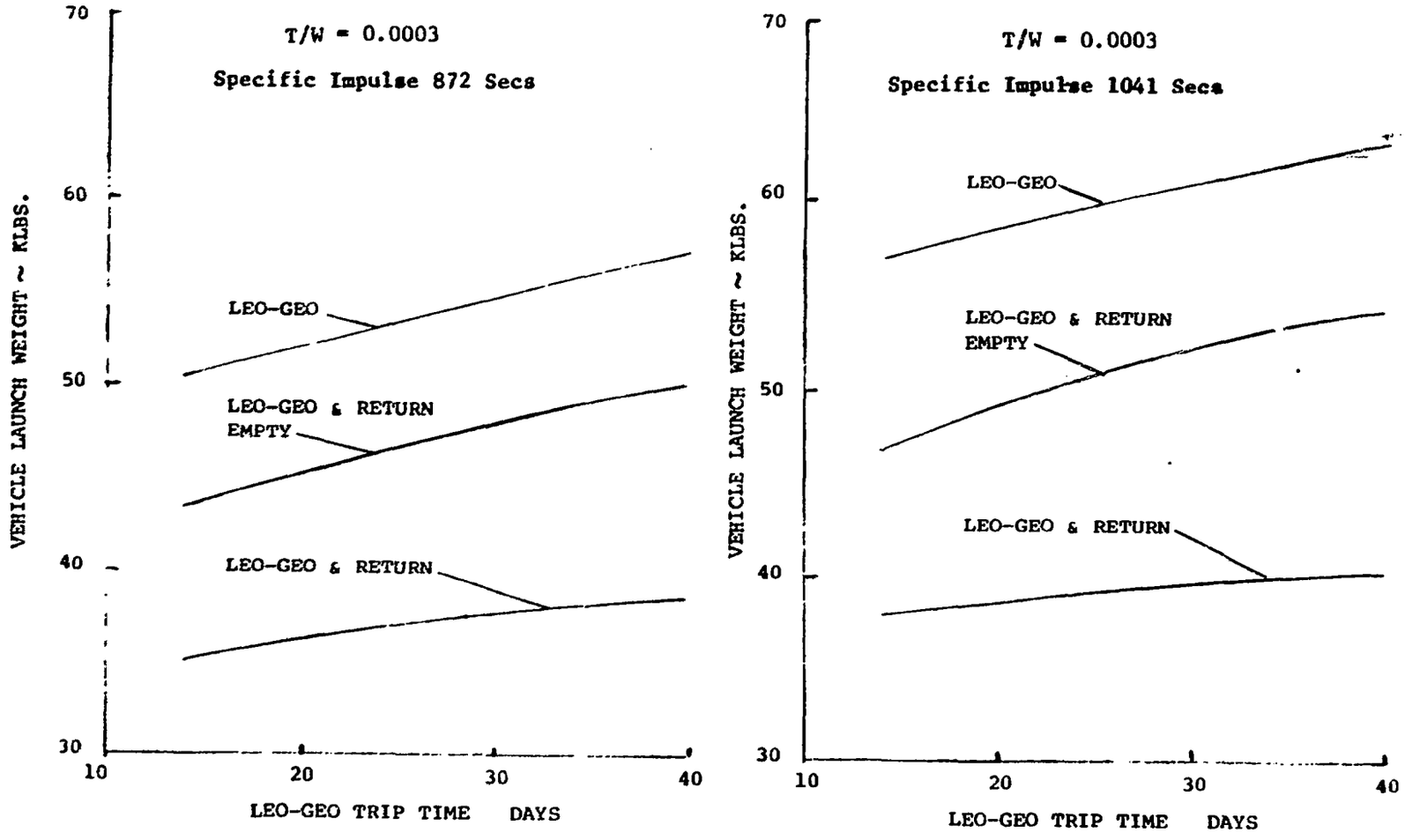

Figure 126. Single Orbiter Launch - Vehicle Launch Weight

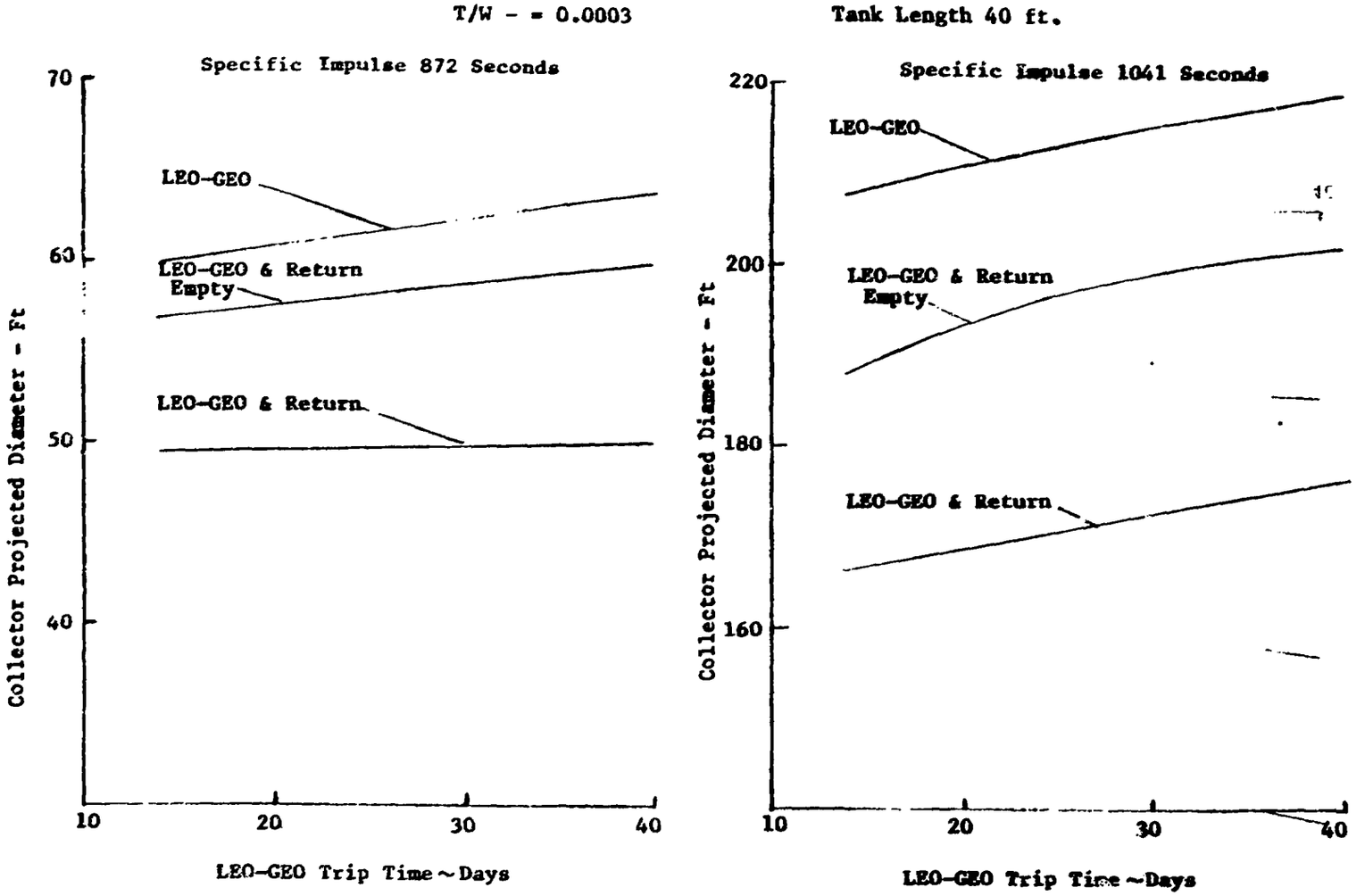

Figure 127. Single Orbiter Launch - Collector Diameters

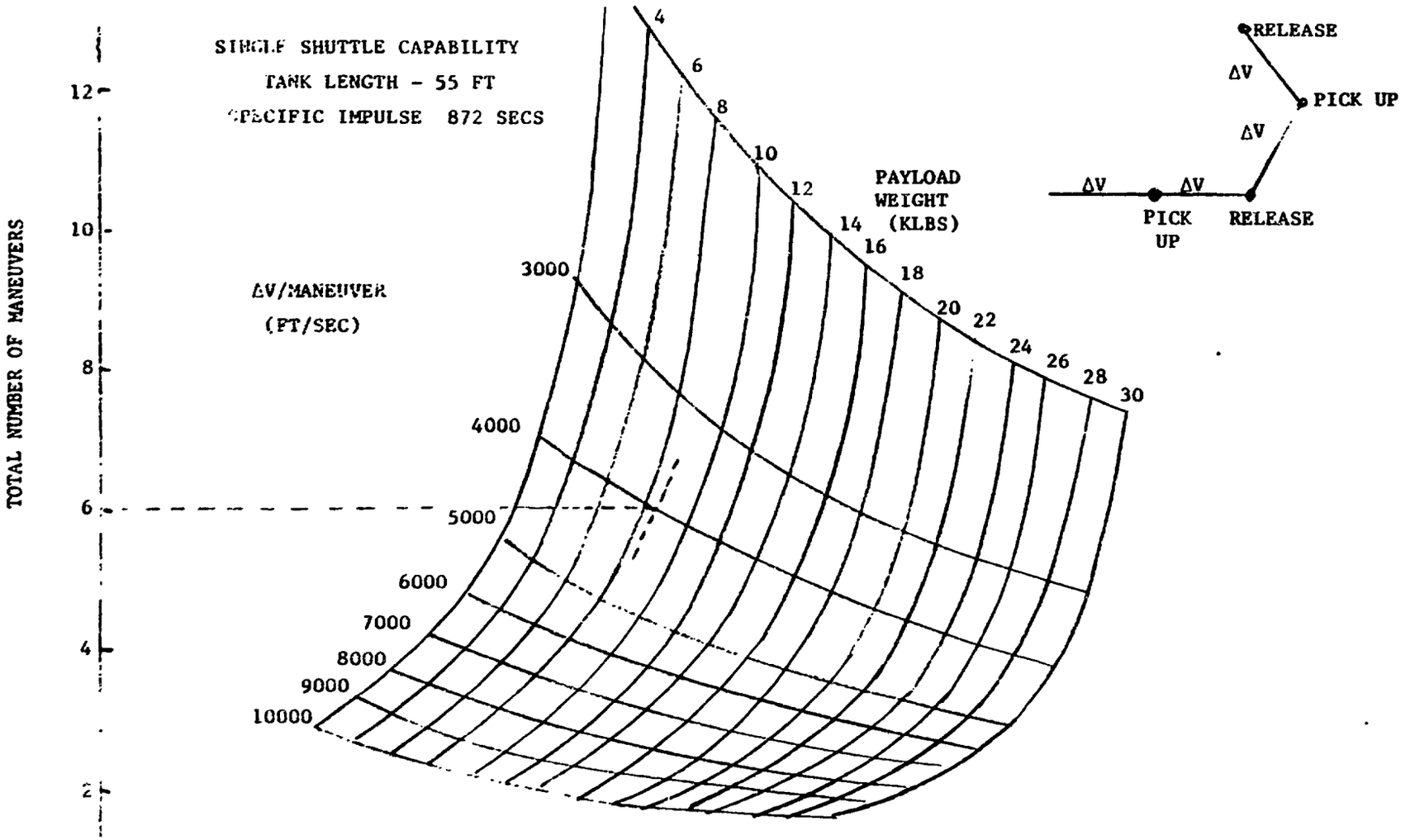

Figure 128. Space Debris Disposal

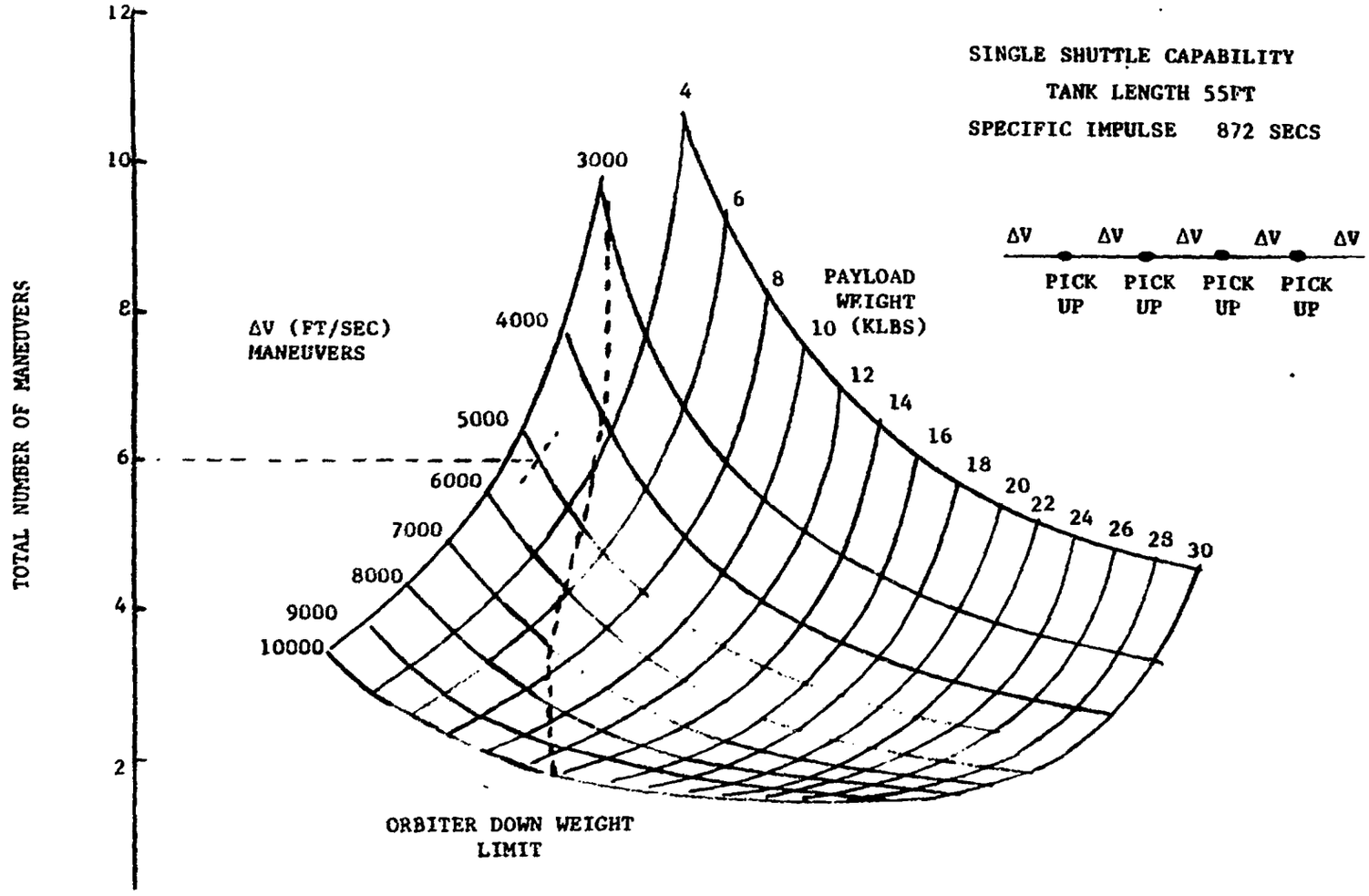

Figure 129. Space Debris Collection

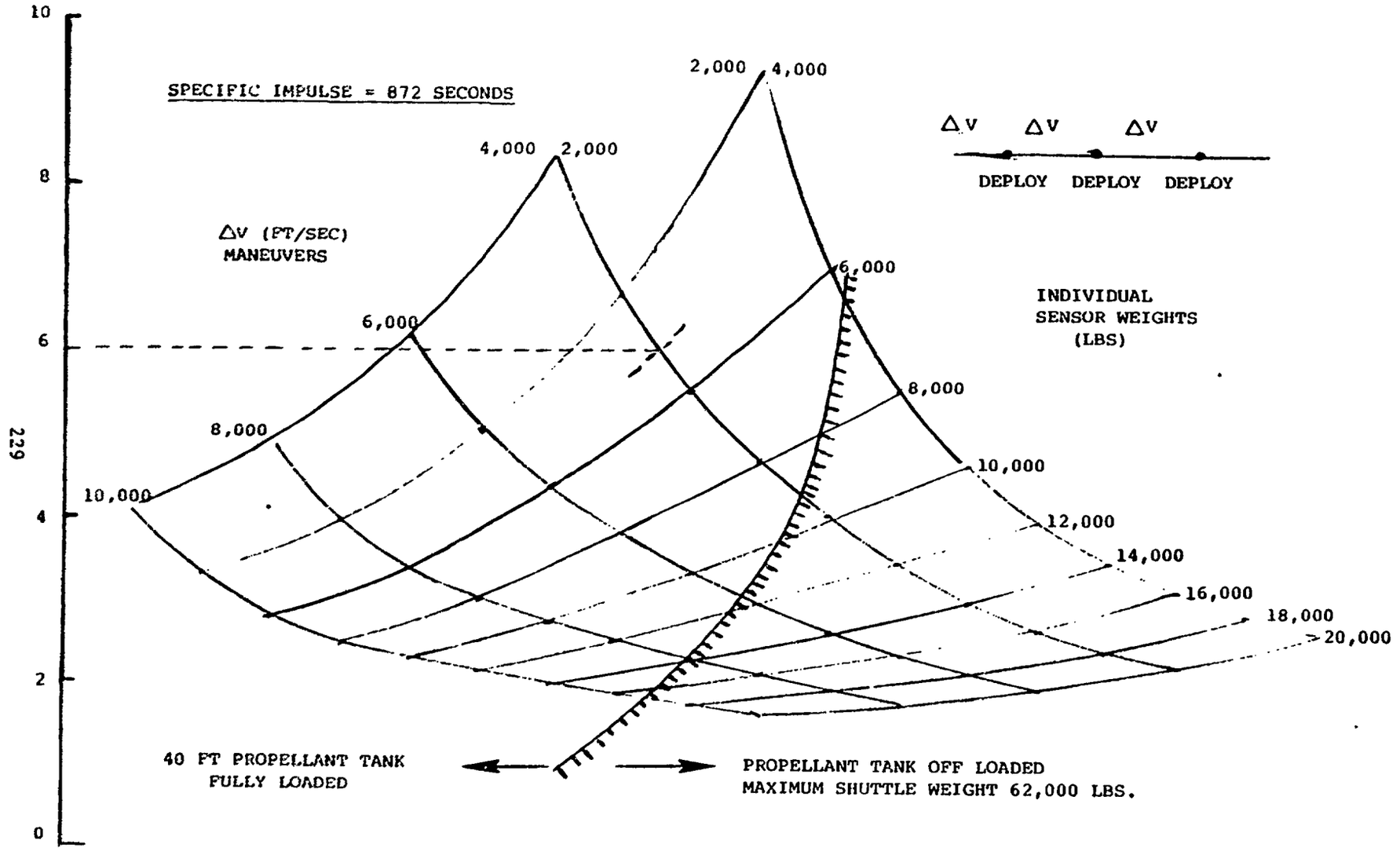

Figure 130. Shuttle Capability For Sensor Deployment

6 sensors weighing 5000 lbs each can be deployed with ΔV = 4000 ft/sec between each deployment. The curves to the left of the boundary line would have a fully loaded 40 ft propellant tank, while those to the right of the boundary line, the tank is off-loaded and the launch weight is constrained to 62,000 lbs.

9.0 CONCLUSIONS AND RECOMMENDATIONS

The material presented below summarizes the conclusions and recommendations drawn at the conclusion of the Solar Rocket System Concept Analysis study.

CONCLUSIONS

1. The 5000°R solar rocket system is within the current state-of-the-art.
2. The 5000°R solar rocket system performance is superior to a second generation LO_2-LH_2 orbit transfer vehicle for multi-day transit times.
3. The payload of the 5000°R solar rocket for the payload-up S/C-down case is significantly greater than the corresponding chemical system.
4. The 7000°R solar rocket system will require a significant development effort but the payoff for the single shuttle launch case is significant.

RECOMMENDED HARDWARE/TEST ACTIVITIES

FY '80

- Proceed with the analysis, design, fabrication and ground test of a 10 lb thrust engine/absorber combination for the 5000°R case.
- Implement the analysis, design, fabrication and test of a 30-40 ft diameter collector.
- Integrate the engine/collector systems for a combined test.

FY '81

- Conduct a shuttle launched space test of a 30-40 ft diameter collector. Consider including a thruster.
- Based on FY '80 results, initiate concept feasibility studies on the 7000°R particulate absorber system.

RECOMMENDED ANALYTICAL STUDIES .

- Pump-fed versus pressure-fed propellants
- Pressurization system design
- Tank insulation design
- Collector optimization (facets, c.g. design)
- Non-uniform stress of parabaloidal membrane
- High accuracy collector fabrication techniques
- Specular reflectance of metallized films
- Defocusing during coast periods
- Collector structural dynamics and thermal deformations
- Optimum steering policy
- Gimballed engines versus RCS jets
- Effect of the multiple restarts requi ed for the perigee burn case on thruster reliability

REFERENCES

1. Investigation of a 15 KW Solar Dynamic Power System for Space Application. Contract AF-33 (615)-7128. Sundstrand Aviation - Denver, A Division of Sundstrand Corporation. Report No. AFAPL-TR-64-156 (Feb. 28, 1965).

2. Centaur D-1 Payload Users Guide. Aerospace Corporation, TOR-066 (5701-07)-1.

3. Orbit-to-Orbit Shuttle Final Report Feasibility Study. Rockwell International, F04701-71-C-0171.

4. Technology Requirements for Future Earth-to-Geosynchronous Orbit Transportation Systems. Contract NAS1-15301, Mid Term Briefing. Boeing Aerospace Company (October 1978).

5. Summary of Centaur-to-Shuttle Integration Studies. General Dynamics Convair Division.

6. Centaur Expands Shuttle Utilization Prior to NOTV Availability. General Dynamics Convair Division (July 19, 1978).

7. Satellite Power Systems (SPS) Concept Definition Study, Final Report, Vol. IV, "SPS Point Design Definition." Contract NASD-32475, DPD541-MA-04. Rockwell International, Space Division, Report No. SD78-AP-0021-4 (April 1978).

8. Project Able, Final Report (U), Vol. I, "Summary." Contract NAS8-20668. Goodyear Aerospace Corporation. Report No. GET-12885 (December 1, 1966).

9. McCusker, Thomas J., Goodyear Aerospace Corporation. Solar Concentrator Design and Construction. Presented as Preprint 64-731 at Third Biennial Aerospace Power Systems Conference, Philadelphia, Sept. 1-4, 1964. Also in "Progress in Astronautics and Aeronautics," Vol. 16 (AIAA), Space Power Systems Engineering (1966).

10. Kreith, F. Radiation Heat Transfer for Spacecraft and Solar Power Plant Design. International Textbook Company (1962).

11. Stephens, C. M., and A. M. Maire. "Internal Design Considerations for Cavity Type Solar Absorbers," Journal of American Rocket Society, 1:896-901 (1961).

12. Space Shuttle System Payload Accommodations, Level II Program Definition and Requirements, Vol. XIV (July 1, 1975).

13. Ramirez, P. Determination of Exhaust Plume Impingement Effects on a Navigational System Spacecraft Insulation Surface During a Roll Maneuver. Rockwell International, Satellite Systems Division, SSD79-0014 (Jan. 17, 1979).

14. Informal Transmittal of Hydrogen Data From J. Shoji, Rockwell Rocketdyne Division, to Paul Ramirez, Rockwell Satellite Systems Division.

15. Improved Scaling Laws for Stage Inert Map Space Propulsion System, Vol. II, "System Modeling and Weight Data." NASA Contract NAS2-6045, Space Systems Group, Rockwell International (June 1971).

16. Saturn SII Advanced Technology Studies: Cryo Storage Thermal Improvement. NASA Contract NAS7-200, Supplemental Agreement 2049. Rockwell International, Space Systems Group (Feb. 1972).